

NASA TECHNICAL
MEMORANDUM

NASA TM X-53189

OCTOBER 1, 1964

NASA TM X-53189

| | | |
|-------------------|-------------------------------|------------|
| FACILITY FORM 602 | N65-24125 | N65-24141 |
| | (ACCESSION NUMBER) | (THRU) |
| | 147 | 1-6 |
| | (PAGES) | (CODE) |
| | TMX-53189 | 34 |
| | (NASA CR OR TMX OR AD NUMBER) | (CATEGORY) |

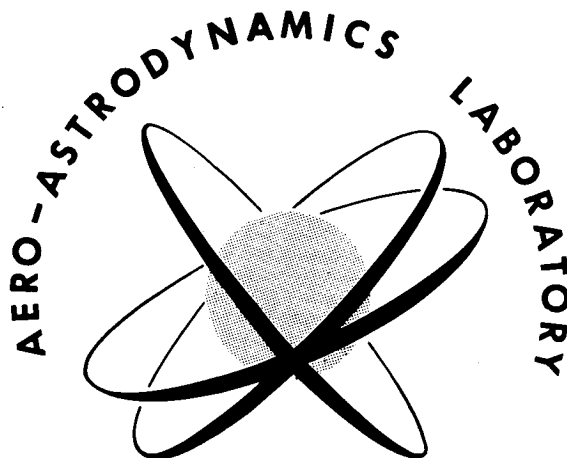
GPO PRICE \$ _____
OTS PRICE(S) \$ _____
Hard copy (HC) \$4.00
Microfiche (MF) \$1.00

**AERO-ASTRODYNAMICS
RESEARCH AND DEVELOPMENT
RESEARCH REVIEW NO. 1**

AERO-ASTRODYNAMICS LABORATORY
RESEARCH AND DEVELOPMENT OPERATIONS
GEORGE C. MARSHALL SPACE FLIGHT CENTER
HUNTSVILLE, ALABAMA

NASA - GEORGE C. MARSHALL SPACE FLIGHT CENTER

TECHNICAL MEMORANDUM X-53189



RESEARCH REVIEW NUMBER ONE
January 1, 1964 - June 30, 1964

RESEARCH AND DEVELOPMENT OPERATIONS
AERO - ASTRODYNAMICS LABORATORY

October 1, 1964

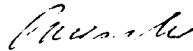
ACKNOWLEDGEMENTS

The articles for this review were contributed by various engineers and physicists of the Aero-Astroynamics Laboratory, reviewed and compiled by William D. Murphree, and edited by Sarah Hightower.

Grateful acknowledgement is given to the Technical Publications Section, Space Systems Information Branch, Management Services Office, MSFC, for preparing the review.

PREFACE

The subjects discussed in this review cover Guidance, Control, Unsteady Aerodynamics, Structural Dynamics, Orbit Theory and Prediction, and selected topics concerning Astrophysics. Other subjects such as Aerothermodynamics and Flight Evaluation will be discussed in forthcoming reviews. It is hoped that these reviews will be interesting and helpful to other organizations engaged in space flight research and related efforts. Criticisms of this review and discussions concerning individual papers with respective authors are invited.



E. D. Geissler
Director, Aero-Astrodynamics Laboratory

I. CONTROL

| | |
|------------------------------------------------------------------------|---|
| Studies in Minimax Control by Kenneth J. Davis and David A. Ford | 2 |
|------------------------------------------------------------------------|---|

II. GUIDANCE

| | |
|--------------------------------------------------------------------------------|----|
| A Boundary Value Formulation For Space Vehicle Guidance by Robert Silber | 12 |
|--------------------------------------------------------------------------------|----|

III. UNSTEADY AERODYNAMICS

| | |
|-----------------------------------------------------------------------------------------------------------------------------------|----|
| Wall Pressure Fluctuations and Skin Vibrations With Emphasis on Free Shear Layers and Oscillating Shocks by Fritz R. Krause | 18 |
| On An Extension of Oswatitsch's Equivalence Rule to Unsteady Flow by M. F. Platzer | 33 |
| On the Pressure Requirements for Structural Response Equations by Richard D. Rechtien | 44 |

IV. STRUCTURAL DYNAMICS

| | |
|---------------------------------------------------------------------------------------------------------------------------------------------------------------------------------------|----|
| Nonlinear Two-Degrees-Of-Freedom Response With Sinusoidal Inputs by Robert S. Ryan | 54 |
| A Simple Method for Determining the Bending Moment Equation That Includes Vehicle Elastic and Sloshing Modes and a Numerical Example by Robert S. Ryan, Fred Swift, and Don Townsend. | 63 |
| On Transient Response of a Multistage Space Vehicle by Frank C. Liu | 69 |
| Nonlinear Vibration of Beams by Frank C. Liu | 74 |
| Lunar Touchdown Dynamics Studies by Robert E. Lavender | 80 |

V. ASTROPHYSICS

| | |
|--------------------------------------------------------------------------------------------------------------------------------|-----|
| A Topographical Study of the F ₂ Region of the Ionosphere by W. T. Roberts and L. G. McDonald. | 88 |
| An Evaluation of a Technique for Predicting Some Indicators of Solar Activity by Jeanette A. Scissum and Robert E. Smith | 93 |
| A Meteoroid Flux and Puncture Model for Near-Earth and Cislunar Space by Charles C. Dalton .. | 96 |
| Surface Properties of Turbulence in the Boundary Layer by Dr. Hans A. Panofsky | 100 |
| Estimation in Mixtures of Two Poisson Distributions by A. Clifford Cohen, Jr. | 104 |

VI. ORBIT THEORY AND PREDICTION

Page

Characteristic Features of Some Periodic Orbits in the Restricted Three-Body Problem
by Wilton E. Causey 110 ✓

Recent Developments in the Prediction of Earth Orbital Satellite Lifetime by H. F. Kurtz, Jr.
and A. R. McNair 119 ✓

VII. PUBLICATIONS AND PRESENTATIONS

A. Publications 126

B. Presentations 136

I. CONTROL

by

Kenneth J. Davis
David A. Ford

N65-24126

SUMMARY

This report presents a new formulation of a minimax problem in launch booster control, and a summary of work done by contractors on the problem. The minimax problem described in the introduction is a mathematical one whose solution would yield a controller which would minimize the maximum possible value of some selected analytical index of booster performance. The work summarized was completed before June 1, 1964, and includes studies by Honeywell (Contract NASw-563) and Control Research Associates (CRA, Contract NAS8-11143). Honeywell's study results in a linear fixed gain controller which minimizes a given criterion under a worst-disturbance condition. CRA has developed a general theory of minimax elements, and has defined a problem whose solution would yield a closed loop controller.

Symbol

Definition

| | |
|------------------------------|--------------------------------------------------------------------------------------------|
| β | Engine swivel angle |
| α_w | Angle of attack due to wind |
| E^n | n-dimensional Euclidean space |
| $F(x)$ | performance index |
| $C(u)$ | "Cost" functional |
| l. u. b. | Least upper bound |
| g. l. b. | Greatest lower bound |
| $x \in X$ | x is a member of the set X |
| l. u. b. $g(x)$ $x \in X$ | Least upper bound of the values $g(x)$ of the function g for x belonging to the set X. |

LIST OF SYMBOLS

| Symbol | Definition |
|------------|------------------------------------------|
| x | n-dimensional state vector |
| A | Constant nxn matrix |
| B, C | Constant n-dimensional vectors |
| $u = u(x)$ | Scalar control law |
| $g = g(t)$ | Scalar disturbance function |
| Ω | Class of control laws $u(x)$ |
| Ψ | Class of proper control laws |
| U | Range of control law $u(x)$ |
| Γ | Class of disturbance functions $g(t)$ |
| T | Terminal time |
| α | Angle of attack |
| ϕ | Angular deviation from reference |
| Z | Lateral deviation (drift) from reference |
| X^0 | Set of controllable initial states |

I. INTRODUCTION

This report records results thus far on a minimax problem related to launch booster control. The motivation for the problem is the reduction of peak values of some selected index of vehicle performance, while at the same time maintaining other vehicle performance characteristics within prescribed bounds.

In section two of this report, a mathematical formulation of the minimax problem is given. This problem statement involves a linear plant, with a time-varying disturbance entering as a forcing term. The bounds on performance characteristics are incorporated as state variable constraints. The objective is the determination of a control law which will minimize the maximum value of a given (nonintegral) performance index. The maximum is taken relative to a particular set of initial conditions and a particular class of disturbances, as well as over a given finite time interval.

Since this type of problem differs from the usual variational problems, and does not yield readily to standard techniques, the statement is given in terms which emphasize the qualitative aspects of the problem.

While the ultimate goal is the development of effective procedures for computing the optimal control, the immediate goal is to obtain mathematical insight into the nature of the problem. Consequently, the problem is stated in general mathematical terms so that it may be amenable to rigorous mathematical treatment.

Section three is a summary of work done under contract by Honeywell, Inc. In this study the case of a general linear plant with a linear controller and a bounded disturbance is considered. Honeywell imposes zero initial conditions and no intermediate or terminal conditions. A linear performance index is treated, and a procedure is developed for finding the maximum value of this cost index for a given linear controller. In addition, Honeywell applied their technique to two second-order and one fourth-order (rigid launch vehicle) example.

The results obtained by Control Research Associates (CRA) are summarized in section four. In contrast to the M-H approach, their efforts have been directed toward the more qualitative aspects of the problem. In particular, they have made a study of the general theory of minimax elements. Their most significant contribution has been in the formulation of a meaningful mathematical statement of the problem.

II. THE PROBLEM STATEMENT

The terms in which the problem will be stated are as follows. The unforced booster dynamics are represented by a homogeneous linear vector matrix differential equation

$$\dot{x} = A x, \quad (2.1)$$

where x is an n -dimensional state vector, and A is an $n \times n$ matrix. The control process for the whole first stage flight will be thought of as being made up of a sequence of shorter processes, each T seconds in length, where the time interval $0 \leq t \leq T$ is sufficiently small to allow the coefficients in the matrix A to be considered constant throughout the interval. The controller enters the system as a scalar u . A scalar g is introduced into the system to represent wind effects in the booster, where mathematically $g = g(t)$ is restricted to a suitable class of functions Γ . With these additions, the system (2.1) is rewritten as

$$\dot{x} = A x + B u + C g, \quad (2.2)$$

where B and C are constant n -vectors.

To clarify the terminology used above, the rigid body booster dynamics will be transformed to the form (2.2). The standard rigid body equations of motion

can be written as

$$\dot{\alpha} = \dot{\phi} + \dot{\alpha}_w - \frac{1}{V} (K_1 \phi + K_2 \alpha + K_3 \beta)$$

$$\dot{\phi} = -C_1 \alpha - C_2 \beta$$

$$\dot{\beta} = K (\beta + \beta_c).$$

(The first equation is the result of combining $\dot{\alpha} - \dot{\alpha}_w = \dot{\phi} - \dot{Z}/V$ and $\dot{Z} = K_1 \phi + K_2 \alpha + K_3 \beta$). This system is transformed into the "state variable" form (2.2) by letting $x_1 = \phi$, $x_2 = \dot{\phi}$, $x_3 = \alpha$, $x_4 = \beta$, $u = \beta_c$ and $g = \dot{\alpha}_w$. In vector matrix notation the rigid body equations become

$$\begin{pmatrix} \dot{x}_1 \\ \dot{x}_2 \\ \dot{x}_3 \\ \dot{x}_4 \end{pmatrix} = \begin{pmatrix} 0 & 1 & 0 & 0 \\ 0 & 0 & -C_1 & -C_2 \\ -\frac{K_1}{V} & 1 & -\frac{K_2}{V} & -\frac{K_3}{V} \\ 0 & 0 & 0 & K \end{pmatrix} \begin{pmatrix} x_1 \\ x_2 \\ x_3 \\ x_4 \end{pmatrix} + \begin{pmatrix} 0 \\ 0 \\ 0 \\ K \end{pmatrix} u + \begin{pmatrix} 0 \\ 0 \\ 1 \\ 0 \end{pmatrix} g.$$

Generally, at MSFC the linear control law is $u = \beta_c = a_0 \phi + a_1 \dot{\phi} + b_0 \alpha$ or $u = k_1 x_1 + k_2 x_2 + k_3 x_3$ and $g = \dot{\alpha}_w$ corresponds to the MSFC design winds (Cape Kennedy). Here, however, the control u is not restricted to be a linear control law; indeed, it may be of nonlinear form such as the optimal bang-bang control law. The control u may depend explicitly on time t or the state vector x . Preferably, however, the control takes the form $u(x)$ of a feedback control law. The range of u is restricted to a bounded set U , and the class of admissible controllers for the problem is denoted by Ω . In some studies concerning the rigid body problem mentioned above, the class of controls might be the set of all linear controls.

To assure adequate booster performance, the state vector x is constrained to lie in a region R in E^n . The characteristics of the region R depend upon the particular system under investigation. For example, it may be necessary to restrict linear combinations of the state variables x so that desirable booster performance can be obtained. These combinations can be written as the dot product $l^i \cdot x$, and the restrictions can be represented by inequalities in the following general form:

$$|l^i \cdot x| \leq L_i, \quad i = 1, 2, \dots, r \quad (2.3)$$

where the L_i are positive constants. To illustrate this formulation, consider the booster rigid-body example and the restriction of maintaining the bending moments on the booster within the structural design limits.

This can be written in the form (2.3) by

$$|\ell_3^1 x_3 + \ell_4^1 x_4| \leq L_1,$$

where $\ell_3^1 = M'_\alpha$, $\ell_4^1 = M'_\beta$, and L_1 is the structural design limit for the bending moments. These restrictions, along with others imposed by the physical situation such as limit on engine deflection angle β and perhaps a limit on attitude angle φ , determine the region R .

Continuing with the general formulation of the problem, it is assumed that a set X^0 of initial states exists having the property that there is a control u in Ω such that for each initial state $x^0 \in X^0$, and each disturbance $g \in \Gamma$, the solution $x(t; u, g, x^0)$ to equation (2) (which is initially $x(0; u, g, x^0) = x^0$) remains in R throughout the time interval $0 \leq t \leq T$. The set X^0 is called the set of controllable initial states. To state this in terms of the booster rigid body system, consider the initial states for the state variables $\phi, \dot{\phi}, \alpha, \beta$ for any interval of flight time (e.g., 60-70 sec.). The initial states are such that, for any wind the vehicle encounters, there exists a control u which will maintain the state variables so as to satisfy all restrictions imposed on them.

Once a controllable set X^0 is given, it is necessary to consider, within the set Ω of allowable controls, only those which control the vehicle from each initial state in X^0 , and for each disturbance $g \in \Gamma$. Let Ψ denote this subset of Ω defined mathematically as follows: $u \in \Psi$ if for each $x^0 \in X^0$, and each $g \in \Gamma$, $x(t; u, g, x^0)$ remains in R for $0 \leq t \leq T$. The members of Ψ will be called proper controls.

A second condition on x , and on the initial region X^0 , stems from the fact that the terminal state $x(T; u, g, x^0)$ is an initial state for the controller in the next time period. Thus, it is required that $x(T; u, g, x^0)$ belong to the set of controllable initial states for the succeeding time period. This amounts to placing terminal conditions on the problem. (The requirement for the terminal conditions on the problem is a result of the approach to the formulation of the problem. The choice was either to consider the problem from a time-varying standpoint or to use a constant parameter (time-invariant) formulation. The latter approach was chosen because of the apparent simplicity in the formulation and tractability of the problem). Since the problem is formulated for the constant coefficient case, the flight region must be broken up into segments in which the parameters are almost constant. It is therefore understandable that the controllable initial states for one segment must be the terminal conditions for the preceding segment.

A minimax problem is now formulated in this setting. A non-negative functional

$$F(x_1, x_2, \dots, x_n) = F(x)$$

is introduced as an index of performance. The "cost" for a given control u is then defined by

$$C(u) = \max_{g \in \Gamma} \max_{x^0 \in X^0} \max_{t \in [0, T]} F(x(t; u, g, x^0)). \quad (2.4)$$

The expression $C(u)$ is a general mathematical representation of a peak value of some vehicle parameter. For example, $C(u)$ could be taken as the peak bending moment under a worst-case wind, for a worst initial condition. Since the object of the minimax controller is the reduction of this peak, the minimax problem is that of finding a controller u^* such that

$$C(u^*) = \min_{u \in \Omega} C(u).$$

The controller u^* would therefore guarantee the peak bending moment to be the smallest value found, within limitations, for any control u which could be considered. The choice of a functional F would generally depend on the constraints placed on x . For example,

$$F(x) = \max_{1 \leq i \leq r} |\ell^i \cdot x|,$$

where the ℓ^i are the constant vectors of expression (2.3). Another possibility would be

$$F(x) = \sum_{i=1}^n |\ell^i \cdot x|,$$

which would minimize an "average" worst case.

The problem will now be summarized. For a particular time interval of length T , the motion is described by the system

$$\dot{x} = A x + B u + C g.$$

For this time interval, we seek a controller $u^* \in \Omega$ such that

(1) u^* forces the system to remain in R throughout the flight time for all disturbances $g \in \Gamma$ and all initial states $x^0 \in X^0$,

(2) each of the possible terminal states for the time interval under consideration is a controllable initial state for the next time period,

(3) u^* minimizes the maximum value of a given function $F(x)$.

The desired controller for the entire flight time will be the combination of the controllers for the particular intervals.

III. HONEYWELL'S STUDY

Honeywell considers the minimax problem for the case of a linear feedback control, zero initial conditions, no state variable constraints, and bounded disturbance. It is shown that, for a given fixed-gain linear control law, the "worst" disturbance, that is, the one which maximizes the peak value of a given (linear) performance index is bang-bang. The performance index chosen has the form

$$F(x) = |\ell \cdot x|,$$

where ℓ is a constant n -vector. Honeywell develops a procedure for determining the worst disturbance and for computing the cost incurred under this disturbance. They then find the minimum cost by using an iteration procedure. They also present examples to illustrate their techniques. The remainder of this section is devoted to summarizing their work.

The class of controls Ω consists of fixed gain linear control laws in the form

$$u(x) = \sum_{i=1}^n k_i x_i, \quad (3.1)$$

where some restriction, such as

$$\sum_{i=1}^n k_i^2 = 1,$$

is placed on the gain coefficients k_i . The subclass Ψ of proper controls is all of Ω in this case, since neither constraints nor terminal conditions are present. The class of disturbances Γ consists of all measurable functions g restricted by $|g| \leq 1$. Only the case of zero initial conditions $x^0 = 0$, is treated. (Honeywell has reported recently that the mathematical difficulties which imposed the zero initial condition have been overcome.)

Since the control u depends only on the state variable, x , substitution of a given control law in equation (2.2) results in a right-hand side which depends only

on x and g . Considering g as the control, the problem of maximizing a performance index is an optimal control problem. This modified system has the form

$$\dot{x} = \hat{A}x + Cg \quad (3.2)$$

where

$$\hat{A} = A + Bk^T$$

and k^T denotes the transpose of the $n \times 1$ matrix (vector) whose components are the gains k_1, k_2, \dots, k_n of (3.1).

The performance index whose maximum value is to be minimized is represented in the form

$$F(x) = |\ell \cdot x|.$$

In accordance with the terminology of section 2, the cost for a given control u is given by

$$C(u) = \max_{g \in \Gamma} \max_{0 \leq t \leq T} |\ell \cdot x(t; u(x), g, 0)| \quad (3.3)$$

or more simply,

$$C(u) = \max_{g \in \Gamma} \max_{0 \leq t \leq T} |\ell \cdot x(t; u, g)|. \quad (3.4)$$

In the report, two useful simplifications of the expression for $C(u)$ are made possible because of the restrictions on x^0 and on g . Since only zero initial conditions are considered, it is found that no generality is lost in assuming that $\max_{0 \leq t \leq T} |\ell \cdot x(t; u, g)|$ always

occurs at the final time T . Furthermore, since $g(t)$ is confined to a symmetric region, it is sufficient to consider the case where $\ell \cdot x(t; u, g)$ is non-negative, and consequently, the absolute values in (3.4) may be dropped. Therefore,

$$C(u) = \max_{g \in \Gamma} [\ell \cdot x(T; u, g)], \quad (3.5)$$

which is the final expression for the "cost."

The main contribution of Honeywell is in the determination of a "worst" disturbance \bar{g} , that is, one which satisfies

$$C(u) = \ell \cdot x(T; u, \bar{g}). \quad (3.6)$$

The central idea, as suggested above, is that of letting the disturbance g in equation (3.2) take the role of a control, and applying the theory of time-optimal control to yield a bang-bang "controller" \bar{g}

which maximizes the performance index

$$I = x(T; u, g)$$

of (3.6).

The solution of this problem leads to the construction of \bar{g} in the following form. Let $y(t)$ denote the solution to the system

$$\dot{y} = -\hat{A}y \quad (3.7)$$

with terminal condition

$$y(T) = I.$$

Then, in terms of this solution,

$$\bar{g}(t) = \text{sgn}[y(t) \cdot C]$$

is the desired "worst" disturbance.

In review, it should be pointed out that the above results apply to the zero initial condition case.

In some cases the cost $C(u)$ is expressible explicitly in terms of the gains k_1, k_2, \dots, k_n , in which case one may attempt to find the control $u(x)$ which minimizes $C(u)$ by analytical techniques. In their report, Honeywell develops such a procedure for the plants $\dot{x} = u + g$ and $\ddot{x} + x = u + g$, where the terminal time T is taken at $+\infty$.

A more usual situation is that the cost is not obtainable explicitly in terms of the gains, but rather a selection of apparently suitable control laws is made, and the cost computed for each. The selected control law yielding the least cost is then chosen as the optimum control law. This approach is used by Honeywell in the example discussed in the following paragraphs.

This example was chosen by the contractor to illustrate the developed techniques for a more or less realistic approximation to the problem of rigid body control of a typical launch vehicle. The conventional rigid body equations of motion were used in conjunction with a control law having fixed gains in the pitch rate feedback loop and in the pitch attitude and normal acceleration filtered feedback loops. The rigid body equations of motion were written in the form of (2), with state variables

$$x_1 = \phi, x_2 = \dot{\phi}, x_3 = \dot{Z}, x_4 = \beta.$$

Cost indices of the form

$$C_i(u) = \max_g r_i(x_i(T; u, g)), i = 1, 2, 3, 4$$

were considered where the weighting factors r_i were chosen to permit comparison of the peak values of the state variables. For each control u , the largest of the values $C_i(u)$ was taken as the cost $C(u)$. The cost was computed for an initial choice of gains, and an iterative procedure for improving the choice was implemented which subsequently reduced the initial cost by 25 percent. The closed loop roots of the optimally controlled system were $-.0047, -.44$, and $-.137 \pm j(1.126)$. The computer time involved was approximately two hours on Honeywell's H-800 digital computer. Transient responses for the extremal disturbances producing the minimum of the $C_i(u)$ are given in Figures 3 through 6.

IV. CRA'S WORK

This section summarizes work done by CRA on the minimax problem during February, March, and April, 1964. The initial interest of the contractors has been in the mathematical theory upon which the problem is based. Accordingly, the earlier reports contain a survey of minimax elements in general. Included in this is a discussion of topological results which are associated with the problem. At this point, the most significant contribution of CRA has been the mathematical formulation of the problem. The formulation conceived is a considerable improvement over earlier statements of the problem.

Some of the general theory presented follows. Let X and Y be spaces and let F be a mapping of $X \times Y$ into a bounded set S of the real numbers. The authors present a proof of the known result

$$\text{g.l.b.}_{y \in Y} [\text{l.u.b.}_{x \in X} F(x, y)] \geq \quad (4.1)$$

$$\text{l.u.b.}_{x \in X} [\text{g.l.b.}_{y \in Y} F(x, y)].$$

Briefly, this says that the minimax is at least as large as the max-min. It is also pointed out that, under the above nonrestrictive conditions, it is possible to obtain a very good approximation of the minimax solution. In particular, it is proved that, if ϵ is any positive number, then there exists a point (x_0, y_0) in $X \times Y$ such that

$$|F(x^0, y^0) - \text{g.l.b.}_{y \in Y} [\text{l.u.b.}_{x \in X} F(x, y)]| < \epsilon. \quad (4.2)$$

To see the significance of this result, we note that, in the case where the minimax exists, we have

$$\text{g.l.b.}_{y \in Y} [\text{l.u.b.}_{x \in X} F(x, y)] = \min_{y \in Y} \max_{x \in X} F(x, y).$$

Thus, this theorem says that, even if the minimax does not exist, we are assured of an approximation of the desired value to within any specified degree of accuracy.

By placing restrictions on the spaces X and Y and on the function F , a more precise theorem is proved concerning the existence of a minimax solution.

Theorem. If each of X and Y is a sequentially compact metric space and F is a continuous real valued function defined on $X \times Y$, then there exists a point $(x^0, y^0) \in X \times Y$ such that

$$F(x^0, y^0) = \min_{x \in X} \max_{y \in Y} F(x, y).$$

This theorem is actually proved as a corollary to a more general theorem involving semicontinuity and general topological spaces.

Turning to the minimax problem in control theory, the contractors considered the system

$$\dot{x} = f(x, u, g), \quad (4.3)$$

where f is an n -vector function and x , u and g are as given in section II. The region R is assumed to be of the form $\|x\| \leq r$

where

$$\|x\|^2 = \sum_{i=1}^n x_i^2.$$

The terminal set X^1 is taken to be all of R .

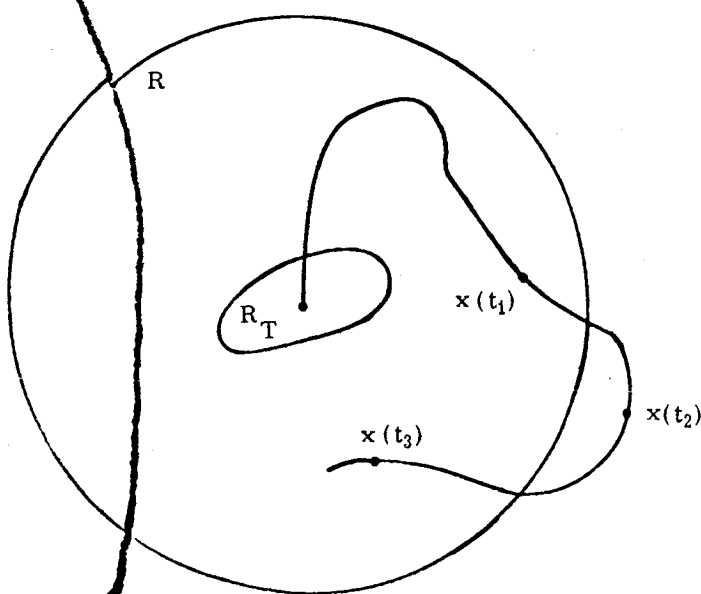


FIGURE 1. ILLUSTRATION OF T-TAME

The contractors introduced two new concepts which are defined below.

Definition 1. The system (4.3) is said to be T -tame with respect to R if there exists a subregion $R_T \subset R$ such that, for any $x^0 \in R_T$ and any $g \in \Gamma$, there exists a control $u \in \Omega$ such that $x(t; u, g, x^0) \in R$ for all t such that $0 \leq t \leq T$ (Fig. 1).

The system indicated in Figure 1 is t_1 -tame but it is not t_2 -tame or t_3 -tame. A typical trajectory is shown in Figure 1.

Definition 2. The system (4.3) is said to be uniformly T -tame with respect to R if there exists a subregion $R_T \subset R$ and a nonvacuous subclass Ψ of Ω such that $x(t; u, g, x^0) \in R$ whenever $x^0 \in R_T$, $g \in \Gamma$, $u \in \Psi$ and $t \in [0, T]$. The idea of T -tameness seems to be of significant importance. When working with a system which is uniformly T -tame, we are assured of the existence of a "controllable set" of initial states and at least one controller which will insure adequate booster performance against all admissible winds. Without this property, we would be in the undesirable position of having our controller $u(x)$ depend explicitly on the wind.

Example:

The system

$$\dot{x}_1 = x_2$$

$$\dot{x}_2 = u + g$$

with $|u| \leq 1$, $|g| \leq 1$, and $T = 2$ sec, is uniformly T -tame with respect to the region R , defined by

$$|x_1| \leq 2$$

$$|x_2| \leq 2.$$

R_T may be taken to consist of the strip in R between the lines $x + 2y = 2$ and $x + 2y = -2$. Any initial state in R_T may be controlled for any g (satisfying $|g| \leq 1$) by taking $u = -\text{sgn } x_2$ (Fig. 2).

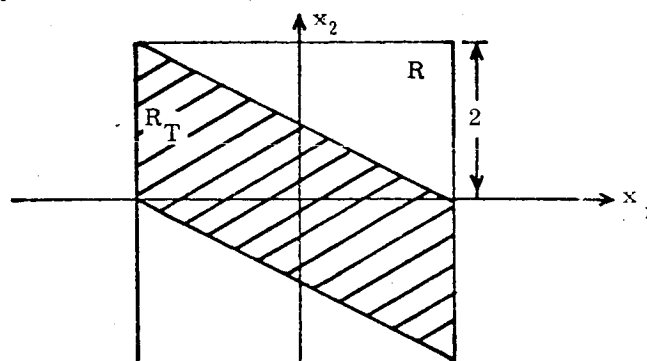


FIGURE 2. REGIONS R AND R_T FOR EXAMPLE

The assumption that our system be uniformly T-tame with respect to R is fundamental in the work of CRA. These concepts have been useful to the contract monitors in preparing the new problem statement. In fact, the R_T in the definitions above can be identified with the X^0 of the problem statement. Furthermore, the statement that the system (4.3) is T-tame is equivalent to the assumption made in the problem statement that an "adequate" controller does exist.

The last progress report from CRA included a discussion of the expression "uniformly T-tame." It contained an explanation of the significance of the term and of its relationship to the (nonuniform) T-tameness

CONCLUSIONS

The introduction of this report provides a complete statement of a minimax problem in launch booster control. Two aspects of this essentially new formulation should be pointed out. First, there is not a particular index of performance which may be singled out as the index of performance for the problem. The second point is that the problem includes terminal constraints on x .

The most useful form for the controller is the $u(x)$ form. Honeywell's study chooses this type of controller, and carries their technique through to a computational algorithm. One shortcoming of this scheme is that the only constraint which they place on their state variable is the undesirable one of zero initial state. Another drawback of Honeywell's procedure is that, in most cases, the optimum $u(x)$ is one of a preselected set of control laws rather than a control law derived from the process. That is, the only thing which they provide is the determination of the worst-case cost for a given controller. Their approach has been applied successfully to in-house studies involving equations for a rigid booster with a first order actuator lag, where the maximum bending moment is to be minimized. A report will be written on this work in the near future.

The work of CRA has centered around obtaining a sound formulation of the problem. Their work contributed heavily to the essentially new statement of the problem given in the introduction to this report.

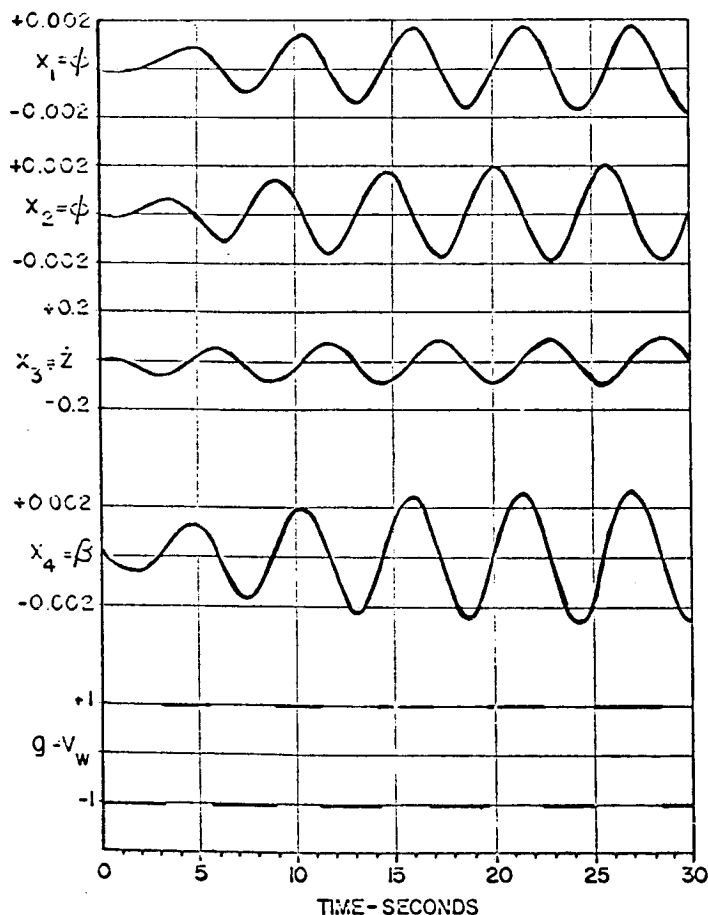


FIGURE 3. RESPONSE TO EXTREMAL DISTURBANCE WHICH MAXIMIZES x_1

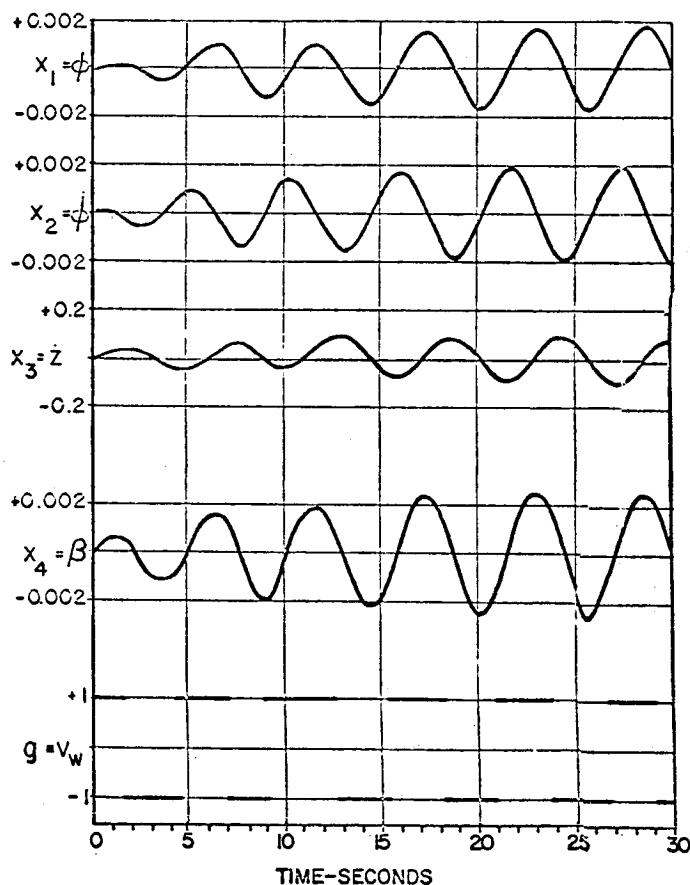


FIGURE 4. RESPONSE TO EXTREMAL DISTURBANCE WHICH MAXIMIZES x_2

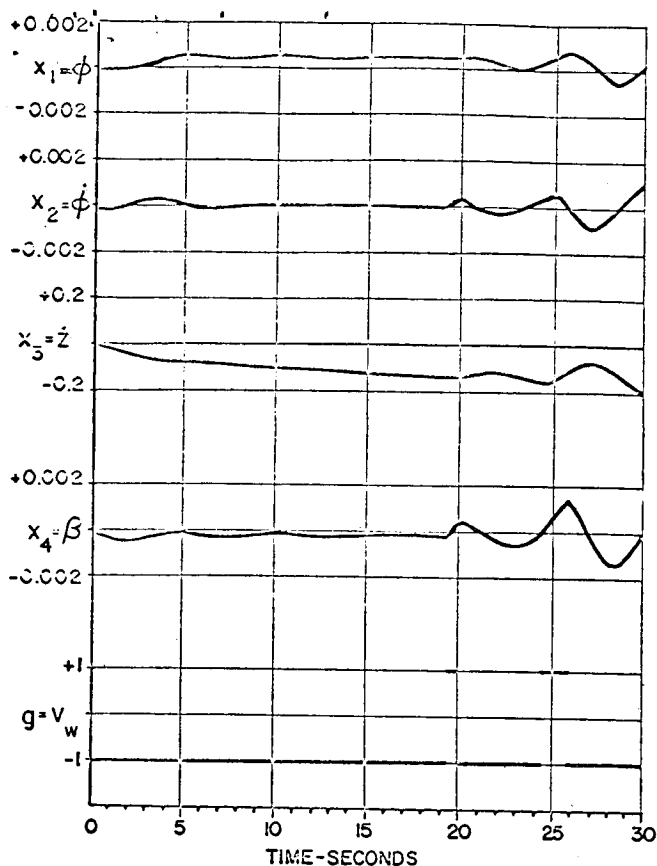


FIGURE 5. RESPONSE TO EXTREMAL DISTURBANCE WHICH MAXIMIZES x_3

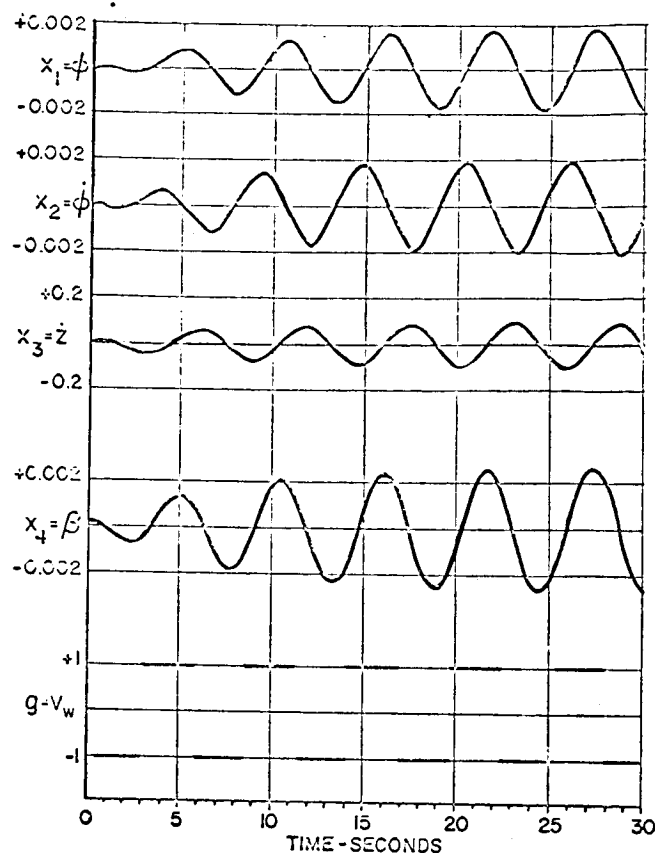


FIGURE 6. RESPONSE TO EXTREMAL DISTURBANCE WHICH MAXIMIZES x_4

REFERENCES

1. Harvey, C. A., Section 14 of final report for Contract NASw-563, "Minimum Disturbance Effects Control of Linear systems With Linear Controllers,"

Military Products Group, Honeywell, Inc., December 30, 1963.

2. Progress report numbers two, three, and four from Contract NAS8-11143, "Advance Research on Control System for the Saturn Launch Vehicle," Control Research Associates, 1964.

II. GUIDANCE

A BOUNDARY VALUE FORMULATION FOR SPACE VEHICLE GUIDANCE

By

Robert Silber

N65-24127

SUMMARY

Part 1 of this two-part paper presents a discussion of the general notion of guidance of space vehicles, the purpose of which is to arrive at an understanding and description of the decision process which is central to the steering of a space vehicle. In many cases, the decision process can be embodied in a set of mathematical functions, called control laws. The second part of the paper is concerned with the numerical representation of the control laws. One way in which this may be accomplished, with the aid of a digital computer, is by the expansion of the control laws in Taylor's series about known data. This procedure is described and explained. A more detailed treatment of the material of this paper can be found in References 1 and 2.

I. SPACE VEHICLE GUIDANCE

A. INTRODUCTION

A convenient starting point for a discussion of fundamentals of space vehicle guidance can be found in the following list of basic inputs:

- (1) Flight Environment
- (2) Vehicle Performance Characteristics
- (3) Mission
- (4) Optimization Criteria.

This introduction consists of considerations of these four items, which are pertinent to steering a space vehicle.

By the flight environment is meant the physical situation in or through which the vehicle is expected to fly, i.e., its universe. Mathematically, this amounts to the total extra-vehicular accelerations experienced by the vehicle during flight. Primary examples are the gravities of neighboring bodies and, in many cases, atmospheric drag. For nonatmospheric flight, it is assumed that in some coordinate system, the environmental accelerations are known functions of, at most, the position and velocity coordinates of the vehicle and, possibly, time. If the vehicle is considered as a point of variable mass, this is sufficient. When rigid body dynamics are of interest, the situation

is slightly more involved. For purposes of this treatment, we shall take the former viewpoint.

By vehicle performance characteristics is meant those parameters pertaining to the vehicle and of significance to its motion. In this category are placed those parameters defining the magnitude and direction of the vehicular thrust vector. For atmospheric flight the effects of vanes, rudders, and more generally of vehicle geometry must be considered. As a special subclass of parameters in this category, we have the flight controls. For steering a space vehicle, certain devices are available for application, within constraints, by a pilot or computer, for the purpose of appropriately influencing the motion of the vehicle. The instantaneous effects of such devices manifest themselves as parameters in the differential equations of motion of the vehicle. These parameters are the above mentioned flight controls. Typical constraints encountered are upper and lower bounds on the values of these parameters as well as the necessity of time - continuous or piecewise continuous variations.

The third item, the mission, is a problem area in itself. Generally speaking, the mission is stated qualitatively. For purposes of space vehicle guidance, the mission must be stated analytically. The transition from one to the other generally brings an investigator face to face with many of the classical unsolved problems of celestial mechanics. However, the modern computer has made feasible many numerical approaches hitherto undeveloped. In any case, the mission is assumed to determine a number of mathematical relationships among the position and velocity coordinates of the vehicle and possible time, the simultaneous satisfaction of which is both a necessary and sufficient condition for mission fulfillment. For our discussion, these relationships, called mission criteria, are assumed known.

In many cases it is advantageous to consider a stated mission as a member of a family of missions. As an example, an earth orbit of given eccentricity, major axis, inclination, etc., can be embedded in a family of earth orbits of varying eccentricities, major axes, inclination, etc. Generally, the family is assumed to be defined by certain parameters, called mission parameters. Each mission of the family differs from the others by alteration of one or more of the mission parameters.

Consider now the fourth item, optimization criteria. It can and does happen that in steering a space vehicle from a given set of conditions, one encounters a multiplicity of possible trajectories leading to mission satisfaction. In such circumstances, it is natural to seek out the best or optimum trajectory. The criteria by which one decides which trajectory offers the most desirable solution shall be called optimization criteria. For our purposes, the optimization criteria are assumed to be dependent on the considered family of missions, but not on individual members.

The preceding comments are sufficient to allow a discussion of the steering decision itself. We shall see how this decision is related to the four items just discussed by way of the differential equations of motion of the vehicle.

B. THE STEERING DECISION AND THE DIFFERENTIAL EQUATIONS OF MOTION

If the flight environment and vehicle performance characteristics are known, then for an assumed set of values for the flight controls, the instantaneous differential equations of motion can be written. To discuss this, we introduce the following notation.

In a three-dimensional Cartesian coordinate system, let x , y , and z be the position coordinates of the vehicle. Let u , v , and w be velocity coordinates: $\dot{x} = u$, $\dot{y} = v$, and $\dot{z} = w$. Let m denote the instantaneous mass of the vehicle. Let F denote the instantaneous magnitude of the vehicular thrust, and let the direction of this thrust vector be defined by the two angles φ and θ . (The actual convention for measuring φ and θ is not pertinent here.) As usual, t denotes time and a dot indicates differentiation with respect to time.

Using Newton's second law and dividing by $m \neq 0$, one can generally obtain expressions of the form

$$\begin{aligned}\dot{x} &= u, \\ \dot{y} &= v, \\ \dot{z} &= w, \\ \dot{u} &= f(F, \varphi, \theta, m, x, y, z, u, v, w, t), \\ \dot{v} &= g(F, \varphi, \theta, m, x, y, z, u, v, w, t), \\ \dot{w} &= h(F, \varphi, \theta, m, x, y, z, u, v, w, t).\end{aligned}$$

Other differential equations may or may not appear, depending on the construction of the vehicle. For example, some vehicles are of constant thrust,

so that additionally

$$\begin{aligned}\dot{F} &= 0 \\ \dot{m} &= c, \text{ a constant.}\end{aligned}$$

When all equations are written, the flight controls, since they are open for selection, will appear on the right hand side of the system, but not on the left. By way of illustration, we consider the constant thrust vehicle. This has the system

$$\left. \begin{aligned}\dot{x} &= u \\ \dot{y} &= v, \\ \dot{z} &= w, \\ \dot{u} &= f(F, \varphi, \theta, m, x, y, z, u, v, w, t), \\ \dot{v} &= g(F, \varphi, \theta, m, x, y, z, u, v, w, t), \\ \dot{w} &= h(F, \varphi, \theta, m, x, y, z, u, v, w, t). \\ \dot{F} &= 0, \\ \dot{m} &= c.\end{aligned} \right\} \quad (1)$$

Since the thrust is of constant magnitude, the pilot has available the direction of thrust for steering. Thus, the flight controls are φ and θ , and these are the two parameters appearing on the right side of (1) for which there are no corresponding differential equations. In this example, the steering decision consists of selecting values at each instant for φ and θ . However, this is not to be done arbitrarily. Consider that the values of φ and θ which are most appropriate will depend on current position, current velocity, current vehicle performance parameters and current time, eventual mission satisfaction, and optimization criteria.

Thus, we can expect the flight controls φ and θ to be functions of current state, current performance parameters, current time, and mission parameters, defined via the optimization criteria. In the more general case, the flight controls will be such functions, called the control laws.

In order to see more explicitly in what way the control laws are defined, we consider a system of the form

$$\begin{aligned}\dot{x}_1 &= g_1(x_1, x_2, \dots, x_m, u_1, u_2, \dots, u_k, t), \\ \dot{x}_2 &= g_2(x_1, x_2, \dots, x_m, u_1, u_2, \dots, u_k, t), \\ &\vdots \\ \dot{x}_m &= g_m(x_1, x_2, \dots, x_m, u_1, u_2, \dots, u_k, t).\end{aligned} \quad (2)$$

This system is to be thought of as representative of the differential equations resulting from application of Newton's second laws. System (1) is thus a special case of system (2). The steering decision now becomes the determination of the quantities u_1, u_2, \dots, u_k as functions of current values of x_1, x_2, \dots, x_m and t . The x_1, x_2, \dots, x_m must be thought of as containing position and velocity coordinates and whatever else is appropriate.

The mission criteria are functions of position and velocity coordinates and time. It will be convenient to write them as functions of all the variables x_1, x_2, \dots, x_m . Thus, the mission criteria are denoted by

$$F_j(x_1, x_2, \dots, x_m, t, c_1, c_2, \dots, c_p) = 0;$$

$$j = 1, 2, \dots, s.$$

The parameters c_1, c_2, \dots, c_p represent the mission parameters.

It is at this point, in many cases, possible to apply an optimization theory such as the calculus of variations in order to impose the optimization criteria. It is beyond the scope of this paper to discuss such a theory; there is abundant literature on the subject. What we need are only the end results of the optimization. Generally, there are three of these. First of all new variables may be introduced into the problem. (This is a consequence of the use of Lagrange multipliers.) The variables x_1, x_2, \dots, x_m, t will remain, but the variables u_1, u_2, \dots, u_k may be replaced by a new set containing k or more variables. The u_1, \dots, u_k can be determined once the new variables are known, and so it is sufficient to work with the new variables.

Secondly, with the new variables, every variable is furnished a first order differential equation. Thus, system (2) is transformed to a system

$$\begin{aligned} \dot{y}_1 &= f_1(y_1, y_2, \dots, y_n, t) \\ \dot{y}_2 &= f_2(y_1, y_2, \dots, y_n, t) \\ &\vdots \\ \dot{y}_n &= f_n(y_1, y_2, \dots, y_n, t). \end{aligned} \quad (3)$$

Unlike system (2), the only variable on the right-hand side of (3) for which there does not appear a differential equation is t . In system (3) we identify the variables y_1, y_2, \dots, y_n . The remaining variables

y_{m+1}, \dots, y_n , take the place of u_1, u_2, \dots, u_k . The steering decision now consists of determining y_{m+1}, \dots, y_n for given y_1, \dots, y_m and t .

Thirdly, the optimization theory furnishes additional end conditions to be met concurrently with the mission criteria. The additional end conditions may involve more variables than the mission criteria; they generally depend on all the y_i and t . We therefore combine the new end conditions with the mission criteria; instead of depending only on y_1, \dots, y_m, t (abstractly), we depend on y_{m+1}, \dots, y_n as well. The result of this is the set of end conditions

$$G_j(y_1, y_2, \dots, y_n, t, c_1, c_2, \dots, c_p) = 0, \quad (4)$$

$j = 1, 2, \dots, n-m+1$. The fact that the total number of end conditions becomes $n - m + 1$ is a result of the optimization theory.

We are now nearly in a position to define the control laws. We need only introduce one further notation. Let the functions

$$Y_i(t, \tau, \eta_1, \eta_2, \dots, \eta_n), \quad i = 1, 2, \dots, n$$

represent the general solution to (3) in terms of initial conditions at τ . Thus, for each i ,

$$Y_i(\tau, \tau, \eta_1, \dots, \eta_n) = \eta_i,$$

and the functions Y_i , considered as functions of t , solve (3) for all initial conditions. Suppose the space vehicle to be at a certain point of flight. The position, velocity, time, and performance parameters dictate the values for $\tau, \eta_1, \eta_2, \dots, \eta_m$. A little reflection reveals that the steering decision consists of the determination of $\eta_{m+1}, \dots, \eta_n$. But each selection of $\eta_{m+1}, \dots, \eta_n$ yields exactly one solution of (3). The question becomes, "Do there exist values of $\eta_{m+1}, \dots, \eta_n$ yielding a solution of (3) which at a later time t satisfies (4)?" Note that there are $n - m + 1$ conditions in (4) and there is available, to satisfy these the selection of the $n - m$ initial conditions, $\eta_{m+1}, \dots, \eta_n$ as well as time t of mission fulfillment.

In reality, therefore, one substitutes the solution

$$y_i = Y_i(t, \tau, \eta_1, \dots, \eta_n); \quad i = 1, 2, \dots, n$$

into (4) and solves the system of $n - m + 1$ equations for the $n - m + 1$ unknowns $\eta_{m+1}, \dots, \eta_n, t$ in terms of $\tau, \eta_1, \dots, \eta_m, c_1, \dots, c_p$.

Let these solutions be denoted by

$$\begin{aligned}\eta_{m+r} &= \beta_r(\tau, \eta_1, \dots, \eta_m, c_1, \dots, c_p); \\ r &= 1, 2, \dots, n-m \\ t &= t_f(\tau, \eta_1, \dots, \eta_m, c_1, \dots, c_p).\end{aligned}\quad (5)$$

The functions in (5) are the control laws and embody the steering decision.

In general, y_i cannot be substituted into (4) and solution for β_r and t_f cannot be obtained, since the functions Y_i are not available. However, the functions in (5) are nevertheless well defined, and can be numerically represented on the basis of the defining properties of the Y_i and the conditions that the β_r and t_f solve (4). This is the subject of the next part.

II. NUMERICAL PRESENTATION OF THE CONTROL LAWS

A. INTRODUCTION

We now concern ourselves with arriving at some numerical representation of the functions $\beta_r(\tau, \eta_1, \dots, \eta_m, c_1, \dots, c_p)$ and $t_f(\tau, \eta_1, \dots, \eta_m, c_1, \dots, c_p)$. One approach is presented here. It is certainly not the only possible solution and is presented merely as a possibility.

First of all, we assume that one solution of the problem is known numerically. That is, for a particular set of values

$$\tau^*, \eta_1^*, \dots, \eta_m^*, c_1^*, \dots, c_p^*,$$

the corresponding values $\eta_{m+r}^* = \beta_r(\tau^*, \eta_1^*, \dots, \eta_m^*, c_1^*, \dots, c_p^*)$, $r = 1, 2, \dots, n-m$ and $t^* = t_f(\tau^*, \eta_1^*, \dots, \eta_m^*, c_1^*, \dots, c_p^*)$ have been numerically determined. This might be accomplished by an iteration on a digital computer. In any case, using the initial values, τ^* , $\eta_1^*, \dots, \eta_m^*$, $\eta_{m+1}^*, \dots, \eta_n^*$, equations (3) are numerically integrated to yield numerical values for

$$Y_i(t, \tau^*, \eta_1^*, \dots, \eta_n^*); i = 1, 2, \dots, n,$$

$$\tau^* \leq t \leq t^*.$$

This particular solution shall be called a reference trajectory.

The idea now is to find the (truncated) Taylor's series for the control laws about the solution

$$\eta_{m+r}^* = \beta_r(\tau^*, \eta_1^*, \dots, \eta_m^*, c_1^*, \dots, c_p^*);$$

$$r = 1, 2, \dots, n-m$$

$$t^* = t_f(\tau^*, \eta_1^*, \dots, \eta_m^*, c_1^*, \dots, c_p^*).$$

This can be accomplished once numerical values are known for the partial derivatives of sufficiently high order of the control laws with respect to their arguments, evaluated at the point $(\tau^*, \eta_1^*, \dots, \eta_m^*, c_1^*, \dots, c_p^*)$. For brevity, we shall only show here how to obtain numerical values of all first partials. The procedure generalizes readily to higher orders.

B. THE FUNDAMENTAL IDENTITIES

The entire procedure is based on three fundamental identities. These are, first, an identity satisfied by the function Y_i by virtue of being solutions of (3), secondly, a second identity satisfied by the functions Y_i characterizing the parameters as initial values, and thirdly, identities satisfied by the control laws by virtue of solving the end conditions. We now list these:

$$\frac{\partial Y_i}{\partial t} = f_i(Y_1, \dots, Y_n, t); i = 1, 2, \dots, n \quad (6)$$

$$Y_i(\tau, \tau, \eta_1, \dots, \eta_n) = \eta_i; i = 1, 2, \dots, n \quad (7)$$

and

$$\begin{aligned}G_j(\tilde{Y}_1, \dots, \tilde{Y}_n, t_f, c_1, c_2, \dots, c_p) &\equiv 0; \\ j &= 1, 2, \dots, n-m+1\end{aligned}\quad (8)$$

in which

$$\begin{aligned}\tilde{Y}(\tau, \eta_1, \dots, \eta_m, c_1, \dots, c_p) &= Y_i(t_f, \eta_1, \dots, \eta_m, \\ &\beta_1, \dots, \beta_{n-m}); i = 1, 2, \dots, n.\end{aligned}\quad (9)$$

Identity (6) is understood to hold in all of the arguments $t, \tau, \eta_1, \dots, \eta_n$. Identity (7) holds in all of the arguments $\tau, \eta_1, \dots, \eta_n$. Identity (8) holds in the arguments of the control laws; i.e., in $\tau, \eta_1, \dots, \eta_m, c_1, \dots, c_p$.

Under certain conditions, the above identities can be differentiated an unlimited number of times with respect to their arguments to yield further identities. We assume this to be the case; for justification, see Reference 1. In particular, using the chain rule, (8) can be differentiated with respect to η_k ; $k = 1, 2, \dots, m, t_f$ or c_ℓ , $\ell = 1, 2, \dots, p$. For η_k we obtain

$$\begin{aligned}\sum_{q=1}^n \frac{\partial G_j}{\partial y_q} \left[\frac{\partial Y_q}{\partial \eta_t} \frac{\partial t_f}{\partial \eta_k} + \frac{\partial Y_q}{\partial \eta_k} + \sum_{r=1}^{n-m} \frac{\partial Y_q}{\partial \eta_{m+r}} \frac{\partial \beta_r}{\partial \eta_k} \right] \\ + \frac{\partial G_j}{\partial t} \frac{\partial t_f}{\partial \eta_k} = 0\end{aligned}$$

$k = 1, 2, \dots, m, j = 1, 2, \dots, n-m+1$. For fixed k , we rewrite the above as the system

$$\sum_{r=1}^{n-m} \left(\sum_{q=1}^n \frac{\partial G_j}{\partial y_q} \frac{\partial Y_q}{\partial \eta_{m+r}} \right) \frac{\partial \beta_r}{\partial \eta_k} + \left(\frac{\partial G_j}{\partial t} + \sum_{q=1}^n \frac{\partial G_j}{\partial y_q} \frac{\partial Y_q}{\partial t} \right) \frac{\partial t_f}{\partial \eta_k} = - \sum_{q=1}^n \frac{\partial G_j}{\partial y_q} \frac{\partial Y_q}{\partial \eta_k}$$

$$j = 1, 2, \dots, n-m+1 \quad (10)$$

and view the system as a system of $n-m+1$ linear equations in the $n-m+1$ unknowns

$$\frac{\partial \beta_r}{\partial \eta_k}; r = 1, 2, \dots, n-m, \frac{\partial t_f}{\partial \eta_k}.$$

Similar systems can be obtained for differentiation with respect to τ or c_ℓ . We take (10) as exemplary.

Now the arguments in (10) are those of the control laws; it has already been pointed out that the expansion is to be made about the point $(\tau^*, \eta_1^*, \dots, \eta_m^*, c_1^*, \dots, c_p^*)$. We therefore evaluate (10) at $(\tau^*, \eta_1^*, \dots, \eta_m^*, c_1^*, \dots, c_p^*)$. Assuming the resultant system to be nonsingular, once the coefficients of the unknowns

$$\frac{\partial \beta_r}{\partial \eta_k}, r = 1, 2, \dots, n-m, \text{ and } \frac{\partial t_f}{\partial \eta_k}$$

are numerically determined, the system can be solved by standard processes for the desired numerical values. As similar statements hold for systems obtained by differentiation of (8) with respect to τ and c_ℓ , we will present only the details for (10).

C. DETERMINATION OF COEFFICIENTS IN (10)

To determine the coefficients in (10), we need numerical values for the quantities (for appropriate arguments):

$$\frac{\partial Y_q}{\partial \eta_k}; q = 1, 2, \dots, n; k = 1, 2, \dots, n.$$

$$\frac{\partial Y_q}{\partial t} \text{ and } \frac{\partial G_j}{\partial t}, \frac{\partial G_j}{\partial y_q}, j = 1, 2, \dots, n-m+1,$$

$$q = 1, 2, \dots, n.$$

Partials of the G_j can be directly calculated from

the end conditions. The only problem is the determination of

$$\frac{\partial Y_q}{\partial \eta_k}, \text{ since } \frac{\partial Y_q}{\partial t}$$

is simply given by evaluation of the right side of (3) at the time of mission satisfaction.

Differentiation of (6) with respect to η_k gives

$$\frac{\partial}{\partial t} \left(\frac{\partial Y_q}{\partial \eta_k} \right) = \sum_{j=1}^n \frac{\partial f_q}{\partial y_j} \frac{\partial Y_j}{\partial \eta_k}, \quad (11)$$

which is a linear homogenous system in the unknown partials

$$\frac{\partial Y_q}{\partial \eta_k}; q = 1, 2, \dots, n; k = 1, 2, \dots, n.$$

Differentiation of (7) yields the initial values for (11) at $t = \tau$; in fact

$$\left. \frac{\partial Y_j}{\partial \eta_k} \right|_{t=\tau} = \delta_{jk}, \text{ the Kronecker } \delta.$$

Also, the functions $\frac{\partial f_q}{\partial y_j}$ are numerically known along

the reference so that (11) can be integrated numerically from $t = \tau^*$. Reading off the integrated values yields the desired results.

As has been pointed out, similar procedures apply to the determination of the remaining first order and higher order partials.

REFERENCES

1. NASA TM-X-53059, "Space Vehicle Guidance - A Boundary Value Formulation," by Robert W. Hunt and Robert Silber, June 8, 1964.
2. NASA TM-X-53100, "Space Vehicle Guidance - A Boundary Value Formulation, Part II: Boundary Conditions with Parameters," by Robert Silber, July 28, 1964.

III. UNSTEADY AERODYNAMICS

WALL PRESSURE FLUCTUATIONS AND SKIN VIBRATIONS WITH EMPHASIS ON FREE SHEAR LAYERS AND OSCILLATING SHOCKS

By

Fritz R. Krause

N65-24128

SUMMARY

Ever since the failure of the first Centaur flights, high frequency skin vibrations have been of much concern. Large wall pressure fluctuations below separated flows and oscillating shocks lead to a dangerous resonance excitation over the entire transonic and supersonic portion of the flight. A new relation between pressure and force correlations has been established for inhomogeneous turbulence in order to account correctly for the largest pressure fluctuations below oscillating separation and reattachment lines. It shows that the power spectra of the generalized forces can be found from rigid model tests by a curve fit of a special pressure cross correlation function. However, a curve fit of experimental pressure correlations is useful only as long as the statistical error of a cross correlation estimate is smaller than the numerical error of the curve fitting procedure. Non-linear transfer functions and dynamic shifts in presently available pressure transducers and tape recorders are so large that the more refined force estimates, which consider the spatial structure of the pressure field, might lead to ambiguous results.

DEFINITION OF SYMBOLS

Geometrical and Panel Parameters:

| Symbol | Definition |
|--------------|--------------------------------|
| a, b | edge lengths |
| A | panel area, ab |
| x | streamwise surface coordinate |
| y | crosswise surface coordinate |
| $\lambda\mu$ | wave number in x, y direction |
| m | number of loops in x direction |
| n | number of loops in y direction |
| h | panel thickness |
| ρ | density of plate material |
| D | flexural rigidity |

Symbol

Definition

| | |
|-------------------------|----------------------------------------------------|
| E | Young's modulus of elasticity |
| ν | Poisson's ratio |
| ν | Eigen value of two-dimensional wave equation |
| M | modal mass |
| ζ | modal damping ratio |
| w | transverse deflection |
| q | generalized coordinate or loop deflection |
| <u>Flow Parameters:</u> | |
| p | wall pressure |
| U | velocity |
| δ | geometrical boundary layer thickness on clean wall |
| F | generalized force |
| S | cross-power spectral density |
| R | cross correlation function |
| t | time |
| τ | time delay |
| b | noise bandwidth in radians/sec |
| ω | angular frequency, radians/sec |
| T | integration time |
| $H(\omega)$ | complex frequency response function |
| $\varphi(\omega)$ | phase shift angle |
| N | number of data transmitting elements |
| $\Delta^2 R$ | Mean square error of cross correlation estimate |

DEFINITION OF SYMBOLS (Concluded)

| Symbol | Definition |
|-----------------------------|---------------------------------------------------------------------------------|
| Δ | perturbation |
| <u>Sub and superscripts</u> | |
| 1 | fixed transducer |
| 2 | moved transducer |
| m, n, k, 1 | summation indices |
| p | pressure |
| F | force |
| \wedge | plane wave approximation |
| o | natural frequency |
| C | convected turbulence |
| * | Space average for a translated transducer pair with fixed separation distances. |
| - | wall pressure approximation with mode shapes |

I. INTRODUCTION

Recent wind tunnel and flight tests indicate that a large booster will experience wall pressure fluctuations during the transonic and supersonic portion of the flight, bigger than the jet noise at the launch. Figure 1 shows some root-mean-square pressures that

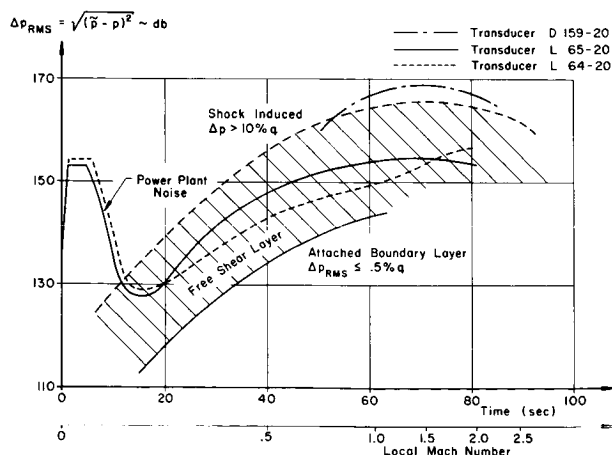


FIGURE 1. ROOT MEAN SQUARE PRESSURE FLUCTUATIONS DURING SA-4 FLIGHT

were measured during the fourth flight of a Saturn I vehicle [1]. At the supersonic Mach number of 1.6, the fluctuation level of the transducer D-159-20 is 14 db higher than at launch. Because of the supersonic flow, an upstream radiation of jet noise is not possible, and the highest level of .16q must be induced by a noise generation process. In subsonic free shear layers the observed pressure fluctuations are below 10 percent of the local dynamic pressure, and in attached boundary layers the RMS values are usually equal to .5 percent [2]. Therefore, the area between the 10 percent and .5 percent dynamic pressure curves has been shaded and called "free shear layer noise." RMS values below the shaded area are called "attached boundary layer noise" and those above 10 percent dynamic pressure "shock induced noise." Apparently the highest fluctuations can be explained only by a free shear layer interacting with an oscillating shock.

The three transducers were located near the S-IV/S-I interstage as indicated by Figure 2. Reproducing the flow field from MSFC wind tunnel shadowgraphs, one sees immediately that the flow above the transducer cross section is indeed separated. The high pressure fluctuations of the transducer D-159-20 were picked up shortly downstream of a sharp I-beam fairing, and an oscillating bow shock might have been the cause.

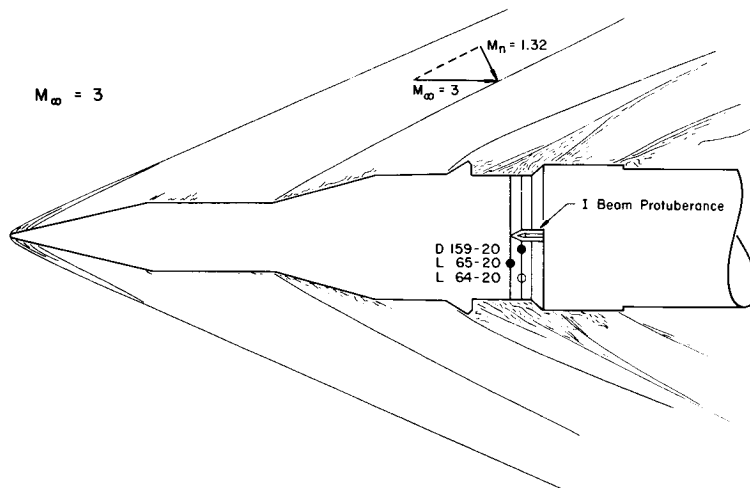


FIGURE 2. FLOW FIELD REPRODUCED FROM WIND TUNNEL SHADOWGRAPH

A power-spectral analysis of the three transducers indicated several peaks which are centered around a Strouhal number of .2, as shown in Figure 3. These peaks are known from the vortex shedding behind two-dimensional cylinders, and thus might be taken as further evidence of a flow separation interacting with an oscillating shock.

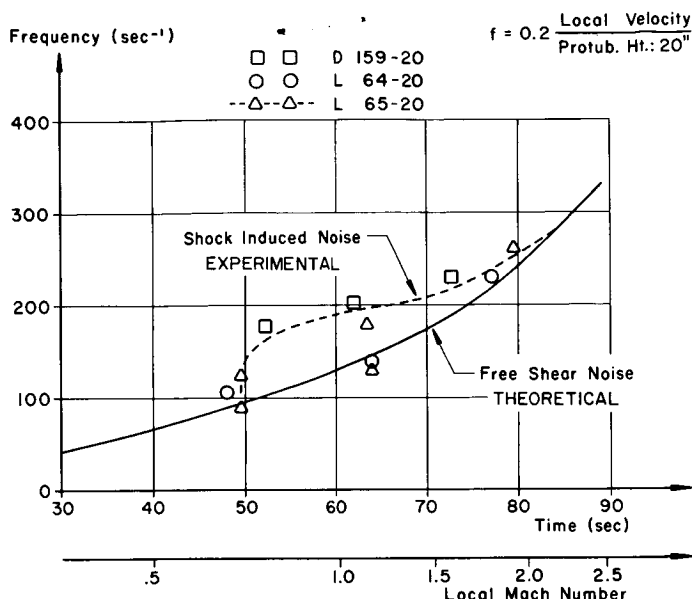


FIGURE 3. FREQUENCIES FOR THE PEAKS OF THE POWER SPECTRA

Unfortunately, the high RMS values occur between frequencies of 120 to 240 cps, which is in the range of fundamental resonance frequencies of individual skin panels. The flat curves of Figure 1 have shown that the high RMS values are not limited to a small Mach number range but do extend over the entire transonic and supersonic portion of the flight. This has been substantiated in model tests that were run at Douglas Aircraft Company [3]. Typical "saw-tooth-type" distributions are shown in Figure 4. They are essentially independent of Mach number. In flight, the dynamic pressure for Mach numbers below 3 is appreciable and

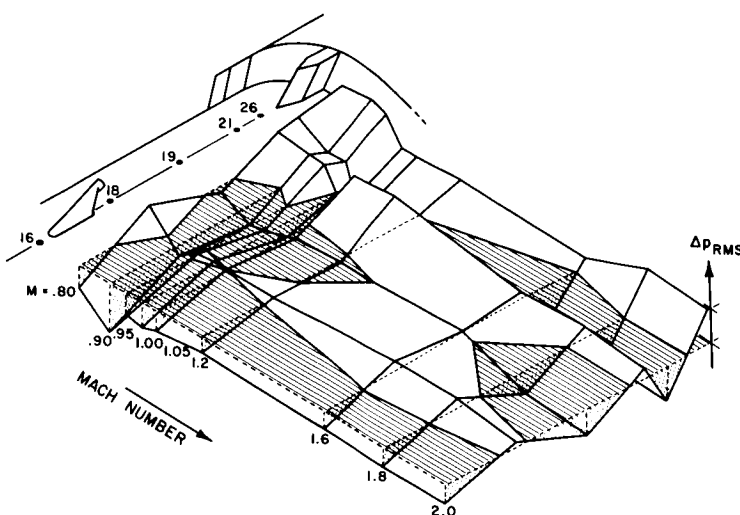


FIGURE 4. ROOT MEAN SQUARE PRESSURE VERSUS MACH NUMBER - DAC MODEL TESTS

the corresponding time interval extends over approximately 30 seconds. Severe fluctuations might therefore cause a dangerous skin excitation over an extended period of time, and every effort should be made to study the intense, high frequency wall pressure fluctuations which are produced by flow separations and oscillating shocks.

II. AERODYNAMIC EXCITATION AND STRUCTURAL RESPONSE

Ames Research center and the Marshall Space Flight Center are working jointly on a wind tunnel program whose purpose is to measure wall pressure fluctuations below free shear layers and oscillating shocks [4]. These pressures will supply a generalized force for each generalized coordinate chosen in the description of the skin vibration tests. The test will be performed on individual forward- and backward-facing interstage areas and local protuberances rather than on a complete Saturn model. This is necessary to obtain Reynolds numbers which are already so high that a further increase to full scale will not change the flow separation and reattachment lines [5,6]. For complete models, the Reynolds numbers are so low that the wanted flow separations and shock oscillations may not occur at all [7].

A local treatment of structural components is possible for all elements which almost conserve their vibration energy [8] (kinetic energy plus work of stresses [13] and pressures). All structural coupling with the rest of the vehicle has to be small. Such elements have been defined in terms of "correlation boundaries" like stiffness and heavy internal masses [19]. They could be found in shake tests on the ground by measuring the acceleration of the skin at different points simultaneously. A correlation boundary exists between two accelerometers if their cross correlation is negligibly small.

The simplest treatment of local panels is given by the classical modal approach [10] which might be viewed as an attempt to curve-fit a flashlight image of the skin deflection with a linear combination of standing flexural waves. For the rectangular flat plate, these waves can be guessed easily (see Fig. 5). From all conceivable flexural waves, the standing ones are those which are continuously reflected to and fro between opposite edges of the plate. This can happen only for waves which run in either x or y direction, provided that the distance between the edges corresponds to a multiple of the distance between nodal points. Denoting the number of loops which are counted in x and y direction by the wave numbers m and n, the distance between the nodal points becomes a/m and b/n ; the wave length of the flexural waves is exactly twice this distance [14].

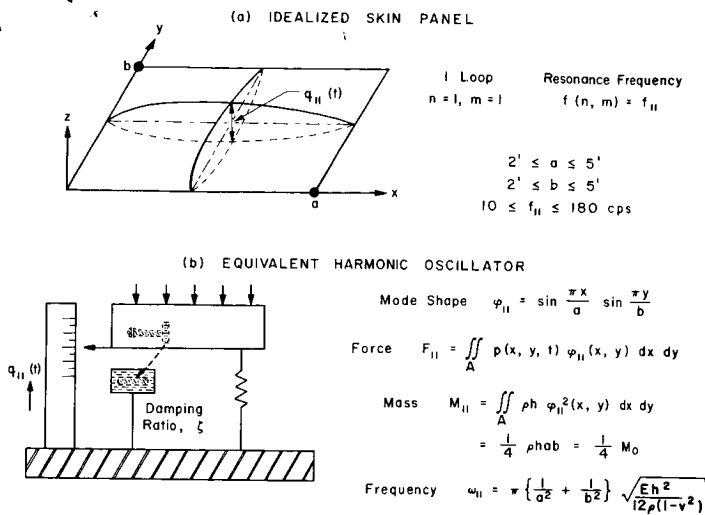


FIGURE 5. TYPICAL SKIN PANEL VIBRATING AT THE FUNDAMENTAL FREQUENCY

Each running wave has a sinusoidal time history of deflection and, because of the continuous reflection at the edges, the distribution in time is converted to a distribution in space. As a result, one determines that the flexural waves of a simple supported, flat plate have a sinusoidal shape.

$$\varphi_{mn}(x, y) = \sin \frac{\pi m x}{a} \sin \frac{\pi n y}{b}. \quad (1)$$

For $n, m = 1, 2, \dots$ the complete set of standing waves is then used to approximate the skin deflection $w(x, y, t)$; all other flexural waves are neglected.

$$w(x, y, t) = \sum_{m=1}^{\infty} \sum_{n=1}^{\infty} q_{mn}(t) \varphi_{mn}(x, y) \quad (2)$$

The coefficients q_{mn} of this curve fit describe a flash-light image of the deflection; they are called the "generalized coordinate" or "responses." Each response is due to the excitation of a generalized force

$$F(m, n, t) = \iint_A p \frac{\partial w}{\partial q} dA = \iint_A p(x, y, t) \varphi_{mn}(x, y) dx dy. \quad (3)$$

The relation between these excitations and the responses q can be illustrated by the forced oscillation of a harmonic oscillator, as shown in Figure 5. The angular natural frequency of the oscillator is

$$\omega(m, n) = \pi^2 \left(\frac{m^2}{a^2} + \frac{n^2}{b^2} \right) \sqrt{\frac{Eh^2}{12(1-\nu^2)\rho}}, \quad (4)$$

and its mass is given by

$$M(m, n) = \iint_A \rho h \varphi_{mn}^2 dx dy = \rho a b h / 4. \quad (5)$$

The inevitable loss of vibration energy is determined by the oscillation decay of a free vibrating panel. The ratio between the energy loss and the work of the bending moments is equal to four times the ratio $\zeta(m, n)$ between two consecutive amplitudes of a standing but decaying flexural wave.

Unfortunately, the wall pressure fluctuations below free shear layers and oscillating shocks are neither sinusoidal nor periodic. Because they are samples of a random process, the generalized force which is their space integral, equation (3), will also be random. Since we have random forcing functions for each of the equivalent oscillators, n and m , statistical methods have to be used. These methods have already been developed in communication theory. The asymptotic response to a random force will therefore be given by comparing the equivalent oscillator to the electronic element of a data reduction chain. The generalized acceleration $F(m, n, t)/M$ is treated as an input signal, and the generalized coordinate $q_{mn}(t)$ as an output signal.

The statistical description of the input and output is based on a frequency decomposition which might be described through the action of an ideal digital filter, as shown in Figure 6. The phase shift, ϕ , across this ideal filter is zero and the gain factor is infinite in an infinitesimal frequency interval around $\omega = \omega(m, n)$

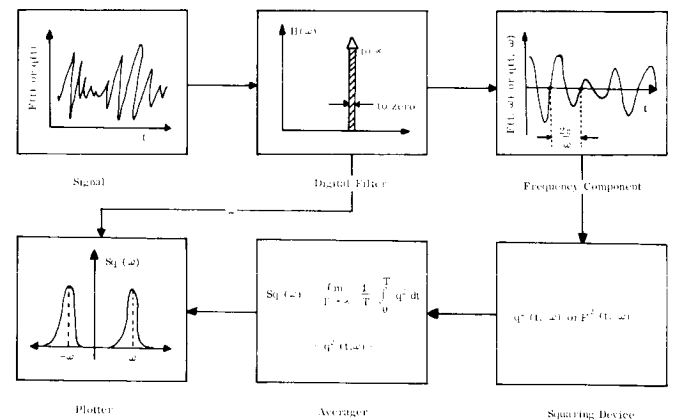


FIGURE 6. POWER SPECTRAL ANALYSIS OF DETERMINISTIC AND RANDOM SIGNALS

such that the area under the frequency response function is one unit. The individual frequency components, $q(t, \omega)$, are the output of such a narrow band digital filter, they are described statistically by their mean

square values or "power spectral densities", $S_q(\omega) = \langle q^2(t, \omega) \rangle$, respectively.

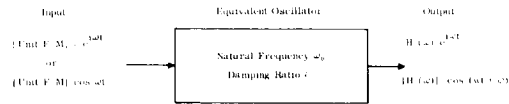
The harmonic oscillator itself is a linear and time invariant element; that is, a pure harmonic output. The transmission of each frequency component is described by the phase shift φ across the oscillator and by the ratio between the output and input amplitudes which are said to constitute the complex frequency response function (Fig. 7),

$$H(\omega) = \frac{\text{deflection amplitude}}{\text{acceleration amplitude}} e^{i\varphi} \quad (6)$$

$$= \frac{1}{\omega^2(m, n) - \omega^2 + 2i\zeta\omega\omega(m, n)}.$$

The power spectrum of the output is then equal to the power spectrum of the input times the squared magnitude of the frequency response function [11].

(a) $H(\omega)$ As Amplitude Response to A Unit Harmonic Input



(b) Absolute Value and Gain Factor

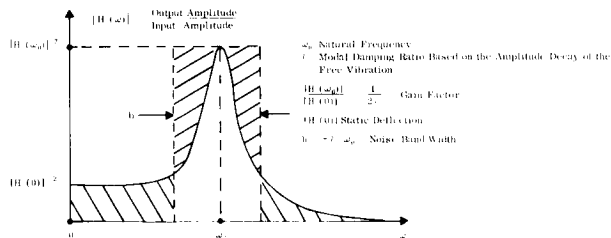


FIGURE 7. THE COMPLEX FREQUENCY RESPONSE FUNCTION $H(\omega)$ OF A MODE

$$S_q(\omega) = |H(\omega)|^2 \frac{S_F(\omega)}{M^2} \quad (7)$$

The local treatment of structural components is possible only if the energy losses, that is, the damping ratios ζ , are small. In this case, the "power transfer function" $|H(\omega)|^2$ has two sharp peaks centered around the frequencies, $\pm \omega_0$, the bandwidth of which is given by

$$b = \frac{1}{2} \int_{-\infty}^{+\infty} \left| \frac{H(\omega)}{H(\omega_0)} \right|^2 d\omega = \pi \zeta \omega_0. \quad (8)$$

Because the oscillator will accept only the two frequency components which are centered at the natural frequency ω_0 , the mean square value of the response becomes

$$\langle q^2(m, n, t) \rangle = 2b |H(\omega_0)|^2 \frac{S_F(\omega_0)}{M^2} \quad (9)$$

$$= \frac{\pi S_F(m, n, \omega(m, n))}{2 \zeta(m, n) \omega^3(m, n)}.$$

This excitation response relation splits the prediction of skin vibrations into a structural part and an aerodynamic part. In the first, one would determine the sizes, natural frequencies, mode shapes and damping ratios of possible panels in shake tests on the ground. The aerodynamic part would be to calculate the power spectrum of the generalized forces $S_F(m, n, t)$ from measured pressure fluctuations.

The relation between aerodynamic excitation, S_F , and structural response $\langle q^2 \rangle$ has been illustrated for the simplest of all cases, the rectangular flat plate with simply supported edges [12]. The derivations and a complete list of assumptions have been prepared such that they might be verified in future tests. It turns out that equation 9 is valid not only for the flat plate but for all structural components, the free vibration of which can be described by orthogonal modes. A similar relation could be obtained for the general case, where structural coupling between components has to be considered [25]. The main difference is that the modal frequency response function, equation 6, is replaced by an overall transfer function, which has to be measured on shake tests on the ground.

III. STANDARD FORCE ESTIMATES

In rigid model tests, the problem is to find the most dangerous generalized forces from measured wall pressure fluctuations. According to the excitation response relation, equation (9), the mean square deflection of a single mode is directly proportional to the power spectral density, S_F , of the corresponding generalized force taken at the natural frequency of the mode. Most rigid model tests are therefore aimed at the measurement of this property.

The power spectrum of the generalized force, S_F , was defined by filtering operations. Writing down the mathematics of this filtering process [11] we find that S_F is the Fourier transform

$$S_F(m, n, \omega) = \frac{1}{2\pi} \int_{-\infty}^{+\infty} R_F(m, n, \tau) e^{-i\omega\tau} d\tau \quad (10)$$

of the force-autocorrelation function

$$R_F(m, n, \tau) = \lim_{T \rightarrow \infty} \frac{1}{T} \int_{-T/2}^{+T/2} F(m, n, t) F(m, n, t+\tau) dt \quad (11)$$

$$= \langle F(m, n, t) F(m, n, t+\tau) \rangle.$$

The wanted relation between forces and pressures is now obtained by substituting the definition of the generalized force

$$F(m, n, t) = \iint_A p(x, y, t) \varphi_{mn}(x, y) dx dy \quad (3)$$

into equation (21). Inverting the order of space and time integration, we obtain an exact, but unwieldy fourth order integral

$$R_F(m, n, \tau) = \iiint_A \iiint_A \langle p(x_1, y_1, \tau) p(x_2, y_2, t+\tau) \rangle \varphi_{mn}(x_1, y_1) \varphi_{mn}(x_2, y_2) dx_1 dy_1 dx_2 dy_2. \quad (12)$$

The first factor of the integrand summarizes all the information that has to be obtained from rigid model tests. It is called the "pressure cross correlation function,"

$$R_p(x_1, y_1, x_2, y_2, \tau) = \langle p(x_1, y_1, t) p(x_2, y_2, t+\tau) \rangle, \quad (13)$$

whose measurement is described in Figure 8. Two transducers, 1 and 2, are located at the points x_1, y_1 and $x_2 = x_1 + \xi; y_2 = y_1 + \eta$. The signal from transducer 1 is delayed by the time τ . Both signals are then multiplied and the wanted pressure cross correlation function is the output from the time averaging element.

For an accurate integration of equation (12), each transducer has to be moved independently over the whole panel surface and the cross correlation repeated over and over again for each combination of the two transducer locations. This is very cumbersome. To obtain design criteria, the process must be repeated for each resonance frequency and for the combinations of Mach number, Reynolds number, upstream boundary layer thickness, wedge angle and step height. The transducer output has to be recorded for approximately 30 seconds to obtain statistically reliable time averages. Evidently, such an approach requires an excessive amount of data, and it is doubtful that the direct evaluations of the fourth order integral could be tried for more than one or two cases.

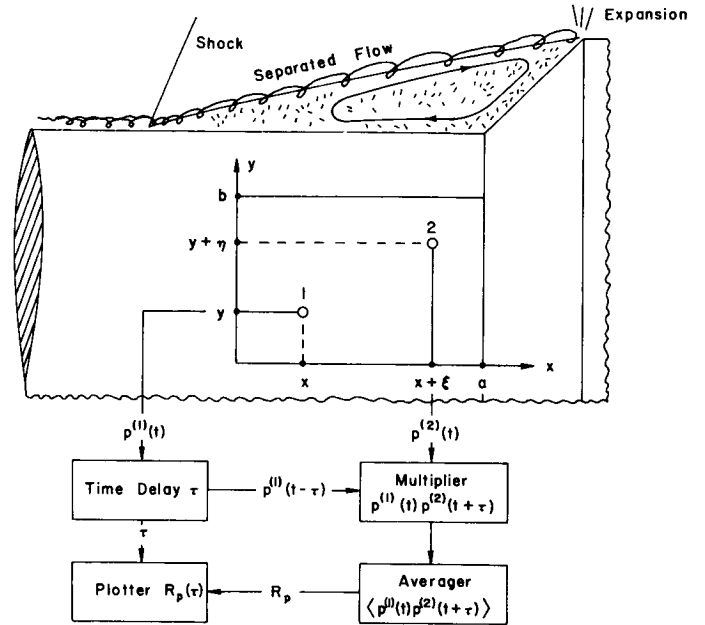


FIGURE 8. MEASUREMENT OF THE STANDARD PRESSURE CROSS CORRELATION

The numerical and experimental effort can be reduced if a conservative estimate of R_F or S_F is acceptable. The most simple of all estimates is obtained by replacing the actual pressure field $p(x, y, t)$ with normal incident pressure waves, the strength of which corresponds to the maximum pressure fluctuation

$$p(x, y, t) \leq \hat{p}(t), \quad \text{"normal wave estimate"}. \quad (14)$$

Substituting equation (14) into equation (12), the power spectrum of the generalized force becomes

$$S_F(m, n, \omega) \leq \left(\frac{4 a b}{\pi^2 m n} \right)^2 S_{\hat{p}}(\omega), \quad (15)$$

which is directly proportional to the power spectrum of the incident pressure wave. As a result, a conservative estimate of the aerodynamic excitation can be obtained by looking at the power spectral density of all wall pressures which have been measured inside the edges of a particular panel. For design estimates, the power spectral density has to be evaluated at the natural frequencies of the panel. From all transducer locations, that one must be found which gives the largest $S_F(\omega(m, n))$.

The plane wave estimate neglects completely the

spatial structure of the pressure field. Several attempts have been made to include spatial characteristics for statistically homogeneous flows. The assumption of homogeneity means that the pressure cross correlation is invariant against a translation [15].

$$R_p = R_p(\xi = x_1 - x_2; \eta = y_1 - y_2), \quad (16)$$

"homogeneous turbulence".

A good summary has been given by Allan Powell [16]. The autocorrelation of the generalized force is, in first approximation,

$$R_F(m, n, \tau) \approx S_p(\lambda = \frac{\pi m}{a}, \mu = \frac{\pi n}{b}) J(m, n) + \dots + S_p(\lambda = -\frac{\pi m}{a}, \mu = -\frac{\pi n}{b}) J(-m, -n), \quad (17)$$

proportional to the wave number components of the pressure field

$$S_p(\lambda, \mu, \tau) = \frac{1}{2\pi} \int_{-\infty}^{+\infty} R_p(\xi, \eta, \tau) e^{-i(\lambda \xi + \mu \eta)} d\xi d\eta, \quad (18)$$

which are centered around the structural wave numbers $\lambda = \pm \frac{\pi m}{a}$, $\mu = \pm \frac{\pi n}{b}$, and some structural weights:

$$J(m, n) = \frac{1}{2\pi} \int_{-\infty}^{+\infty} \left| \iint_A \varphi_{mn}(x, y) e^{i(\lambda x + \mu y)} dx dy \right|^2 d\lambda d\mu. \quad (19)$$

The wave number components S_p might be viewed as influence coefficients which are necessary to curve-fit the pressure cross correlation R_p with harmonic spatial waves $e^{i(\lambda x + \mu y)}$. In a sense, the autocorrelation of the generalized force is therefore obtained by the curve fit of a measured cross correlation function. In homogenous turbulence the measurement of R_p requires that only one transducer be moved. The fourth order integration of equation (12) is then reduced to the double integral of equation (18).

Unfortunately, intense noise sources seem to be connected with inhomogeneous flows. Homogeneous turbulence represents uniform flows behind grids [15], whereas the main noise sources are associated with attached [17], [18] and separated (jet) boundary layers [19], [20]. High shear and homogeneous turbulence are theoretically incompatible.

In supersonic flow additional noise sources must be expected. The presently conducted wind tunnel program indicates that flow separation lines (shock) and reattachment lines are always unstable and lead

to a very high noise level. In these regions, a constant convection speed does not exist, and the assumption of homogeneity is very questionable.

IV. FORCE APPROXIMATIONS FOR INHOMOGENEOUS TURBULENCE

The largest pressure fluctuations are expected for inhomogeneous flows, and a new simplification of the pressure field is needed which is not restricted to homogeneous pressure fields. In this paper, it is proposed to curve-fit a flashlight image of the pressure fields with a set of orthogonal eigen functions:

$$p(x, y, t) \approx \bar{p}(x, y, t) = \sum_{m=1}^{\infty} \sum_{n=1}^{\infty} f_{mn}(t) \varphi_{mn}(x, y). \quad (20)$$

Approximations of this kind are very general and should fit almost all pressure distribution which occur in flows, except in the vicinity of the edges. In principle, any set of orthogonal eigen functions might be chosen. Using the mode shapes, however, has the advantage that the coefficients f_{mn} are directly proportional to the generalized forces, equation (3). The mean square deviation between the given pressure, p , and its approximation \bar{p} is a minimum, if

$$f_{mn}(t) = \frac{F(m, n, t)}{\iint_A q_{mn}^2(x, y) dx dy} = \frac{4}{A} F(m, n, t). \quad (21)$$

One could argue that the curve fit of equation (20) is very impractical since it has to be repeated for each instant of time and might require a large number of coefficients. In fact, the individual coefficients should never be calculated. They are rather the basis of a statistical procedure where the individual coefficient is immaterial and only the average over a large number of curve fits is used. For homogeneous turbulence, this has been tried by establishing the relation between the pressure cross correlation and the force autocorrelation. The forces are then found by curve fitting R_p with complex waves. If we wish to find a similar relation for inhomogeneous turbulence, this function should be based on a translation of both transducers (Fig. 8) since this is required in the accurate fourth order integration, equation (12). In view of these considerations, a "special pressure cross correlation" R_p^* is now introduced which ties the wanted force correlations to the measurable pressure cross correlations, R_p .

The measurement of the special cross correlation R_p^* is shown on Figure 9. A pair of pressure transducers is moved across the panel such that the separation distances remain fixed. The special cross correlation R_p^* is then nothing but the space average of

the "standard" cross correlation R_p ,

$$R_p^* = \int_{y=0}^{b-\eta} \int_{x=0}^{a-\xi} \frac{p(x,y,t) p(x+\xi, y+\eta, t+\tau)}{(a-\xi)(b-\eta)} dx dy. \quad (22)$$

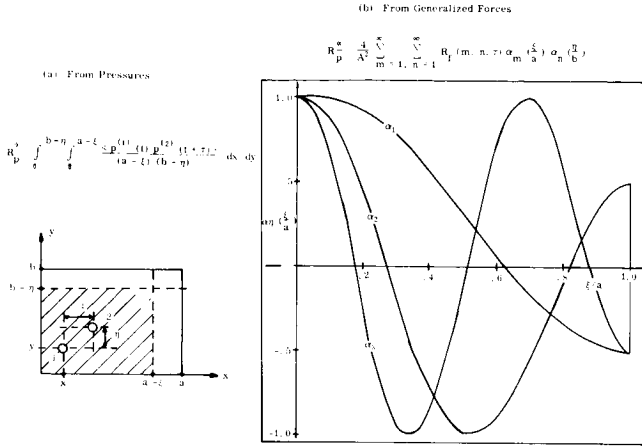


FIGURE 9. THE SPECIAL CROSS CORRELATION FUNCTION R_p^*

The wanted relation between R_p^* and the force correlation is found by establishing the special correlation for the simplified pressure model

$$R_p^* = \int_{y=0}^{b-\eta} \int_{x=0}^{a-\xi} \frac{\bar{p}(x,y,t) \bar{p}(x+\xi, y+\eta, t+\tau)}{(a-\xi)(b-\eta)} dx dy. \quad (23)$$

Substituting equations (20) and (21) and neglecting the force cross correlation between modes [12], we find the wanted relation

$$R_p^*(\xi, \eta, \tau) = \sum_{m=1}^{\infty} \sum_{n=1}^{\infty} \frac{4}{A^2} \psi_{mn}(\xi, \eta) R_F(m, n, \tau). \quad (24)$$

The structural weights ψ_{mn} are completely determined by the mode shapes

$$\begin{aligned} \psi_{mn}(\xi, \eta) &= \\ \frac{4}{(a-\xi)(b-\eta)} \int_0^{a-\xi} \int_0^{b-\eta} \varphi_{mn}(x, y) \varphi_{mn}(x+\xi, y+\eta) dx dy \\ &= \alpha_m \left(\frac{\xi}{a} \right) \alpha_n \left(\frac{\eta}{b} \right). \end{aligned} \quad (25)$$

For the rectangular flat plate with simply supported edges, they are shown in Figure 9.

According to equation (24), the wanted force correlations R_F are the influence coefficients of a curve fit which approximates measured R_p^* pressure cross correlations with known structural weighting functions $\psi_{mn}(\xi, \eta)$. Once again the unknown coefficients are determined by the method of least squares. The mean square error between the measured R_p^* and the approximated special cross correlation, R_p^*

$$\Delta^2 R_p^* = \frac{1}{A} \int_0^a \int_0^b (R_p^* - R_p^*)^2 d\eta d\xi =$$

$$\frac{1}{A} \int_0^a \int_0^b [R_p^*(\xi, \eta, \tau) - \frac{4}{A^2} \sum_{m=1}^{\infty} \sum_{n=1}^{\infty} R_F(m, n, \tau) \cdot \quad (26)$$

$$\alpha_m \left(\frac{\xi}{a} \right) \alpha_n \left(\frac{\eta}{b} \right)]^2 d\eta d\xi$$

is required to be a minimum. This will happen when the partial derivatives $\partial(\Delta^2 R_p^*)/\partial R_F$ vanish. Writing this condition of extremum down for all combinations $k, l = 1, 2, \dots, \infty$, we obtain an infinite system of algebraic equations:

$$\frac{1}{A} \int_0^a \int_0^b (R_p^* - R_p^*) \psi_{kl}(\xi, \eta) d\eta d\xi = 0. \quad (27)$$

In explicit form

$$\begin{aligned} \frac{1}{A} \int_0^a \int_0^b R_p^*(\xi, \eta, \tau) \alpha_k \left(\frac{\xi}{a} \right) \alpha_l \left(\frac{\eta}{b} \right) d\xi d\eta \\ = \frac{4}{A^2} \sum_{m=1}^{\infty} \sum_{n=1}^{\infty} R_F(m, n, \tau) C(m, k) C(n, l). \end{aligned} \quad (28)$$

The constants $C(m, k)$ are an abbreviation of the following integral:

$$C(m, k) = \int_0^1 \alpha_m \left(\frac{\xi}{a} \right) \alpha_k \left(\frac{\xi}{a} \right) \frac{d\xi}{a}. \quad (29)$$

The same equation holds for the constants $C(n, l)$ if n and l are substituted for m and k .

The right-hand side of equation (28) approaches zero as $1/n^2$. The left-hand side of equation (28) represents a space average of a special correlation function which is weighted with the functions α_k and α_l . For higher values of k and l , these weights approach cosine functions, the signs change rapidly with the separation distances ξ and η , and the integral goes to zero. Consequently, one might truncate the system since all coefficients $C(m, k)$ and $C(m, l)$ with $m, n, \neq k, l$ decay rapidly with increasing difference

between m and k and n and l . The solution of the finite system of algebraic equations can therefore be approximated in first order by considering the diagonal elements only

$$R_F^{(0)}(k, l, \tau) = \frac{A}{4 C(k, k) C(l, l)} \int_0^a \int_0^b R_p^* \alpha_k \alpha_l d\eta d\xi. \quad (30)$$

Higher approximations are found most easily by actually solving the finite system of linear equations, preferably in an iterative fashion.

The curve fit of the special cross correlation R_p^* is an attempt to replace the accurate but unwieldy fourth order integration of equation (12) with something more practical. As far as the numerical effort is concerned, the curve fit is indeed simpler since the fourth order integral is reduced to a system of algebraic equations between double integrals. A reduction of the experimental effort is not so immediately apparent. The determination of the special correlation function, equation (22), requires moving both transducers over the entire panel, and nothing more is required in the exact solution, equation (12). The great advantage of the special correlation function is that the number of measurements can be matched easily to the present statistical theories of turbulence and to the flow type. If the turbulence is homogeneous, then the special correlation R_p^* and the standard correlation R_p are identical; that is, the position of one transducer can be fixed. Furthermore, the integral of equation (22) does not depend on the location or the size of the integration domain; that is, the rigid model test is completely independent from all structural considerations.

In the case of high shear flows, the rapid decay of the short waves might change with the streamwise position. The inhomogeneous behavior must be considered, if the integral scales of turbulence are small compared to the panel size. However, the turbulent structure of attached and free shear layers does not change rapidly and the change of R_p with pair position x will be smooth. For an almost linear dependence, the number of pair locations is given by the streamwise extent of the largest panels. Two or three pair locations might already be sufficient. In the crosswise direction, the flow is probably still homogeneous, and no additional pair locations will be needed.

Below separation and reattachment, the inhomogeneous behavior of $R_p(x, y)_{\xi, \eta, \tau}$ is difficult to predict. However, in any case, the aerodynamic engineer could pick a minimum number of pair locations in a streamwise direction, such that the integral of equation (22) stays within prescribed error margins (see

Section VII). There is no reason why the turbulent fluctuations should be inhomogeneous along the separation and reattachment lines in two-dimensional or axisymmetric flows. Therefore, panel size and location are of no concern in a crosswise direction, and no additional pair translations will be necessary.

V. QUICK LOOK PROCEDURES

Any statistical program requires a large amount of data and the determination of generalized forces from rigid model tests is a particularly bad case. The success of such a program depends largely upon whether or not the most dangerous cases can be isolated at an early stage. A "quick look" for large frequency components of the generalized forces should precede any program which uses the spatial structure of the pressure field to arrive at "true" force estimates.

For quick look purposes, it is probably sufficient to concentrate on the two limiting cases of broad band and narrow band excitation, Figure 10. In a broad band excitation, the integral over $S_F(\omega)$ will be large. This integral is given by the autocorrelation at zero time lag (mean square value) and a probably dangerous broad band excitation of a single mode could therefore be detected by looking at mean square values only.

The detection of large narrow band components is much more laborious. In the derivation of the excitation response relation, equation (9), it was shown that the structure will accept only very narrow bands, the width of which is only a few percent of the center frequency. This means that the quick look should be performed with equally narrow bandwidth; otherwise, some dangerous narrow band components might be

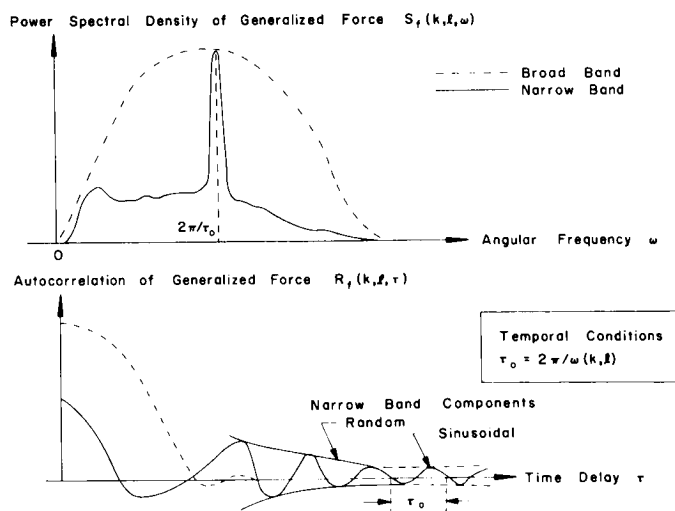


FIGURE 10. DANGEROUS EXCITATIONS OF A SINGLE MODE

integrated out. If a larger region of the frequency domain must be covered, the narrow bandwidth leads to a very large number of center frequencies, and therefore large computation times. The numerical effort could be reduced considerably by using the autocorrelation instead of the power spectrum. The two are related by Fourier transform pairs; it is a general feature of these operations that the transform is broad if the transform function is narrow. To be more specific, a narrow band peak of $S_F(\omega)$ is present whenever the autocorrelation does not vanish, but oscillates at time lags that are large compared to the fundamental period of the panel oscillation $\tau_0 \gg 2\pi/\omega(1,1)$. Instead of looking at a large number of center frequencies, it might be possible to concentrate on the autocorrelation at zero time lag and one selected interval of large time lags.

In view of these considerations, a quick look procedure is sought which detects a rough, quick estimate of the force autocorrelations $R_F(m,n,\tau)$ from measured wall pressures. Obviously, the reliability of the force estimate depends very much on the pressure model which is used. In many cases, the plane wave approximation, equation (15), is already sufficient. In this case, a temporal Fourier transform of equation (15) shows that the wanted autocorrelation of the forces $R_F(m,n,\tau)$ is directly proportional to the autocorrelation of the pressures $R_p^*(0,0,\tau)$. A broad band excitation is present as soon as the RMS-pressure (zero lag autocorrelation) is large. A narrow band excitation might occur as soon as $R_p^*(0,0,\tau)$ shows a sinusoidal wiggle. If more than one mode is excited, the correspondent asymptotic autocorrelation of the pressures deviates from a simple sinusoidal pattern. A Fourier decomposition of $R_p^*(0,0,\tau)$ will indicate the time periods which receive the largest contribution of the asymptotic wiggles. A dangerous vibration becomes possible as soon as these time periods coincide with the time periods of standing flexural waves.

Unfortunately, it is not possible to restrict the "look" for asymptotic $R_p^*(\tau)$ wiggles to those combinations of geometrical and flow parameters which were indicated by large rms values since all narrowband excitations are overlooked where the area under the narrowband peak of $S_F(m,n,\omega)$ is small compared to the area under the complete curve (mean square value) as shown in Figure 10. Both "looks" must therefore be carried out for all combinations of geometrical and flow parameters.

The flight data of Figures 1 and 3 already indicate that the plane wave approximation might give a large number of "dangerous" Mach numbers. One might want to further reduce the number of geometrical and flow parameters which have to be considered in the

final analysis. For this purpose, the pressure model must retain the spatial structure. The model of homogeneous turbulence implies that the power spectral density analysis must be repeated for the spatial wave numbers or frequencies λ and μ , equations (17) and (18). Again the "quick look" could be based on the general feature of Fourier transforms which has been discussed above. It seems sufficient to measure $R_p^*(\xi,\eta,\tau)$ for selected large separations only. The zero lag case has been treated in the plane wave approximation. A dangerous excitation is then detected as soon as the asymptotic pressure correlation $R_p^*(\xi,\eta)_{\tau \rightarrow \infty}$ wiggles at large separation distances such that the distance between zero crossings coincides with the "space periods" a/m and b/n .

The "quick look" becomes very powerful, if the pressure fluctuations are due to a convected pattern of steady decaying turbulence [16] which has been observed in attached- [17] [18], separated- [19], and jet-boundary layers [20]. In these cases, the pressure time history at one point resembles the flash light image of the pressures taken along the upstream portion of the streamline ($\eta = 0$). Therefore, a narrow band component of the pressure power spectrum, which is centered around the angular frequency, $\omega = 2\pi/\tau_0$, indicates a spatial cross correlation function, $R_p^*(\xi,\eta,\tau)$, which has the space period $\lambda = U_c \cdot \tau_0$. Thus, the spatial and temporal wave numbers are no longer independent and the criterion for large excitations may be reduced to one single condition,

$$U_c = \frac{\omega(k, \ell) a}{2\pi k}, \quad k, \ell = 1, 2, 3 \quad (31)$$

for the convection speed U_c of the pressure fluctuations.

To check whether or not the measured wall pressure fluctuations are due to convected turbulence, one needs only two transducers which are separated along the streamline $\eta = 0$ as indicated in Figure 11. A convection is present as soon as the temporal cross correlation between the two transducers is comparable to the displaced autocorrelation of the upstream transducer. A "resemblance" exists as soon as the cross correlation function has a distinct maximum and an average convection speed U_c [21] might be based on the time delay, τ_m , at which the maximum occurs

$$U_c = \frac{\xi}{\tau_m} \quad (32)$$

In the quick look, one is concerned with the convection speed over large separation distances which are comparable to the largest edge lengths, a , b . The dominant nondecayed portion of $R_p^*(\xi,\eta,\tau)$ would be statistically homogeneous if this convection speed is constant

across the panel. However, for homogeneous turbulence, the special cross correlation, R_p^* , is reduced

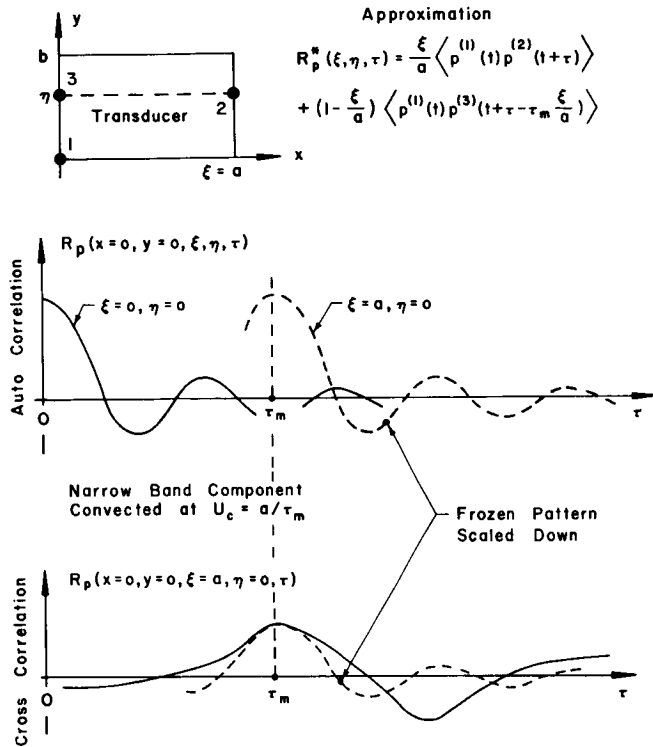


FIGURE 11. CRUDE APPROXIMATION OF R_p^* BY THE STANDARD CROSS CORRELATION R_p BETWEEN THREE TRANSDUCERS ON OPPOSITE PANEL EDGES

to the standard cross correlation, R_p . Expressing the decayed portion by the change between the auto and cross correlations

$$R_p(0, \tau - \tau_m \xi/a) - R_p(\xi, \tau)$$

one obtains an approximation:

$$R_p^*(\xi, \eta, \tau) \simeq (1 - \frac{\xi}{a}) R_p(x=0, y=0, \xi=0, \eta, \tau - \tau_m \xi/a) + \frac{\xi}{a} R_p(x=0, y=0, \xi=a, \eta, \tau). \quad (33)$$

Thus, the estimate of the special pressure cross correlation requires only to change the crosswise separation of three transducers, Figure 11.

In the vicinity of boundary layer separation and reattachment lines, we cannot expect a constant convection speed, U_c . However, an average speed was

already estimated by using the largest separation $\xi=a$ between the upstream transducer 1 and the downstream transducer 2. It is hoped that the space average of the standard cross correlation is reflected approximately by taking the average convection speed instead.

The observed convected patterns of turbulence often show that the ratio between convection velocity, U_c , and the free stream velocity, U_{∞} , is often independent of Mach and/or Reynolds number. In this particular case, we can gather all the necessary information about convection speeds at a particular convenient combination of M and/or Re . For all other operating conditions, the convection speed follows by calculating the free stream velocity U_{∞} . The autocorrelation function (or power spectrum) could be obtained by scaling with the Strouhal number [22]. The concept of convected turbulence is therefore a very powerful tool. It reduces both the number of correlations and the number of Mach and Reynolds numbers that are necessary in a quick look procedure.

VI. TOLERABLE ERRORS

In the curve fit of a given cross correlation, it has always been assumed that the statistical analysis of the measured wall-pressure fluctuations is exact. In reality, the measured R_p^* values are only estimates of a true value. The curve-fitting procedure gives ambiguous influence coefficients as soon as the error, σ_{R^*} , of an R_p^* estimate is equal to or bigger than the root mean square error $(\Delta^2 R_p^*)^{1/2}$, between the estimated R_p^* distribution and the approximation R_p^* which was given in equation (26). The condition

$$\sigma_{R^*} < (\Delta^2 R_p^*)^{1/2} \quad (34)$$

should therefore be checked in each wind tunnel program which tries to predict the autocorrelation of the generalized forces, $R_F(m, n, \tau)$, by a curve fit of experimental cross correlations. The predicted R_F values are meaningful only if the condition of equation (34) is met.

The true value of the even space-time correlation function, R_p^* , was defined in equation (22). It is based on an "ideal test" which meets the following requirements:

- (1) The wall pressure fluctuations are a stationary and ergodic process [11].
- (2) The pressure records are infinitely long [23].
- (3) The complex frequency response function of the two narrow band filters and/or the time delay is a Dirac function [24].

(4) The transducers and all data processing elements are both linear and time invariant.

In the actual tests, all four requirements will be violated, and additional calibration tests are needed to find the error σ_R^* ,

$$\sigma_R^* = [(\Delta^2 R^*)_1 + \dots + (\Delta^2 R^*)_4]^{\frac{1}{2}}, \quad (35)$$

which accounts for the accumulated deviations from the "ideal test."

The largest error is due to nonlinear effects and time shifts on the data reduction chain. Contrary to the other three errors, $(\Delta^2 R^*)_4$ cannot be reduced by a proper choice of the data reduction equipment and/or repeated runs. This is, therefore, the error which will ultimately decide whether or not the tests are meaningful. Also, it is useless to make the first three errors much smaller than the fourth. A good choice for the tolerable upper limit of error mentioned above would be

$$(\Delta^2 R^*)_l \leq \frac{1}{3} (\Delta^2 R^*)_4; \quad l = 1, 2, 3. \quad (36)$$

An estimate of $(\Delta^2 R^*)_4$ is now possible for a data reduction chain which is linear and time invariant enough such that the amplitude dependence and the time shifts of the frequency response function might be treated as random disturbances. As an example, a data reduction chain is treated which consists of $N = 6$ elements.

- $l = 1$ Transducer
- 2 Transmission line
- 3 Tape recorder channel
- 4 Filter or time delay
- 5 Multiplier
- 6 Integrator

The average action of each element is now completely described by its complex frequency response function,

$$H_l(\omega) = |H_l(\omega)| e^{i\varphi_l(\omega)}. \quad (37)$$

The elements $l = 1, 2, 3, 4$ are used in pairs because the pressures from the points $j = 1$ and $k = 2$ are handled independently as indicated in Figure 8. For each pair of elements, the cross-power spectrum of the two inputs j and k is related to the cross-power spectrum of the two outputs by

$$\begin{aligned} S_{jk}(\omega) \Big|_{\text{out}} &= H_l^j(\omega) [H_l^k(\omega)]^* \cdot S_{jk}(\omega) \Big|_{\text{in}} \\ &= |H_l^j(\omega)| \cdot |H_l^k(\omega)| \\ &\quad \left[e^{i[\varphi_l^j(\omega) - \varphi_l^k(\omega)]} S_{jk}(\omega) \right]_{\text{in}} \end{aligned} \quad (38)$$

The cross-power spectrum of the output is equal to the cross-power spectrum of the input multiplied by the gain factor and the exponential phase difference of the two transmitting elements. This input-output relation might be viewed as an extension of the power spectral analysis of equation (9). The two equations are identical if one demands that $H_l^j(\omega) = H_l^k(\omega)$ for all elements that transmit both pressures p^j and p^k simultaneously. In the above data transmission line this happens at the multiplier and any following element.

The output of the element l is the output of the element $l + 1$ and the action of the complete chain is therefore given by multiplying the factors of equation 38. Therefore,

$$\begin{aligned} S_{jk}(\omega) \Big|_{\text{output from averager}} &= \\ &= S_{jk}(\omega) \text{ pressure} \prod_{l=1}^{N=6} |H_l^j| \cdot |H_l^k| \cdot e^{i(\varphi_l^j - \varphi_l^k)}. \end{aligned} \quad (39)$$

Using equation 39 it is possible to eliminate systematic signal distortions in the final data presentation. However, the gain factors and phase shifts of the individual elements are known only within the statistical errors $\Delta |H_l^j|$, $\Delta |H_l^k|$ and $\Delta(\varphi_l^j - \varphi_l^k)$, which summarize the effects of nonlinearity (amplitude dependent frequency-response function), time variance (time shift of calibration curves), and the errors that were inherent in the calibration device used to measure response functions $H_l(\omega)$. For small and random derivations, the accumulated error is then given by the error propagation law:

$$\begin{aligned} (\Delta^2 S_{jk})_4 &= \sum_{l=1}^N \left\{ \left(\frac{\partial S_{jk}}{\partial |H_l|} \Delta |H_l| \right)^2_{j+k} + \left(\frac{\partial S_{jk}}{\partial \varphi_l} \Delta \varphi_l \right)^2_{j-k} \right\} \\ &= S_{jk}(\xi, \eta, \omega) \cdot \sum_{l=1}^N \left\{ \left(\frac{\Delta |H_l^j|}{|H_l^j|} \right)^2 + \left(\frac{\Delta |H_l^k|}{|H_l^k|} \right)^2 \right. \\ &\quad \left. + [\Delta(\varphi_l^j - \varphi_l^k)]^2 \right\}. \end{aligned} \quad (40)$$

In presently available commercial data reduction equipment, the biggest errors are introduced by dynamic phase shifts between transducers and between the channels of tape recorders [24]. Relative mean square errors of

$$\frac{[(\Delta^2 S_{jk})_4]^{\frac{1}{2}}}{|S_{jk}(\omega)|} \approx 20\% \quad (41)$$

are to be expected even for carefully selected elements. It seems that nonlinear effects and dynamic shifts in the transducer and in the data transmitting elements are so big that the more refined force estimates, which consider the spatial structure of the pressure field, might lead to ambiguous results.

Equation (40) gives the error of a cross power estimate in a form which is directly applicable to dynamic calibration tests. The wanted error of the cross correlation estimate follows from a Fourier transformation in time. This shows that the statistical errors will be of the same order of magnitude whether the statistical analysis is done in the frequency domain or in the time domain. The error analysis and the inherent demand for dynamic calibration are therefore quite general and not restricted to the cross correlation technique. In future calibration programs, one has to measure not only the "average" frequency response function but the disturbances of the gain factors and phase differences that are produced by nonlinear and dynamic effects in the transducer, in the data reduction chain, and in the calibration device.

Equation (40) could be used as a basis for a survey of optimum linear and time invariant elements and calibration procedures. Measuring the standard deviations for the gain factors and phase shifts of each data transmitting element, the smallest pressure cross correlation could be calculated which is still meaningful in acoustic wind tunnel tests.

VIII. CONCLUSIONS

Recent flight and wind tunnel tests indicate that the skin of large launch vehicles might suffer a high frequency vibration caused by flow separation and oscillating shocks. This paper discusses the feasibility of obtaining the aerodynamic forcing functions at an early design stage by a cross correlation of wall pressure fluctuations, which have been measured on rigid wind tunnel models.

The relation between generalized forces and wall pressures is illustrated for the simplest of all cases,

the rectangular flat plate with simply supported edges. All simplifying assumptions will be listed in a separate report and may be verified in future tests. A simple excitation response relation is given which is valid not only for the flat plate but also for all panel configurations and all edge conditions, the free vibration of which can be described by orthogonal modes.

The accurate prediction of skin vibrations requires the power spectrum of the autocorrelation of the generalized forces which act on the individual modes. Their exact determination would lead to a fourth order integration over the cross correlation function of two transducers which are independently moved across the panel. The experimental and numerical effort in this exact solution is prohibitive and simple models of the pressure field have to be tried instead. The approximation with normal incident plane waves and the assumptions of homogeneous turbulence are reviewed. The first neglects the spatial structure of the pressure field completely and the second might lead to ambiguous results for high shear flows and/or supersonic flows with boundary layer separation and reattachment.

Unfortunately, the largest pressure fluctuations are mostly associated with inhomogeneous flow. It is shown that the force autocorrelations might be obtained for inhomogeneous flows by a curve fit of a "special" pressure cross correlation function. For homogeneous turbulence, this curve fitting procedure is equivalent to Allan Powell's spatial Fourier decomposition ("joint acceptance").

The experimental and numerical effort of any curve fitting procedure is still so large and costly that it can be applied only to very few cases where simpler pressure models give marginal results. A quick look is described which estimates the space-time cross correlation by the use of only three transducers on opposite panel edges. It is based on the concept of convected turbulence and shows that only very few Mach and Reynolds numbers are necessary in "quick look" tests provided that convected turbulence is the dominant noise source.

A curve fit of experimental pressure correlations is useful only as long as the statistical error of a cross correlation estimate is smaller than the numerical error of the curve fitting procedure. An analysis of systematic and random errors indicates that nonlinear effects and dynamic shifts in the data transmitting elements might produce relative mean square errors up to 20 percent. The refined estimate of generalized force, which is based on the spatial structure of the pressure-space-time correlation function, might therefore lead to ambiguous results. The pressure

transducer and the data reduction chain must be calibrated very accurately not only for the time average frequency response but also for dynamic shifts of gain factor and phases. Dynamic errors are particularly severe in small pressure transducers and tape recorders.

The interest, discussions and constructive criticism of Dr. W. H. Heybey, Dr. R. D. Rechtien, and Mr. K. D. Johnston, Mr. G. A. Wilhold, Mr. L. A. Schutzenhofer, and Mr. R. Thornton are gratefully acknowledged.

REFERENCES

1. Krause, F.: "Preliminary Results of SA-4 Acoustic Flight Tests," Memo M-AERO-A-48-63.
2. Eldred, K.; Roberts, W. M. and White, R. W.: "Structural Vibrations in Space Vehicles," WADD Technical Report 61-02 (1961).
3. Ailman, C. M.: "Wind Tunnel Investigations of the Fluctuation Pressures on the Surface of a Saturn I Vehicle, 2.75 Model "C"," Douglas Report S. M. - 44148.
4. Krause, F.: "Initiation of Acoustic Tests, Pt. 2: Coordination with NASA-ARC," MSFC Memorandum M-AERO-A-72-63.
5. Kuehn, D.: "Experimental Investigation of the Pressure Rise Required for Incipient Separation of Turbulent Boundary Layers in Two-Dimensional Supersonic Flow," NASA TR-117 (1961).
6. Kuehn, D.: "Turbulent Boundary Layer Separation Induced by Flares on Cylinders at Zero Angle of Attack," NASA TR-R-117 (1961).
7. Krause, F.: "Initiation of Acoustic Tests, Pt. 1: Coordination with NASA-LRC," MSFC Memorandum M-AERO-A-70-63.
8. Ziegler, H.: *Mechnik III*, Birkhäuser Verlag, Basel-Stuttgart, 2nd Ed. 1956.
9. Francken, P. A.; Lyon, R. N.: "Estimation of Sound Induced Vibration by Energy Methods with Application to the Titan Missile," DOD Shock, Vibration and Associated Environments, Symposium 31, Pt. 3 (Oct. 1962) 12-26.
10. Ritz: "Über eine neue Methode zur Lösung gewisser Variationsprobleme der mathematischen Physik." *Journal fuer die reine und angewandte Mathematik*, Vol. 135 (1909) pp -161.
11. Crandall, S. H.: "Random Vibration in Mechanical Systems" Academic Press (1963), New York, N. Y.
12. White, R. W.: "Structural Response to Pressure Fluctuations and Oscillating Shocks," Wyle Labs. - Southeast Div., Report WR-63-12, Sept. 1963.
13. Lamb, H.: "The Dynamical Theory of Sound, 2nd Ed. (A25), reprinted Dover (1960) N. Y.
14. Rayleigh, F. R. S.: "The Theory of Sound, Vol. 1 (1894), Chapter 10, Reprint, Dover (1945) N. Y.
15. Batchelor, G. K.: "The Theory of Homogeneous Turbulence," Cambridge University Press, Student's Edition, 1960.
16. Powell, A.: "On the Response of Structures to Random Pressures and to Jet Noise in Particular," Random Vibration, Vol. 1, The MIT Press, Cambridge, Mass., 1958.
17. Bull, M. K.; Wilby, J. F.; Blackman, D. R.: "Wall Pressure Fluctuations in Boundary Layer Flow and Response of Simple Structures to Random Pressure Fields," University of Southampton, AASU Rep. 243 (1963) Contract AF 611052)358.
18. Kistler, A. L. and Chen, W. S.: "The Fluctuating Pressure Field in a Supersonic Turbulent Boundary Layer," JPL Report 32-277 (1962).
19. Kistler, A. L.: "The Fluctuating Wall Pressure Under a Separated Supersonic Flow," Fluid Dynamics Panel of AGARD, "Rhode-Saint-Genese, Belgium, Apr. 1-5, 1963.
20. Davies, P. O. A. L.; Fisher, M. J. and Barrett, M. T.: "The Characteristics of the Turbulence in the Mixing Region of a Round Jet," *Journal of Fluid Mechanics*, Vol. 15 (1962) pp 337-367.
21. Wills, J. A. A.: "On Convection Velocities in Turbulent Shear Flows," NPL-Aero-Report 1050, (1963).
22. Rainey, A. G.: "Progress on the Launch Vehicle Buffeting Problem, 5th AIAA Structures and Materials Conference, Apr. 1-4; 1964, Palm Springs, Calif.
23. Bendat, J. S.: "Measurement and Interpretation of Correlation Functions," Lecture at Data Reduction and Analysis Symposium, Jan. 22-23, 1964, Huntsville, Alabama.

24. Schulze, G. H. : "Tape Recording Errors," ISA Reprint, Sagamo Electric Company, Springfield, Ill.
25. Rechtien, R. D. : "On the Pressure Requirements for Structural Response Equations," R-AERO-AU presentation, Aug. 19, 1964, to be published as NASA TN.

ON AN EXTENSION OF OSWATITSCH'S EQUIVALENCE RULE TO UNSTEADY FLOW

By

M. F. Platzer

N65-24129

SUMMARY

This paper outlines an approximation theory for the calculation of the linearized subsonic and supersonic flow around pulsating bodies of low aspect ratio, extending K. Oswatitsch's and F. Keune's theories for steady flow to these unsteady flow cases.

In a first approximation, the flow around pulsating bodies of low aspect ratio consists of two terms:

- A two-dimensional cross-flow.
- A spatial influence which depends only on the sum of the source-elements over the cross-section.

This spatial influence reduces the flow over pulsating low aspect ratio wings to the flow over the equivalent pulsating body of revolution. A similarly characteristic structure of the flow field is found also for the higher order flow terms.

In addition to the basic conditions for linearization, the range of validity of this approximation theory is essentially bound by certain combinations of aspect ratio, Mach number, and reduced frequency.

These order of magnitude considerations can be further substantiated by comparing the approximation theory with certain exact solutions of the unsteady linearized potential equation. Such solutions are found for the infinitely long tube or ribbon pulsating harmonically in subsonic or supersonic flow.

LIST OF SYMBOLS

| Symbol | Definition |
|--------|----------------------------------------|
| A | Amplitude of cross-sectional pulsation |
| c | Free-stream velocity of sound |
| C | Euler's constant = 0.5772 |
| Ci | Integral cosine function |

| Symbol | Definition |
|---------------------|-------------------------------------------------------------------------|
| $d(x, y)$ | Amplitude of pulsation |
| $E^{[n]}(x, y, z)$ | Sum of source-moments of nth order over the cross section |
| $H_0^{(1)}$ | Hankel function of first kind, zeroth order |
| $H_0^{(2)}$ | Hankel function of second kind, zeroth order |
| i | imaginary unit |
| k | $\frac{\omega L}{U}$ reduced frequency |
| K_0 | Modified Bessel function of second kind, zeroth order |
| L | Characteristic length (wing-root, body-length, wavelength of pulsation) |
| $m^{[n]}$ | Source-moment of nth order |
| M | $\frac{U}{c}$, free-stream Mach number |
| p | Laplace transform variable |
| $Q(x)$ | Amplitude of cross-sectional pulsation |
| $q(\xi, \eta)$ | Source-distribution |
| r, θ | Cylindrical coordinates |
| s(x) | Half-span of wing |
| Si | Integral sine function |
| t | time |
| U | Free-stream velocity |
| V(x) | Definition equation 2.8 |
| x, y, z | Cartesian coordinates Figure 2 |
| $\overline{\alpha}$ | $\frac{\omega}{c(M+1)}$ |

LIST OF SYMBOLS (Concluded)

| Symbol | Definition |
|--------------------|-----------------------------------------------------------------------|
| α' | $\frac{\omega}{c(1-M)}$ |
| α'' | $\frac{\omega}{c(M-1)}$ |
| β | $\sqrt{1-M^2}$ |
| $\cot \alpha$ | $\sqrt{M^2-1}$ |
| $\Phi(x, y, z, t)$ | Disturbance potential |
| $\phi(x, y, z)$ | Amplitude of disturbance potential |
| $\phi_q(x, y, z)$ | Cross-flow potential |
| $\phi_R(x)$ | Spatial influence |
| γ | $\frac{2\pi}{L}$, Wave-number of pulsation |
| κ | $\frac{\omega}{c\beta^2}$, $\frac{\omega}{c \cot^2 \alpha}$ |
| μ | $\frac{\omega U}{c^2 \beta^2}$, $\frac{\omega U}{c^2 \cot^2 \alpha}$ |
| ω | Circular frequency |
| σ | $\frac{s}{L}$, reduced span |
| ξ, η | Source coordinates |

I. INTRODUCTION

The problem of steady linearized subsonic and supersonic flow about bodies of low aspect ratio at zero and small angles of attack has been treated by M. Munk [2], H. S. Tsien [3], R. T. Jones [4], G. N. Ward [5], M. C. Adams - W. R. Sears [6], F. Keune-K. Oswatitsch [7], [8], and M. A. Heaslet - H. Lomax [9].

M. Munk [2] first recognized that the flow about bodies of revolution at small angles of attack may be considered two-dimensional when viewed in cross sections perpendicular to the longitudinal axis. With this idealization, the local lift distribution can be obtained from simple momentum considerations. R. T. Jones [4] later found that this concept also holds for low aspect ratio wings. Garrick [10] and Miles [11] finally could show that the Munk-Jones hypothesis of two-dimensional, incompressible flow in planes normal to the flight direction retains considerable usefulness also for harmonically oscillating slender pointed

wings and bodies. Thus, the velocity potential of the transverse flow pattern satisfies in both cases, steady and unsteady flow, Laplace's equation in two dimensions. However, for unsteady flow the condition of sufficiently low reduced frequency must be fulfilled in addition to the condition of very low aspect ratio. For high reduced frequencies, the concept of two-dimensional cross-flow may be extended to compressible flow, the velocity potential satisfying now the two-dimensional wave equation of acoustics [16].

In all these cases there is only a cross-flow to be considered reducing the original three-dimensional problem to a two-dimensional one. This is an important simplification explaining the general use of this slender-body concept in modern missile aerodynamics.

We want to turn now to the corresponding symmetrical steady and unsteady flow cases; namely, the flow about bodies of low aspect ratio at zero angle of attack whose skin may be stationary or execute time-dependent breathing vibrations (pulsations).

The steady flow about bodies of low aspect ratio at zero angle of attack has been treated by G. N. Ward [5], M. C. Adams-W. R. Sears [6], F. Keune-K. Oswatitsch [7] [8] a.o. This case proves to be more difficult than the calculation of a lift distribution on a lifting delta wing, according to R. T. Jones, or on a lifting body of revolution, according to M. M. Munk. The lifting effect corresponds to the effects of a dipole distribution and produces disturbances only within a short distance. Therefore, the influence of the parts of the body in front of or behind a given cross section is of higher order and may be disregarded. In the non-lifting flow case, however, the effect of body thickness corresponds to a source-sink distribution producing disturbances over a large distance. Considering the incompressible cross-sectional flow alone, therefore, would neglect the "spatial influence" of the parts of the body in front of or behind this cross section. This influence being of the same order of magnitude as the cross-sectional flow has therefore always to be retained in order to obtain a correct description of the nonlifting flow about bodies of low aspect ratio.

Representing the wing by a source distribution, the disturbance potential of the cross-sectional flow is given by

$$\phi(x, y, z) = \frac{1}{2\pi} \int_{-s(x)}^{+s(x)} q(x, \eta) \ln \sqrt{(y-\eta)^2 + z^2} d\eta + \phi_R(x), \quad (1.1)$$

where $q(x, y)$ is determined by the boundary condition at the body, and $\phi_R(x)$ is an additional function of x whose meaning was not always clear in the literature

of the slender body approximation (compare the discussion in Ref. 6). Oswatitsch and Keune [7, 8] could show that this function is just the spatial influence mentioned previously and can be extracted from the exact solution of the linearized potential equation for low aspect ratio wings at zero angle of attack.

$$\phi(x, y, z) = -\frac{1}{4\pi} \iint_F \frac{q(\xi, \eta) d\xi d\eta}{\sqrt{(x-\xi)^2 + \beta^2(y-\eta)^2 + \beta^2 z^2}}$$

for $M < 1$

(1.2)

$$\phi(x, y, z) = -\frac{1}{2\pi} \iint_S \frac{q(\xi, \eta) d\xi d\eta}{\sqrt{(x-\xi)^2 - \cot^2 \alpha (y-\eta)^2 - \cot^2 \alpha z^2}}$$

for $M > 1$

After proper expansion of this double-integral with respect to the source distance from the axis, two terms are obtained. One is the cross-sectional flow i.e., the first term in equation (1.1); the other main term reads

$$\phi_R(x, r) = -\frac{1}{4\pi} \int_0^L \frac{V(\xi) d\xi}{\sqrt{(x-\xi)^2 + \beta^2 r^2}} - \frac{V(x)}{2\pi} \ln r$$

for $M < 1$

(1.3a)

$$\phi_R(x, r) = -\frac{1}{2\pi} \int_0^{x-r \cot \alpha} \frac{V(\xi) d\xi}{\sqrt{(x-\xi)^2 - \cot^2 \alpha r^2}} - \frac{V(x)}{2\pi} \ln r \text{ for } M > 1$$

and reduces in the immediate vicinity of the body to

$$\phi_R(x) = \frac{V(x)}{2\pi} \ln \frac{\sqrt{M^2-1}}{2} - \frac{1}{4\pi} \frac{\partial}{\partial x} \int_0^x V(\xi) \ln(x-\xi) d\xi + \frac{\epsilon-1}{4\pi} \frac{\partial}{\partial x} \int_0^L V(\xi) \ln(\xi-x) d\xi + \frac{\epsilon-2}{4\pi} \frac{\partial}{\partial x} \int_0^x V(\xi) \ln(x-\xi) d\xi$$

(1.3b)

$$\epsilon = \begin{cases} 2 & \text{for } M < 1 \\ 1 & \text{for } M > 1 \end{cases}$$

by a proper limiting process $r \rightarrow 0$. The function $V(x)$ in equation (1.3) is defined by

$$V(x) = \int_{-s(x)}^{+s(x)} q(x, \eta) d\eta. \quad (1.4)$$

Thus, the spatial influence, equation 1.3, is dependent only on the sum of the source distribution over the cross section. It is easily interpreted as the difference of the potential of a body of revolution whose source distribution is given by equation (1.4) and its cross-sectional flow potential. The spatial influence of a given low aspect ratio wing and the spatial influence of its equivalent body of revolution, i.e., that body having the same total source strength in all cross sections, therefore, are the same. Since the total source strength is proportional to the cross-sectional area, equivalent bodies are defined as bodies having the same cross-sectional area distribution (Fig. 1).

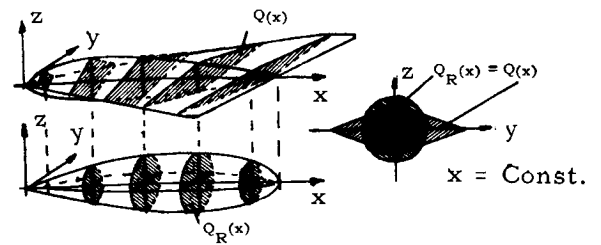


FIGURE 1. LOW ASPECT RATIO WING AND ITS EQUIVALENT BODY OF REVOLUTION

These considerations led Oswatitsch to the postulation of an equivalence rule for both the linearized subsonic and supersonic flow regimes and the nonlinear transonic region which he first communicated at the VIIIth International Congress for Applied Mechanics [12] in 1952. At nearly the same time, experimental investigations on equivalent bodies in the transonic range were carried out by R. T. Whitcomb [13]. His main interest was in finding bodies of low drag; he arrived in this way at the equivalence concept by noticing that the shock waves in the transonic range become axisymmetrical in a rather short distance and that they tend to become of the same shape as the shock waves of the equivalent body of revolution. These results are generally known as the "area rule."

2. EXTENSION OF OSWATITSCH'S EQUIVALENCE RULE TO PULSATING FLOW

We want to extend now the work of Oswatitsch and Keune to unsteady flow and consider a wing of low aspect ratio in linearized subsonic or supersonic flow whose skin performs a symmetric harmonic pulsation

(Fig. 2).¹ We mention that the problem is identical to the problem of a vibrating low aspect ratio panel embedded in the xy-plane, which is of considerable interest for panel flutter investigations.

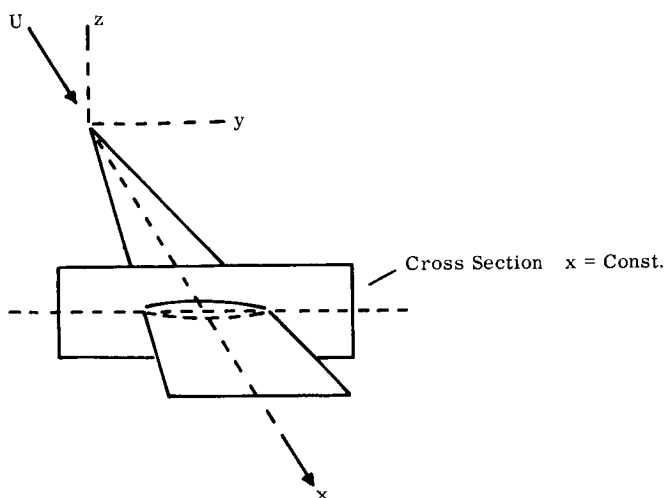


FIGURE 2. SYMMETRIC HARMONIC PULSATION

Assuming harmonic pulsation, we may write the disturbance potential $\Phi(x, y, z, t)$ in the form

$$\Phi(x, y, z, t) = \phi(x, y, z) e^{i\omega t}, \quad (2.1)$$

and, similarly, the pulsation amplitude

$$D(x, y, t) = d(x, y) e^{i\omega t}. \quad (2.2)$$

We assume the pulsation amplitude to be zero at the edges of the wing,

$$d(x, s(x)) = d(x, -s(x)) = 0,$$

and restrict ourselves to the first pulsation mode symmetrical to the xz-plane.

Within the framework of linearized theory, the problem is entirely determined by the exact velocity potential equation (2.3a) for subsonic flow,

$M < 1$:

$$\begin{aligned} \phi(x, y, z) &= -\frac{1}{4\pi} \iint_F \frac{q(\xi, \eta) e^{-i\kappa \sqrt{(x-\xi)^2 + \beta^2(y-\eta)^2 + \beta^2 z^2}}}{\sqrt{(x-\xi)^2 + \beta^2(y-\eta)^2 + \beta^2 z^2}} e^{i\mu(x-\xi)} d\xi d\eta \\ &\quad (F = \text{wing projection area}) \end{aligned} \quad (2.3a)$$

and by equation 2.3b supersonic flow

$M > 1$:

$$\begin{aligned} \phi(x, y, z) &= -\frac{1}{2\pi} \iint_S \frac{q(\xi, \eta) \cos[\kappa \sqrt{(x-\xi)^2 - \cot^2 \alpha (y-\eta)^2 - \cot^2 \alpha \cdot z^2}]}{\sqrt{(x-\xi)^2 - \cot^2 \alpha (y-\eta)^2 - \cot^2 \alpha \cdot z^2}} e^{-i\mu(x-\xi)} d\xi d\eta \\ &\quad (S = \text{area cut out by the upstream Mach cone}) \end{aligned} \quad (2.3b)$$

As is well known in steady aerodynamics (e.g., Ref. 1, pp. 498 and 514), the source distribution can be expressed also for pulsating flow by the normal velocity on the wing surface,

$$q(x, y) = 2 w(x, y, 0), \quad (2.4)$$

where $w(x, y, 0)$ can be related to the pulsation amplitude by means of the linearized boundary condition on the surface of the pulsating wing:

$$w(x, y, 0) = \pm [i\omega d(x, y) + U \frac{\partial d(x, y)}{\partial x}]. \quad (2.5)$$

The evaluation of the double integral equation (2.3) for arbitrary plan forms, frequencies and Mach numbers can be achieved only by tedious numerical integration. Therefore, an approximation theory will be developed which generalizes the approach first given by Oswatitsch and Keune for the case of steady flow [7, 8].

Since the coordinate y of a source element on the wing area is always small compared to the root length L , we may write for the velocity potential (considering first only subsonic flow)

$$\phi(x, y, z) = -\frac{1}{2\pi} \iint_F \frac{w(\xi, \eta) e^{-i\kappa \sqrt{(x-\xi)^2 + \beta^2(y^2 + z^2)}}}{\sqrt{(x-\xi)^2 + \beta^2(y^2 + z^2)}} e^{i\mu(x-\xi)} d\xi d\eta + \Delta\phi(x, y, z) \quad (2.6)$$

¹The author wishes to thank Professor K. Oswatitsch, Vienna Institute of Technology, Austria, for his suggestions and encouragements.

where

$$\Delta\phi(x, y, z) = -\frac{1}{2\pi} \int_{-s(x)}^{+s(x)} w(\xi, \eta) \left[\frac{e^{-i\kappa \sqrt{(x-\xi)^2 + \beta^2(y-\eta)^2 + \beta^2 z^2}}}{\sqrt{(x-\xi)^2 + \beta^2(y-\eta)^2 + \beta^2 z^2}} - \frac{e^{-i\kappa \sqrt{(x-\xi)^2 + \beta^2(y^2 + z^2)}}}{\sqrt{(x-\xi)^2 + \beta^2(y^2 + z^2)}} \right] d\xi d\eta \quad (2.7)$$

For large distances from the wing $\Delta\phi(x, y, z)$ will become negligibly small compared to the first term in the expansion and the potential becomes with

$$V(x) = \int_{-s(x)}^{+s(x)} q(x, \eta) d\eta = 2 \int_{-s(x)}^{+s(x)} w(x, \eta) d\eta = i\omega Q(x) + U Q_x(x) \quad (2.8)$$

for $r = \sqrt{y^2 + z^2} \rightarrow \infty$

$$\phi(x, y, z) = -\frac{1}{4\pi} \int_0^L \frac{V(\xi) e^{-i\kappa \sqrt{(x-\xi)^2 + \beta^2 r^2}}}{\sqrt{(x-\xi)^2 + \beta^2 r^2}} e^{i\mu(x-\xi)} d\xi \quad (2.9)$$

where

$$Q(x) = 2 \int_{-s(x)}^{+s(x)} d(x, \eta) d\eta \quad (2.10)$$

is the amplitude of the cross-sectional pulsation of the wing. For points near the wing, however, $\Delta\phi(x, y, z)$ is of equal order of magnitude as the first term in the expansion. Here the term $x-\xi$ approaches zero; therefore the term $y-\eta$ has an important influence on $\Delta\phi(x, y, z)$. The main influence of this second term can be taken into account, however, by replacing the variable source distribution $w(\xi, \eta)$ by the source distribution at a given cross section $\xi=x$; thus

$$\Delta\phi(x, y, z) = -\frac{1}{2\pi} \int_{-s(x)}^{+s(x)} w(x, \eta) \left[\int_{x_L(\eta)}^{x_T(\eta)} \left\{ \frac{e^{-i\kappa \sqrt{(x-\xi)^2 + \beta^2(y-\eta)^2 + \beta^2 z^2}}}{\sqrt{(x-\xi)^2 + \beta^2(y-\eta)^2 + \beta^2 z^2}} - \frac{e^{-i\kappa \sqrt{(x-\xi)^2 + \beta^2(y^2 + z^2)}}}{\sqrt{(x-\xi)^2 + \beta^2(y^2 + z^2)}} \right\} e^{i\mu(x-\xi)} d\xi \right] d\eta \quad (2.11)$$

If we make now the further approximation that instead of integrating from the leading edge $x_L(\eta)$ to the trailing edge $x_T(\eta)$ we extend this integration in the inner integral of equation 2.11 to $-\infty$ and $+\infty$, then a closed form solution is obtained:

$$\Delta\phi(x, y, z) = \frac{1}{2} \int_{-s(x)}^{+s(x)} w(x, \eta) \left[H_0^{(2)} \left(\frac{\omega}{c} \sqrt{(y-\eta)^2 + z^2} \right) - H_0^{(2)} \left(\frac{\omega}{c} \sqrt{y^2 + z^2} \right) \right] d\eta. \quad (2.12)$$

There remain two terms K_1 and K_2 [14] which can be

shown to be of higher order. Hence, the final result can be written in the following form:

$$\phi(x, y, z) = \frac{1}{2} \int_{-s(x)}^{+s(x)} w(x, \eta) H_0^{(2)} \left(\frac{\omega}{c} \sqrt{(y-\eta)^2 + z^2} \right) d\eta + \phi_R(x, y, z), \quad (2.13)$$

where

$$\phi_R(x, y, z) = -\frac{1}{4\pi} \int_0^L \frac{V(\xi) e^{-i\kappa \sqrt{(x-\xi)^2 + \beta^2 r^2}}}{\sqrt{(x-\xi)^2 + \beta^2 r^2}} e^{i\mu(x-\xi)} d\xi - \frac{1}{4} V(x) H_0^{(2)} \left(\frac{\omega}{c} r \right). \quad (2.14)$$

We mention without proof that a similar approach for supersonic flow leads to [14] [15]

$$\phi(x, y, z) = \frac{1}{2} \int_{-s(x-r \cot \alpha)}^{+s(x-r \cot \alpha)} w(x-r \cot \alpha, \eta) H_0^{(2)} \left(\frac{\omega}{c} \sqrt{(y-\eta)^2} \right) d\eta + \phi_R(x, y, z), \quad (2.15)$$

where

$$\phi_R(x, y, z) = -\frac{1}{2\pi} \int_0^{x-r \cot \alpha} \frac{V(\xi) \cos[\kappa \sqrt{(x-\xi)^2 - \cot^2 \alpha \cdot r^2}]}{\sqrt{(x-\xi)^2 - \cot^2 \alpha \cdot r^2}} e^{-i\mu(x-\xi)} d\xi - \frac{1}{4} V(x-r \cot \alpha) H_0^{(2)} \left(\frac{\omega}{c} r \right) \quad (2.16)$$

Hence, the induced flow field consists of two potential flows, a two-dimensional flow satisfying the Helmholtz equation

$$\phi_{yy} + \phi_{zz} + \frac{\omega^2}{c^2} \phi = 0, \quad (2.17)$$

and being induced by the source distribution equation 2.4 plus a three-dimensional flow being induced by the source distribution equation 2.8. This flow is identical with the flow around a pulsating body of revolution, equation (2.9) with equal variation of the cross-sectional pulsation, along the X-axis. Comparing equations (2.13) and (2.15), it is seen that the two-dimensional flow is the same for subsonic and supersonic flow. The spatial influences $\phi_R(x, y, z)$ equations (2.14) and (2.16) are different, however, for subsonic and supersonic flow and represent the influence of the parts of the body in front and behind a given cross section. They are obtained, as in the steady flow case [7], by subtracting from the potential of the pulsating body of revolution its cross-flow potential.

Of particular importance are velocity and pressure distribution on the wing surface. These quantities can be obtained from equations (2.13 - 2.16) by a limiting process $z \rightarrow 0$, $r \rightarrow 0$. Then we obtain immediately for the cross-flow in subsonic and supersonic flow

$$\phi_q(x, y, z) = \frac{1}{2} \int_{-s(x)}^{+s(x)} w(x, \eta) H_0^{(2)} \left(\frac{\omega}{c} |y - \eta| \right) d\eta, \quad (2.18)$$

and after some manipulation for the spatial influences,

$$\begin{aligned} M < 1: \\ \phi_R(x) = \frac{V(x)}{4\pi} \left\{ -Ci \left[\frac{\omega x}{c(1+M)} \right] - Ci \left[\frac{\omega(L-x)}{c(1-M)} \right] - i\pi + i Si \left[\frac{\omega x}{c(1+M)} \right] \right. \\ \left. + i Si \left[\frac{\omega(L-x)}{c(1-M)} \right] \right\} + \frac{1}{4\pi} \int_0^x \frac{V(\xi) - V(x)}{x - \xi} e^{-i \frac{\omega(x-\xi)}{c(1+M)}} d\xi \\ - \frac{1}{4\pi} \int_0^L \frac{V(\xi) - V(x)}{\xi - x} e^{-i \frac{\omega(\xi-x)}{c(1-M)}} d\xi \end{aligned} \quad (2.19)$$

$$\begin{aligned} M > 1: \\ \phi_R(x) = \frac{V(x)}{4\pi} \left\{ -Ci \left[\frac{\omega x}{c(M-1)} \right] - Ci \left[\frac{\omega x}{c(M+1)} \right] - i\pi + i Si \left[\frac{\omega x}{c(M-1)} \right] \right. \\ \left. + i Si \left[\frac{\omega x}{c(M+1)} \right] \right\} + \frac{1}{4\pi} \int_0^x \frac{V(\xi) - V(x)}{x - \xi} \left(e^{-i \frac{\omega(x-\xi)}{c(M-1)}} + e^{-i \frac{\omega(x-\xi)}{c(M+1)}} \right) d\xi \end{aligned} \quad (2.20)$$

where Ci and Si are the Integral Cosine and Integral Sine Functions. This approach which was rather based on physical considerations about the main influences upon the flow field can be supplemented by two other mathematically more rigorous approaches. For this purpose, we generalize a method first used by F. Keune for the steady flow problem [18] and rewrite the potential for the pulsating wing equation (2.3a) in the form

$$2\pi \phi(x, y, z) = I_1 + I_2 \quad (2.21)$$

$$I_1 = \int_0^x \int_{-s(\eta)}^{+s(\eta)} w(\xi, \eta) e^{-i\kappa \sqrt{(x-\xi)^2 + \beta^2 a^2}} e^{i\mu(x-\xi)} \cdot \frac{\partial}{\partial x} \ln \left[x - \xi + \sqrt{(x-\xi)^2 + \beta^2 a^2} \right] d\xi d\eta \quad (2.21a)$$

$$I_2 = \int_0^L \int_{-s(\xi)}^{+s(\xi)} w(\xi, \eta) e^{-i\kappa \sqrt{(x-\xi)^2 + \beta^2 a^2}} e^{i\mu(x-\xi)} \cdot \frac{\partial}{\partial x} \ln \left[\xi - x + \sqrt{(\xi-x)^2 + \beta^2 a^2} \right] d\xi d\eta \quad (2.21b)$$

$$\text{where } a^2 = (y - \eta)^2 + z^2.$$

Integration by parts and proper expansion gives in a first order approximation for the potential function of the pulsating wing in subsonic flow

$$\phi(x, y, z) = \phi_q^*(x, y, z) + \phi_R^*(x) \quad (2.22)$$

$$\phi_q^*(x, y, z) = \frac{1}{\pi} \int_{-s(x)}^{+s(x)} w(x, \eta) \ln \sqrt{(y-\eta)^2 + z^2} d\eta \quad (2.22a)$$

$$\begin{aligned} \phi_R^*(x) = -\frac{1}{4\pi} \left(\frac{\partial}{\partial x} + \frac{i\omega}{1+M} \right) \int_0^x V(\xi) e^{-i \frac{\omega(x-\xi)}{c(1+M)}} \ln(x-\xi) d\xi \\ + \frac{1}{4\pi} \left(\frac{\partial}{\partial x} - \frac{i\omega}{1-M} \right) \int_x^L V(\xi) e^{-i \frac{\omega(\xi-x)}{c(1-M)}} \ln(\xi-x) d\xi + \frac{V(x)}{2\pi} \ln \frac{\beta}{2}. \end{aligned} \quad (2.22b)$$

The second approach can be obtained by generalizing the Adams-Sears method [6] to pulsating flow. We show this for supersonic flow and use, therefore, Laplace transformation

$$\bar{\phi}(p, y, z) = \int_0^\infty e^{-px} \phi(x, y, z) dx.$$

transforming the potential equation into

$$\bar{\phi}_{yy} + \bar{\phi}_{zz} - \lambda^2 \bar{\phi} = 0, \quad (2.23)$$

where

$$\lambda^2 = \cot^2 \alpha \cdot p^2 + 2 \frac{i\omega U}{c^2} p - \frac{\omega^2}{c^2}. \quad (2.24)$$

A proper solution of this equation is

$$\bar{\phi}(p, y, z) = -\frac{1}{\pi} \int_{-s}^{+s} \bar{w}(p, \eta) K_0(\lambda a) d\eta. \quad (2.25)$$

We are looking for a solution near the body and expand, therefore, the modified Bessel function with respect to its argument

$$K_0(\lambda a) = -C - \ln \frac{\lambda a}{2} + \frac{(\lambda a)^2}{4} \left[1 - C - \frac{\lambda a}{2} \right] + \dots \quad (2.26)$$

C = Euler's constant.

Retaining in a first approximation again only the linear terms gives after inversion for the potential function

of the pulsating wing in supersonic flow,

$$\phi(x, y, z) = \phi_q^*(x, y, z) + \phi_R^*(x) \quad (2.27)$$

$$\phi_q^*(x, y, z) = \frac{1}{\pi} \int_{-s(x)}^{+s(x)} w(x, \eta) \ln \sqrt{(y-\eta)^2 + z^2} d\eta \quad (2.27a)$$

$$\begin{aligned} \phi_R^*(x) = & \frac{V(x)}{2\pi} \ln \frac{\cot \alpha}{2} - \frac{1}{4\pi} \left(\frac{\partial}{\partial x} + \frac{i \frac{\omega}{c}}{M-1} \right) \int_0^x V(\xi) e^{-i \frac{\omega(x-\xi)}{c(M+1)}} \ln(x-\xi) d\xi \\ & - \frac{1}{4\pi} \left(\frac{\partial}{\partial x} + \frac{i \frac{\omega}{c}}{M-1} \right) \int_0^x V(\xi) e^{-i \frac{\omega(x-\xi)}{c(M-1)}} \ln(x-\xi) d\xi. \end{aligned} \quad (2.27b)$$

Equations 2.22 and 2.27 show that these approaches lead to different definitions for cross-flow and spatial influence, the cross-flow being again the same for subsonic and supersonic flow, but satisfying now the two-dimensional Laplace equation.

It can be shown that the representations, equations (2.18) - (2.20) and equations (2.22) - (2.27) are equivalent, this being quite analogous to the different forms found in steady flow (compare M. D. van Dyke, Second-Order Slender Body Theory: NASA TR-R-47, equations 7 and 8).

It is also easy to verify that, for vanishing frequency, F. Keune's solutions for steady flow are obtained (equations 2.10, 3.10, 4.1 and 4.2 in Reference 8).

Similarly, a further limiting case for $M = 1$ can be obtained [14], [15]. For the transonic flow case, however, the frequency must be kept sufficiently high in order not to violate the assumption of linearization.

Summarizing our results, we have found that the flow near the body can be considered two-dimensional in every cross section and is easy to be calculated from the Laplace equation

$$\phi_{yy} + \phi_{zz} = 0. \quad (2.28)$$

Hence, the disturbance potential is

$$\begin{aligned} \phi(x, y, z) = & \frac{1}{2\pi} \int_{-s(x)}^{+s(x)} q(x, \eta) \ln \sqrt{(y-\eta)^2 + z^2} d\eta \\ & + \phi_R^*(x). \end{aligned} \quad (2.29)$$

As in the stationary case, the solution is dependent on an additional function $\phi_R^*(x)$, namely the spatial influence. Generalizing Oswatitsch's and Keune's

conception, we have obtained for this spatial influence

$$\begin{aligned} \phi_R^*(x) = & \frac{V(x)}{2\pi} \ln \frac{\sqrt{|M^2-1|}}{2} - \frac{1}{4\pi} \left(\frac{\partial}{\partial x} + \frac{i \frac{\omega}{c}}{M+1} \right) \int_0^x V(\xi) e^{-i \frac{\omega(x-\xi)}{c(1+M)}} \ln(x-\xi) d\xi \\ & + \frac{\epsilon-1}{4\pi} \left(\frac{\partial}{\partial x} + \frac{i \frac{\omega}{c}}{1-M} \right) \int_x^L V(\xi) e^{-i \frac{\omega(\xi-x)}{c(1-M)}} \ln(\xi-x) d\xi \\ & + \frac{\epsilon-2}{4\pi} \left(\frac{\partial}{\partial x} + \frac{i \frac{\omega}{c}}{M-1} \right) \int_0^x V(\xi) e^{-i \frac{\omega(x-\xi)}{c(M-1)}} \ln(x-\xi) d\xi, \end{aligned} \quad (2.30)$$

where $\epsilon = 2$ for $M < 1$
1 for $M > 1$.

Having essentially replaced a solution to the complete linearized unsteady potential equation

$$\left(1 - \frac{U^2}{c^2}\right) \phi_{xx} + \phi_{yy} + \phi_{zz} - \frac{2U}{c^2} \phi_{xt} - \frac{1}{c^2} \phi_{tt} = 0, \quad (2.31)$$

by a solution of the Laplace equation (2.28), the following restrictions have to be imposed in addition to the conditions for linearization (cf. J. W. Miles, The Potential Theory of Unsteady Supersonic Flow, Cambridge 1959).

$$|1 - M^2| \sigma^2 \ll 1 \quad kM^2 \sigma^2 \ll 1 \quad k^2 M^2 \sigma^2 \ll 1, \quad (2.32)$$

where k is a reduced frequency and σ a measure of the lateral extent of the wing.

We want to mention that the range of validity of the solution can be extended by keeping the higher order terms of our expansion of the velocity potential. This can be done in generalizing Keune's method for steady flow [17], [19] or generalizing the Adams-Sears procedure [6]. Keune's method is physically more appealing, however, showing that the higher order flow terms are built up by certain higher order moments of the basic source distribution.

We remember that in our first approximation we needed:

- The local source distribution $q(x, \eta)$
- The sum of the sources over the cross section.

$$V(x) = \int_{-s(x)}^{+s(x)} q(x, \eta) d\eta$$

We introduce now after Keune [12] also for pulsating flow the higher order moments of these quantities, namely,

$$m^{[n]}(x, y, z, \eta) = q(x, \eta) a^n = q(x, \eta) [(y-\eta)^2 + z^2]^{\frac{n}{2}} \quad (2.33)$$

and the sum of these source moments over the cross section

$$E^{[n]}(x, y, z) = \int_{-s(x)}^{+s(x)} q(x, \eta) [(y - \eta)^2 + z^2]^{\frac{n}{2}} d\eta. \quad (2.34)$$

The significance of these quantities can be seen from Figure 3

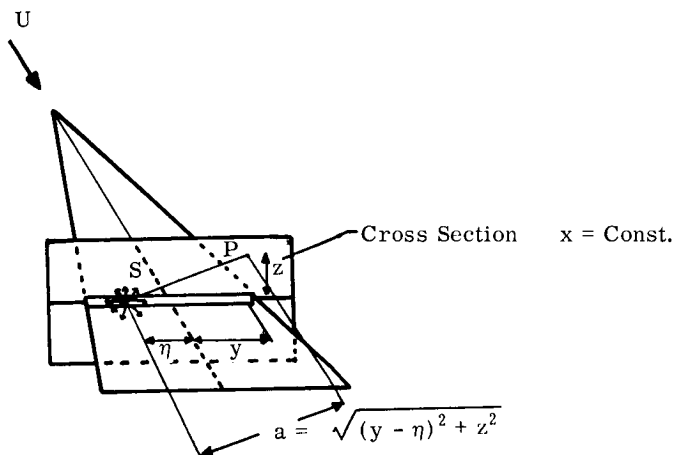


FIGURE 3. PHYSICAL SIGNIFICANCE OF SOURCE MOMENTS

$a = \overline{PS}$ = distance of a point P in the cross section $x = \text{const.}$ from a source-element at point S.

It turns out that also the higher order terms of the expanded velocity potential of the pulsating wing equation (2.3) can be interpreted as a generalized cross-flow and a generalized spatial influence if instead of the local source distribution $q(x, \eta)$ and its sum over the cross section $V(x)$ the higher order moments $m^{[n]}$ and $E^{[n]}$ are used. A more detailed discussion is given in [14, 15]. Thus, a relatively simple theory is obtained for pulsating bodies in compressible flow which extends appreciably the range of validity of the first approximation equations (2.29) and (2.30).

Furthermore, it should be mentioned here that these developments for the pulsating wing can be used to obtain another and quite elementary approach to "quasi-slender body theory" for oscillating wings and bodies of revolution which gives some new insight to the basic structure of the flow field around oscillating bodies, too [14] [15].

3. Comparison With Exact Solutions

The usefulness of the approximation theory developed in the previous section can best be assessed by comparing it with exact results. There are configurations for which exact solutions of the linearized unsteady potential equation can be found. We mention the infinitely long pulsating tube and ribbon.

Consider first a tube of small diameter whose axis coincides with the X-axis and whose flexible wall executes a pulsation of wavelength L. We assume this wavelength to be large compared to the diameter of the tube. The wave number of the pulsation is $\gamma = \frac{2\pi}{L}$ and the subsonic or supersonic flow is aligned to the tube, i. e., in the direction of the positive X-axis (Fig. 4).

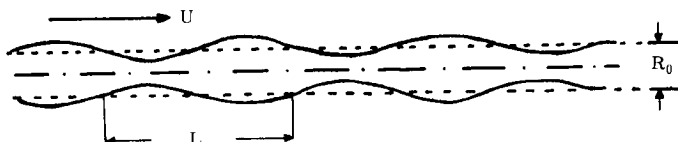


FIGURE 4. INFINITELY LONG PULSATING TUBE

The spatial influence equation (2.19) for subsonic flow simplifies for the infinitely long pulsating tube to [14], [15]

$$\begin{aligned} M < 1: \\ \phi_R(x) = \frac{1}{4\pi} \int_{-\infty}^x \frac{q(x) - q(\xi)}{x - \xi} e^{-i \frac{\omega(x-\xi)}{c(1-M)}} d\xi \\ - \frac{1}{4\pi} \int_x^{\infty} \frac{q(\xi) - q(x)}{\xi - x} e^{-i \frac{\omega(\xi-x)}{c(1-M)}} d\xi \end{aligned} \quad (3.1)$$

Inserting the appropriate source-distribution for the pulsating tube leads to the following final form for this spatial influence with A as amplitude of the cross-sectional pulsation:

$$\begin{aligned}
\phi_R(x) = \frac{A\omega}{4\pi} & \left\{ \left[\frac{1}{2} \cos \gamma x \ln \left| \frac{\bar{\alpha} + \gamma}{\bar{\alpha} - \gamma} \right| + \frac{\pi}{2} \sin \gamma x - \sin \gamma x \begin{cases} \pi/2 & \bar{\alpha} > \gamma > 0 \\ \pi/4 & \bar{\alpha} = \gamma \\ 0 & \gamma > \bar{\alpha} > 0 \end{cases} \right] \right. \\
& + i \left[\frac{1}{2} \sin \gamma x \ln \left| 1 - \frac{\gamma^2}{\bar{\alpha}^2} \right| + \cos \gamma x \begin{cases} \pi/2 & \gamma > \bar{\alpha} \\ \pi/4 & \gamma = \bar{\alpha} \\ 0 & \bar{\alpha} > \gamma \geq 0 \end{cases} \right] \\
& + \left[\frac{\pi}{2} \sin \gamma x - \sin \gamma x \begin{cases} \pi/2 & \alpha' > \gamma \\ \pi/4 & \alpha' = \gamma \\ 0 & \gamma > \alpha' \end{cases} - \frac{1}{2} \cos \gamma x \ln \left| \frac{\alpha' + \gamma}{\alpha' - \gamma} \right| \right] \\
& + i \left[\frac{1}{2} \sin \gamma x \ln \left| 1 - \frac{\gamma^2}{\alpha'^2} \right| - \cos \gamma x \begin{cases} \pi/2 & \gamma > \alpha' \\ \pi/4 & \gamma = \alpha' \\ 0 & \alpha' > \gamma \geq 0 \end{cases} \right] \\
& + \frac{A\gamma U}{4\pi} \left\{ \left[\frac{1}{2} \cos \gamma x \ln \left| 1 - \frac{\gamma^2}{\bar{\alpha}^2} \right| - \sin \gamma x \begin{cases} \pi/2 & \gamma > \bar{\alpha} \\ \pi/4 & \gamma = \bar{\alpha} \\ 0 & \bar{\alpha} > \gamma > 0 \end{cases} \right] \right. \\
& + i \left[\frac{1}{2} \sin \gamma x \ln \left| \frac{\bar{\alpha} + \gamma}{\bar{\alpha} - \gamma} \right| - \frac{\pi}{2} \cos \gamma x + \cos \gamma x \begin{cases} \pi/2 & \bar{\alpha} > \gamma > 0 \\ \pi/4 & \bar{\alpha} = \gamma \\ 0 & \gamma > \bar{\alpha} > 0 \end{cases} \right] \\
& + \left[\frac{1}{2} \cos \gamma x \ln \left| 1 - \frac{\gamma^2}{\alpha'^2} \right| + \sin \gamma x \begin{cases} \pi/2 & \gamma > \alpha' \\ \pi/4 & \gamma = \alpha' \\ 0 & \alpha' > \gamma \geq 0 \end{cases} \right] \\
& + i \left[\cos \gamma x \begin{cases} \pi/2 & \alpha' > \gamma > 0 \\ \pi/4 & \alpha' = \gamma \\ 0 & \gamma > \alpha' \geq 0 \end{cases} - \frac{\pi}{2} \cos \gamma x - \frac{1}{2} \sin \gamma x \ln \left| \frac{\alpha' + \gamma}{\alpha' - \gamma} \right| \right] \Bigg\} \quad (3.2)
\end{aligned}$$

where

$$\bar{\alpha} = \frac{\omega}{c(1+M)} \text{ and } \alpha' = \frac{\omega}{c(1-M)}. \quad (3.3)$$

A similar expression is obtained for supersonic flow [14, 15]. We note that $\phi_R(x) = 0$, for $\gamma = 0$. If the wavelength of the standing pulsation is infinitely large, i.e., the tube is pulsating with constant amplitude over the tube length, then there is no spatial influence. In this case, sources of constant strength are distributed over the entire x-axis, and as is well known, a solution is given by the cross-flow, i.e., the cylindrical solution. There is a spatial influence, however, for non-zero γ , which may even become infinite if one of the "matching conditions" $\gamma = \bar{\alpha}$ or $\gamma = \alpha'$

is fulfilled, i.e., if the wavelength of the advancing or receding acoustic wave coincides with the wavelength of the standing tube pulsation.

To find an exact solution for this case, we have to extend the limits of integration in equation (2.9) and to insert the proper source distribution, thus obtaining, for $M < 1$,

$$\phi(x, r) = -\frac{A}{4\pi} \int_{-\infty}^{+\infty} \frac{[i\omega \sin \gamma \xi + U\gamma \cos \gamma \xi] e^{-ik\sqrt{(x-\xi)^2 + \beta^2 r^2}}}{\sqrt{(x-\xi)^2 + \beta^2 r^2}} e^{i\mu(x-\xi)} d\xi \quad (3.4a)$$

for $M > 1$

$$\phi(x, r) = -\frac{A}{2\pi} \int_{-\infty}^{+\infty} \frac{[i\omega \sin \gamma \xi + U\gamma \cos \gamma \xi] \cos[k\sqrt{(x-\xi)^2 - \cot^2 \alpha r^2}]}{\sqrt{(x-\xi)^2 - \cot^2 \alpha r^2}} e^{-i\mu(x-\xi)} d\xi. \quad (3.4b)$$

An evaluation of these integrals is possible [14, 15] and leads to the following closed form solution:

$$\phi(x, r) = -\frac{A}{8\pi} (\omega + \gamma U) e^{i\gamma x} P_1(r) - \frac{A}{8\pi} (-\omega + \gamma U) e^{-i\gamma x} P_2(r), \quad (3.5)$$

with

$$P_1(r) = -i\pi H_0^{(2)} \left[r\beta \sqrt{(\bar{\alpha} + \gamma)(\alpha' - \gamma)} \right] \quad \alpha' > \gamma \quad (3.6a)$$

$$= 2K_0 \left[r\beta \sqrt{(\bar{\alpha} + \gamma)(\gamma - \alpha')} \right] \quad \alpha' < \gamma, \quad (3.6b)$$

$$P_2(r) = -i\pi H_0^{(2)} \left[r\beta \sqrt{(\bar{\alpha} - \gamma)(\alpha' + \gamma)} \right] \quad \bar{\alpha} > \gamma \quad (3.6c)$$

$$= 2K_0 \left[r\beta \sqrt{(\gamma - \bar{\alpha})(\alpha' + \gamma)} \right] \quad \bar{\alpha} < \gamma \quad (3.6d)$$

for subsonic flow,

and

$$P_1(r) = -i\pi H_0^{(2)} \left[r \cot \alpha \sqrt{(\bar{\alpha} + \gamma)(\alpha'' + \gamma)} \right] \quad (3.7a)$$

$$P_2(r) = -i\pi H_0^{(2)} \left[r \cot \alpha \sqrt{(\bar{\alpha} - \gamma)(\alpha'' - \gamma)} \right] \quad \begin{matrix} \bar{\alpha} > \gamma \\ \alpha'' > \gamma \end{matrix} \quad (3.7b)$$

$$= i\pi H_0^{(1)} \left[r \cot \alpha \sqrt{(\gamma - \bar{\alpha})(\gamma - \alpha'')} \right] \quad \begin{matrix} \gamma > \bar{\alpha} \\ \gamma > \alpha'' \end{matrix}$$

$$= 2K_0 \left[r \cot \alpha \sqrt{(\gamma - \bar{\alpha})(\alpha'' - \gamma)} \right] \quad \begin{matrix} \gamma > \bar{\alpha} \\ \alpha'' > \gamma \end{matrix}$$

for supersonic flow.

$$(3.7d)$$

This solution for the infinitely long pulsating tube which we have obtained here directly from the potential equation (3.4) can be found also according to R. W. Leonard and J. M. Hedgepeth [20] by considering first the solutions for traveling waves and composing them to the standing wave solution.

We mention without proof that proper expansion of the exact solutions, equations (3.6) and (3.7), with respect to the argument and retaining only the linear terms leads to equation (3.2), thus providing a quantitative check on the range of validity of this solution [14, 15].

A further interesting exact solution can be found for the infinitely long pulsating ribbon of constant width. Assuming sinusoidal pulsation over the x-direction, the chordwise integration again can be carried out which reduces the double integral to a single integral over the functions, equations (3.6) and (3.7), which had already been obtained for the axisymmetric case. This solution appears to give good approximations for the aerodynamic pressure distribution on fluttering panels of high length/width ratio. Thus, a relatively simple aerodynamic theory might evolve for panels of length-width ratios comparable to those occurring on Saturn V panels. This problem area is now under detailed study.

CONCLUSIONS

An approximation theory has been developed to calculate the linearized subsonic and supersonic flow around pulsating bodies of low aspect ratio which generalizes the theories of K. Oswatitsch and F. Keune [7, 8, 17, 18, 19] to unsteady flow.

The flow around pulsating bodies of low aspect ratio consists of two terms, a two-dimensional cross-flow and a spatial influence which depends only on the sum of the source elements over the cross section.

A similarly characteristic structure of the flow field is found also for the higher order terms by introducing after Keune [17] higher order source moments and the sum of these quantities over the cross section.

In addition to the basic conditions for linearization, the range of validity of this approximation theory is essentially bound by sufficiently small aspect ratio, Mach number, and reduced frequency, so that

$$\sigma \sqrt{|1-M^2|} < 1 \quad kM\sigma < 1$$

is fulfilled.

These order of magnitude considerations can be further substantiated by comparing this approximation theory with certain exact solutions of the unsteady linearized potential equation. Such solutions are found for the infinitely long tube or ribbon pulsating harmonically in subsonic or supersonic flow.

REFERENCES

1. K. Oswatitsch, *Gasdynamics*, Academic Press, New York, 1956.
2. M. M. Munk, *The Aerodynamic Forces on Airship Hulls*, NACA Report 184, 1923.
3. H. S. Tsien, *Supersonic Flow Over an Inclined Body of Revolution*, *J. Aeron. Sci.*, Vol. V, 1938, p. 480.
4. R. T. Jones, *Properties of Low Aspect Ratio Pointed Wings at Speeds Below and Above the Speed of Sound*, NACA Report 835, 1946.
5. G. N. Ward, *Supersonic Flow Past Slender Pointed Bodies*, *Quart. J. Mech. Appl. Math.*, Vol. 2, 75-97, 1949.
6. M. C. Adams, W. R. Sears, *Slender Body Theory, Review and Extension*, *J. Aeron. Sci.*, Vol. 20, 1953, p. 85-98.
7. F. Keune, K. Oswatitsch, *Nicht Angestellte Körper kleiner Spannweite in Unter- und Überschallströmung*, *Z. f. Flugwiss.*, Vol. I, Nov. 1953, pp. 85-98.
8. F. Keune, *Low Aspect Ratio Wings With Small Thickness at Zero Lift in Subsonic and Supersonic Flow*, KTH-Aero TN 21, Stockholm, June 1952.
9. M. A. Heaslet, H. Lomax, *The Calculation of Pressure on Slender Airplanes in Subsonic and Supersonic Flow*, NACA Report 1185 (1954).
10. I. E. Garrick, *Some Research on High Speed Flutter*, 3rd Anglo-American Aeron. Conference, 1951, p. 419.
11. J. W. Miles, *On Nonsteady Motion of Slender Bodies*, *Aeron. Quart.*, Vol. II, Nov. 1950, p. 183-194.

12. K. Oswatitsch, Die theoretischen Arbeiten über schallnahe Strömung am Flugtechnischen Institut der Königlich Technischen Hochschule, Stockholm. F. Keune, K. Oswatitsch, Nicht angestellte Körper kleiner Spannweite in Unter- und Überschallströmung, Proceedings of the VIIIth International Congress for Applied Mechanics, Istanbul 1952.
13. R. T. Whitcomb, A Study of Zero-Lift Drag-Rise Characteristics of Wing-Body Combinations Near the Speed of Sound, NACA RM L52H08, September 1952; or: NACA Details Area Rule Breakthrough, Aviation Week, September 1955.
14. M. Platzer, Doctoral Dissertation, Vienna Institute of Technology, February 1964.
15. M. Platzer, to be published in "Acta Mechanica," Wien, Springer Verlag.
16. H. Merbt, M. Landahl, Aerodynamic Forces on Oscillating Low Aspect Ratio Wings in Compressible Flow, KTH Aero TN 30, Stockholm, 1953.
17. F. Keune, Grundsätzliche Betrachtungen zur Unter- und Überschallströmung um Körper nicht mehr kleiner Streckung, Z. f. Flugwiss. 5, 1957, p. 121.
18. F. Keune, Reihenentwicklung des Geschwindigkeits potentials der linearen Unter- und Überschallströmung für Körper nicht mehr kleiner Streckung, Z. f. Flugwiss. 5 (1957) p. 243-247.
19. F. Keune, Strömung an Körpern nicht mehr kleiner Streckung in auftriebsloser linearer Unter- und Überschallströmung, WGL Jahrbuch 1957, p. 67-82.
20. R. W. Leonard, J. M. Hedgepeth, On Panel Flutter and Divergence of Infinitely Long Unstiffened and Ring-Stiffened Thin-Walled Circular Cylinders, NACA Report 1302, 1957.

By

Richard D. Rechten

N65 24130

SUMMARY

DEFINITION OF SYMBOLS (CONT'D)

The fluctuating pressure requirements for the calculation of flight vehicle vibration environments are reviewed in light of the development of a "lumped" impedance approach to the response problem. This response approach demonstrates that the only fluctuating pressure information required is the pressure cross-power spectral densities.

For homogeneous anisotropic flow conditions, a considerable simplification in the response equations result. For this flow condition it is suggested that the pressure cross-power spectral density information be reduced to a more elementary form.

DEFINITION OF SYMBOLS

| Symbol | Definition |
|--------|------------|
|--------|------------|

| | |
|--------------------------|------------------------------|
| $H(\bar{r}, \bar{s}, w)$ | Structural transfer function |
|--------------------------|------------------------------|

| | |
|--------------------------|----------------------------------------------------------|
| $H(\bar{r}, \bar{k}, w)$ | Wave number spectrum of the structural transfer function |
|--------------------------|----------------------------------------------------------|

| | |
|-----------------|-------------------------------------------------|
| $F(\bar{s}, t)$ | Applied sinusoidal force at the point \bar{s} |
|-----------------|-------------------------------------------------|

| | |
|-------------------|-----------------------------------------------------------------------|
| $U_s(\bar{r}, t)$ | Structural response at \bar{r} due to the applied load at \bar{s} |
|-------------------|-----------------------------------------------------------------------|

| | |
|-------------------|--------------------------------------------------------------------------------------|
| $\phi_s(\bar{r})$ | Phase difference between the response at \bar{r} and the applied load at \bar{s} |
|-------------------|--------------------------------------------------------------------------------------|

| | |
|----------------|--------------------------------------------------------------------------------------------------------|
| $A_s(\bar{r})$ | Magnitude of the response at \bar{r} due to a sinusoidal load of unit amplitude applied at \bar{s} |
|----------------|--------------------------------------------------------------------------------------------------------|

| | |
|-----------------|----------------------------------------------------|
| $P(\bar{s}, t)$ | Fluctuating pressure acting at the point \bar{s} |
|-----------------|----------------------------------------------------|

| | |
|-------------------------|-----------------------------------------|
| $R_R(\bar{r}) \Delta w$ | Narrow-band response coherence function |
|-------------------------|-----------------------------------------|

| | |
|---------------------|---------------------------------|
| $PSD_p(\bar{s}, w)$ | Pressure power spectral density |
|---------------------|---------------------------------|

| | |
|--------------------------------|---------------------------------------|
| $CPSD_p(\bar{s}, \bar{s}', w)$ | Pressure cross-power spectral density |
|--------------------------------|---------------------------------------|

| Symbol | Definition |
|--------|------------|
|--------|------------|

| | |
|---------------------|---------------------------------|
| $PSD_R(\bar{r}, w)$ | Response power spectral density |
|---------------------|---------------------------------|

| | |
|----------------------------|-------------------------------------------------------------|
| $Co(\bar{s}, \bar{s}', w)$ | Co-spectrum-the real part of $CPSD_p(\bar{s}, \bar{s}', w)$ |
|----------------------------|-------------------------------------------------------------|

| | |
|------------------------------|--------------------------------------------------------------------|
| $Quad(\bar{s}, \bar{s}', w)$ | Quad-spectrum-the imaginary part of $CPSD_p(\bar{s}, \bar{s}', w)$ |
|------------------------------|--------------------------------------------------------------------|

| | |
|-------------------|--------------------------------------------------------|
| $M_p(\bar{k}, w)$ | Wave number spectrum of $CPSD_p(\bar{s}, \bar{s}', w)$ |
|-------------------|--------------------------------------------------------|

| | |
|--------|--------------------------|
| $Z(w)$ | Point impedance function |
|--------|--------------------------|

| | |
|-----------------|--------------------------------|
| γ, β | Orthogonal surface coordinates |
|-----------------|--------------------------------|

| | |
|-----------|----------------------------------------------------|
| \bar{r} | Position vector for the response measurement point |
|-----------|----------------------------------------------------|

| | |
|-----------|------------------------------------------------|
| \bar{s} | Position vector for the load application point |
|-----------|------------------------------------------------|

| | |
|-----|--------------------|
| w | Circular frequency |
|-----|--------------------|

| | |
|------------|---------------------|
| Δw | Frequency bandwidth |
|------------|---------------------|

| | |
|-----------|--------------------|
| \bar{k} | Vector wave number |
|-----------|--------------------|

| | |
|------------------|-----------------------|
| $\Delta \bar{k}$ | Wave number bandwidth |
|------------------|-----------------------|

| | |
|----------|-------------------|
| δ | Separation vector |
|----------|-------------------|

| | |
|-----|------|
| t | Time |
|-----|------|

| | |
|-----|-------------|
| i | $\sqrt{-1}$ |
|-----|-------------|

| | |
|------------|--------------------------|
| ΔA | Incremental surface area |
|------------|--------------------------|

| | |
|-------|----------------------|
| U_o | Free stream velocity |
|-------|----------------------|

| | |
|-------|------------------|
| f_o | Center frequency |
|-------|------------------|

| | |
|-----------|---------------|
| \bar{u} | Wave velocity |
|-----------|---------------|

| | |
|-------------|--------------------------------|
| \bar{k}_c | Coincidence vector wave number |
|-------------|--------------------------------|

I. INTRODUCTION

The structural integrity of present day flight vehicles depends to a large degree on the accuracy with which one can predict the dynamic stress levels that the structure will endure under operational conditions. Such stress levels are derived from the anticipated vibrational environment, which in turn is deduced from available fluctuating pressure information. The accuracy of the predicted stress environment, therefore, merely reflects the adequacy, or inadequacy, with which the dynamic characteristics of the structure and the characteristics of the fluctuating pressure field can be described. These characteristics are ultimately coupled by means of a mathematical formalism to produce an environmental response calculation.

Under operational conditions, the flight vehicle is subjected to a wide variety of dissimilar fluctuating pressure environments, of which those that fall within the broad classifications of engine aerodynamic noise and inflight aerodynamic noise sustain a position of great importance. Now "noise" is a word which has many meanings; thus, it is important that it should be clear what the word is to mean in the present context. Here, noise will be regarded not just as "unwanted sound" but as something more explicit, a random disturbance, and will include those processes or experiments in which the results fluctuate irregularly. Hence, noise in the present context refers to pressures which fluctuate randomly in time. Randomness, on the other hand, is a less restrictive phrase and may be extended to describe also the spatial distribution of the fluctuating pressures in that they are irregularly distributed and this distribution is unpredictable. Thus, the term "random," as used in the present context, refers to processes where both the time fluctuations and spatial distribution are unpredictable.

The common feature of all "noise" environments experienced by the operational vehicle is that they are random, both in space and time, and the associated measured pressure quantities can be considered only in a statistical sense in an "average" sort of way. As the exciting pressure environment is random, so also is the structural response, and again statistics come into play in its description.

Various statistical measures of fluctuating pressure and response constitute an input-output system in which the proportionality factor is referred to as the structural transfer function. This input-output relation can attain any degree of complexity depending on the degree of rigor with which one attacks the problem, and the format of pressure and structural

information. For a statistical response approach, the calculated response quantity is a matter of personal choice. One may, for example, be concerned with the mean-square, autocorrelation, cross-correlation, power spectral density or cross-power spectral density of either a displacement, velocity, acceleration or strain. The choice of measure of a particular response quantity depends on the needs of the response analyst. The choice of the statistical pressure measure required for the computation of response is, however, not quite so arbitrary; but yet it is independent of the desired statistical response measure. That is to say, regardless of the desired response measure, the format of the required pressure information remains the same.

The third necessary response quantity, the structural transfer function, is also arbitrary to a degree in that its form depends on the choice of the manner in which one couples the external exciting pressure to the structure. It is restricted in the sense that it must act as a unit conversion system which changes the units of pressure to units of response. In this regard, it is dependent to a limited extent on the desired response measure, but it is quite independent of the format of the required pressure information.

The foregoing statements concerning response equations are not quite true in general, for if one views the family of allied response forms that have emerged in the past few decades, he finds that in most cases the structural transfer function is intimately connected with the pressure distribution. However, if one also scrutinizes the derivation of those response relations which do not conform to the foregoing statements, he will also find that these response relations are merely degenerates of a rigorous approach (as they must be) where the intimacy of the pressure distribution and transfer function has resulted from a specialization of either the statistical pressure quantities or the transfer function independently or by a simplification of the combination of these quantities. Thus, the statements of the preceding paragraph are essentially true only if the response approach is rigorous in the sense that specialization to a particular structure or pressure distribution has not been made. These statements are precisely valid if in addition one can state that the motion of the vibrating structure yields no reaction to the exciting pressure field thereby modifying its characteristics. We are speaking now of small lateral displacements of a structure. For example, the magnitude of the displacement caused by aerodynamic noise is of the order of a few percent of the boundary layer thickness (Baroudi et al., 1963).

The conditions of smallness of the lateral displacements of the structure come into play also in the development of the response relations. It is always desirable that the structure be linear; that is, its motion should be describable by a linear partial differential equation, so that the principle of superposition may apply.

For a linear structure and for conditions of small displacements, a rigorous approach to response calculations allows the response problem to be conveniently separated into two independent areas of interest: structural and aerodynamic research. Although ultimately the results of investigations within these two fields of interest must be combined in some fashion to produce a response calculation, the structural and aerodynamic information can be obtained from quite dissimilar investigations. Thus, the value of rigid model wind tunnel experiments becomes evident, as also dynamic testing on full scale vehicles, or segments thereof, using nonaerodynamic exciting sources (i.e., electromagnetic vibrators). In this way, the structural analyst has at his disposal the necessary pressure information from wind tunnel tests which may have been designed for an entirely different purpose.

This paper undertakes to describe the complete response problem from a semi-intuitive point of view, in contrast to a strictly mathematical approach. This is to demonstrate the relative role of fluctuating pressure information in the response problem. It will also be shown that, for a given format of structural and pressure information, the response problem can be considerably reduced to a rapid, accurate, and practical calculation.

The first part of this report considers the structural transfer function in a way that is compatible with recent trends in structural experimentation. By approaching the problem experimentally, one is led intuitively to the exact response equation. The second part of this paper considers the external pressure field to be spatially homogeneous. This assumption allows the response equation to be readily reduced to a practical form.

A rigorous derivation of the results of this method will be published in a paper by the author (Rechtién 1964).

II. DEVELOPMENT OF THE RESPONSE RELATION

The attitude taken in this approach to the response problem presupposes that the structure in question, or a dynamically similar model, materially exists and can be subjected to physical experimentation. Of

immediate interest is a function $H(\bar{r}, \bar{s}, w)$ which describes the transfer of vibrational energy from a point \bar{s} to a point \bar{r} on the surface of the structure. In order to demonstrate the interpretation of this function, its physical measurement will first be described.

Consider any typical vehicle structure for which the position of any point on its surface is expressible by an orthogonal set of surface coordinates (γ, β) . The vector $\bar{s}(\gamma, \beta)$ represents the location at which a force, $F(\bar{s}, t)$, is applied and $\bar{r}(\gamma, \beta)$ represents the position vector where the response $U_s(\bar{r}, t)$ to the applied load at \bar{s} is measured (see Fig. 1).

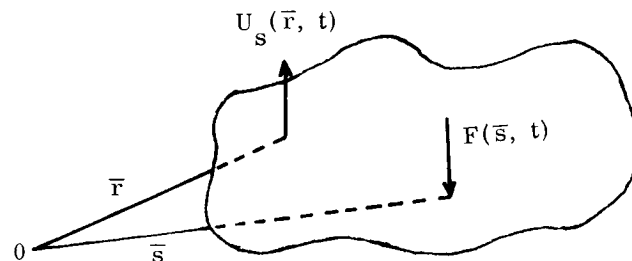


FIGURE 1. COORDINATE CONFIGURATION

The force, $F(\bar{s}, t)$, applied at \bar{s} , shall be considered to be a sinusoid of unit amplitude and circular frequency w ,

$$F(\bar{s}, t) = e^{iwt} \quad (1)$$

which is being continuously monitored by some force measuring device. At location \bar{r} on the surface of the structure there exists a response detector, for example, a velocity pickup, which also is continuously being monitored. It is then assumed that a sufficient length of time has elapsed since the initial application of the load so that a steady-state condition exists. The amplitude of the response at \bar{r} , $A_s(\bar{r})$, and the phase difference, $\phi_s(\bar{r})$, relative to the force at \bar{s} , are then measured. The response at \bar{r} can then be related to the applied force at \bar{s} by the input-output relation

$$U_s(\bar{r}, t) = H(\bar{r}, \bar{s}, w) e^{iwt}, \quad (2)$$

where the transfer function $H(\bar{r}, \bar{s}, w)$ is given by

$$H(\bar{r}, \bar{s}, w) = A_s(\bar{r}) e^{i\phi_s(\bar{r})} \quad (3)$$

and shall have the units of response quantity per unit of force. The inverse of this function is generally referred to as the transfer impedance function. This function reflects, implicitly, the totality of those mechanisms which act to modify the vibrational energy being transferred along many paths through the structure to the point of measurement. When the point of measurement and the position of the applied load coincide, that

is, when $\bar{r} = \bar{s}$, then $[H(\bar{r}, \bar{s}, w)]^{-1}$ reduces to the well-known point impedance function.

Having now discussed the physical measurement of the structural transfer functions, an analogous problem with a higher degree of complexity shall be considered. Let the force applied at \bar{s} be, in actuality, a pressure $P(\bar{s}, t)$ acting over an incremental area ΔA of the surface. Further, it is supposed that this pressure is not sinusoidal but a stationary*, ergodic** random function of time. Next, it is supposed that this random pressure fluctuation is being continuously monitored by passing the signal from the pressure transducer through a filter with a very narrow bandwidth of center frequency, w . The resulting signal would resemble a sinusoid in that the zero crossings would tend to be regular. However, the amplitude of the signal would be quite random. The response at \bar{r} due to this filtered portion, $P(\bar{s}, t)_{\Delta w}$, of the total pressure, $P(\bar{s}, t)$, acting at \bar{s} is given approximately by,

$$U_{\bar{s}}(\bar{r}, t)_{\Delta w} = H(\bar{r}, \bar{s}, w) P(\bar{s}, t)_{\Delta w} \Delta A, \quad (4)$$

where $H(\bar{r}, \bar{s}, w)$ has the same meaning as equation (3), and the subscripts refer to narrow-band filtered quantities.

Suppose now that at another point \bar{s}' of the structure a second pressure $P(\bar{s}', t)$ is simultaneously applied over an incremental area $\Delta A'$. Its narrow-band contribution to the response at \bar{r} is given by

$$U_{\bar{s}'}(\bar{r}, t)_{\Delta w} = H(\bar{r}, \bar{s}', w) P(\bar{s}', t)_{\Delta w} \Delta A'. \quad (5)$$

The question now arises as to the degree of coherence between the narrow-band vibrational energy at \bar{r} arriving from the two different sources. We are essentially asking what degree of similarity exists between the two narrow-band response signals, or alternately, what is the degree of dissimilarity due to the difference in transmission paths and due to the difference in phase and amplitude between the two sources. A measure of the degree of coherence between the two response signals, considered as being separable, is given by the time average of the product of the narrow-band response signal of one times the complex conjugate of the other,

* One implies by the condition of stationarity that the statistical measures of $P(\bar{s}, t)$ are invariant with respect to time translations.

** The ergodic hypothesis implies that if a given experiment were repeated a number of times under constant conditions, the results of any one such experiment would be representative of the ensemble.

$R_R(\bar{r})_{\Delta w}$ = narrow-band response coherence function

$$= \lim_{T \rightarrow \infty} \frac{1}{2T} \int_{-T}^{+T} U_{\bar{s}}(\bar{r}, t)_{\Delta w} U_{\bar{s}'}^*(\bar{r}, t)_{\Delta w} dt, \quad (6)$$

where (*) designates the complex conjugate of the corresponding quantity. The complex conjugate of the response function is necessary since the response coherence function is required to be real.

Substituting (4) and (5) into (6) one finds that

$$R_R(\bar{r})_{\Delta w} = H(\bar{r}, \bar{s}, w) H^*(\bar{r}, \bar{s}', w) \left\{ \lim_{T \rightarrow \infty} \frac{1}{2T} \int_{-T}^{+T} P(\bar{s}, t)_{\Delta w} P^*(\bar{s}', t)_{\Delta w} dt \right\} \Delta A \Delta A'. \quad (7)$$

The bracketed quantity is just the narrow-band pressure coherence function between the spatial points (\bar{s}, \bar{s}') , and measures the degree of similarity between the two filtered pressure signals. To be more consistent with the current literature, this function shall be referred to as the pressure cross-power spectral density, $\text{CPSD}_p(\bar{s}, \bar{s}', w)$. Similarly, the product of the transfer functions, $H^* H$, can be considered as a measure of the similarity of the two different transmission paths. Thus,

$$R_R(\bar{r})_{\Delta w} = H(\bar{r}, \bar{s}, w) H^*(\bar{r}, \bar{s}', w) \text{CPSD}_p(\bar{s}, \bar{s}', w) \Delta A \Delta A'. \quad (8)$$

| | | |
|------------------------|---------------------------------|------------------------|
| response similarity | transmission path similarity | pressure similarity |
|------------------------|---------------------------------|------------------------|

Now the response coherence function is a statistical measure and obviously deals with pairs of quantities. In practice, one is always faced with pressure fields that are continuously distributed over the entire surface of the structure. Obviously, one could then speak of coherence functions, or cross-power spectral densities, associated with an infinite number of pressure pairs, each pair generating a distinct narrow-band response coherence function at the point of measurement. The sum of all of these distinct narrow-band response coherence functions is nothing more than the narrow-band mean square response at the measurement point \bar{r} . This measure is commonly referred to as the response power spectral density

$$\text{PSD}_R(\bar{r}, w) = \sum_{\text{all pairs}} R_R(\bar{r})_{\Delta w} \quad (9)$$

Thus, by summing the response coherence functions at \bar{r} from all possible filtered pressure pairs and passing to the limit as the incremental areas ΔA , and $\Delta A'$ become small, the following integral is generated,

$$\text{PSD}_R(\bar{r}, w) = \int_A \int_{A'} H(\bar{r}, \bar{s}, w) H^*(\bar{r}, \bar{s}', w) \text{CPSD}_p(\bar{s}, \bar{s}', w) dA dA', \quad (10)$$

where the integrations are to be taken over the entire structural surface.

The power spectral density of the response at a given point of the structure is the quantity most desired by the response analyst. Therefore, in essence, equation (10) is the fundamental response formula. The fact that the power spectral density of response is here presented in integral form presupposes that both the transfer functions and the pressure cross power spectral density are known as continuous variables of the spatial coordinates. For practical structures, the determination of such transfer functions for the total structure would not be practical. However, one generally finds that local stiffening elements, such as ring frames in flight vehicles, considerably restrict the transfer function to have non-negligible values only in relatively localized areas. Thus, such structural elements would limit the integration of (10) to local regions of response significance.

The continuously distributed pressure fields which one deals with in practice not only fluctuate randomly in time, but are randomly distributed in space. That is, if one were to measure the instantaneous pressure along a profile on the structural surface, the instantaneous pressure value at a given position could not be predicted from knowledge of the instantaneous pressure values at well separated points. However, such a profile would constitute a continuous pressure curve. Without being at all rigorous, the idea of continuity is that the instantaneous pressure curve should be smooth from one position to the next. Consideration of this leads to the conclusion that the instantaneous pressure at a given position is dependent to a certain extent on the instantaneous pressure at adjacent positions. Intuitively, if at one position a large positive value is recorded, a large negative value will not be recorded at an adjacent point at the same instant. That is, the instantaneous pressures at adjacent points have a high degree of similarity, or dependence. But as the interval between the two observed positions is increased, the dependence between them clearly decreases, and if the separation interval between the observation positions is large enough there will be practically no dependence, or correlation.

We are here speaking of the total pressure field. But the same arguments would hold true for the narrow-band filtered components. Thus, the pressure cross-power spectral density is actually a measure of the degree of dependence of the narrow-band pressure components at two different locations on the structural surface. Such dependencies give rise to characteristic curves for the pressure cross-power spectral density, as shown in Figure 2. The pressure cross-power

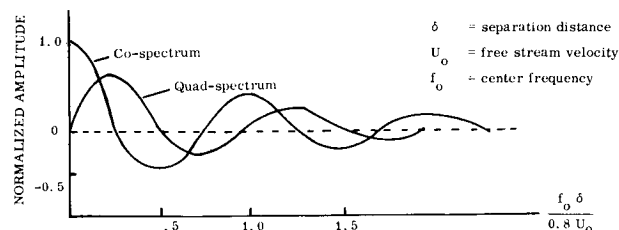


FIGURE 2. NORMALIZED CROSS-POWER SPECTRA FOR SUBSONIC ATTACHED TURBULENT BOUNDARY LAYERS (AFTER HARRISON 1958).

spectral density is by its very nature a complex quantity and is generally represented in terms of its real and imaginary parts,

$$\text{CPSD}_p(\bar{s}, \bar{s}', w) = \text{Co}(\bar{s}, \bar{s}', w) + i \text{Quad}(\bar{s}, \bar{s}', w), \quad (11)$$

where Co and Quad are referred to as the co- and quad-spectrum, respectively. These are the quantities shown in Figure 2. The decaying characteristics of these curves reflect the degree of dissimilarity of the narrow-band pressure components at adjacent positions. For subsonic turbulent boundary layer fluctuations, Harrison (1958) shows that the co- and quad-spectra fall to less than one-half of their peak value for a separation distance of

$$|\bar{s} - \bar{s}'| \approx \frac{U_0}{f_0}, \quad (12)$$

where U_0 is the free stream velocity and f_0 is the center frequency of the filtered quantities. For separation distances of twice this length, the magnitudes fall to within 10 percent of the peak values. Thus, for subsonic flows, the pressure fluctuations within a turbulent boundary layer are correlated only over distances of a few feet for intermediate frequencies. For supersonic flows, Kistler and Chen (1962) show that the distances over which the pressures are correlated are reduced by an order of magnitude as compared to subsonic flow conditions. For other flow characteristics, such as separation and oscillating shock phenomena, the correlated regions may be increased by an order of magnitude as compared to their turbulent boundary layer counterparts. But the point is that all of these pressure fluctuations are only correlated in localized

regions of the structural surface. Moreover, such areas of correlation are generally of an order of magnitude smaller than those areas defined by the previously discussed regions of response significance. Therefore, in general, the effective area of integration of the response relation (10) will be governed by the area of correlation of the fluctuating pressure distribution. Since this area is small, as compared to the total area of the structure, the response relation as given by (10) is not as formidable as it may first appear. However, even though the transfer function and the pressure cross-power spectral density may be known pseudo-analytically within this area of correlation, the evaluation of a double integration over this area may still not be practical. Thus, an alternate form of the response equation which would allow a rapid and accurate means of estimating the vibrational environment would be most desirable. However, to simplify the response relation as given by (10) one must idealize the external fluctuating pressure field to a limited degree. In particular, the pressure distribution must be taken as having a homogeneous character; that is, its statistical measures must be taken to be invariant with respect to a spatial translation. Such will be assumed in the following section, the consequences of which will yield a more conservative estimate of the vibrational environment.

III. THE RESPONSE RELATION FOR HOMOGENEOUS, ANISOTROPIC PRESSURE FIELDS

In the development of the response relation (10), quantities of time were essentially transformed (by narrow-band filtering) to the frequency domain, thus giving rise to spectral quantities. In this section a further transformation shall be applied, primarily for the purpose of eliminating the area integrations of equation (10).

The pressure-cross power spectral density, as given in (10), is a function of the spatial locations, (\bar{s}, \bar{s}') , at which the narrow-band filtered pressures are compared. As a consequence of the assumption of homogeneity, this function is no longer dependent on the spatial locations, but only on the separation vector $\bar{\delta}$,

$$\bar{\delta} = \bar{s} - \bar{s}' \quad (13)$$

That is, the pressure-cross power spectral density is assumed to be invariant with respect to a translation so that the magnitude and direction of the separation vector is preserved. The pressure cross-power spectral density can then be written as

$$\text{CPSD}_p(\bar{s}, \bar{s}', w) = \text{CPSD}_p(\bar{\delta}, w) \quad (14)$$

Now, just as a function of time may be decomposed into a spectrum of elementary waves in the frequency domain, so can a function of separation be decomposed into a spectrum of spatial waves in the wave-number domain. Thus, the wave-number decomposition of the pressure cross-power spectral density is given by the Fourier integral relation (Powell, 1958),

$$\text{CPSD}_p(\bar{\delta}, w) = \int_{\bar{k}} M_p(\bar{k}, w) e^{i\bar{k} \cdot \bar{\delta}} d\bar{k} \quad (15)$$

where $d\bar{k}$ represents the differential area, $dk_x dk_y$, in the wave number domain, and the integral over \bar{k} extends over all wave numbers.

Physically, by this transformation, the external pressure field is considered to be made up of a superposition of harmonic traveling waves of amplitude $M_p(\bar{k}, w)$. Now the frequency generated by a particular wave as it is convected past a particular point in the flow will be equal to the scalar dot product of the vector wave number \bar{k} and the velocity \bar{u} of the elementary wave

$$w = \bar{k} \cdot \bar{u} \quad (16)$$

If all of these elementary waves were traveling with the same velocity, then there would be only one vector wave number, or essentially only one wave, which would generate a given frequency at a fixed point in the flow by nature of its convection. Since the pressure cross-power spectral density is defined for only one frequency, this would imply that it was composed of only one wave and would not have a wave number decomposition such as (15). In this case, the pressure cross-power spectral density would have the form of a non-decaying spatial sinusoid, which contradicts the available experimental results (see Fig. 2 or Wills (1963) for example). This contradiction leads one to the conclusion that the velocity of the elementary harmonic traveling waves is not constant, but assumes a broad spectrum of values for fluctuating flows in general. This is a most important point, as shall be demonstrated, in the estimation of vibrational environments.

If the transform relation (15) is substituted into equation (10), it can easily be shown* that this response relation can be transformed to an integral representation over wave-number (Rechtien 1964),

$$\text{PSD}_R(\bar{r}, w) = 16\pi^4 \int_{\bar{k}} M_p(\bar{k}, w) \left| H(\bar{r}, \bar{k}, w) \right|^2 d\bar{k} \quad (17)$$

* For a similar treatment, see Powell (1958).

where $H(\bar{r}, \bar{k}, w)$ is the two-dimensional inverse Fourier transform of the structural transfer function,

$$H(\bar{r}, \bar{k}, w) = \frac{1}{4\pi^2} \int_A H(\bar{r}, \bar{s}, w) e^{-i\bar{k} \cdot (\bar{s} - \bar{r})} dA \quad (18)$$

Equation (17) is the basic form of the response equation for homogeneous flow conditions. The properties of this relation shall not be discussed, and the relative advantage of this wave-number representation should be clearly evident.

IV. PROPERTIES OF THE RESPONSE EQUATION

In the previous section the structural transfer function, as well as the pressure cross-power spectral density, was transformed into the wave-number domain. By this representation, the instantaneous deflection of the structural surface due to the application of a sinusoidal force (which the structural transfer function essentially describes) is considered as a linear superposition of structural surface waves. Now the structural transfer function is experimentally determined at a given forcing frequency, w . The structural waves that will be excited by this disturbance will be those for which the scalar dot product of the structural vector wave-number and velocity of propagation (i.e., the material velocity of sound) is equal to the forcing frequency. The velocity of sound in the material will not vary greatly in the structure, and therefore only a few structural waves can be excited at this frequency. In other words, the wave-number spectral representation $|H(\bar{r}, \bar{k}, w)|^2$ will be extremely peaked, as shown in Figure 3 for the one-dimensional case. This spectral distribution may exhibit more than one peak as in the case when the material speed of sound changes drastically across a surface discontinuity.

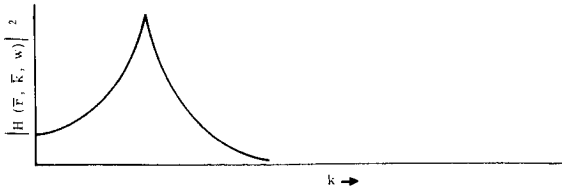


FIGURE 3. WAVE-NUMBER SPECTRUM OF THE STRUCTURAL TRANSFER FUNCTION.

The wave number spectral representation of the pressure cross-power spectral density, $M_p(\bar{k}, w)$, possesses a similar distribution as shown in Figure 4. This curve was obtained, for the purpose of illustration, by transforming the curves of Harrison given in Figure 2. Since the co- and quad-spectra are characteristically damped cosine and sine curves,

respectively, the transformed cross-power spectrum will generally exhibit the character of Figure 4. But the relative peakedness of this curve will depend entirely on the fluctuating pressure conditions.

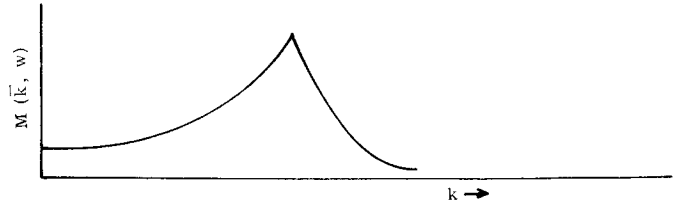


FIGURE 4. WAVE-NUMBER SPECTRUM OF THE CROSS-PANEL SPECTRUM

Since the product of the two peaked spectral functions, $M_p(\bar{k}, w)$ and $|H(\bar{r}, \bar{k}, w)|^2$, comprises the integrand of the response relation, equation (17), the degree of similarity between them will determine the magnitude of the response power spectral density. When the peak values of the two distributions occur at the same wave number, a coincidence condition will exist. Coincidence is defined as that condition for which the dominant pressure wave vector and convection velocity for a given frequency match the structural wave vector and the velocity of sound in the material. This condition is illustrated in Figure 5A. For this coincidence condition, the response integral of equation (17) can be accurately approximated by evaluating the integrand at the coincidence value \bar{k}_c of the distributions and multiplying by an appropriate bandwidth of integration,

$$PSD_R \approx 16\pi^4 M_p(\bar{k}_c, w) |H(\bar{r}, \bar{k}_c, w)|^2 \Delta \bar{k} \quad (19)$$

In Figure 5B, another limiting case is considered where the peak value of the pressure spectral distribution falls well below that of the structural spectral function. In this case, the structural spectral function can be considered constant once the effective bandwidth of integration and the integral (15) approximates to

$$PSD_R \approx 16\pi^4 |H(\bar{r}, \bar{k}_p, w)|^2 \int_{\bar{k}} M_p(\bar{k}, w) d\bar{k} \quad (20)$$

The integral of (18) is defined as the power spectral density of the pressure at the point \bar{r} , $PSD_p(\bar{r}, w)$. Therefore, equation (18) reduces to

$$PSD_R \approx 16\pi^4 |H(\bar{r}, \bar{k}_p, w)|^2 PSD_p, \quad (21)$$

which yields the response for forced oscillations (non-resonant conditions).

Figure 5C illustrates the reverse situation in which the peak of the structural spectral function falls well below that of the pressure spectrum. In this

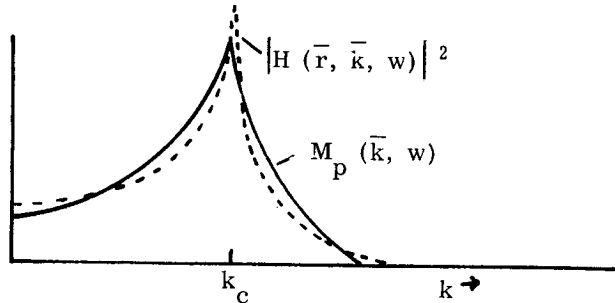
case, the pressure spectrum can be considered as constant over the effective bandwidth of integration and the integral (17) approximates to

$$\text{PSD}_R \approx 16\pi^4 M_p(\bar{k}_s, w) \int_{\bar{k}} |H(\bar{r}, \bar{k}, w)|^2 d\bar{k}. \quad (22)$$

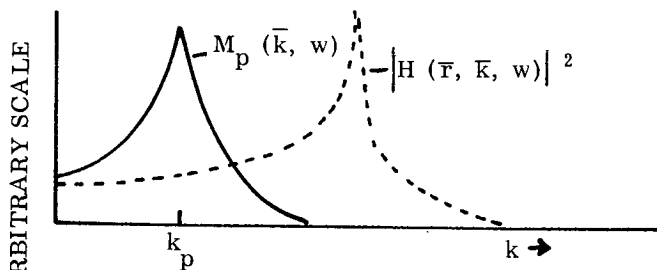
The integral of (20) is simply the inverse of a point load impedance $Z(w)$, and equation (22) reduces to

$$\text{PSD}_R = 16\pi^4 \frac{M_p(\bar{k}_s, w)}{Z(w)}. \quad (23)$$

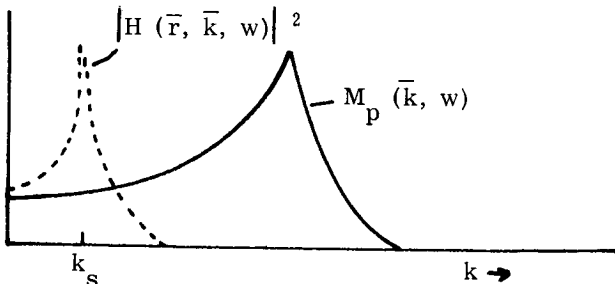
This condition corresponds to the limiting case in which the narrow-band pressure fluctuations at adjacent points on the structural surface are completely uncorrelated.



A. Coincident conditions



B. Nonresonant conditions



C. Uncorrelated pressure conditions

FIGURE 5. LIMITING CASES OF THE SUPERPOSED WAVE-DISTRIBUTIONS

Both of the limiting cases given by equations (21) and (23) will yield a negligible response relative to a near-coincidence condition. In practice one should generally encounter a degree of coincidence lying somewhere in the intermediate regions between pure

coincidence and the above limiting cases. One must then rely on intuition to make a reasonable approximation. But the real advantage in specifying the wave number distributions of the structural transfer function and the pressure cross-power spectral density lies in the fact that the degree of coincidence, and therefore the degree of response, can immediately be determined by inspection of the superposed distributions. A quick estimate of the response level could then be obtained without requiring a rigorous evaluation of the response integral.

V. CONCLUSIONS

An attempt was made herein to provide a basic understanding of the response problem, to demonstrate the relative role of fluctuating pressure information, and to show that, for a particular format of structural and pressure information, the response problem cannot only be entirely separated into two completely independent areas of experimentation but also can be considerably reduced to a rapid, accurate, and practical calculation.

A dynamically scaled model of the Saturn V vehicle is now being fabricated at the Langley Research Center. Experimental programs to determine the structural transfer function for this model would yield the necessary structural information required as input to the response equation (17). This information, along with wind tunnel pressure data for rigid models, would provide, by using the response relation given herein, the means for obtaining a good estimate of the in-flight vibrational environment.

REFERENCES

1. Baroudi, Ludwig, Ribner, "An Experimental Investigation of Turbulence-Excited Panel Vibration and Noise (Boundary-Layer Noise)," AGARD Report 465, 1963.
2. Rechtiem, R., "On the Pressure Requirements for Structural Response Equations," (to be published).
3. Harrison, M., "Pressure Fluctuations on the Wall Adjacent to a Turbulent Boundary Layer," David Taylor Model Basin Report 1260, 1958.
4. Kistler, A., and Chen, W., "The Fluctuating Pressure Field in a Supersonic Turbulent Boundary Layer," JPL Report 32-277, 1962.

5. Powell, O., Random Vibration, Chapter 8, The Press of the Massachusetts Institute of Technology and John Wiley & Sons, Inc., New York, Chapman & Hall, Ltd., London, 1958.

6. Wills, J. A. B., "On Convection Velocities in Turbulent Shear Flows," AGARD Report 457, 1963.

IV. STRUCTURAL DYNAMICS

NONLINEAR TWO-DEGREES-OF-FREEDOM RESPONSE WITH SINUSOIDAL INPUTS

By

Robert S. Ryan

SUMMARY

The study of a forced vibrational system is very difficult if the system is nonlinear. This becomes apparent because the principle of superposition does not hold as it does for linear systems.

In studying the behavior of linear systems, it is useful to deal with sinusoidal inputs and resulting outputs which are harmonic. By definition the complex ratio of the output to input is called a transfer function. This transfer function, since it is complex, can be written as two parts: the modulus and the argument. The first describes the so-called response curves, and the second the phase angle between the two harmonic oscillations. Because of the property of superposition inherent in linear systems, these transfer functions become the basis for a complete description of the system.

In the nonlinear system, the output of the system to sinusoidal inputs is no longer sinusoidal, but contains harmonics of both higher and lower frequencies. Neither does the superposition principle hold; therefore, a study using sinusoidal inputs does not yield the wide scope of information obtained in the linear case. There are other shortcomings in studying the system using sinusoidal inputs; nevertheless, the sinusoidal input functions provide a convenient way of studying the nonlinear system.

This analysis proposes to solve the nonlinear forced oscillation of a vehicle using air springs for vibration isolation. Both a single and a two-degrees-of-freedom system will be studied where the force applied is considered to be sinusoidal in nature. The single-degree-of-freedom system is also solved in the free vibration state using phase plane methods.

I. INTRODUCTION

The isolation of machinery against vibration or outside excitation has long been a goal of engineers.

The problem was first attacked by linearizing the problem. In studying the behavior of linear systems, it is useful to deal with sinusoidal inputs and resulting outputs which are harmonic. By definition the complex ratio of the output to input is called a transfer function.

This transfer function, since it is complex, can be written as two parts: the modulus and the argument. The first describes the so-called response curves, and the second the phase angle between the two harmonic oscillations. Because of the property of superposition inherent in linear systems, these transfer functions become the basis for a complete description of the system.

The study of nonlinear systems cannot be attacked in this simple manner. In the nonlinear system, the output of the system to sinusoidal inputs is no longer sinusoidal, but contains harmonics of both higher and lower frequencies. Neither does the superposition principle hold; therefore, a study using sinusoidal inputs does not yield the wide scope of information obtained in the linear case. There are other shortcomings in studying the system using sinusoidal inputs; nevertheless, the sinusoidal input functions provide a convenient way of studying the nonlinear system.

The Ritz-Galerkin averaging method is presented as an ideal method for solving nonlinear problems. Most solutions given in literature solve simple systems which are nearly linear in nature and have odd restoring forces, and therefore present no real difficulties. The Ritz method can be used to study highly nonlinear restoring force systems that are general in nature.

II. BASIC METHODS FOR SOLUTION

There is usually considerable advantage in finding an analytical solution for the governing differential equations of a physical system when it is possible to do so. The solution is obtained in algebraic form and often gives basic insight into the system. If, however, no insight is available from the algebraic form itself, then the equations are in a form suitable for parametric, numerical studies, thus leading to a detailed look at the system.

The basic method presented is the Ritz Averaging Method. It is a very powerful method applicable to both autonomous and nonautonomous systems. The method will not satisfy the differential equation point by point, but will satisfy it only in some mean or weighted average.

To arrive at the Ritz condition, it is best to start with the variational problem since many problems in engineering and physics can be formulated as a minimum problem. The solution is then one that gives some integral expression a minimum value.

To begin, let $F(\eta, \dot{\eta}, t)$ be a continuous function where η and $\dot{\eta}$ are the functions of time; then

$$I = \int_{t_0}^t F(\eta, \dot{\eta}, t) dt \quad (1)$$

has some meaning.

The problem now is to choose $\eta(t)$ such that I is a minimum. This is done by variation of $\eta(t)$. If $\bar{\eta}(t)$ is a neighborhood function of $\eta(t)$, then

$$\bar{\eta}(t) = \eta(t) + \epsilon Y(t),$$

where ϵ is a small arbitrary number and Y is an arbitrary function.

This is a problem of calculus of variations, and the extremum I may be obtained by letting

$$\left| \frac{dI}{d\epsilon} \right|_{\epsilon=0} = \int_{t_0}^{t_1} \left\{ \frac{\partial F}{\partial \eta} Y + \frac{\partial F}{\partial \dot{\eta}} \dot{Y} \right\} dt = 0.$$

The main idea of the Ritz method is to let extremum I depend on a finite number of parameters only, by approximating $\eta(t)$ by a function $\bar{\eta}(t)$, where

$$\bar{\eta}(t) = \sum_{i=1}^n \alpha_i \psi_i(t). \quad (2)$$

Then $\psi_i(t)$'s are known functions, and α_i 's are coefficients to be determined. The problem is now to give I a minimum value when I depends on a finite number of parameters. Minimizing the functional integral I with respect to the undetermined coefficient α_i leads to the following n equations:

$$\frac{\partial I}{\partial \alpha_i} = \int_{t_0}^{t_1} \left[\frac{\partial F}{\partial \eta} \psi_i + \frac{\partial F}{\partial \dot{\eta}} \dot{\psi}_i \right] dt = 0. \quad i = 1, 2, \dots, n. \quad (3)$$

Integrating the second term by parts yields

$$\frac{\partial I}{\partial \alpha_i} = \int_{t_0}^{t_1} \left\{ \frac{\partial F}{\partial \eta} - \frac{d}{dt} \frac{\partial F}{\partial \dot{\eta}} \right\} \psi_i dt + \left[\psi_i \frac{\partial F}{\partial \dot{\eta}} \right]_{t_0}^{t_1} = 0. \quad (4)$$

If the second term vanishes for the limits t_0 to t_1 - this can be accomplished by proper choice of ψ_i - then

$$\frac{\partial I}{\partial \alpha_i} = \int_{t_0}^{t_1} \frac{\partial F}{\partial \eta} - \frac{d}{dt} \frac{\partial F}{\partial \dot{\eta}} \psi_i dt = 0. \quad (5)$$

In the braces are Euler equations or the differential equations of the system. Therefore,

$$\int_{t_0}^{t_1} D(\bar{\eta}) \psi_i dt = 0 \quad (6)$$

is the minimum problem with $D(\bar{\eta})$ the differential equation of the problem. It coincides with the Euler equation of the corresponding variational problem written as a function of the assumed function in equation (2). However, this equation will not vanish at every point as the Euler equation does. This method has, however, the advantage of operating with the differential equation and not some expression I ; in fact, I does not have to be known if the differential equation is known. The weight functions correspond to the coordinate function of equation (2).

The procedure for solution of nonlinear equations is now straightforward and contains the following steps:

First, assume the approximate solution

$$\bar{\eta}(t) = \sum_{i=1}^n \alpha_i \psi_i(t). \quad (7)$$

Second, solve the integrals

$$\int_{t_0}^{t_1} D(\bar{\eta}) \psi_i dt = 0. \quad i = 1, 2, \dots, n \quad (8)$$

Third, solve the resulting algebraic equations for the coefficients α_i .

The obvious disadvantage of the method is that some idea of the nature of solution is necessary for choosing the weight functions. Otherwise, too many terms will be necessary to get accurate results.

III. APPLICATION OF METHOD TO A SPECIFIC PROBLEM

A. DERIVATION OF BASIC EQUATIONS DESCRIBING SYSTEM

To illustrate the use of the Ritz method, the response of a traveling vehicle to sinusoidal force inputs is chosen where the spring is an air spring. Both single and two degrees-of-freedom are studied.

The first step in describing the characteristics of the system is to derive the expression for the restoring force of an air spring. This is accomplished by assuming that adiabatic conditions hold for the gas (air); therefore, the characteristics of an air spring under the influence of a load can be determined using the relationship between volume and pressure in the form

$$P = \frac{P_0 V_0^\gamma}{V^\gamma}, \quad (9)$$

where V_0 and P_0 are the equilibrium volume and pressure of the gas column in a cylinder at static equilibrium, V and P the displaced volume and the corresponding pressure, and γ the ratio of specific heats.

Let x be the displacement of the piston from equilibrium; then the volume at any displacement x is

$$V(x) = V_0 - A_0 x, \quad (10)$$

where A_0 is the cross-sectional area of the cylinder.

If ℓ_0 is by definition the height of the piston from the bottom of the cylinder at the equilibrium position, then

$$V_0 = A_0 \ell_0.$$

Substituting the foregoing equation and equation (5) into equation (4) yields the pressure as a function of the displacement as

$$P(x) = P_0 \left(1 - \frac{x}{\ell_0}\right)^{-\gamma}. \quad (11)$$

The following diagram depicts the above definitions and coordinate system.

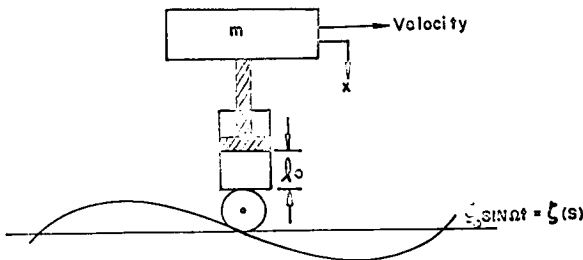


FIGURE 1. THE SINGLE-DEGREE-OF-FREEDOM SYSTEM

The total force acting on the piston, since it is evenly distributed, yields

$$F_p = P_0 A_0 \left(1 - \frac{x}{\ell_0}\right)^{-\gamma}. \quad (12)$$

Since the weight is balanced by part of the total force, the weight of the mass must be subtracted from the total force to get the restoring force. By definition, $w = mg = P_0 A_0$; thus, the restoring force becomes

$$R(x) = P_0 A_0 \left[\left(1 - \frac{x}{\ell_0}\right)^{-\gamma} - 1 \right]. \quad (13)$$

The restoring force as derived is of a general nature and is valid for each spring of the two-degrees-of-freedom system and the single-degree-of-freedom system. Figure 2 is a plot of the restoring force as a function of displacement.

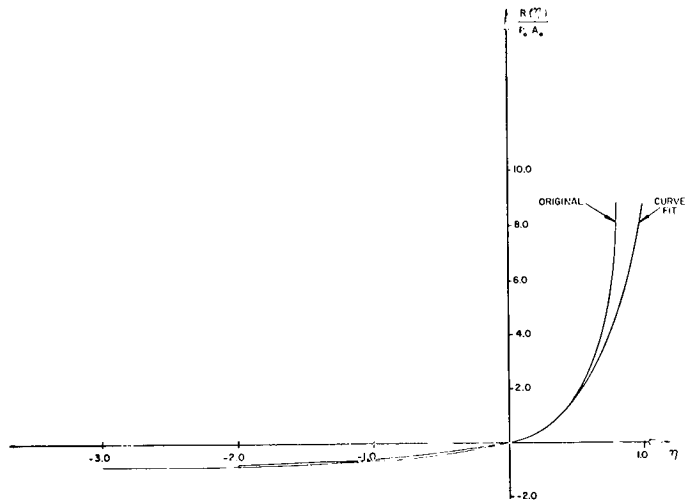


FIGURE 2. COMPARISON OF CURVE FIT TO ORIGINAL RESTORING FORCE FOR $\gamma = 1.4$

The equation of motion reads, by using equation (13),

$$m\ddot{x} + P_0 A_0 \left[\left(1 - \frac{x + \xi(t)}{\ell_0}\right)^{-\gamma} - 1 \right] = 0. \quad (14)$$

Dividing (14) by m and assuming that

$$\frac{x(t) + \xi(t)}{\ell_0} = \eta(t) \quad (15)$$

yields

$$\ddot{\eta} + \omega_o^2 \left[(1 - \eta)^{-\gamma} - 1 \right] = -\Omega^2 \bar{\zeta}_o \sin \Omega t, \quad (16)$$

where

$$\omega_o = \sqrt{\frac{P_o A_o}{m \ell_o}} = \sqrt{\frac{g}{\ell_o}}$$

and

$$\bar{\zeta}_o = \frac{\zeta_o}{\ell_o}, \quad (17)$$

where ω_o is the undamped natural frequency of the linearized and transformed system. The time is $t = S/v$ in which v is the traveling velocity of the vehicle. Equation (11) is then the basic equation of motion for a single-degree-of-freedom vehicle with an air spring.

A two-degrees-of-freedom system should adequately represent a traveling vehicle if the system is considered to have two air springs sinusoidally forced with a phase lag between them. The following diagram depicts the system.

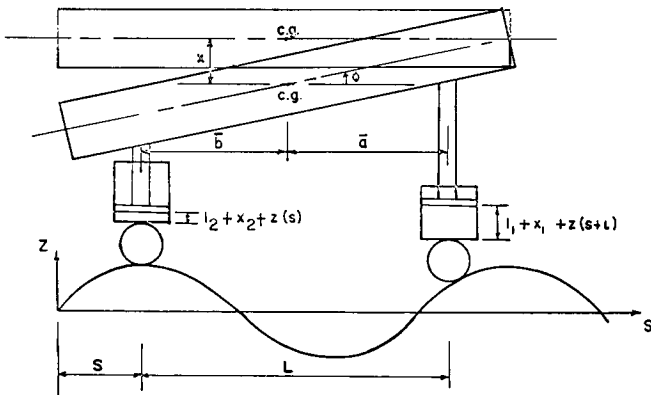


FIGURE 3. THE TWO-DEGREES-OF-FREEDOM SYSTEM

In the diagram, x is the displacement of the center of gravity of the system, and φ is the angular rotation about the center of gravity.

The equations of motion can now be written as

$$m\ddot{x} + R_1(x_1) + R_2(x_2) = 0 \quad (18)$$

$$I\ddot{\varphi} + \bar{a} R_1(x_1) - \bar{b} R_2(x_2) = 0, \quad (19)$$

where

m = vehicle mass

I = moment of inertia of vehicle mass about center of gravity

$R_1(x_1)$ = restoring force on piston 1

$R_2(x_2)$ = restoring force on piston 2

x_1 = total displacement of air in piston 1

x_2 = total displacement of air in piston 2

$\bar{a} + \bar{b} = L$.

Since x_1 and x_2 were defined as the total displacement of the air column from equilibrium, their respective definitions become

$$x_1 = x + \bar{a} \varphi + \zeta(s) \quad (20)$$

$$x_2 = x - \bar{b} \varphi + \zeta(s + L), \quad (21)$$

where s is the displacement along path and L is the distance between the pistons.

By using equations (13), (20), and (21), equations (18) and (19) become

$$\ddot{x} + k_1 \left[\left(1 - \frac{x + \bar{a} \varphi + \zeta(s)}{\ell_1} \right)^{-\gamma} - 1 \right] + \quad (22)$$

$$+ k_2 \left[\left(1 - \frac{x - \bar{b} \varphi + \zeta(s + L)}{\ell_2} \right)^{-\gamma} - 1 \right] = 0$$

$$\ddot{\varphi} + k_3 \left[\left(1 - \frac{x + \bar{a} \varphi + \zeta(s)}{\ell_1} \right)^{-\gamma} - 1 \right] - \quad (23)$$

$$- k_4 \left[\left(1 - \frac{x - \bar{b} \varphi + \zeta(s + L)}{\ell_2} \right)^{-\gamma} - 1 \right] = 0,$$

where

$$k_1 = \frac{P_1 A_1}{m} \quad (24a)$$

$$k_2 = \frac{P_2 A_2}{m} \quad (24b)$$

$$k_3 = \frac{\bar{a} P_1 A_1}{I} \quad (24c)$$

$$k_4 = \frac{\bar{b} P_2 A_2}{I}. \quad (24d)$$

Now letting

$$z_1 = \frac{x + \bar{a}\varphi + \zeta(s)}{\ell_1} \quad (25a)$$

$$z_2 = \frac{x - \bar{b}\varphi + \zeta(s + L)}{\ell_2} \quad (25b)$$

$$\zeta(s) = \zeta_0 \sin \Omega t \quad (25c)$$

$$\zeta(s + L) = \zeta_0 \sin (\Omega t + \alpha) \quad (25d)$$

in which the phase lag α can be determined in terms of the vehicle velocity v and its length L , equations (17) and (18) yield

$$\begin{aligned} \bar{b} \ddot{z}_1 + \frac{\ell_2}{\ell_1} \bar{a} \ddot{z}_2 + \frac{L}{\ell_1} k_1 \left[(1 - z_1)^{-\gamma} - 1 \right] \\ + \frac{L}{\ell_1} k_2 \left[(1 - z_2)^{-\gamma} - 1 \right] = - \bar{b} \Omega^2 \bar{\zeta}_0 \sin \Omega t \end{aligned} \quad (26)$$

$$\begin{aligned} - \bar{a} \Omega^2 \bar{\zeta}_0 \sin (\Omega t + \alpha) \\ = - \Omega^2 \bar{\zeta}_0 \left[\sin \Omega t (\bar{b} + \bar{a} \cos \alpha) + \bar{a} \cos \Omega t \sin \alpha \right] \\ \ddot{z}_1 - \frac{\ell_2}{\ell_1} \ddot{z}_2 + \frac{L}{\ell_1} k_3 \left[(1 - z_1)^{-\gamma} - 1 \right] - \frac{L}{\ell_1} k_4 \left[(1 - z_2)^{-\gamma} - 1 \right] \\ = - \Omega^2 \bar{\zeta}_0 \sin \Omega t + \Omega^2 \bar{\zeta}_0 \sin (\Omega t + \alpha) \quad (27) \\ = \Omega^2 \bar{\zeta}_0 \left[\sin \Omega t (\cos \alpha - 1) + \cos \Omega t \sin \alpha \right], \end{aligned}$$

where

$$\bar{\zeta}_0 = \frac{\zeta_0}{\ell_1} \quad (28)$$

B. SOLUTION OF EQUATIONS

To solve the nonlinear forced response (equation (16)) by the Ritz method, a solution is assumed for η . This solution must contain a constant term since the restoring force is not symmetrical about the η -axis. This leads to

$$\eta = M + Q \sin \Omega t, \quad (29)$$

where M and Q are constants to be determined. Since

$$\frac{\partial F}{\partial \dot{\eta}} (1) \Bigg|_0^{2\pi} = Q \cos \tau \Bigg|_0^{2\pi} = 0 \quad (30)$$

and

$$\frac{\partial F}{\partial \dot{\eta}} \sin \tau \Bigg|_0^{2\pi} = Q \cos \tau \sin \tau \Bigg|_0^{2\pi} = 0, \quad (31)$$

conditions (46) of the Ritz method then yield

$$\begin{aligned} \int_0^{2\pi} D(\eta) d\tau = 0 \\ \int_0^{2\pi} D(\eta) \sin \tau d\tau = 0. \end{aligned} \quad (33)$$

Replacing the second term of equation (11) by a power series yields

$$\ddot{\eta} + \omega_0^2 \sum a_i \eta^i = - \Omega^2 \bar{\zeta}_0 \sin \Omega t. \quad (34)$$

The coefficient a_1 is equal to 1, and the a_0 coefficient is zero since the curve must pass through the origin. Using the approximated differential equation (60) leads to two algebraic equations in M and Q , the simultaneous solution of which gives the forced response. These equations are, if the series is cut off as the 5th power,

$$\begin{aligned} 8(a_1 M + a_2 M^2 + a_3 M^3 + a_4 M^4 + a_5 M^5) + 4(a_2 + 3a_3 M + \\ + 6a_4 M^2 + 10a_5 M^3) Q^2 + 3(a_4 + 5a_5 M) Q^4 = 0 \end{aligned} \quad (35)$$

$$\begin{aligned} -r^2(\bar{\zeta}_0 + Q) + (a_1 + 2a_2 M + 3a_3 M^2 + 4a_4 M^3 + 5a_5 M^4) Q^3 \\ + \frac{3}{4}(a_3 + 4a_4 M + 10a_5 M^2) Q^5 + \frac{5}{8} a_5 Q^7 = 0 \end{aligned} \quad (36)$$

where

$$r^2 = \frac{\Omega^2}{\omega_0^2}. \quad (37)$$

To solve these equations, the method of steepest descent was used. The results of these equations are shown on Figures 4 and 5, and show the response in absolute maximum amplitude denoted by $\bar{\eta}$ versus the frequency ratio with the force amplitude as parameter. When $\bar{\zeta}_0$ equals zero, the backbone curve, or frequency, as a function of amplitude appears.

It can be seen that the system first softens for small amplitudes and then hardens for larger amplitudes approaching a constant value as the frequency increases.

A jump in amplitude will occur at any point where the slope of the amplitude curve is infinite. By observing the amplitude curve, it is seen that, as the

frequency ratio is increased, a jump in amplitude will occur giving large amplitudes of oscillations. Starting with a large frequency ratio and decreasing the value will first give a jump of increased amplitude and then a jump to a lower amplitude. It seems advisable, therefore, for the natural frequency of the system to be above the forcing frequency by a factor of two or three to maintain a low response value.

C. TWO-DEGREES-OF-FREEDOM SYSTEM

Equations (26) and (27) described the basic equations of motion of a rigid two-degrees-of-freedom vehicle. These equations are again nonlinear.

To solve the nonlinear two-degrees-of-freedom system, a polynomial of fifth order will be used to represent the restoring force function of equations (26) and (27); therefore,

$$(1 - z_i)^{-\gamma} - 1 = z_i + a_2 z_i^2 + a_3 z_i^3 + a_4 z_i^4 + a_5 z_i^5. \quad (38)$$

This leads to

$$\begin{aligned} \bar{b} \ddot{z}_1 + \frac{2}{\ell_1} \bar{a} \ddot{z}_2 + \frac{L}{\ell_1} K_1 [z_1 + a_2 z_1^2 + a_3 z_1^3 + a_4 z_1^4 + a_5 z_1^5] \\ + \frac{L}{\ell_1} K_2 [z_2 + a_2 z_2^2 + a_3 z_2^3 + a_4 z_2^4 + a_5 z_2^5] = \end{aligned} \quad (39)$$

$$- \Omega^2 \zeta_0 [\sin \Omega t (\bar{b} + \bar{a} \cos \alpha) + \bar{a} \cos \Omega t \sin \alpha].$$

$$\begin{aligned} \ddot{z}_1 - \frac{2}{\ell_1} \ddot{z}_2 + \frac{L}{\ell_1} K_3 [z_1 + a_2 z_1^2 + a_3 z_1^3 + a_4 z_1^4 + a_5 z_1^5] \\ - \frac{L}{\ell_1} K_4 [z_2 + a_2 z_2^2 + a_3 z_2^3 + a_4 z_2^4 + a_5 z_2^5] = \end{aligned} \quad (40)$$

$$\Omega^2 \zeta_0 [\sin \Omega t (\cos \alpha - 1) + \cos \Omega t \sin \alpha].$$

Again the Ritz method is applied. Since the system has nonsymmetric restoring forces, and the forcing functions have both sine and cosine terms, the assumed solution takes the form

$$\bar{z}_i = M_i + Q_i \cos \Omega t + R_i \sin \Omega t. \quad (41)$$

Substituting equation (41) into equations (39) and (40) leads to the differential equations in terms of the assumed solution (41).

Application of the Ritz method yields the following six integrals:

$$\int_0^{2\pi} D_i(z_i) d\tau = 0 \quad i = 1 \text{ and } 2 \quad (42)$$

$$\int_0^{2\pi} D_i(z_i) \cos \tau d\tau = 0 \quad i = 1 \text{ and } 2 \quad (43)$$

$$\int_0^{2\pi} D_i(z_i) \sin \tau d\tau = 0 \quad i = 1 \text{ and } 2, \quad (44)$$

where $D_i(z_i)$ are the differential equations with the assumed solution (41) applied.

Applying equations (42), (43), and (44) gives the following set of nonlinear algebraic equations for the coefficients M_i , Q_i , R_i .

$$\begin{aligned} \sum_{i=1}^2 \bar{K}_{1i} \left[2M_i + 2M_i^2 a_2 + 2M_i^3 a_3 + 2M_i^4 a_4 + 2M_i^5 a_5 + a_2 Q_i^2 \right. \\ + a_2 R_i^2 + 3a_3 M_i Q_i^2 + 3a_3 M_i R_i^2 + \frac{3}{4} a_4 Q_i^4 + \frac{3}{4} a_4 R_i^4 \\ + 6a_4 M_i^2 Q_i^2 + 6a_4 M_i^2 R_i^2 + \frac{6}{4} a_4 Q_i^2 R_i^2 + \frac{15}{4} a_5 M_i Q_i^4 \\ + \frac{15}{4} a_5 M_i R_i^4 + 10a_5 M_i^3 Q_i^2 + 10a_5 M_i^3 R_i^2 + \frac{30}{4} a_5 M_i Q_i^2 R_i^2 \left. \right] = 0 \end{aligned} \quad (45)$$

$$\begin{aligned} \sum_{i=1}^2 \bar{K}_{2i} \left[2M_i + 2a_2 M_i^2 + 2a_3 M_i^3 + 2a_4 M_i^4 + 2a_5 M_i^5 + a_2 Q_i^2 \right. \\ + a_2 R_i^2 + 3a_3 M_i Q_i^2 + 3a_3 M_i R_i^2 + \frac{3}{4} a_4 Q_i^4 + \frac{3}{4} a_4 R_i^4 \\ + 6a_4 M_i^2 Q_i^2 + 6a_4 M_i^2 R_i^2 + \frac{6}{4} a_4 Q_i^2 R_i^2 + \frac{15}{4} a_5 M_i Q_i^4 \\ + \frac{15}{4} a_5 M_i R_i^4 + 10a_5 M_i^3 Q_i^2 + 10a_5 M_i^3 R_i^2 + \frac{30}{4} a_5 M_i Q_i^2 R_i^2 \left. \right] = 0 \end{aligned} \quad (46)$$

$$\begin{aligned} \Omega^2 \left[- \sum_{i=1}^2 A_{1i} Q_i + \zeta_0 (\bar{b} + \bar{a} \cos \alpha) \right] + \sum_{i=1}^2 \bar{K}_{1i} \left[Q_i \right. \\ + 2a_2 M_i Q_i + \frac{3}{4} a_3 Q_i^3 + 3a_3 M_i^2 Q_i + \frac{3}{4} a_3 Q_i R_i^2 + 3a_4 M_i Q_i^3 \\ + 4a_4 M_i^3 Q_i + 3a_4 M_i Q_i R_i^2 + \frac{15}{24} a_5 Q_i^5 + \frac{30}{4} a_5 M_i^2 Q_i^3 \\ + 5a_5 M_i^4 Q_i + \frac{30}{4} a_5 M_i^2 Q_i R_i^2 + \frac{5}{16} a_5 Q_i R_i^4 + \frac{10}{16} a_5 Q_i^3 R_i^2 \left. \right] = 0 \end{aligned} \quad (47)$$

$$\begin{aligned} & \Omega^2 \left[- \sum_{i=1}^2 A_{2i} Q_i + \bar{\zeta}_0 (1 - \cos \alpha) \right] + \sum_{i=1}^2 \bar{K}_{2i} \left[Q_i \right. \\ & + 2a_2 M_i Q_i + \frac{3}{4} a_3 Q_i^3 + 3a_3 M_i^2 Q_i + \frac{3}{4} a_3 Q_i R_i^2 + 3a_4 M_i Q_i^3 \\ & + 4a_4 M_i^3 Q_i + 3a_4 M_i Q_i R_i^2 + \frac{15}{24} a_5 Q_i^5 + \frac{30}{4} a_5 M_i^2 Q_i^2 \\ & + 5a_5 M_i^4 Q_i^2 + \frac{30}{4} a_5 M_i^2 Q_i R_i^2 + \frac{5}{16} a_5 Q_i R_i^4 + \frac{10}{16} a_5 Q_i^3 R_i^2 \left. \right] \\ & = 0. \end{aligned} \quad (48)$$

$$\begin{aligned} & \Omega^2 \left[- \sum_{i=1}^2 A_{ii} R_i + \bar{a} \bar{\zeta}_0 \sin \alpha \right] + \sum_{i=1}^2 \bar{K}_{ii} \left[R_i + 2a_2 M_i R_i \right. \\ & + \frac{3}{4} a_3 R_i^3 + 3a_3 M_i^2 R_i + \frac{3}{4} a_3 Q_i^2 R_i + 3a_4 M_i R_i^3 + 4a_4 M_i^3 R_i \\ & + 3a_4 M_i Q_i^2 R_i + \frac{15}{24} a_5 R_i^5 + \frac{30}{4} a_5 M_i^2 R_i^3 + 5a_5 M_i^4 R_i \\ & + \frac{30}{4} a_5 M_i^2 Q_i^2 R_i + \frac{10}{16} a_5 Q_i^2 R_i^3 + \frac{5}{16} a_5 Q_i^4 R_i \left. \right] = 0. \end{aligned} \quad (49)$$

$$\begin{aligned} & \Omega^2 \left[- \sum_{i=1}^2 a_{2i} R_i - \bar{\zeta}_0 \sin \alpha \right] + \sum_{i=1}^2 \bar{K}_{2i} \left[R_i + 2a_2 M_i R_i \right. \\ & + \frac{3}{4} a_3 R_i^3 + 3a_3 M_i^2 R_i + \frac{3}{4} a_3 Q_i^2 R_i + 3a_4 M_i R_i^3 + 4a_4 M_i^3 R_i \\ & + 3a_4 M_i Q_i^2 R_i + \frac{15}{24} a_5 R_i^5 + \frac{30}{4} a_5 M_i^2 R_i^3 + 5a_5 M_i^4 R_i \\ & + \frac{30}{4} a_5 M_i^2 Q_i^2 R_i + \frac{10}{16} a_5 Q_i^2 R_i^3 + \frac{5}{16} a_5 Q_i^4 R_i \left. \right] = 0, \end{aligned} \quad (50)$$

where

$$\bar{K}_{11} = \frac{L P_1 A_1 \gamma}{\ell_1 m} \quad (51)$$

$$\bar{K}_{12} = \frac{L P_2 A_2 \gamma}{\ell_1 m} \quad (52)$$

$$\bar{K}_{21} = \frac{L \bar{a} P_1 A_1 \gamma}{\ell_1 I} \quad (53)$$

$$\bar{K}_{22} = \frac{-L \bar{b} P_2 A_2 \gamma}{\ell_1 I} \quad (54)$$

$$A_{11} = \bar{b} \quad (55)$$

$$A_{12} = -\frac{\bar{a} \ell_2}{\ell_1} \quad (56)$$

$$A_{21} = \ell_1 \quad (57)$$

$$A_{22} = -\frac{\ell_2}{\ell_1} \quad (58)$$

These algebraic equations are solved by using the method of steepest descent as was done for the single-degree-of-freedom system.

Information of the dependency of the amplitudes M_1 , M_2 , Q_1 , Q_2 , R_1 , and R_2 on the system parameters is shown on Figures 6 through 11. Of main concern are the forcing frequency, the amplitude of forcing function $\bar{\zeta}_0$, and the phase (α) of the forcing frequency Ω , with the other parameters r , α , and $\bar{\zeta}_0$ noted on the respective curves. Since the meaning of the curves seems to be clear, they require little comment. It is obvious that two resonance conditions occur with the backbone curve appearing when $\bar{\zeta}_0$ is equal to zero. The system contains the jump phenomenon discussed under the single-degree-of-freedom system with the significant difference that it occurs near each resonance frequency. The effect of changing the ratio of specific heat γ is not significant. The changing of the forcing function amplitude $\bar{\zeta}_0$ does not give a larger maximum response due to the nonlinearity, but does give larger amplitudes away from resonance.

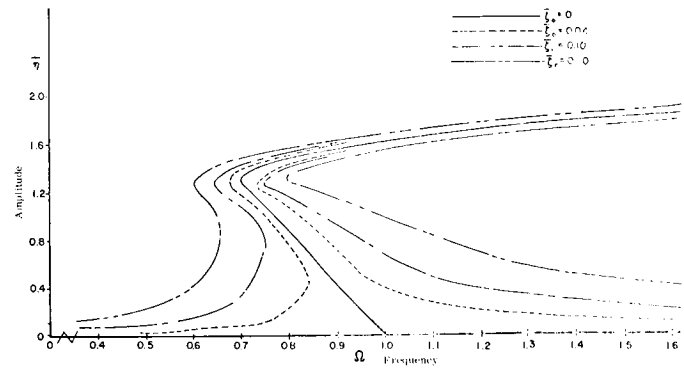


FIGURE 4. SINGLE DEGREE OF FREEDOM RESPONSE $\gamma = 1.4$

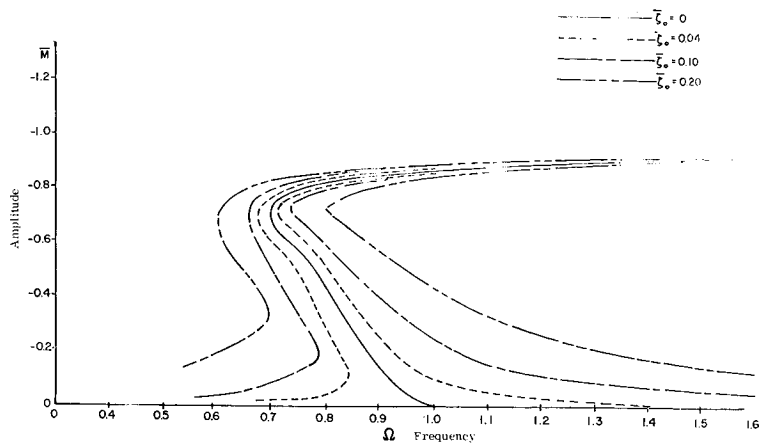


FIGURE 5. SINGLE DEGREE OF FREEDOM RESPONSE $\gamma = 1.4$

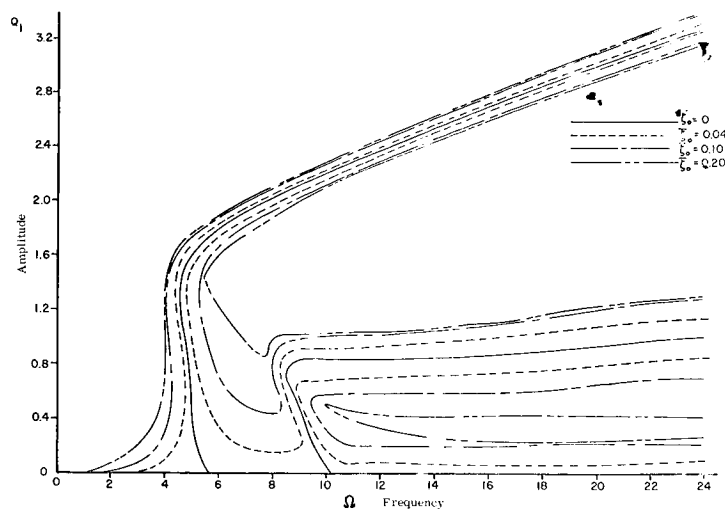


FIGURE 8. TWO DEGREE OF FREEDOM RESPONSE $\gamma = 1.4, \alpha = 45$ DEGREES

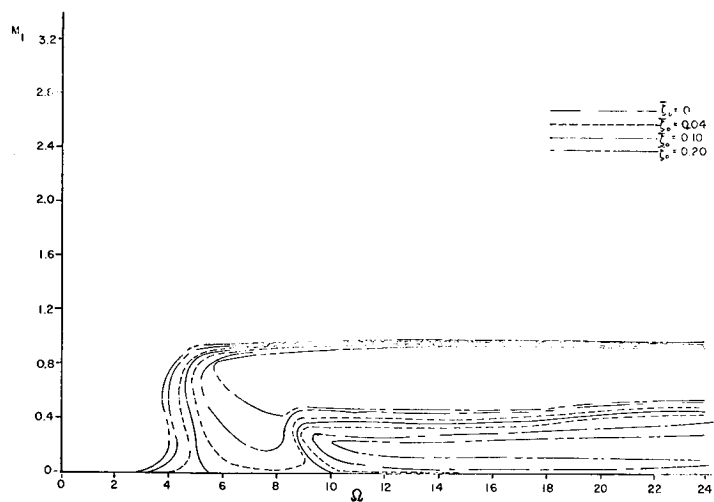


FIGURE 6. TWO DEGREE OF FREEDOM RESPONSE $\gamma = 1.4, \alpha = 45$ DEGREES

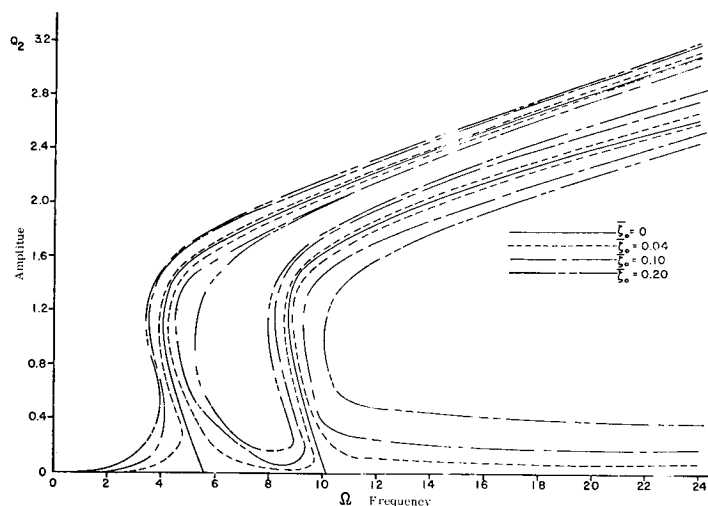


FIGURE 9. TWO DEGREE OF FREEDOM RESPONSE $\gamma = 1.4, \alpha = 45$ DEGREES

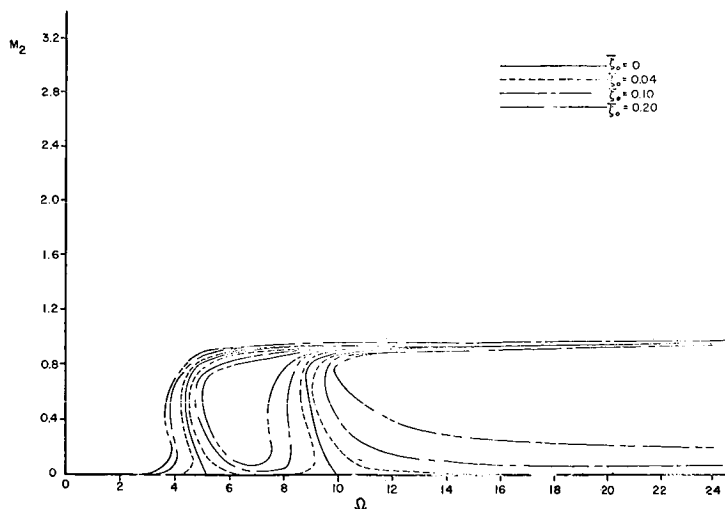


FIGURE 7. TWO DEGREE OF FREEDOM RESPONSE $\gamma = 1.4, \alpha = 45$ DEGREES

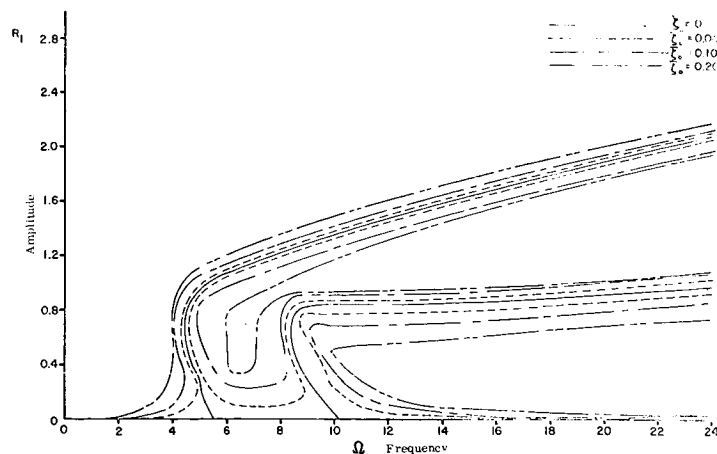


FIGURE 10. TWO DEGREE OF FREEDOM RESPONSE $\gamma = 1.4, \alpha = 45$ DEGREES

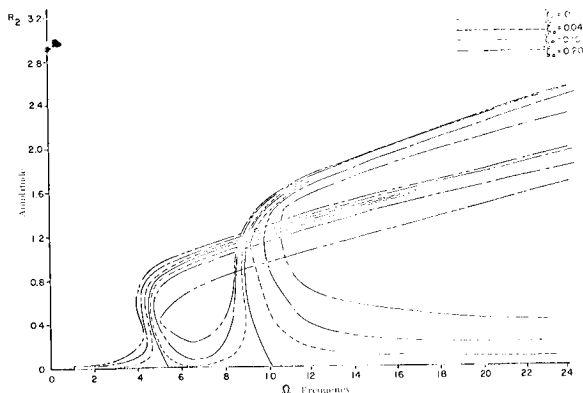


FIGURE 11. TWO DEGREE OF FREEDOM RESPONSE
 $\gamma = 1.4$, $\alpha = 45$ DEGREES

REFERENCES

1. Klotter, K. and P. R. Cobb, "On the Use of Non-sinusoidal Approximating Functions for Nonlinear Oscillation Problems," *Journal of Applied Mechanics*, Sept., 1960, pp. 579-583.
2. Klotter, K., "Nonlinear Vibration Problems Treated by the Averaging Method of W. Ritz: Part I Fundamentals of the Method," Stanford University Tech Report No. 17, Part 1, May 1951.
3. Klotter, K., "Nonlinear Vibration Problems Treated by the Averaging Method of W. Ritz: Part II Single Degree of Freedom Systems, Single Term Approximations," Stanford University Report 17, Part II, June 1951.
4. Burgess, John C., "Harmonic and Subharmonic Response for Single Degree of Freedom Systems of the Duffing Type," Stanford University, Technical Report 27, Sept. 1954.
5. Arnold, Frank, "Steady-State Oscillations in Nonlinear Systems of Two Degrees of Freedom," Stanford University Technical Report 24, December 1963.
6. Klotter, K. and J. Plough, "Nonlinear Vibration Problems Treated by the Averaging Method of W. Ritz: Part III Single Degree of Freedom Systems Non-Odd Restoring Forces Two Term Approximations," Stanford University Technical Report 17, Part III, June 1952.

A SIMPLE METHOD FOR DETERMINING THE BENDING MOMENT EQUATION THAT INCLUDES VEHICLE ELASTIC AND SLOSHING MODES AND A NUMERICAL EXAMPLE

By **N65 24131**

Robert S. Ryan, Fred Swift, and Don Townsend

SUMMARY

This paper describes a method for deriving the bending moment of a vehicle in terms of pertinent control parameters. The equation is presented in a form that is easier to use for control optimization techniques, particularly if the bending moment at some critical station is chosen as the value to be optimized. The form of the equation lends itself to any technique used in vehicle dynamic response studies. Also in this form, the effect of various parameters is completely separated allowing a better survey of causes and effects. A numerical example is given and the effects of angle of attack, engine deflection, bending dynamics, and propellant oscillations determined. The trade-off between angle of attack and engine deflection is shown graphically.

DEFINITION OF SYMBOLS

| Symbol | Definition |
|--------|----------------------------------------|
| a_o | Attitude control gain |
| b_o | Angle of attack control gain |
| C_z | Local normal force coefficient |
| D_o | Reference diameter of vehicle |
| F_s | Swivel thrust |
| $F(s)$ | Alpha channel filter transfer function |
| I | Moment of inertia |
| M | Mass of vehicle |
| $M(x)$ | Local mass distribution |
| M' | Aerodynamic Moment coefficient |
| N' | Aerodynamic normal force coefficient |
| q | Dynamic pressure |
| s | Vehicle reference area |
| $T(s)$ | Actuator transfer function |

Symbol

Definition

| | |
|--------------------------------------------------------------------|------------------------------------------------------|
| V | Vehicle velocity |
| V_w | Wind velocity |
| X | Vehicle station |
| X_{cg} | Location of vehicle center of gravity |
| X_E | Gimbal station |
| X_K | Vehicle station about which moments are taken |
| X_T | Vehicle station at aft end of vehicle |
| X_y | Vehicle station at nose of vehicle |
| $Y_{\psi}(x)$ | Normalized deflection of vehicle |
| $Y'_{\psi}(x)$ | Slope of deflection curve |
| $Y''_{\psi}(x)$ | Rate of change of slope of deflection curve |
| y | Translation normal to trajectory |
| α | Angle of attack |
| α_w | Angle of attack due to wind |
| $\alpha(x)$ | Local angle of attack |
| β | Engine gimbal angle |
| η_{ψ} | Elastic deflection of vehicle |
| φ | Attitude angle of vehicle with respect to trajectory |
| $\ddot{\tau}$ | Acceleration normal to vehicle center-line |
| E_{γ} \bar{E}_{γ} $A_{\mu\gamma}$ D_{μ} | Aerodynamic coefficients |

DEFINITION OF SYMBOLS

| Symbol | Definition |
|---------|---------------------------|
| $C_1 =$ | $\frac{M'}{I}$ |
| $C_2 =$ | $\frac{F_s \bar{X}_E}{I}$ |

I. INTRODUCTION

The ascent of a space vehicle through the atmosphere subjects it to many disturbances, including wind magnitude, wind shear, and turbulence or gusts. The loads induced on the flight vehicle due to these disturbances are of major concern in designing the vehicle structure. Therefore, we must be able to predict the probable loads. Of great concern is a means of optimization of control systems in such a manner that the loads are reduced at the critical station, while at the same time not building up excessive loads at another station making it the critical one. Obviously, this type of load reduction can place more payload in space by optimization of the structure. The form of the bending moment equation as used by stress engineers is not readily applicable to the control engineer's optimization techniques. These forms of the equation are the mode displacement and mode acceleration methods. A study of these equations shows that the effects of the various parameters are not completely separated so that a good physical insight into the phenomenon cannot be obtained. Also in using equations in this form, large numbers of terms or modes are necessary for good convergence. In some cases, numerical accuracy is not good due to the subtraction of large numbers.

The bending moment equation is presented in a form which allows the effects of the various parameters to be completely separated and at the same time retain a form readily applicable to optimization studies by the control engineer and eliminate the numerical error. To illustrate this, a numerical example for the Saturn V space vehicle is included showing the effects of rigid body angle of attack, engine deflection, bending dynamics, and sloshing dynamics. Of particular interest to the control engineer is a curve presenting the trade-off between angle of attack and engine deflection.

II. DERIVATION OF BENDING MOMENT EQUATIONS

A. COORDINATE SYSTEM AND EQUATIONS OF MOTION

The coordinate system chosen to describe the system is a two-dimensional trajectory-fixed system. The origin coincides with that of the vehicle center of gravity on a nominal trajectory. The positive x-axis is tangent to the trajectory and in the direction of flight. The positive y-axis conforms with that of a right-handed coordinate system. Lateral translation is measured on the y-axis and rotation (ϕ) is measured counterclockwise from the positive x-axis. This is illustrated in the following diagram for a rigid vehicle.

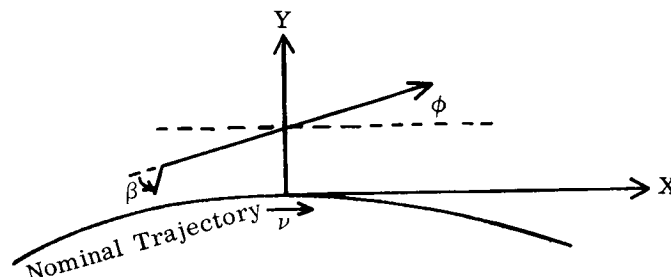


FIGURE 1. COORDINATE SYSTEM

Figure 2 is a vectorial representation of components of the angle of attack.

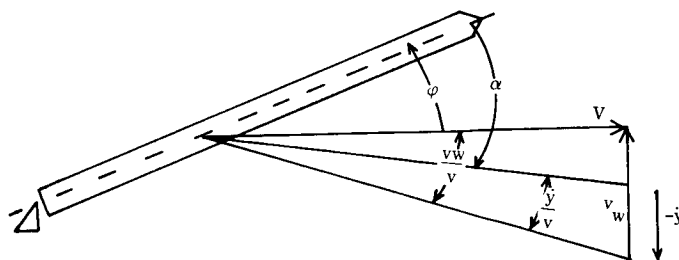


FIGURE 2. RIGID ANGLE OF ATTACK

$$\alpha = -\frac{y}{v} + \frac{v_w}{v}$$

To include vehicle bending, it is assumed that the vehicle's structure can be approximated by the superposition of several free-free beam modes from the relationship

$$y(x, t) = \sum_v \eta_v(t) Y_v(x), \quad (1)$$

which defines the centerline displacement of the structure; $Y(x)$ is the free-free normalized mode shape and η the generalized coordinate. These mode shapes are computed with the liquid mass and engine masses included, but assumed to be frozen in.

The dynamics of the liquid are represented by a mechanical model attached to the vehicle tank walls. This model exactly duplicates the forces and moments determined from the hydrodynamical solution and accurately duplicates the fluid oscillations within the assumptions made for the hydrodynamical solution (incompressible, irrotational fluid with small disturbances).

Bases upon these considerations and assumptions, the equations of motion and various relationships become:

1. Local angle of attack

$$\alpha(x) = \varphi - \frac{\dot{Y}}{V} + \alpha_w - \frac{\bar{X}\dot{\varphi}}{V} - \sum_{\nu} \eta_{\nu} Y_{\nu}(x) - \sum_{\nu} \frac{\dot{\eta}_{\nu}}{V} Y_{\nu}(x) \quad (2)$$

$$= \alpha_{\text{rigid}} + \alpha_{\text{rotation}} + \alpha_{\text{bending}}$$

$$\text{where } \alpha_{\text{rigid}} = \varphi - \frac{\dot{Y}}{V} + \alpha_w,$$

$$\alpha_{\text{rotation}} = -\frac{\bar{X}\dot{\varphi}}{V}, \text{ and}$$

$$\alpha_{\text{bending}} = -\sum_{\nu} \eta_{\nu} Y_{\nu}(x) - \sum_{\nu} \frac{\dot{\eta}_{\nu}}{V} Y_{\nu}(x).$$

2. Rotation equation

$$\ddot{\varphi} - \sum_s \frac{m_s \bar{X}}{I} \ddot{\xi}_s + C_1 \alpha + C_2 \beta + \sum_{\nu} Q \bar{E}_{\nu} \eta_{\nu} \quad (3)$$

3. Translation equation (perpendicular to vehicle centerline)

$$\ddot{\tau} - k_2 \alpha - k_3 \beta + \sum_s \frac{m_s}{m} \ddot{\xi}_s + \sum_{\nu} Q E_{\nu} \eta_{\nu} \quad (4)$$

4. Bending equation

$$\ddot{\eta}_{\mu} + 2 \xi_B \alpha_B \dot{\eta}_{\mu} + \omega_B^2 \eta_{\mu} + \sum_{s,\nu} \frac{m_s}{M_B} Y_{\nu}(x_s) \ddot{\xi}_s$$

$$+ \bar{g} \sum_{s,\nu} \frac{m_s}{M_B} \xi_s Y'_{\nu}(x_s) - 2 Q D_{\mu} \alpha + \sum_{\nu} Q A_{\mu\nu} \eta_{\nu} \quad (5)$$

5. Sloshing equation

$$\ddot{\xi}_s + 2 \xi_s \omega_s \dot{\xi}_s + \omega_s^2 \xi_s + \ddot{Y} - \bar{X}_s \ddot{\varphi} + \sum_{\nu} \ddot{\eta}_{\nu} Y_{\nu}(x_s) - \bar{g} \varphi + \bar{g} \sum_{\nu} \eta_{\nu} Y'_{\nu}(x_s) = 0 \quad (6)$$

6. Control equation

$$\beta = a_o \varphi_i + a_i \dot{\varphi}_i + b_o \alpha_i \quad (7)$$

where

$$\varphi_i = \varphi - \sum_{\nu} \eta_{\nu} Y'_{\nu}(x_{\varphi})$$

and

$$\alpha_i = \varphi - \frac{\dot{Y}}{V} + \alpha_w - \sum_{\nu} \eta_{\nu} Y'_{\nu}(x_v) - \sum_{\nu} \frac{\dot{\eta}_{\nu}}{V} Y_{\nu}(x_v) - \frac{\bar{X}_v \dot{\varphi}}{V}.$$

B. BENDING MOMENT EQUATIONS

The bending moment arises from the lateral forces acting on the vehicle. By summing from a particular station to one end of the vehicle, the product of these lateral forces times the distance to the desired station gives the moment value at that station. The lateral forces have three sources: aerodynamical forces dependent upon local angle of attack, inertial forces dependent upon local acceleration, and lateral components of thrust due to engine swiveling. The moment due to thrust misalignment arising from vehicle bending will be neglected. This leads to the following equations for bending moment.

$$M_B^{\text{Aero}} = \frac{qS}{D_o} \int_{x_k}^{x_E} C'_{z\alpha} (x-x_k) \alpha(x) dx \quad (8)$$

$$M_B^{\text{Inertial}} = - \int_{x_k}^{x_E} M'(x) (x-x_k) \ddot{\tau}_i(x) dx - \sum_s m_s (x_k - x_s) \ddot{\xi}_s \quad (9)$$

The $M'(x)$ considers the sloshing mass as rigidly attached at a point; therefore, the sloshing dynamics show up as the second summation term.

$$M_B \text{ Thrust} = F_s \beta (X_E - X_k) + m_s (X_k - X_s) \quad (10)$$

Assuming that the bending contribution in equations (3) and (4) are negligible (this should be a valid assumption since this is the contribution of bending to the local angle of attack and should be small), the lateral acceleration of the center of gravity becomes

$$\ddot{\tau}_{cg} = k_2 \alpha + k_3 \beta - \sum_s \frac{m_s}{m} \ddot{\xi}_s \quad (11)$$

and rotational acceleration becomes

$$\ddot{\varphi} = -C_1 \alpha(x) - C_2 \beta + \sum_s \frac{m_s}{I} (x_{cg} - x_s) \ddot{\xi}_s \quad (12)$$

Substituting these relationships into equations (8) and (9) neglecting small terms yields for the bending moment

$$M_{B(x_k)} = M'_\alpha \alpha_{\text{rigid}} + M'_\beta \beta + \sum_\nu \ddot{\eta}_\nu M'_\nu(x) + \sum_s M'_s \ddot{\xi}_s \quad (13)$$

where

$$\begin{aligned} M'_\alpha(x_k) &= \frac{q s}{D_0} \int_{x_k}^{x_E} C'_{z\alpha}(x_k - x) dx \\ &- \frac{N'}{m} \int_{x_k}^{x_E} M'(x) (x_k - x) dx \\ &+ \frac{M'}{I} \int_{x_k}^{x_E} M'(x) (x_k - x) (x_{cg} - x) dx \end{aligned} \quad (14)$$

$$\begin{aligned} M'_\beta(x_k) &= F_s (x_k - x_E) - \frac{F_s}{m} \int_{x_E}^{x_k} M'(x) (x_k - x) dx \\ &- \frac{F_s (x_k - x_E)}{I} \int_{x_E}^{x_k} M'(x) (x_k - x) (x_{cg} - x) dx \end{aligned} \quad (15)$$

$$M'_\mu(x_k) = - \int_{x_E}^{x_k} M'(x) (x_k - x) Y_\mu(x) dx \quad (16)$$

$$\begin{aligned} M'_\delta(x_k) &= \sum \left[\frac{m_s}{m} \int_{x_E}^{x_k} M'(x_k - x) dx \right. \\ &\left. + \frac{m_s}{I} (x_{cg} - x_s) \int_{x_E}^{x_k} M'(x_{cg} - x) (x_k - x) dx \right] \quad (17) \end{aligned}$$

$$+ m_s (X_k - X_s) \quad \Bigg] .$$

By taking the limit of the integrals over the total vehicle we can see that each of these coefficients satisfies the boundary conditions (moment zero at end of vehicle). These analytical results are not included, but can be verified by consulting the plots of these coefficients presented in the next section.

Representing the bending moment in this form has numerous advantages to the control engineer. Among these advantages are

(1) complete separation of the effects of the various control parameters,

(2) weighting or trade-off of the various parameter effects as a function of vehicle station, thus, leading to optimization possibilities at the weakest sections,

(3) the moment is not as sensitive to numerical errors because the coefficients can be computed on large computers using large numbers of terms, and

(4) greater physical insight into the problem of load reduction.

II. NUMERICAL EXAMPLE

The bending moment coefficients as derived were computed for the Saturn V space vehicle at 70 seconds flight time (Figures 3-6). The ratio of the coefficient of angle of attack to the coefficient of engine deflection is shown on Figure 7. It can be readily seen that any control law that increases the ratio of engine deflection to angle of attack will be detrimental to the bending moment.

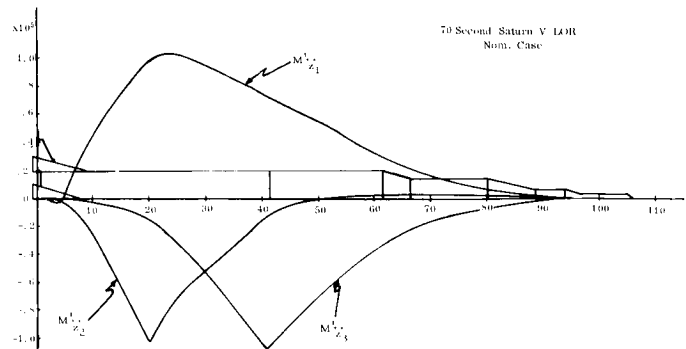


FIGURE 3. M'_s VERSUS VEHICLE STATION

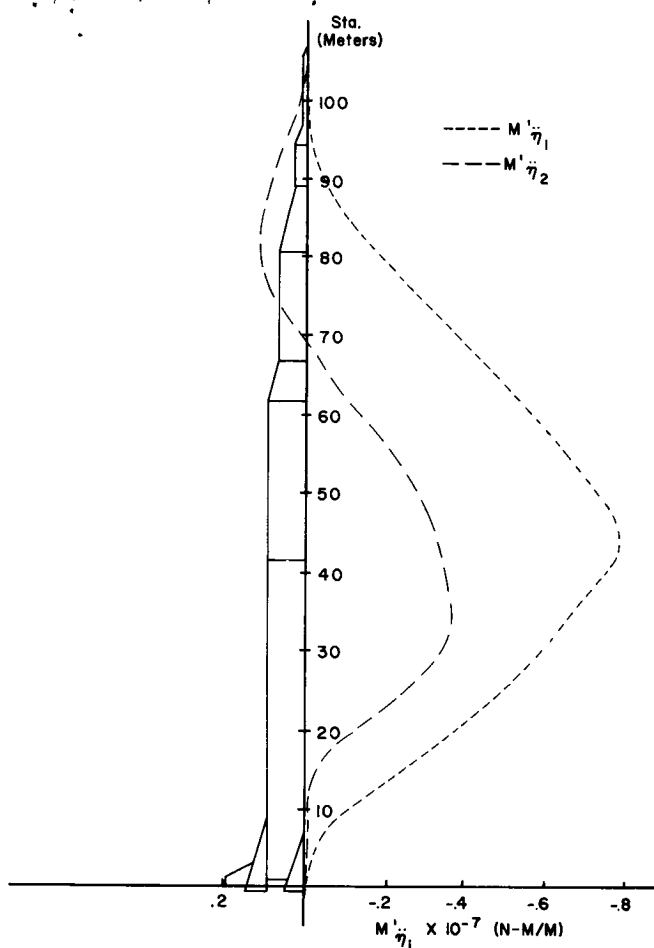


FIGURE 4. SATURN V LOR, 70 SEC, M'_{η_i} VERSUS VEHICLE STATION

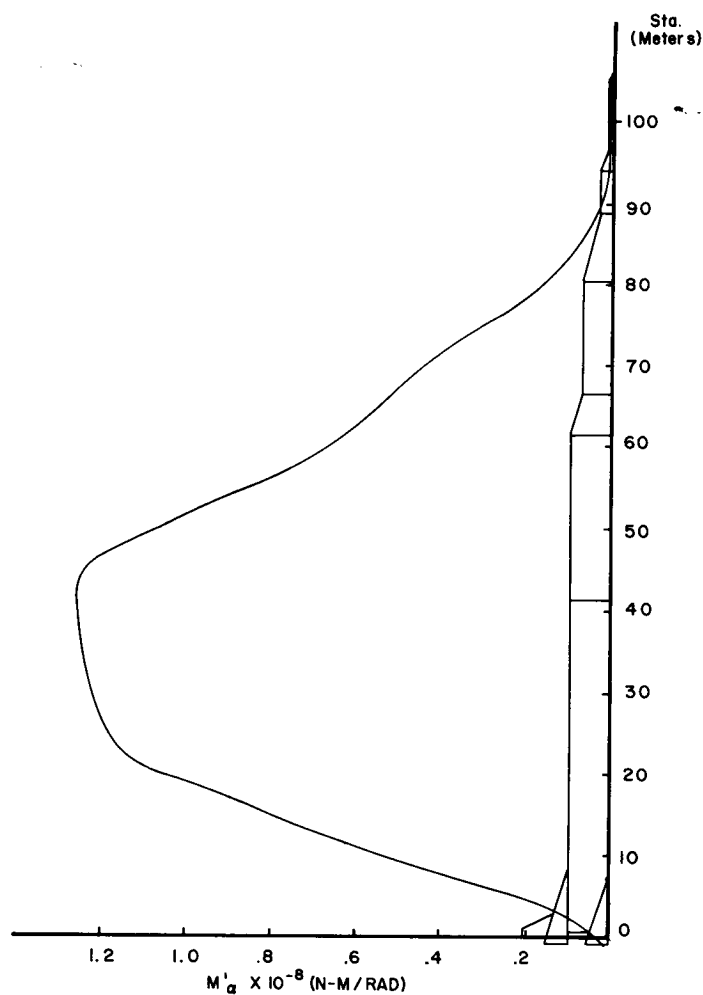


FIGURE 6. SATURN V LOR, 70 SEC, M'_α VERSUS VEHICLE STATION

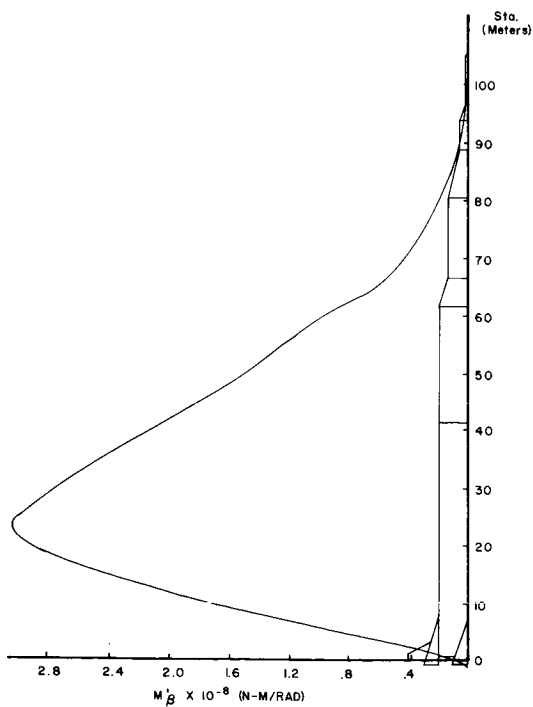


FIGURE 5. SATURN V LOR, 70 SEC M'_β VERSUS VEHICLE STATION

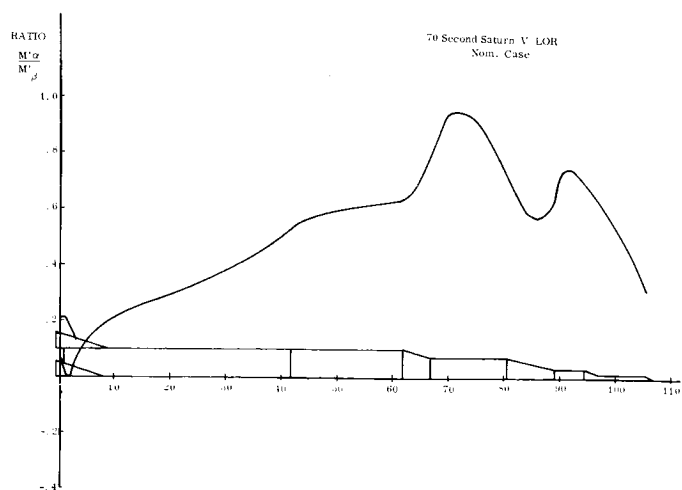


FIGURE 7. RATIO $\frac{M'_\alpha}{M'_\beta}$ VERSUS VEHICLE STATION

To determine the effects of the various parts on the total bending moment, a response of the vehicle was made. The control equation was assumed to be ideal with the rate gyro located at the vehicle tail for bending mode stability. All sloshing modes were damped by introducing adequate damping into the slosh equation. The input force was the Marshall synthetic profile with 99 percent wind shear, 95 percent wind magnitude and the superimposed 9 m/sec^2 gust. Plots of the total bending moment and the various parts are shown on Figures 8 and 9. Bending dynamics have an

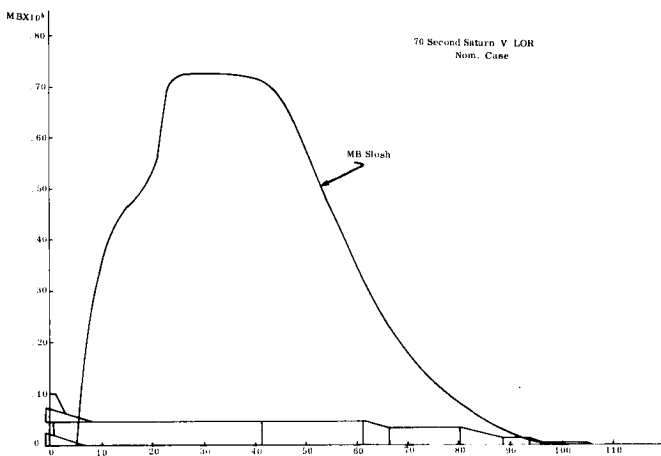


FIGURE 8. BENDING MOMENT DUE TO SLOSHING VERSUS VEHICLE STATION

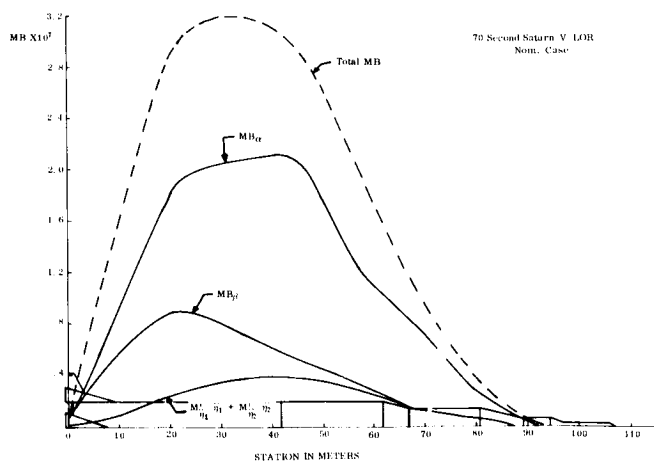


FIGURE 9. CONTRIBUTING PARTS TO BENDING MOMENT VERSUS VEHICLE STATION

effect of from 5 percent to 50 percent depending on the vehicle station. The maximum effect of propellant oscillations is 3 percent. The contributions of angle of attack and engine deflection are about equal.

Figure 10 is a plot of some representative failing moment (not actual since this was not available) with the bending moment obtained superimposed. It becomes quite clear that optimizing the moment at the two or three critical stations would give better structural integrity. Since the purpose of this paper was to present the equations, no attempt at optimization is made, however, it is believed that the results shown give ample evidence of the advantage of writing the bending moment equation in this simple form.

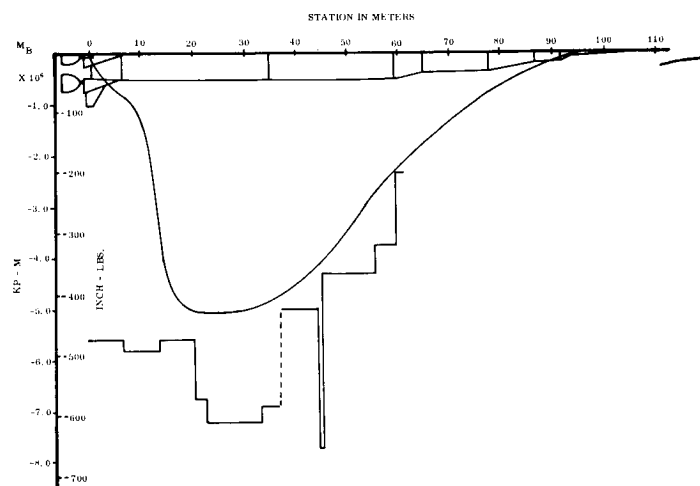


FIGURE 10. SATURN V FAILING MOMENT VERSUS STATION, 70 SEC

CONCLUSION

A simple representation for the bending moment has been given. It can be concluded from the results presented that the form of the equations leads to greater physical insight and provides the control engineer with a tool that can be readily used in optimization techniques.

ON TRANSIENT RESPONSE OF A MULTISTAGE SPACE VEHICLE

by

Frank C. Liu

N65-24132

SUMMARY

Presented in this paper is an analytical solution for the transient response of a multistage space vehicle to a general external load. The structure of the vehicle is considered to be a stepped beam with uniform sections.

William type modal solution for a uniform beam is assumed for each section of the beam. Upon imposing the conditions of continuity of these sectional continuous functions, these functions should yield equal magnitudes of deflection, slope, bending moment and shear force at the junctions; and the boundary conditions at two ends, the characteristic determinant of natural vibration, and the arbitrary constants of the solutions are determined. The differential equations of the generalized coordinates are obtained by making use of the orthogonality relation of the eigenfunctions.

LIST OF SYMBOLS

| Symbol | Definition |
|----------|------------------------------------------------|
| a | $= EI/A_s G l^2$ |
| A | cross-sectional area of beam |
| A_s | effective shear-carrying area of cross section |
| $[A^n]$ | column matrix, arbitrary constants |
| b | $= I/A l^2$ |
| $[C^n]$ | column matrix, arbitrary constants |
| c | $= EI/m l^4$ |
| D | characteristic matrix |
| D_{mk} | element of the adjoint matrix of D |
| E | Young's modulus of elasticity |
| g | row matrix defined by equation (16) |
| I | moment of inertia of cross section |

| Symbol | Definition |
|-----------|---------------------------------------------|
| K^n | square matrix defined by equation (15) |
| l | length of one section of beam |
| L | total length of beam |
| m | mass of beam per unit length |
| M | bending moment or total mass of beam |
| N | total number of section of the stepped beam |
| P_i | generalized load defined by equation (24) |
| q | external load |
| \bar{q} | $= q l^3 / EI$ |
| Q^k | square matrix defined by equation (13) |
| S | rigid body translation |
| t | time variable |
| V | shear force |
| W | static deflection |
| x | coordinate |
| \bar{x} | $= x/l$ |
| y | transverse deflection |
| z | $= y/l$ |
| Z_i | natural vibration mode |
| τ | $= \sqrt{ct}$, dimensionless time variable |
| ψ | rotation of cross section |
| Ψ | natural vibration mode of ψ |
| ω | natural frequency of beam |
| Ω | static part of rotation ψ |

| Symbol | Definition |
|--------------|-----------------------------------------|
| ϕ_i | generalized coordinates |
| Superscripts | |
| n | designates quantity of the nth section. |

INTRODUCTION

In the dynamic analysis of a rocket or a missile, the structure is usually treated as a uniform beam in very crude approximations, or as a beam with many uniform sections in using matrix methods. Obviously, the first approach gives a very poor result for a multi-stage space vehicle because of the abrupt change of structural parameters from one stage to another. In matrix analysis, the structure can be represented accurately, but the quality of the result depends on fineness of the breakdowns of the structure. This often leads to manipulation of large size matrices. Hence, the limited capacity of the digital computer and the excessive cost and time required to invert and to find eigenvalues of a large size matrix are disadvantages of the matrix method.

In the proposed method of this paper, the space vehicle is treated as a uniform stepped beam. Each stage of the vehicle may be further broken down into steps as desired. The differential equation of beam vibration considered is the Timoshenko type which is written in the form of simultaneous equations in two variables with a general external load function. Our analysis is to find the response of the stepped beam to a general external load. The solution given by this paper is exact and maximum size of the matrix in the calculation is 4 by 4.

We now outline the analysis as follows:

(1) Assuming a solution of the beam differential equations in the form given by Leonard [3] for each section of the beam independently, we can obtain solutions which are sectional continuous functions with undetermined arbitrary constants;

(2) By imposing the conditions of continuity to the section or continuous functions such that the assumed solutions yield equal deflection, slope, bending moment and shear force at the junctions of the sections, we can express the arbitrary constants of the solution for each section in terms of arbitrary constants of the two end-sections through chain relations;

(3) Applying the natural boundary conditions at the two ends of the beam to the solutions, we formulate the characteristic equation from which the eigenvalues can be computed, and in turn, the eigenvectors of the arbitrary constants are obtained;

(4) Using the orthogonality relation of the eigenfunctions, we determine the differential equations of the generalized coordinates of natural vibration.

II. ANALYSIS

A. EQUATION OF MOTION OF A UNIFORM BEAM

The well known differential equation of transverse vibration of a uniform beam, including rotary inertia and shear deformation effects, may be written in the form of simultaneous equations of two variables of the form [3]

$$\begin{cases} EI \frac{\partial^2 \psi}{\partial x^2} + A_s G \left(\frac{\partial y}{\partial x} - \psi \right) - \frac{mI}{A} \frac{\partial^2 \psi}{\partial t^2} = 0 \\ A_s G \left(\frac{\partial^2 y}{\partial x^2} - \frac{\partial \psi}{\partial x} \right) - m \frac{\partial^2 y}{\partial t^2} = -q(x, t), \end{cases} \quad (1)$$

where y is the transverse displacement and ψ is the rotation of the cross section of the beam. Expressing the above equations in dimensionless form, we have

$$\begin{cases} \psi'' + \frac{1}{a} (z' - \psi) - b \ddot{\psi} = 0 \\ \frac{1}{a} (z'' - \psi') - \ddot{z} = -\bar{q}, \end{cases} \quad (2)$$

in which the primes and dots denote the derivatives with respect to the dimensionless spatial coordinate \bar{x} and the time variable τ , respectively.

A great deal of work has been done in solving this system of partial differential equations. The solution given by Leonard [3] is presented here. Leonard assumes the solution of (1) in the form

$$\begin{aligned} z(\bar{x}, \tau) &= S(\tau) + W(\bar{x}, \tau) + \sum_{i=0}^{\infty} \phi_i(\tau) Z_i(\bar{x}) \\ \psi(\bar{x}, \tau) &= \Omega(\bar{x}, \tau) + \sum_{i=0}^{\infty} \phi_i(\tau) \psi_i(\bar{x}), \end{aligned} \quad (3)$$

where $S(\tau)$ is the rigid body translation of the beam, $W(\bar{x}, \tau)$ and $\Omega(\bar{x}, \tau)$ are the static deflection and rotation, $Z_i(\bar{x})$ and $\psi_i(\bar{x})$ are the natural vibration

modes, and $\phi_i(\tau)$ are the generalized coordinates. We will use the same form of solution for a stepped beam.

B. EQUATION OF MOTION OF A STEPPED BEAM

Consider a stepped beam consisting of N uniform sections as shown in Figure 1. The spatial coordinate of the beam x and the beam parameters will be designated by a superscript "n" to indicate the nth section of the beam. These parameters are assumed constant in each section of the beam, but may vary from section to section.

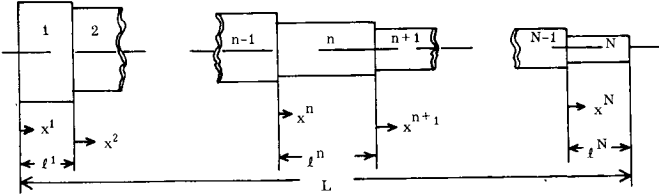


FIGURE 1. COORDINATE SYSTEM OF MULTIPLE SECTION BEAM

It is obvious that for each section alone the system partial differential equations are still governing equation of motions, and the solution given by equation (3) is still valid within each section. These solutions are sectional continuous functions. Conditions of continuity at the junctions of the sections must be satisfied, and the natural boundary conditions at two ends of the beam must be fulfilled by these functions.

1. Conditions of Continuity. The following are the conditions of continuity:

$$\begin{aligned} [y(x^n, t)]_{x^n=0} &= [y(x^{n-1}, t)]_{x^{n-1}=l^{n-1}} \\ \left[\frac{\partial}{\partial x^n} y(x^n, t) \right]_{x^n=0} &= \left[\frac{\partial}{\partial x^{n-1}} y(x^{n-1}, t) \right]_{x^{n-1}=l^{n-1}} \\ [M(x^n, t)]_{x^n=0} &= [M(x^{n-1}, t)]_{x^{n-1}=l^{n-1}} \\ [V(x^n, t)]_{x^n=0} &= [V(x^{n-1}, t)]_{x^{n-1}=l^{n-1}} \end{aligned} \quad (4)$$

2. Boundary Conditions. Four types of boundary conditions will be considered:

$$\text{Displacement zero} \quad z = 0$$

$$\text{Total slope zero} \quad z' = 0$$

$$\text{Moment zero} \quad \psi' = 0 \quad (5)$$

$$\text{Shear zero} \quad z' - \psi = 0.$$

3. Orthogonality of the Eigenfunctions. The orthogonality relation for a uniform beam can be extended to a stepped beam. As shown in Appendix D of Ref. 1, we have

$$\int_0^L m l^3 (Z_i Z_j + b \Psi_i \Psi_j) dx = 0 \quad i \neq j \quad (6)$$

C. THE GENERAL SOLUTIONS

We now proceed to determine the terms given in equation (3).

1. The Rigid Body Translation. The rigid body translation of the beam is the same for all sections. It can be obtained by direct integration of the total external load acting on the beam and dividing by the total mass of the beam:

$$S(t) = \int \int \int_0^L q(x, t) dx dt / M. \quad (7)$$

2. The Static Solution. Setting the inertia of rotation term equal to zero in the first equation of (1) and replacing the inertia term of linear motion by the inertia due to rigid body motion in the second equation of (1), we have

$$\begin{aligned} \Omega''(\bar{x}^n, \tau^n) + \frac{1}{a^n} [W'(\bar{x}^n, \tau^n) - \Omega(\bar{x}^n, \tau^n)] &= 0 \\ \frac{1}{a^n} [W''(\bar{x}^n, \tau^n) - \Omega'(\bar{x}^n, \tau^n)] &= -q^n(\bar{x}^n, \tau^n / \sqrt{c^n}) \\ &+ \ddot{S}(\tau^n / \sqrt{c^n}). \end{aligned} \quad (8)$$

Eliminating the variable Ω from these equations, we can obtain the solution for W by direct integration:

$$\begin{aligned} W(\bar{x}^n, \tau^n) &= \int \int \int q^n(d\bar{x}^n)^4 - a^n \int \int q^n(d\bar{x}^n)^2 \\ &+ \frac{1}{24} (\bar{x}^n)^4 \ddot{S}(\tau^n / \sqrt{c^n}) + \left\{ 1 \bar{x}^n \frac{1}{2} (\bar{x}^n)^2 \frac{1}{6} (\bar{x}^n)^3 \right\} [C^n] \end{aligned} \quad (9)$$

when $[C^n]$ is a column matrix of four arbitrary constants of integration. These constants are determined from the conditions that the static solution W satisfies both the conditions of the continuity, equation (4), and the natural boundary conditions, equation (5). The formulation of C^n is given in Appendix A of Ref. 1.

3. Solution of Natural Vibrations. Since the natural vibration of the beam is harmonic with frequency ω_i , we may replace $\ddot{\Psi}_i$ by $-(\omega_i^2/c) \Psi_i$ and \ddot{Z}_i by $-(\omega_i^2/c) Z_i$ in equation (2). This yields

$$a^n \Psi_i'''(\bar{x}^n) + Z_i'(\bar{x}^n) - \Psi_i'(\bar{x}^n) + (b^n/c^n) \omega_i^2 \Psi_i(\bar{x}^n) = 0 \quad (9)$$

$$Z_i''(\bar{x}^n) - \Psi_i'(\bar{x}^n) + (a^n/c^n) \omega_i^2 Z_i(\bar{x}^n) = 0$$

$$i = 0, 1, 2, \dots$$

The solution of the above equations is

$$Z_i(\bar{x}^n) = \left(\cosh \alpha_i^n \bar{x}^n \sinh \alpha_i^n \bar{x}^n \cos \beta_i^n \bar{x}^n \sin \beta_i^n \bar{x}^n \right) \begin{bmatrix} A_i^n \end{bmatrix} \quad (10)$$

$$\Psi_i(\bar{x}^n) = \left(d_i^n \sinh \alpha_i^n \bar{x}^n d_i^n \cosh \alpha_i^n \bar{x}^n - e_i^n \sin \beta_i^n \bar{x}^n e_i^n \cos \beta_i^n \bar{x}^n \right) \begin{bmatrix} A_i^n \end{bmatrix},$$

where A_i^n is the i^{th} eigenvector of A_i^n and

$$d_i^n = \left(\alpha_i^n + a^n \omega_i^2 / c^n \right) \alpha_i^n, \quad e_i^n = \left(\beta_i^n - a^n \omega_i^2 / c^n \right) \beta_i^n,$$

where α_i and β_i are the real and imaginary roots, respectively, of the algebraic equation

$$\lambda_i^4 + \lambda_i^2 (a+b) \omega_i^2 / c - (ab \omega_i^2 / c - 1) \omega_i^2 / c = 0. \quad (12)$$

We now form a column matrix which consists of four elements: deflection, slope, bending moment, and shear force. It is readily seen from equation (10) that

$$\left\{ Y(x^n), \frac{dY(x^n)}{dx^n}, M(x^n), V(x^n) \right\}^T = Q''(\bar{x}^n) A^n, \quad (13)$$

where

$$Q(x) = \begin{bmatrix} \ell \cosh \alpha \bar{x} & \ell \sinh \alpha \bar{x} & \ell \cos \beta \bar{x} & \ell \sin \beta \bar{x} \\ \alpha \sinh \alpha \bar{x} & \alpha \cosh \alpha \bar{x} & -\beta \sin \beta \bar{x} & \beta \cos \beta \bar{x} \\ -\frac{EId\alpha}{\ell} \cosh \alpha \bar{x} & \frac{EId\alpha}{\ell} \sinh \alpha \bar{x} & \frac{EIc\beta}{\ell} \cos \beta \bar{x} & \frac{EIc\beta}{\ell} \sin \beta \bar{x} \\ \frac{EI(\alpha-d)}{a^2} \sinh \alpha \bar{x} & \frac{EI(\alpha-d)}{a^2} \cosh \alpha \bar{x} & \frac{EI(c-\beta)}{a^2} \sin \beta \bar{x} & \frac{EI(c-\beta)}{a^2} \cos \beta \bar{x} \end{bmatrix}$$

Let us denote

$$Q_0^n = \left[Q(\bar{x}^n) \right]_{\bar{x}^n=0} \quad \text{and} \quad Q_1^n = \left[Q(\bar{x}^n) \right]_{\bar{x}^n=1}$$

With the aid of the above notations, the conditions of continuity given by equation (4) may be written simply in the form

$$Q_0^n A^n = Q_1^{n-1} A^{n-1}. \quad (14)$$

By successive substitution of equation (14), A^n can be expressed in terms of A^1 ,

$$A^n = K^n A^1 \quad (15)$$

where

$$K^n = (Q_0^n)^{-1} Q_1^{n-1} (Q_0^{n-1})^{-1} Q_1^{n-2} \dots (Q_0^2)^{-1} Q_1^1.$$

By making use of equations (13), (14), (15) and the following row matrices

$$g_1 = \{1 \ 0 \ 0 \ 0\} \quad \text{for deflection,}$$

$$g_2 = \{0 \ 1 \ 0 \ 0\} \quad \text{for slope,}$$

$$g_3 = \{0 \ 0 \ 1 \ 0\} \quad \text{for bending moment,}$$

$$g_4 = \{0 \ 0 \ 0 \ 1\} \quad \text{for shear force,}$$

we may express the natural boundary conditions simply as

$$DA^1 = 0, \quad (17)$$

where

$$D = \begin{bmatrix} \begin{bmatrix} g_r \\ g_s \end{bmatrix} & Q_0^1 \\ \begin{bmatrix} g_t \\ g_u \end{bmatrix} & Q_1^N K^N \end{bmatrix} \quad r, s, t, u = 1, 2, 3, 4.$$

Hence, the characteristic equation is obtained by letting the determinant of D equal to zero

$$|D| = 0, \quad (18)$$

from which the eigenvalues or the natural frequencies ω_i , $i=1, 2, \dots$ are computed. Let $D_{mk}(\omega_i)$ denote the elements of the adjoint matrix of the matrix D ; then the eigenvector of A_i^1 is

$$A_i^1 = \begin{bmatrix} A_1^1 \\ A_2^1 \\ A_3^1 \\ A_4^1 \end{bmatrix} = \begin{bmatrix} 1 \\ D_{21}(\omega_i)/D_{11}(\omega_i) \\ D_{31}(\omega_i)/D_{11}(\omega_i) \\ D_{41}(\omega_i)/D_{11}(\omega_i) \end{bmatrix} \quad (19)$$

and

$$A_i^n = K^n(\omega_i) A_i^1. \quad (20)$$

The general procedure of computing ω_i is suggested as follows:

1. Assume a value of ω_i .
2. Find α_i^n and β_i^n for $n = 1, 2, \dots, N$ from equation (12)
3. Compute Q_0^n and Q_1^n for $n = 1, 2, \dots, N$ from equations (13) to (15).
4. Compute $|D(\omega_i)|$ from equation (17).
5. Repeat steps 1 to 4, until $|D(\omega_i)|$ approaches to zero.

4. The Generalized Coordinates, $\phi_i(t)$.

Substituting the assumed solution, equation (3), into the differential equation of motion (2), and making use of equations (8) and (10) yields

$$\sum_{i=0}^{\infty} \left[\frac{d^2 \phi_i(t)}{dt^2} + \omega_i^2 \phi_i(t) \right] Z_i(\bar{x}^n) = - \frac{\partial}{\partial t^2} W(\bar{x}^n, \sqrt{c^n} t) \quad (21a)$$

$$\sum_{i=0}^{\infty} \left[\frac{d^2 \phi_i(t)}{dt^2} + \omega_i^2 \phi_i(t) \right] \Psi_i(x^n) = - \frac{\partial}{\partial t^2} \Omega(\bar{x}^n, \sqrt{c^n} t) \quad (21b)$$

Now, we multiply equation (21a) by $m \ell^3 Z_j$ and equation (21b) by $b m \ell^3 \Psi_j$, then integrate the sum over the range $0 \leq x \leq L$. Making use of the orthogonality relation given by equation (6) we find that

$$\frac{d^2 \phi_i}{dt^2} + \omega_i^2 \phi_i = - \frac{1}{m_i} \frac{d^2 P_i(t)}{dt^2} \quad i = 0, 1, 2, \dots \quad (22)$$

The generalized mass and the generalized load appearing in the above equation are defined, respectively, as

$$m_i = \sum_{n=1}^N \int_0^1 m^n (\ell^n)^3 \left[Z_i^2(\bar{x}^n) + b^n \Psi_i^2(x^n) \right] d\bar{x}^n \quad (23)$$

$$P_i(t) = \sum_{n=1}^N \int_0^1 m^n (\ell^n)^3 \left[W(\bar{x}^n, \sqrt{c^n} t) Z_i(\bar{x}^n) + b^n \Omega(\bar{x}^n, \sqrt{c^n} t) \Psi_i(x^n) \right] d\bar{x}^n \quad (24)$$

For the rigid body mode ($\omega_0 = 0$), $\Psi_0 = 0$ and $Z_0 = C$ from equations (23) and (24),

$$m_0 = \sum_{n=1}^N m^n (\ell^n)^3 Z_0^2 \quad (25)$$

$$P_0(t) = Z_0 \sum_{n=1}^N \int_0^1 m^n (\ell^n)^3 W(\bar{x}^n, \sqrt{c^n} t) d\bar{x}^n \quad (26)$$

If the beam is assumed initially at rest and undeformed, we have

$$\begin{aligned} z(x^n, 0) &= 0 \\ \dot{z}(x^n, 0) &= 0 \\ \psi(x^n, 0) &= 0 \\ \dot{\psi}(x^n, 0) &= 0. \end{aligned} \quad (27)$$

Consequently, the initial conditions for ϕ_i are

$$\begin{aligned} \phi_i(0) &= -P_i(0)/m_i \\ \dot{\phi}_i(0) &= -\dot{P}_i(0)/m_i. \end{aligned} \quad (28)$$

$$i = 0, 1, 2, \dots$$

Finally, equation (22) may be solved by standard procedures.

REFERENCES

1. Liu, F. C., "On Transient Response of a Stepped Beam," Aero-Astrodynamic Internal Note 50-63, Dec. 1963.
2. Timoshenko, S., "Vibration Problems in Engineering," D. Van Nostrand, 1959, p. 331.
3. Leonard, R. W., "On Solutions for the Transient Response of Beams," NASA TR R-21, 1959.
4. Williams, D., "Displacements of Linear Elastic System Under a Given Transient Load," British S. M. R. C/7219/DW/19, August 1946.

by

Frank C. Liu

SUMMARY

N65-24133

This paper deals with vibration of uniform beams with large amplitude. Two sets of system of nonlinear partial differential equations of two variables are derived in Ref. 1 for the vibratory motions of a beam. One set treats beams with axially fixed ends; the other concerns beams free of axial constraints. The linear parts of the beam equation in both cases are the Timoshenko type, while the nonlinear terms are triple product of the first and second derivatives of the displacement variables.

For practical purposes, the nonlinear terms may be regarded as small quantities; thus, an approximate solution in the form of a power series is developed based on Krylov-Bogoliunov's principle by using the linear solution as a generating function: Two illustrative problems, a simple supported beam and a free-free beam, are presented with numerical examples to show the variation of the undamped frequency with respect to amplitude of vibration.

LIST OF SYMBOLS

| Symbol | Definition |
|--------|--------------------------------------------------------|
| A_o | dimensionless amplitude of Y_o |
| a | $= k'G/E$ |
| a' | $= 1/a$ |
| b^2 | $= EI/\rho AL^2$ |
| A | cross sectional area of beam |
| E | modulus of elasticity |
| G | modulus of shear |
| h_i | unknown constants, equation (6) |
| I | bending moment of inertia of beam |
| k' | shear coefficient |
| L | length of half-length of beam or differential operator |

| | |
|----------|------------------------------------------------------------------------------------------------------|
| p^2 | $= \frac{1}{2} \left[(a' + 1)\beta\omega^2 + \sqrt{(a' + 1)^2\beta^2\omega^2 + 4\omega^2} \right]$ |
| q^2 | $= \frac{1}{2} \left[-(a' + 1)\beta\omega^2 + \sqrt{(a' - 1)^2\beta^2\omega^2 + 4\omega^2} \right]$ |
| s | dimensionless time variable ($=bt$) |
| t | time variable |
| T_N | nonlinear period of vibration |
| T_o | linear period of vibration |
| U | dimensionless longitudinal displacement ($=u/L$) |
| x | coordinate along beam |
| Y | dimensionless deflection ($=y/L$) |
| Z | dimensionless transverse displacement due to shear ($=y_q/L$) |
| z | $= x/L$ |
| β | $= I/AL^2$ |
| β' | $= (1 + a')\beta$ |
| ρ | mass density of beam |

Subscripts "z" and "s" are partial derivatives.

I. INTRODUCTION

In dealing with dynamic control problems of a space vehicle to external disturbances in flight, it is often required to know the precise natural frequency of the vehicle. It is well known that the natural frequency of an elastic body varies with its amplitude of vibration; however, there have been few analytical results published. This phenomenon has little significance when the amplitude is small. It is usually referred to as linear vibration and the frequency is regarded as constant.

The nonlinearity in transverse vibration of a uniform beam is mainly caused by one of three factors:

(1) large curvature of bending, (2) longitudinal extension of the beam, and (3) large deflection and longitudinal strain. In deriving the nonlinear differential equation of beam vibration, it is desirable to reduce the number of variables to minimum, since the complication of a nonlinear problem increases rapidly with the number of dependent variables. Consequently, the author proposes that the nonlinear vibration of beams be treated individually according to its cause of nonlinearity.

In this analysis, beam vibrations with large amplitude fall into two categories according to their boundary conditions:

(1) Beam With Axially Fixed Ends:

For beam with two ends fixed axially, the longitudinal stress caused by the large transverse displacement becomes an important factor of the nonlinear vibration. In Ref. 1, the Lagrangian method is used to obtain a system of differential equations in two dependent variables: the transverse and longitudinal displacement. The nonlinear terms in the differential equations are a result from the nonlinear strain

$\epsilon_x = \frac{\partial u}{\partial x} + \frac{1}{2} \left(\frac{\partial y}{\partial x} \right)^2$ used in the strain energy expression.

(2) Beam Free From Axial Constraints:

The longitudinal stress due to the transverse displacement in this case is very small compared with the bending and shear stresses. A system of differential equations of the transverse displacement and displacement due to shear is formulated based on dynamic equilibrium.

The linear parts of the beams equation of both cases are of the Timoshenko type, i.e., rotary and shear effect are included, and the nonlinear terms are of triple products of the first and second derivatives of the variables. Difference methods are generally employed for numerical solution of partial differential equations of second order. There has been no systematic scheme, to the author's knowledge, developed for the approximate solution of nonlinear partial differential equations for higher order. A few papers dealing with special nonlinear beam vibration problems have been found [5 through 8]; however, these methods are not completely general.

In solving nonlinear ordinary differential equations, Krylov-Bogoliubov [3,4] has employed the linear solution as generating function in expanding the

dependent as well as independent variables in power series of a small parameter. For practical purposes, the nonlinear terms in the nonlinear beam equations can be regarded as small quantity; by the same token, the approximate solution may be considered as the linear solution plus some functions with a small parameter as their coefficients. Based on this principle, the present method is developed.

II. EQUATION OF MOTION

The equations of vibration of a uniform beam with large amplitude have been derived in Ref. 1 for two cases. In Case I the beam is treated free to move longitudinally. Consideration of dynamic equilibrium of a beam element results in partial differential equations with the transverse displacement and the displacement due to shear as unknown variables. The beam is restrained axially at two ends of Case II. The longitudinal and transverse displacement are taken as unknown variables of the partial differential equations which are obtained by using Lagrangian equations. The detail of the derivation of these equations is given in Ref. 1; here, we simply present these equations in their final nondimensional form.

Case I. Beam With No Axial Constraints

$$L(Y) = \mu F = M(H_1) \quad (1a)$$

$$H_1 = Y_z^2 \left[a Z_{zz} - (3\beta/2) Y_{ss} \right] - a Y_z Y_{zz} Z_z, \quad (1b)$$

$$Z_{zzz} - \beta Z_{zss} - (a/\beta) Z_z = - Y_{zss} + Y_{zzz}. \quad (1c)$$

Case II. Beam With Axial Constraints

$$L(Y) = \mu F = M(H_2) \quad (2a)$$

$$H_2 = \left(U_z Y_z + \frac{1}{2} Y_z^3 \right) \quad (2b)$$

$$U_{zz} = \beta U_{ss} = - Y_z Y_{zz}, \quad (2c)$$

In the above equations, the subscripts z and s denote partial derivatives with respect to the nondimensional spatial and time variables, respectively; L and M are partial differential operator defined as follows:

$$L = \frac{\partial^4}{\partial z^4} - \beta' \frac{\partial^4}{\partial z^2 \partial s^2} + \frac{\partial^2}{\partial s^2} + a' \beta^2 \frac{\partial^4}{\partial s^4}$$

$$M = 1/\beta - a' \left(\frac{\partial^2}{\partial z^2} - \frac{\partial^2}{\partial s^2} \right) \quad (3)$$

Notice that the differential equation, $L(Y) = 0$, is a Timoshenko beam equation, and the terms μF on the right-hand side of equations (1a) and (2a) are the nonlinear functions.

III. METHOD OF SOLUTION

The method of solution proposed here is based on the assumption that the beam equations are slightly nonlinear; in other words, the nonlinear function is a small quantity. Hence, we may extend Krylov-Bogoliubov's principle [3] for ordinary differential equations to the beam equation and use the linear solution as a generating function. First, we expand both the dependent variables and the independent time variable in a power series in terms of a small quantity μ ,

$$Y = Y_0 + \mu Y_1 + \mu^2 Y_2 + \dots \quad (4)$$

$$W = W_0 + \mu W_1 + \mu^2 W_2 + \dots \quad (5)$$

$$s = \frac{\tau}{\omega} (1 + \mu h_1 + \mu^2 h_2 + \dots), \quad (6)$$

where W represents either Z of equation (1c) or U of (2c), Y_i and W_i are unknown functions, and h_i ($i = 1, \dots$) are unknown constants.

Substitution from equations (4) through (6) into (1a) and (2a) results in

$$\begin{aligned} & (1 + \mu h_1 + \dots)^4 (Y_0 + \mu Y_1 + \dots)_{zzzz} \\ & - \beta' \omega^2 (1 + \mu h_1 + \dots)^2 \frac{\partial^2}{\partial \tau^2} (Y_0 + \mu Y_1 + \dots)_{zz} \\ & + \omega^2 (1 + \mu h_1 + \dots)^2 \frac{\partial^2}{\partial \tau^2} (Y_0 + \mu Y_1 + \dots) \\ & + a' \beta^2 \omega^4 \frac{\partial^4}{\partial \tau^4} (Y_0 + \mu Y_1 + \dots) \\ & = (1 + \mu h_1 + \dots)^4 \mu F [(Y_0 + \mu Y_1 + \dots), (W_0 + \\ & + \mu W_1 + \dots)]. \end{aligned} \quad (7)$$

Collecting the terms with the same power of μ and equating them to zero, we obtain from the above equation

$$\mu^0: L[Y_0] = 0 \quad (8a)$$

$$\begin{aligned} \mu^1: L[Y_1] = & -2h_1 (2Y_0_{zzzz} - \beta' \omega^2 Y_{0zz\tau\tau} + \\ & + \omega^2 Y_{0\tau\tau}) + F_1(Y_0, W_0) \end{aligned} \quad (8b)$$

$$\begin{aligned} \mu^2: L[Y_2] = & -[4h_1 Y_1 + 2(2h_2' + 3h_1^2) \dot{Y}_0]_{zzzz} \\ & + \beta' \omega^2 [2h_1 Y_1 + (2h_2 + h_1^2) Y_0]_{zz} \\ & - \omega^2 [2h_1 Y_1 + (2h_2 + h_1^2) Y_0]_{\tau\tau} \\ & + F_2(Y_0, Y_1, W_0, W_1, h_1), \end{aligned} \quad (8c)$$

.....

where the F 's are the results of the expansion of the nonlinear function μF ,

$$\begin{aligned} \mu F [(Y_0 + \mu Y_1 + \dots), (W_0 + \mu W_1 + \dots)] (1 + \mu h_1 \\ + \dots) = & \mu F_1(Y_0, W_0) + \mu^2 F_2(Y_0, Y_1, W_0, W_1, h_1) \\ & + \dots \end{aligned} \quad (9)$$

Solution of the linear differential equation (8a) for various boundary conditions may be found in Ref. 2. Using the linear solution for Y_0 , the approximate solution of the second variable Z or U can be readily obtained from the following equations,

$$\begin{aligned} (Z_1)_{zzz} - \beta (Z_1)_{zss} - (a/\beta) (Z_1)_z = & -\beta (Y_1)_{zss} + \\ (Y_1)_{zzz} \end{aligned} \quad (10)$$

$i = 1, 2, \dots$

$$(U_0)_{zz} - \beta (U_0)_{ss} = - (Y_0)_z (Y_0)_{zz} \quad (11a)$$

$$(U_1)_{zz} - \beta (U_1)_{ss} = - (Y_0)_z (Y_1)_{zz} - (Y_1)_z (Y_0)_{zz} \quad (11b)$$

.....

Since the effect of the homogeneous solution of the second variable to the transverse vibration, Y , has little physical significance, it may be neglected for simplicity.

Now, the terms on the right-hand side of equation (8b) are known from the solution of equations (8a) and (10) or (11a). Since the left-hand sides of equations (8a) and (8b) are identical, the natural frequency of Y_1 , i.e., the frequency of the homogeneous equations (8b), and the frequency of Y_0 are equal. The condition for Y_1 to have a periodic solution is that the secular terms on the right-hand side of equation (8b)

must vanish. Apparently, this condition cannot be satisfied for all values of z . Letting this condition be satisfied for the fundamental mode only should yield a useful approximation and permits the constant h_1 to be determined. Hence,

$$h_1 = \frac{\int_0^1 \int_0^{2\pi} F_1(Y_0, W_0) \cos \tau \eta_0(z) d\tau dz}{2 \int_0^1 \int_0^{2\pi} (2Y_{0zzzz} - \beta' \omega^2 Y_{0zz\tau\tau} + \omega^2 Y_{0\tau\tau}) \cos \tau \eta_0(z) d\tau dz} \quad (12)$$

Next, solving for Y_1 from equation (8b) with consideration of equation (12), we find

$$Y_1 = A_1 \cos \tau + Y_{1p}, \quad (13)$$

and in turn we solve for the second variable W_1 . In the above equation, Y_{1p} is a particular solution of equation (8b), and the arbitrary constant A_1 and the unknown constant h_2 are to be determined from equation (8c) by letting the secular terms of both the first and second harmonic vanish simultaneously.

The amount of work necessary to carry out higher approximation is greatly increased; however, the first approximation is quite adequate for engineering purposes. The nonlinear period of vibration is

$$T_N = \frac{2\pi}{\omega} (1 + \mu h_1 + \mu^2 h_2 + \dots) \quad (14)$$

IV. EXAMPLES

A. SIMPLY SUPPORTED BEAM WITH SYMMETRIC MODE

Considering a simply supported beam with the two end supports being fixed axially, we apply the system of differential equations given by (2). The linear solution found in Reference 2 is

$$Y_0 = A_0 \cos pz \cos \tau. \quad (15)$$

Using this solution and the boundary conditions $U_0 = 0$, when $z = 0$ and 1 , the solution of equation (11a) is obtained:

$$U_0 = \frac{p^3 A_0^2}{8(p^2 - \beta \omega^2)} \sin 2pz \cos^2 \tau. \quad (16)$$

Note that (1) this solution is not exact - it is off by a constant term and (2) the homogeneous solution

which represents the longitudinal traveling stress is omitted.

Substituting Y_0 and U_0 from equations (15) and (16) into equations (2b) and (9) results in

$$\mu F = \mu \sum_{m,n=1,3} f_{mn} \cos npz \cos m\tau, \quad (17)$$

where

$$f_{mn} = -\frac{3n}{m} (1/\beta + n^2 a' p^2 - m^2 a' \beta \omega^2) \left[(3-n)p^2 + \frac{3(n-2)}{n} \beta \omega^2 \right]$$

$$\mu = A_0^3 p^4 / 32 (p^2 - \beta \omega^2).$$

Consequently, equation (8b) becomes

$$L[Y_1] = -2h_1 (2p^4 - \beta' \omega^2 p^2 - \omega^2) A_0 \cos pz \cos \tau + \sum_{m,n=1,3} f_{mn} \cos npz \cos m\tau. \quad (18)$$

From the condition of periodicity of the solution Y_1 that the coefficient of $\cos \tau$ must vanish, we have, by neglecting $\cos 3pz$,

$$h_1 = -\frac{3(1/\beta + a' p^2 - a' \beta \omega^2) (2p^2 - 3\beta \omega^2)}{2(2p^4 - \beta' \omega^2 p^2 - \omega^2) A_0} \quad (19)$$

Now, the solution for Y_1 from equations (18) and (19) is

$$Y_1 = A_1 \cos pz \cos \tau + \sum_{n=1,3} C_n \cos npz \cos 3\tau \quad (20)$$

$$C_n = f_{3n} / (n^4 p^4 - 9n^2 \beta' \omega^2 p^2 - 9\omega^2 + 81a' \beta' \omega^4).$$

The arbitrary constant A_1 and unknown constant h_2 may be determined from the second approximation which will not be given here.

Numerical Results

To show the magnitude of β , we consider beams of the following:

- a. Solid cylindrical beam with $D/L = 1/10$ (D = diameter)

$$\beta = I/AL^2 = (D/4L)^2 = 1/1600.$$

b. Thin hollow cylindrical beam (neglect shell effect), $D/L = 1/10$

$$\beta = 2(D/4L)^2 = 1/800.$$

T_N/T_O vs A_O

| A_O | $\beta = 1/1600$ | $\beta = 1/800$ |
|-------|------------------|-----------------|
| 1/100 | 1 - .015 | 1 - .0075 |
| 1/50 | 1 - .06 | 1 - .03 |
| 1/25 | 1 - .18 | 1 - .12 |

Note that A_O is the ratio of amplitude to half length of the beam.

B. FREE-FREE BEAM WITH SYMMETRIC MODE

Since the ends of a free-free beam are free of shear force and bending moment which can be expressed conveniently by the variables Y and Z , we use the system of differential equations given by (1). The mode function for symmetric mode given by Ref. 2 is

$$Y_O = \eta_O \cos \tau \quad (21)$$

$$\eta_O(z) = A_O (q \sin p \operatorname{ch} qz - p \operatorname{sh} q \cos pz) / a_O$$

$$a_O = (q \sin p \operatorname{ch} q - p \operatorname{sh} q \cos p) - (q \sin p - p \operatorname{sh} q).$$

As a result of equation (21) the solution for Z_O found from equation (10) is

$$Z_O = A_O (b_1 \operatorname{ch} qz + b_2 \cos pz) \cos \tau, \quad (22)$$

where

$$b_1 = q(\beta\omega^2 + q^2) \sin p / (q^2 + \beta\omega^2 - a/\beta) a_O$$

$$b_2 = p(\beta\omega^2 - p^2) \operatorname{sh} q / (p^2 - \beta\omega^2 + a/\beta) a_O.$$

The homogeneous solution of Z_O is omitted.

To obtain the nonlinear function, we substitute equations (21) and (22) into equations (2b) and (9), then expand in series by eigenfunction expansion and take only the fundamental mode,

$$\mu F = -M(H_O) = (K_1 \cos \tau + K_3 \cos 3\tau) \eta_O(z), \quad (23)$$

where

$$K_m = -\frac{3R}{4} \int_0^1 [(1/m\beta - ma'\beta\omega^2) H_O - \frac{a'}{m} H_{OZZ}] \eta_O(z) dz \quad (24)$$

$$m = 1, 3$$

$$R = \frac{1}{\int_0^1 \eta_O^2(z) dz}$$

$$\begin{aligned} H_O(z) &= -\eta_{Oz}^2 (a \zeta_{OZZ} + \frac{3}{2} \beta\omega^2 \eta_O) + a \eta_{Oz} \eta_{OZZ} \zeta_{Oz} \\ &= a(a_1 b_2 - a_2 b_1) [\operatorname{sh} qz \sin pz (a_1 q^2 \operatorname{ch} qz + a_2 p^2 \cos pz) \\ &\quad - p q (\operatorname{sh}^2 qz \cos pz + \operatorname{ch} qz \sin^2 pz)] + \\ &\quad + \frac{3}{2} \beta\omega^2 (a_1 q \operatorname{sh} qz - a_2 p \sin pz)^2. \end{aligned}$$

$$a_1 = A_O q \sin p \quad a_2 = A_O p \operatorname{sh} q.$$

Similarly, it follows from equation (12), that

$$h_1 = K_1 / 2R \int_0^1 (2\eta_{OZZZZ} + \beta'\omega^2 \eta_{OZZ} - \omega^2 \eta_O) \eta_O dz.$$

This results in

$$L[Y_1] = K_3 \eta_O(z) \cos 3\tau. \quad (25)$$

The solution for Y_1 may be readily written in the form

$$Y_1 = A_1 \eta_O(z) \cos \tau + K_3 (B_1 \operatorname{ch} qz + B_2 \cos pz) \cos 3\tau, \quad (26)$$

where A_1 is an unknown constant and

$$B_1 = \frac{1}{[q^4 + 9\beta'\omega^2 q^2 - 9\omega^2(1 - a'\beta^2\omega^2)]}$$

$$B_2 = \frac{1}{[p^4 - 9\beta'\omega^2 p^2 - 9\omega^2(1 - a'\beta^2\omega^2)]}.$$

The unknown constants A_1 and h_2 can be determined from equation (8c).

The change of frequency of a free-free beam is much smaller than that of a simply supported beam. For $\beta = 1/800$, the values of T_N/T_O vs A_O are as follows:

$$A_O = 1/10 \quad T_N/T_O = 1 - .0019$$

$$A_O = 1/5 \quad T_N/T_O = 1 - .0075$$

REFERENCES

1. Liu, Frank C., "Nonlinear Vibration of Beams," R-AERO-IN-2-64, MSFC, NASA, Huntsville, Alabama, 1964.
2. Traill-Nash, R. W. and A. R. Collar, "The Effects of Shear Flexibility and Rotary Inertia on the Bending Vibrations of Beams," Q. J. Mech. Appl. Math., Vol. VI, Pt. 2, 1953, pp. 186-222.
3. Minorsky, N., "Nonlinear Oscillations," D. Van Nostrand, N. Y., 1962.
4. Bogoliubov, N. N. and Y. A. Mitropolsky, "Asymptotic Methods in the Theory of Nonlinear Oscillations," Translated from Russian, Gordon and Breach, N. Y., 1961.
5. Carrier, G. H., "On the Nonlinear Vibration Problem of the Elastic String," Q. Appl. Math., Vol. III, 1954, pp. 157-165.
6. Eringen, A. C., "On the Nonlinear Vibration of Elastic Bars," Q. Appl. Math., Vol. IX, 1947, pp. 361-369.
7. McDonald, P. H., "Nonlinear Dynamic Coupling in a Beam," J. Appl. Mech., December 1955, pp. 573-576.
8. Pisarenko, G. S., "Vibrations of Elastic Systems Taking Account of Energy Dissipation in the Material," WADD TR60-582, February 1962.
9. Davis, H. T., "Introduction to Nonlinear Differential and Integral Equations," U.S. AEC, 1960, pp. 133, 207.

by

Robert E. Lavender

SUMMARY

N65 4134

Results are presented from five brief investigations which have been conducted concerning lunar touchdown dynamics. These investigations concern the use of a rocket motor to achieve a stable touchdown, effect of elasticity on touchdown stability, comparison of MSFC results with Grumman Aircraft Engineering Corporation (GAEC) analytical results, landing dynamics for a cryogenic landing stage, and comparison of MSFC results with GAEC scale model drop tests.

LIST OF SYMBOLS

| Symbol | Definition |
|----------|--------------------------------------------------------------------------------------------------|
| C_m | Crushing force of main strut |
| C_s | Crushing force of support strut |
| D | Landing gear diameter |
| k | Radius of gyration about c.g. |
| k_e | Effective spring constant per leg parallel to vehicle's longitudinal axis |
| L_2 | Original height of center of gravity |
| $L.F.$ | Load factor; total external force divided by earth weight for vertical landing on level surface. |
| N | Number of legs |
| T | Stabilization rocket motor thrust |
| t_b | Stabilization rocket motor burning time |
| V_v | Vertical velocity |
| V_h | Horizontal velocity |
| V_r | Rebound velocity from a vertical landing |
| W_e | Earth weight (based on $g_e = 9.80665 \text{ m/s}^2$) |
| δ | Stroke parallel to vehicle's longitudinal axis |

| | |
|----------------|--------------------------------------------|
| θ | Lunar slope, negative for downhill landing |
| ϕ_0 | Initial pitch attitude, positive nose up |
| $\dot{\phi}_0$ | Initial pitch angular rate |
| μ | Coefficient of friction |

I. INTRODUCTION

In August, 1962, the George C. Marshall Space Flight Center began a study of a Lunar Logistic System (LLS) based on the Saturn V launch vehicle. This system was designed to "soft-land" large payloads on the moon. Results of the study included a volume on the touchdown dynamics aspects of the system (Ref. 1). The system was designed to land safely on lunar slopes up to 30 degrees, but unfortunately, the landing gear required under such a condition was large and heavy. The results of Ref. 1 have been extended to include vehicles with from three to six legs and various deceleration load factors. These results, along with a description of the mathematical model, are presented in Ref. 2.

While the method of Ref. 2 accounts for crushing and sliding, it does not consider the effects of elasticity in the vehicle's structure or the fact that the legs are hinged to the vehicle resulting in a variable landing gear diameter during the touchdown motion. A mathematical model including these effects is described in Ref. 3. The author is indebted to John D. Capps, Computation Laboratory, who has programmed both methods for digital computation.

The purpose of the present paper is to present results of additional investigations made recently in the field of lunar touchdown dynamics.

II. DISCUSSION

A. USE OF STABILIZATION ROCKET MOTOR TO OBTAIN STABLE TOUCHDOWN

The purpose of this investigation is to obtain additional information on stabilization rocket motor

requirements necessary to obtain a stable touchdown. Ref. 2 shows that use of a stabilization rocket motor is very effective in providing a stable touchdown. Results of Fig. 9, Ref. 2, correspond to a particular landing gear diameter and initial velocity components. This investigation provides the rocket motor requirements as a function of the landing gear diameter for several values of initial horizontal velocity.

The investigation was conducted for a four-legged spacecraft landing on a 30-degree lunar slope with a horizontal velocity component in the downhill direction. The vehicle impacts on two uphill legs, goes into free flight, and then impacts on two downhill legs. A stabilization rocket motor is assumed mounted on top of the payload and directed downward through the vehicle's center of gravity. The motor ignites when the downhill legs contact the lunar surface. The same results would be obtained for a number of smaller rockets mounted around the vehicle equidistant from the center of gravity. The vehicle's attitude angle at touchdown is considered to be less than the lunar slope so that the first legs to sense contact will be the uphill legs.

For any given landing gear diameter, there is a minimum thrust below which the vehicle's center of gravity will rotate over the downhill feet. This minimum thrust is shown in Fig. 1 as a function of the landing gear diameter for two values of the horizontal

velocity. The corresponding burning time, also shown, is essentially independent of the horizontal velocity for the two values considered. The thrust given in Fig. 1 will reverse the vehicle's sense of rotation just as the center of gravity becomes vertical above the point of rotation. A higher thrust motor of constant total impulse would be somewhat better from a touchdown stability standpoint. However, extremely high thrust motors of very short burning time may present motor development problems.

For a horizontal velocity of 2 m/s, a landing gear diameter to center-of-gravity height ratio of 3.51 is needed without any stabilization rocket motor. Using a thrust equal to the vehicle's earth weight, this ratio is reduced to 2.26 resulting in a landing gear diameter which is only 64.4 per cent as large. Some additional reduction in landing gear diameter is obtained by using higher thrust motors. For large logistics vehicles, which are designed to land on steep lunar slopes, use of a stabilization rocket motor appears to be useful in reducing the required landing gear diameter. These results were obtained using the method described in Ref. 2 which does not consider elasticity effects. Additional study of the concept of stabilization rocket motors in conjunction with the vehicle's elastic characteristics would be profitable.

B. EFFECTS OF ELASTICITY ON TOUCHDOWN STABILITY DURING LUNAR LANDING

After the MSFC Lunar Logistics System Study was completed, the Space Technology Laboratories was awarded a contract, NAS8-11022, titled, "Comparative Design Study of Modular Stage Concepts for Lunar Supply Operations." Results of the touchdown dynamics portion of the study are included in Ref. 4. Results of their analyses indicate that the effect of elasticity is very important, increasing the required landing gear diameter about 30 per cent compared to that of Ref. 2. The method of analysis used by STL accounts for the elasticity in the structure, but does not consider the legs to be hinged, resulting in a variable landing gear diameter during touchdown motion.

The purpose of this investigation is to determine the effect of elasticity on touchdown stability for a basic case using the method of Ref. 3. The discussion is restricted to the following conditions:

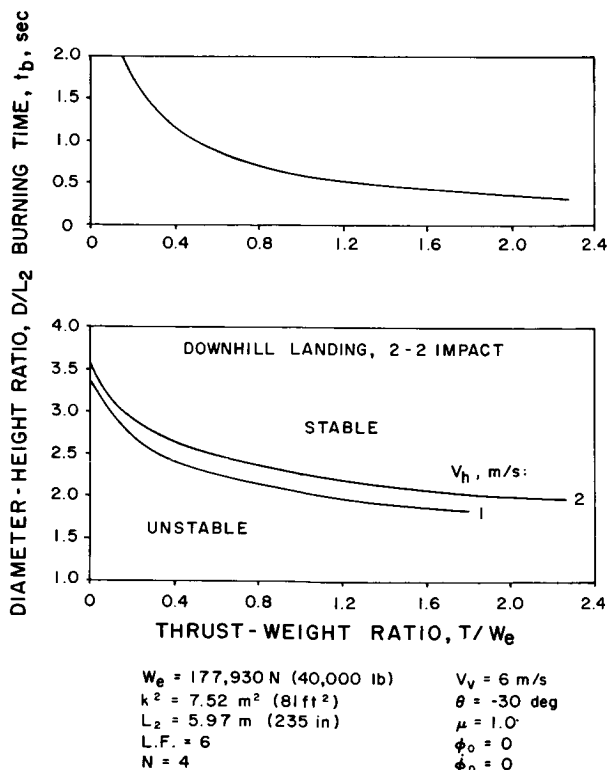


FIGURE 1. STABILIZATION ROCKET MOTOR REQUIREMENTS

$$W_e = 177,930 \text{ N (40,000 lb)}$$

$$k^2 = 7.52 \text{ m}^2 (81 \text{ ft}^2)$$

$$L_2 = 6.32 \text{ m (249 in)}$$

$$N = 4$$

$$D = 20.17 \text{ m (794 in)}$$

$$L.F. = 3$$

$$V_v = 6 \text{ m/s}$$

$$V_h = 1 \text{ m/s}$$

$$\mu = 1.0$$

For these conditions, the vehicle had been found to be stable (Ref. 2) for lunar slopes up to 30 degrees. Landing is in the downhill direction with a 2-2 impact.

Results of the investigation using the method of Ref. 3 indicate that the combined effect of elasticity and hinged legs is compensating to the extent that only about 5 per cent increase in landing gear diameter is required over the results from Ref. 2. Using an effective vertical spring constant of 2.452 MN/m (14,000 lb/in), the vehicle is still stable for lunar slopes up to 27.8 degrees. Increasing the landing gear diameter to 22.35 m (880 in) provides stability up to 32.6 degrees. Therefore, a diameter of about 21.13 m (832 in) will provide stability on slopes up to 30 degrees. This diameter is only 4.8 per cent larger than the results from Ref. 2.

C. COMPARISON OF MSFC AND GAEC TOUCHDOWN STABILITY ANALYTICAL RESULTS

This investigation compares some results of touchdown stability obtained by the Grumman Aircraft Engineering Corp. (Ref. 5) with results using an MSFC program (Ref. 3). Such comparisons serve to indicate the extent of agreement or disagreement between different approaches to the touchdown dynamics problem. Results presented in Ref. 5 include stability boundaries for a series of configurations with various landing gear diameters, height of the center of gravity, and number of legs. Results using Ref. 3 have been obtained for only one configuration. The configuration chosen for comparison has the following characteristics:

$$W_e = 44,482 \text{ N (10,000 lb)}$$

$$k^2 = 2.69 \text{ m}^2 (28.95 \text{ ft}^2)$$

$$L_2 = 3.30 \text{ m (130 in)}$$

$$D = 8.84 \text{ m (348 in)}$$

$$N = 4.$$

The load factor, in earth g's, experienced upon landing vertically on a level surface depends upon the coefficient of friction between the foot pads and lunar surface. For the configuration chosen, GAEC shows the load factor to vary from 5.6 for zero friction to 16.4 for a coefficient of friction of 1.0. The maximum load factor is obtained when both upper and lower leg members are stroking in compression.

Values were chosen for the crushing strength of the honeycomb crushable material in the upper and lower leg members of the two-dimensional model of Ref. 3 such that the load factors given in the above paragraph were obtained. In addition, it was assumed that the upper and lower leg members of the two-dimensional model have elastic deflection of one inch before crushing takes place.

During a symmetrical landing (vertical landing on a level surface) with zero friction, the foot pads slide outward with the upper leg members in compression and the lower leg members in tension. The vertical stroke (parallel to the vehicle's centerline), which exists at the moment crushing begins, together with the normal force acting on the foot pads, determines the effective vertical spring constant for each leg. When the vertical landing velocity is reduced to zero, the foot pads begin to slide inward reducing the compression load in the upper leg members and the tension load of the lower members. The vehicle begins a rebound motion and lifts off the surface as the normal force on each foot pad reduces to zero. During a symmetrical landing with high friction, the foot pads remain stationary with both upper and lower leg members compressing elastically until the crushing strengths of the honeycomb material are reached. The vehicle rebounds as the elastic energy stored in compression is released.

Results of the symmetrical landing analysis are shown in Fig. 2. The load factor and effective vertical spring constant vary in such a way that the vertical elastic stroke varies from 0.069 m (2.7 in) for zero friction to 0.033 m (1.3 in) for high friction. The corresponding total vertical stroke is shown to vary from 0.775 m (30.5 in) to 0.292 m (11.5 in). It is interesting to observe that the velocity with which the vehicle rebounds into free flight decreases as the coefficient of friction increases, until the friction is sufficient to keep the feet from sliding. The rebound velocity at high friction (no sliding) is larger than that at zero friction because the energy stored in elastic deflection is larger.

Results of the downhill landing analysis are shown in Fig. 3. The vehicle initially contacts the lunar

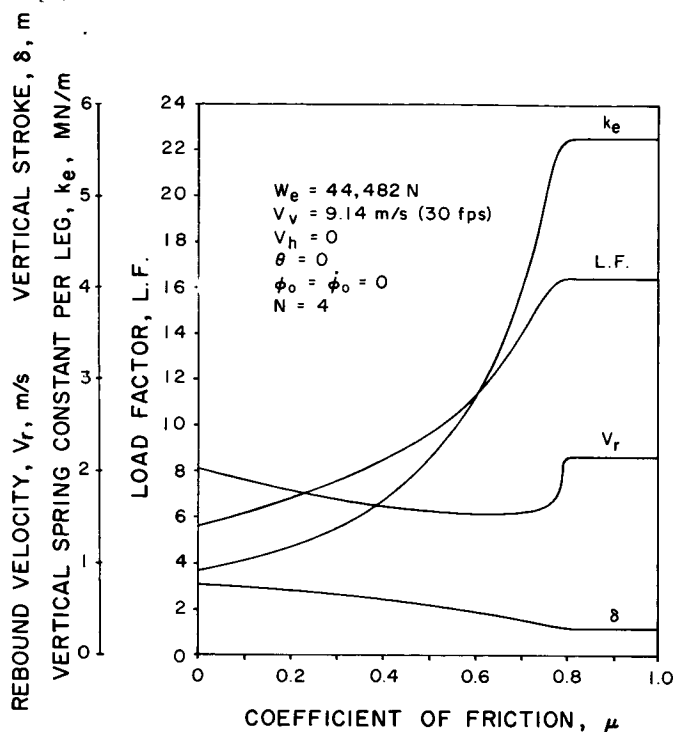


FIGURE 2. SYMMETRICAL LANDING RESULTS

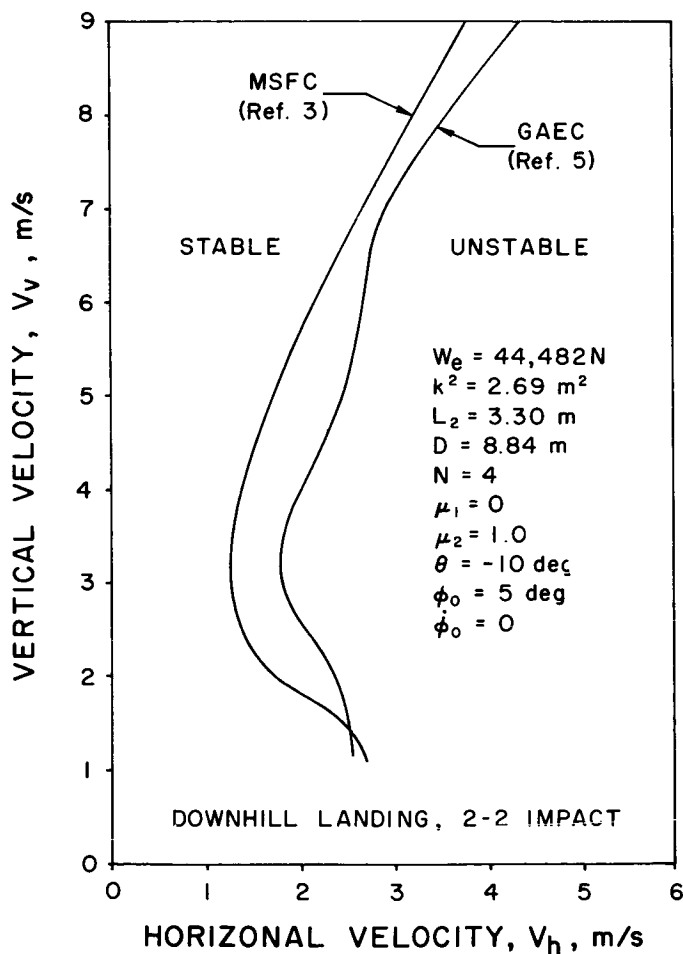


FIGURE 3. STABILITY BOUNDARY FOR DOWNHILL LANDING

surface on two feet with an initial attitude of 5 degrees nose up. The vehicle then rotates over and goes into free flight. Zero friction is assumed for the uphill contact since GAEC (Ref. 5) states that this results in maximum initial overturning moment. Actually, for low vertical velocity and high horizontal velocity combinations, the uphill feet drag downhill so that friction would result in higher initial overturning moment. High friction is assumed for the downhill contact so that no sliding occurs. Comparison of the stability boundaries shows that the MSFC result is somewhat more pessimistic. This may be due to the MSFC assumption regarding the elastic properties for the landing gear. It is not too clear from Ref. 5 what GAEC assumed for the elastic characteristics. However, general agreement is shown between the two methods.

D. TOUCHDOWN DYNAMICS FOR CRYOGENIC LANDING STAGE

Touchdown dynamics analysis has been performed to establish stability boundaries for configurations in the size and weight class for a cryogenic landing stage which has been under recent study. Results of the analysis can be used to estimate the landing gear diameter required for stable touchdown as influenced by the height of the center of gravity and the elasticity in the vehicle. A load factor of 4 was assumed for the case of a level landing on all four legs simultaneously.

The analysis was based upon a downhill landing with a 2-2 impact. Walton, Herr, and Leonard (Ref. 6) have presented, however, both experimental and analytical evidence that the 2-2 impact orientation is not the most critical orientation. The experimental evidence was obtained by dropping a block of aluminum vertically (no horizontal velocity) upon an inclined surface. The same general trend has also been established by the Bendix Corporation from drop tests with a dynamically scaled model (Ref. 7). However, further drop tests by Bendix with a horizontal velocity in the direction of maximum slope show that the most critical landing obtained is the 2-2 impact with maximum horizontal velocity. Additional drop tests are planned which will obtain the effect of cross-slope velocity. The writer is indebted to B. T. Howard and T. L. Powers of Bellcomm for the Bendix data.

Results of the analysis for the cryogenic landing stage using the method described in Ref. 2 are shown in Fig. 4. The vehicle did not go into free flight whenever crushing stopped in the uphill legs for most of these cases. Rather, the vehicle rotated as a rigid body until the downhill legs made contact and began crushing. After the downhill legs stopped crushing, the vehicle rotated as a rigid body until it became unstable or until the rotation was reversed and a stable touchdown achieved. High friction was assumed

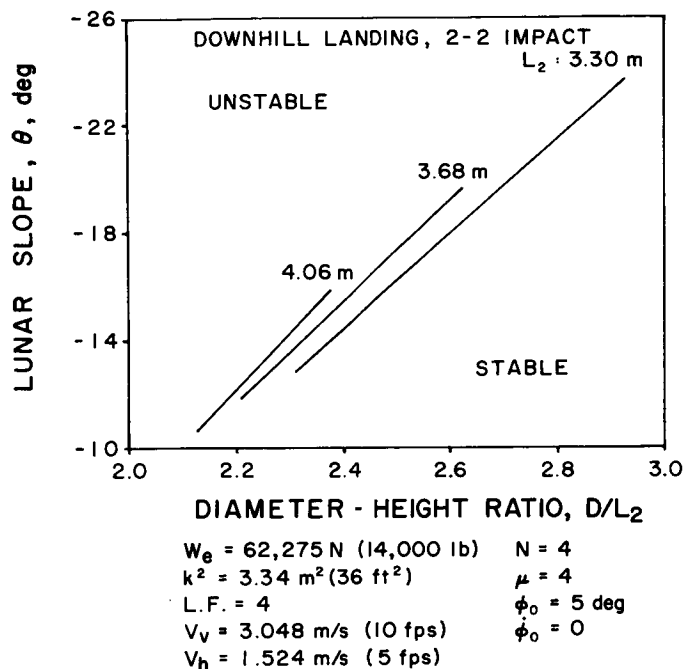


FIGURE 4. DIAMETER-HEIGHT RATIO VERSUS LUNAR SLOPE

between the pads and lunar surface resulting in essentially no pad motion. For any given lunar slope, the required landing gear diameter increases with increasing height of the center of gravity, but the ratio of diameter to height decreases.

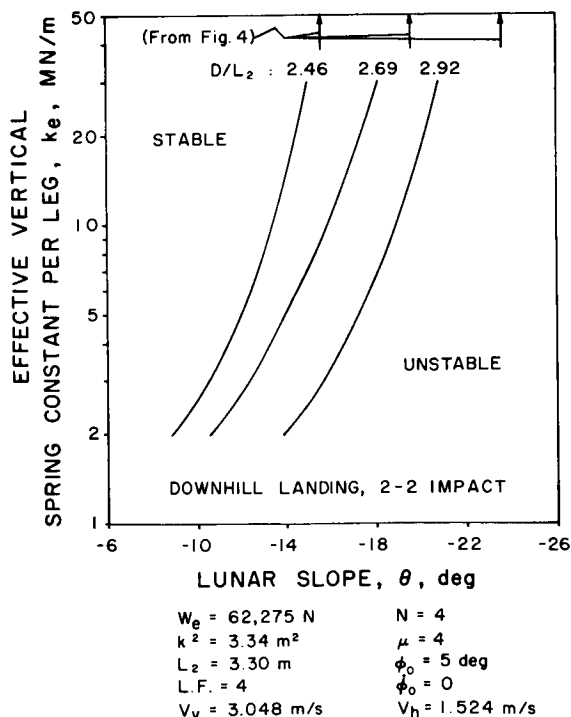


FIGURE 5. EFFECT OF ELASTICITY ON TOUCH-DOWN STABILITY

For a particular height of the center of gravity (3.30 m, 130 in), the effect of elasticity in the vehicle's structure has been obtained for three landing gear diameters. Results are shown in Fig. 5 and were obtained by the method of Ref. 3. The arrows shown correspond to data from Fig. 4 which assumes essentially an infinite spring constant. The lunar slope for a stable touchdown decreases as the effective vertical spring constant decreases.

An important consideration in the application of the method described in Ref. 3 which does not occur for the method of Ref. 2 is the question of the crushing force of the support struts. For Fig. 5, as the vehicle impacts on the downhill legs, both main and support struts crush after some elastic deflection. The crushing forces in these struts have been chosen so that the reaction force on each pad in the plane of motion tangent to the surface is about 0.7 times the force normal to the surface. This selection of crushing loads is merely a choice and does not represent the optimum solution.

Using this method the vehicle did not rotate as a rigid body about the uphill legs after crushing ceased, but rather sprang into free flight. In the same manner, there was no rotation about the downhill legs as a rigid body after crushing ceased. The vehicle sprang back into free flight from the downhill legs. A considerable number of bounces can take place on the downhill legs before the vehicle either tumbles or a stable touchdown assured.

As seen from Figure 5, there is serious loss in stability as the spring constant is reduced. For example, the method of Ref. 2 indicates that with a diameter-to-height ratio of 2.46 the vehicle is stable for slopes up to 15.6 degrees. However, to achieve this same capability using an effective vertical spring constant of 3 MN/m (17,130 lb/in) requires a diameter-to-height ratio of 2.92. This corresponds to an increase in the required landing gear diameter of 18.7 per cent. This effect has been found to be less severe for the Lunar Logistic System where only about 5 per cent increase in diameter was indicated, as discussed in Part B. It is worth noting that the larger vehicle (LLS) landing on a 30-degree slope went into free flight from the uphill legs using either method of analysis and also that a coefficient of friction of 1.0 was assumed with no crushing of the support struts. Therefore, as the vehicle crushed on the downhill legs, the overturning radius increased during the motion. Finally, a word of explanation is offered for the odd values of diameter-to-height ratio shown in Figure 5. These curves were originally obtained for landing gear diameters of 320, 350, and 380 inches with a center-of gravity height of 130 inches.

E. COMPARISON OF MSFC TOUCHDOWN STABILITY ANALYTICAL RESULTS WITH GAEC DROP TESTS

The purpose of this investigation is to compare MSFC analytical results with GAEC scale model drop test results. The writer is indebted to Harold Benson, MSC, for a copy of the GAEC results (Ref. 8). The drop tests correspond to a one-sixth scale model of an early four-legged configuration of the LEM landing gear. The model data and corresponding full scale values are given in Table I. The writer has adjusted the weight, center-of-gravity location, and radius of gyration to include the mass of the pad assemblies as shown for the overall vehicle.

From the crushing strengths of the struts and the geometry of the landing gear, the writer determined that a load factor of 21 is developed during a vertical landing whenever the friction coefficient is high enough to prevent sliding. This corresponds to a load factor of 3.5 for the full scale vehicle which was used in the MSFC analytical methods. This load factor is applied to the basic module which does not include the mass of the unsprung pad assemblies. Such a landing produces a force on each pad such that, for this vehicle, the component of force tangent to the surface is 1.50 times the component normal to the surface. However, for a 2-2 impact landing, the tangent force parallel to the plane of motion is reduced by the cosine of 45 degrees. Therefore, in the application of the two-dimensional method described in Ref. 3, the crushing forces of the main and support struts were determined such that the reaction force tangent to the surface, in the plane of motion, was about 1.06 times the normal force.

Insufficient data were available to determine the elastic properties. For the MSFC analysis using the method described in Ref. 3, elastic deflections were assumed for the main and support struts such that the

TABLE I. MODEL AND FULL SCALE CONFIGURATION DATA

| Basic Module Data | Scale Factor | Full Scale Data |
|------------------------------------------------------|--------------|-----------------------------------------------|
| W_e : 175.13 N (39.37 lb) | 216 | 37830 N (8504 lb) |
| k^2 : 0.406 m ² (4.37 ft ²) | 36 | 14.6 m ² (157 ft ²) |
| L_2 : 0.665 m (26.2 in) | 6 | 3.99 m (157 in) |
| D : 1.197 m (47.12 in) | 6 | 7.183 m (282.8 in) |
| C_m : 623 N (140 lb) | 36 | 22420 N (5040 lb) |
| C_s : 623 N (140 lb) | 36 | 22420 N (5040 lb) |
| <u>Pad Assemblies (Unsprung Mass)</u> | | |
| W_e : 27.27 N (6.13 lb) | 216 | 5890 N (1324 lb) |
| <u>Overall Vehicle</u> | | |
| W_e : 202.4 N (45.50 lb) | 216 | 43,720 N (9828 lb) |
| k^2 : 0.427 m ² (4.60 ft ²) | 36 | 15.38 m ² (165.6 ft ²) |
| L_2 : 0.577 m (22.7 in) | 6 | 3.46 m (136 in) |

effective vertical spring constant per leg was 4.90 MN/m (28,000 lb/in) for the full scale vehicle.

Results of the MSFC analytical analyses and the GAEC drop tests are shown in Fig. 6. Since the GAEC model was a one-sixth scale vehicle, the experimental velocity profile obtained applies directly (velocity scale factor of unity) to the full scale vehicle landing on the moon. The test model pads were equipped with small prongs to simulate a restrained condition on all pads. A large coefficient of friction was assumed for the analytical analyses. Using the method described in Ref. 2, which does not consider elasticity effects, the analytical results are somewhat optimistic. Using the method of Ref. 3, the analytical results are in general agreement with the experimental data but are more nonlinear.

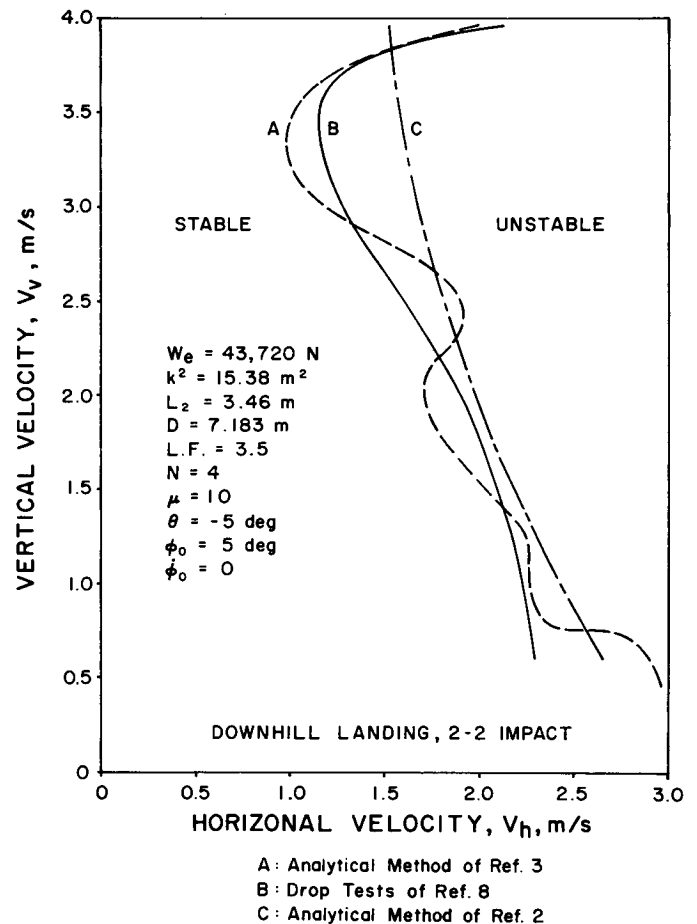


FIGURE 6. COMPARISON OF ANALYTICAL AND EXPERIMENTAL RESULTS

REFERENCES

1. Lavender, Robert E., "Lunar Logistic System - Lunar Touchdown," NASA TM X-50404, March 15, 1963.

2. Lavender, Robert E., "Touchdown Dynamics Analysis of Spacecraft for Soft Lunar Landing," NASA TN D-2001, January, 1964.
3. Lavender, Robert E., "Equations for Two-Dimensional Analysis of Touchdown Dynamics of Spacecraft With Hinged Legs Including Elastic, Damping, and Crushing Effects," MSFC MTP-AERO-63-76, November 6, 1963.
4. "A Comparative Design Study of Modular Stage Concepts for Lunar Supply Operations (U)," TRW Space Tech. Labs. Rpt. 8495-6015-RL000, Vol. IIA, December 12, 1963. (Confidential)
5. Floyd, J. and Taglarinè, T., "LLS/LEM Landing Investigation," GAEC Structural Memo 63-S-7, March 27, 1963.
6. Walton, W. C., Jr., R. W. Herr, and H. W. Leonard, "Studies of Touchdown Stability for Lunar Landing Vehicles," AIAA Aerospace Sciences Meeting, January, 1964. (AIAA Preprint 64-94).
7. "Mid-Term Report of Lunar Landing Dynamics Systems Investigation," Bendix Corp. Rpt. MM-64-4, June 18, 1964.
8. Donroe, F., "Results of Landing Gear Stability Drop Tests on 1/6 Scale Model," GAEC Rpt. LTR 904-16001, September 6, 1963.

V. ASTROPHYSICS

by

W. T. Roberts
and
L. G. McDonald

SUMMARY

N65-24135

Several aspects of the F₂ layer (the region of highest electron density) of the ionosphere are investigated. Contour maps of constant critical frequency of the F₂ peak, and height of the F₂ layer over the earth reveal a seasonal variability which may be predictable. The preliminary study shows that further work is necessary in this area and that diurnal, as well as solar cycle variations, must be established.

I. INTRODUCTION

Of the many problems encountered in the orbiting of space vehicles, one of the most difficult is determining the atmospheric drag effects. One aspect of this problem is the question of how coulomb drag forces affect the vehicle. One of the first steps in resolving this problem is to determine the number of ions above the earth's surface and how they vary seasonally, diurnally, and with the solar cycle. The Space Environment Group, Aero-Astrodynamics Laboratory, is carrying out a study of the electron density (and therefore the supposed ion content) of the F₂ peak of the ionosphere, as well as the height variabilities involved.

The purpose of this study is to determine global regions of high electron content, and to attempt to establish patterns for these points. The parameters being studied are f_oF_2 , the maximum plasma frequency which can be reflected from the ionosphere, and $h'F$, the height at which this frequency is reflected. Monthly average values of the critical frequency of the F₂ peak, f_oF_2 , and associated height data, $h'F$, reported by the participating stations in the Annals of the International Geophysical Year, were used in this analysis [1].

II. METHOD OF STUDY

About one hundred and twenty stations scattered throughout the world supplied data on ionospheric parameters during the IGY. A value of either f_oF_2 or $h'F$ for 1800 GMT was plotted at the geographical location of the station on a graph of latitude versus longitude. On these graphs, isometric lines of either

constant frequency or height were drawn. The resulting graphs show the rough variation in the monthly average value of the parameter over the globe. It is obvious that such a method does not allow an examination of the fine structure. The fine structure in the ionosphere either may be averaged out over a month's time, or is not detectable between the widely scattered points on the graph. There are places on the graph where several stations are located in the same general area, and at these points the contours become more complex. One example of such a place is around 50° N latitude and 10° E longitude. In several of the graphs, "kinks" are noticed in the otherwise smooth contours at this point. This comes from trying to follow the micro-patterns resulting from stations in near proximity.

Figures 1 through 8 are contours of either constant frequency or height for the months of March, June, September, and December, 1958. These months are normally selected for studies, since March and September are months of equinox and June and December are the solstice months.

The frequency contours represent electron densities at the F₂ peak of the ionosphere by the relation

$$N = 1.24 \times 10^4 f^2,$$

where N is in electrons per cubic centimeter and f is the reflected frequency in megacycles per second. This equation neglects electron collision damping, but is a wholly acceptable approximation. Electron densities are measured by generating a sweep frequency radio wave vertically into the ionosphere. The time delay is a measure of the height, and the frequency is a measure of the electron content at that height. As the frequency is increased, the wave penetrates higher into the ionosphere, until at a certain frequency a further increase in frequency produces no reflection from the ionosphere. This simply means that the maximum electron content has been reached at this point, and the signal is passing through the ionosphere into space. The frequency at which this phenomenon occurs is the ionospheric parameter f_oF_2 .

III. DATA ANALYSIS

Figures 1 and 2 are contours of constant critical frequency and height, respectively, of the F_2 layer for the month of March 1958. It is interesting that the contours tend to form into either high or low cells at various geographical locations throughout the map. Figure 1 shows that the electron density reaches a maximum during the day as expected; however, the increase in electron density in the nighttime hours beginning at about 70° E around the geomagnetic equator

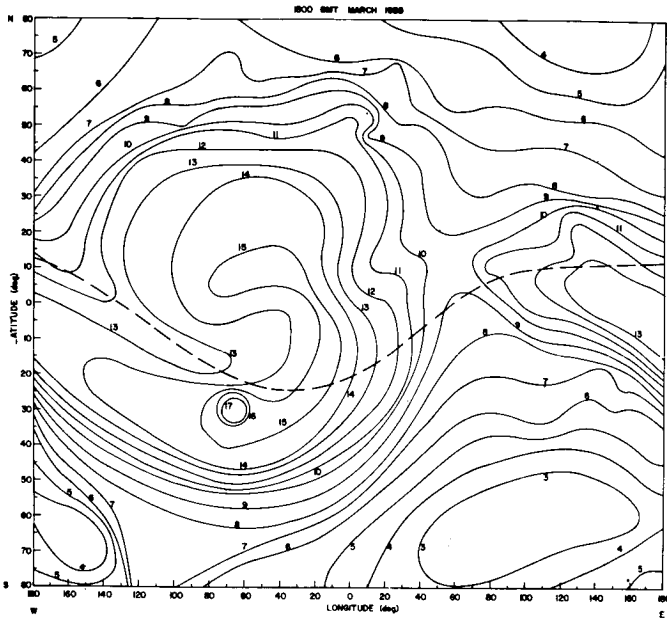


FIGURE 1. CONTOURS OF CONSTANT FREQUENCY (MEGACYCLES PER SECOND) OF THE F_2 PEAK AT 1800 GMT FOR THE MONTH OF MARCH 1958. THE HEAVY DASHED LINE IS THE PROJECTED GEOMAGNETIC EQUATOR

is not so easily explained. In the area outside of $\pm 30^\circ$ latitude electron densities act as one might ordinarily expect; that is, they decrease to a nighttime low. In Figure 2 the height contours are generally lower during the day than at night; however, one also observes the contours of height beginning to increase around the geomagnetic equator at about 80° E longitude.

Figure 3 represents the critical frequency of the F_2 peak during the month of June. The contours show that at 1800 GMT the electron density begins to increase around 100° E longitude, or about 00:40 LMT which once again is long before sunrise. There is also an anomalous increase in electron density at about 0° to 40° E longitude and 5° to 25° N latitude.

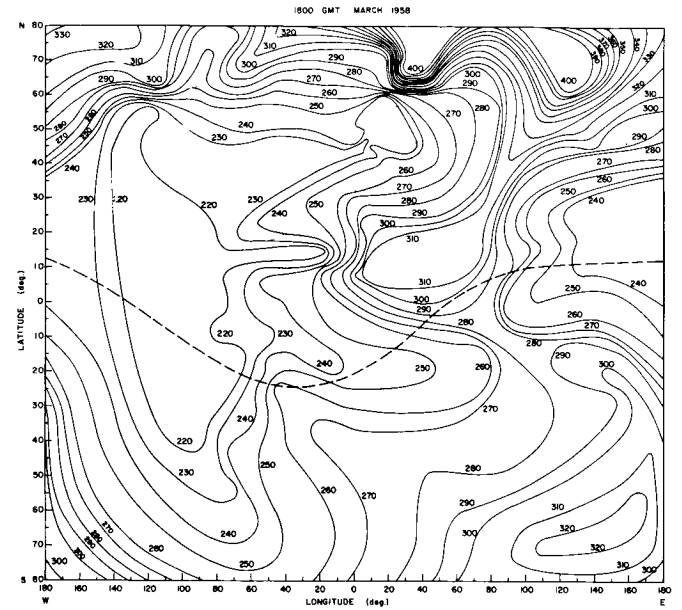


FIGURE 2. CONTOURS OF CONSTANT HEIGHT OF THE F_2 PEAK AT 1800 GMT FOR THE MONTH OF MARCH 1958. THE HEAVY DASHED LINE IS THE PROJECTED GEOMAGNETIC EQUATOR. HEIGHTS ARE IN KILOMETERS.

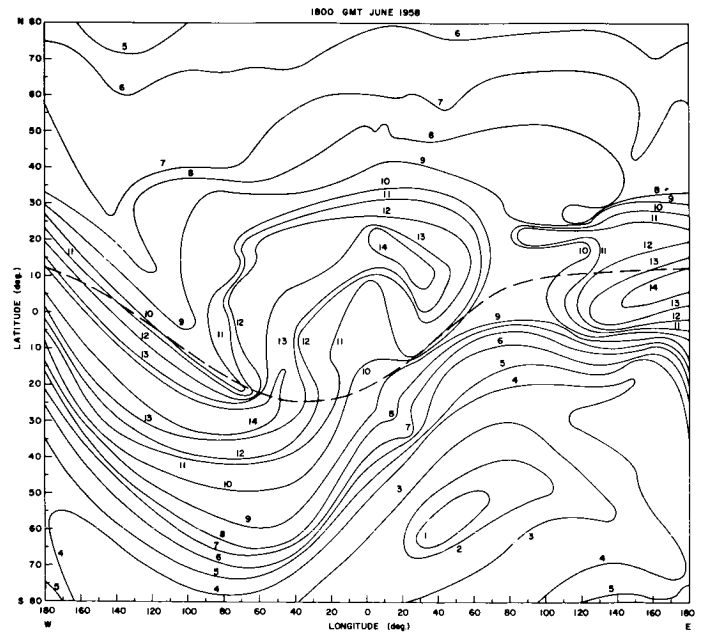


FIGURE 3. CONTOURS OF CONSTANT FREQUENCY (MEGACYCLES PER SECOND) OF THE F_2 PEAK AT 1800 GMT FOR THE MONTH OF JUNE 1958. THE HEAVY DASHED LINE IS THE PROJECTED GEOMAGNETIC EQUATOR.

Figure 4 is the associated graph for h'F for the month of June. This graph indicates a much more variable ionospheric height structure than the previous height graph. This graph is filled with "cells" of maximum and minimum heights. Probably the most interesting of these cells are those which occur from 100° to 180°W longitude. At about 40 degrees north there is a low cell with a height of 190 kilometers. Near the

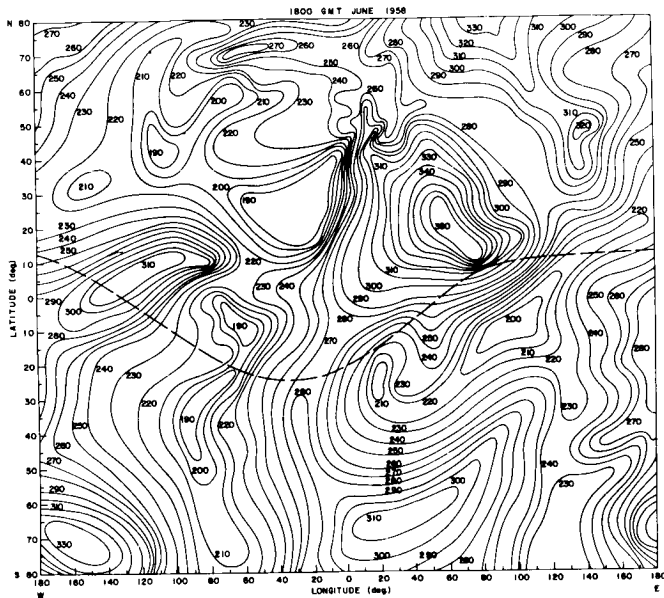


FIGURE 4. CONTOURS OF CONSTANT HEIGHT OF THE F₂ PEAK AT 1800 GMT FOR THE MONTH OF JUNE 1958. THE HEAVY DASHED LINE IS THE PROJECTED GEOMAGNETIC EQUATOR. HEIGHTS ARE IN KILOMETERS.

equator, there is a high cell with a central height of 310 km; and at about 70 degrees south, there is another high cell with a height of 330 kilometers. During the night the northern hemisphere tends to have cells with high altitudes, whereas the southern hemisphere has predominantly cells with low altitude.

The electron density distribution for the month of September is shown in Figure 5. The highs which occur during the day tend to stretch into the night in the northern hemisphere, but the southern hemisphere tends to act fairly normal.

Figure 6 shows contours of constant height for this same month, and appears to be fairly normal except at about 10° north latitude and 30°E longitude where there appears a very high cell dropping to a low at about 120°E longitude.

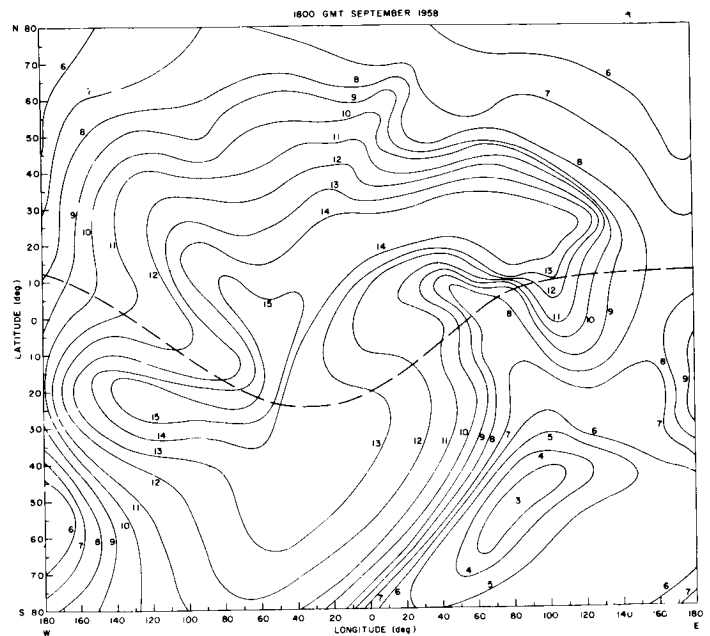


FIGURE 5. CONTOURS OF CONSTANT FREQUENCY (MEGACYCLES PER SECOND) OF THE F₂ PEAK AT 1800 GMT FOR THE MONTH OF SEPTEMBER 1958. THE HEAVY DASHED LINE IS THE PROJECTED GEOMAGNETIC EQUATOR.

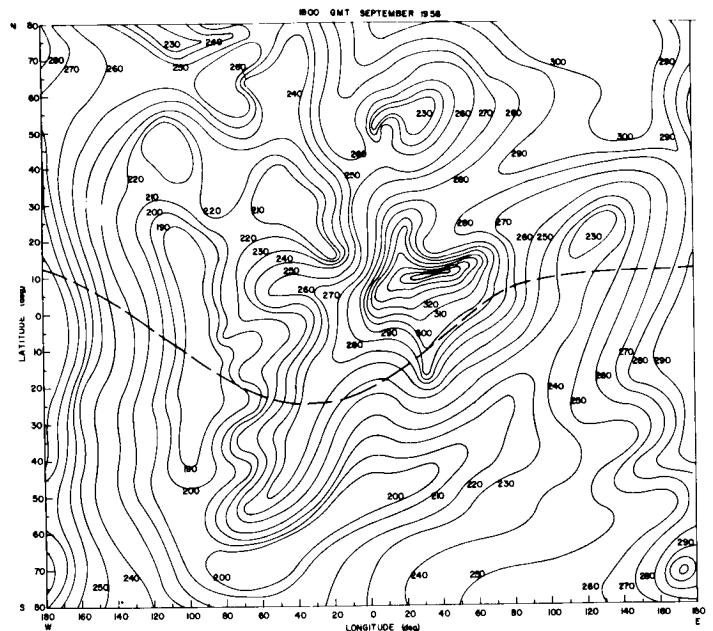


FIGURE 6. CONTOURS OF CONSTANT OF THE F₂ PEAK AT 1800 GMT FOR THE MONTH OF SEPTEMBER 1958. THE HEAVY DASHED LINE IS THE PROJECTED GEOMAGNETIC EQUATOR. HEIGHTS ARE IN KILOMETERS.

The low cell of f_oF_2 which occurs at about 20° N latitude and 70° W longitude in Figure 7 is very unusual. This indicates that during the day in the northern hemisphere there occurs a decrease in electron density at this location. It is also interesting to notice the way in which electron content tends to remain constant into the night around the equator. There is even an increase in electron density at about 80° E longitude.

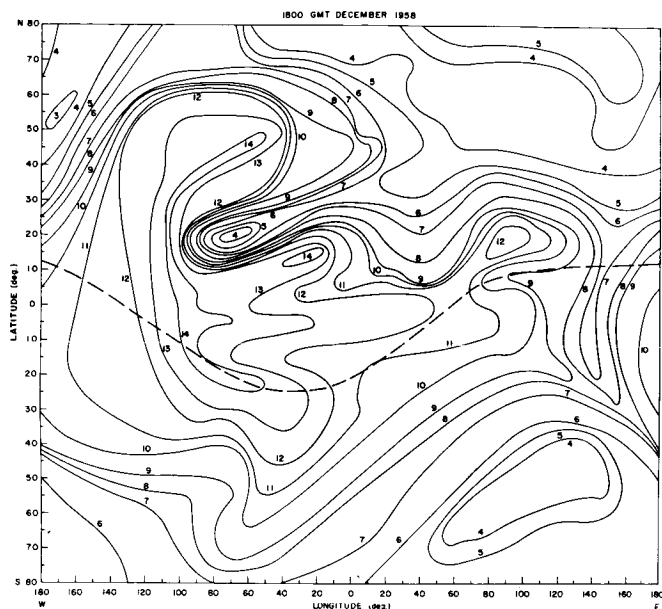


FIGURE 7. CONTOURS OF CONSTANT FREQUENCY (MEGACYCLES PER SECOND) OF THE F_2 PEAK AT 1800 GMT FOR THE MONTH OF DECEMBER 1958. THE HEAVY DASHED LINE IS THE PROJECTED GEOMAGNETIC EQUATOR

Figure 8 shows the height of the F_2 peak during December. The high cell which occurs in the northern hemisphere during the day is unusual, and the nighttime low in the northern hemisphere with a high cell in the nighttime southern hemisphere appears to be the reverse of what was said of Figure 4.

In the frequency graphs the southern hemisphere appears to be fairly consistent throughout the year with nighttime densities consistently lower than the daytime densities. Around the equator the situation is quite different. In March there tends to be a buildup in electron density shortly after midnight, while in June, September, and December, the electron density contours tend to drag out into the night with little or no change. In the northern hemisphere the contours tend to be rather consistent above about 45 degrees, but between 10° N and 45° N latitude the seasonal variability is rather difficult to understand. It is also noticeable

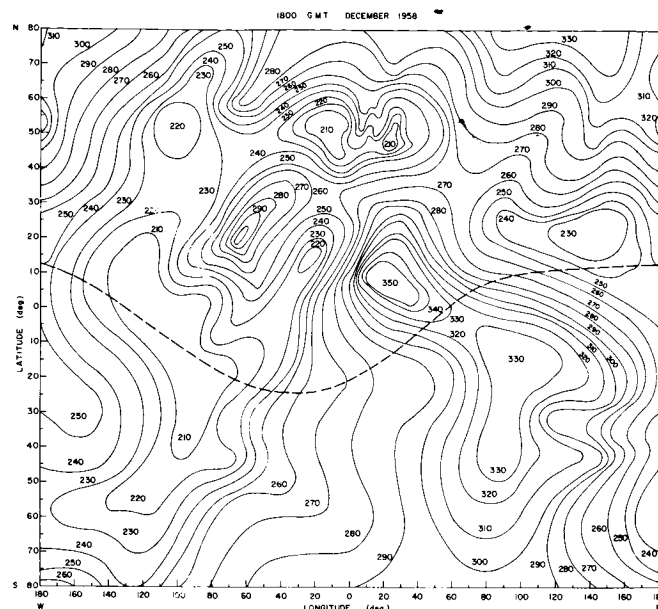


FIGURE 8. CONTOURS OF CONSTANT HEIGHT OF THE F_2 PEAK AT 1800 GMT FOR THE MONTH OF DECEMBER 1958. THE HEAVY DASHED LINE IS THE PROJECTED GEOMAGNETIC EQUATOR. HEIGHTS ARE IN KILOMETERS.

that the geomagnetic equator tends to exert an influence on the data. In the morning hours the regions of high electron density tend to lie south of the geomagnetic equator, whereas in the afternoon the highs tend to be north of the geomagnetic equator.

The height contours appear to be most complex during the solstice months and least so around the equinox months. March appears to be especially calm, with September showing considerably more variation. The main feature which is always present is the increase in height of the F_2 peak just after nightfall just north of the geomagnetic equator. During the day there are generally low height cells except in the month of June when a high cell occurred in the morning hours. Generally, there appear to be nighttime low cells in the northern hemisphere and nighttime high cells in the southern hemisphere, except, once again, for the month of June, when this situation is reversed.

It is apparent from the foregoing discussion that more data are needed to make a more thorough evaluation of the ionospheric variations. We have looked into the nighttime peak in height at the geomagnetic equator and the electron density increases after sunset. These two anomalies will be studied to determine the diurnal variations which each experiences.

IV. FUTURE PLANS

Ionospheric data have been ordered from the World Data Center for the International Year of the Quiet Sun. These data will be analyzed in the same way as the IGY data. They will also be compared with the IGY data to study variations appearing in the data from time of maximum solar activity to time of minimum solar activity. The methods of analysis which will be pursued in the continuation of this study will be (a) to construct graphs for each month of the year 1958 to study the progression of the various "cells" of high and low electron densities and the associated height contours, and (b) to construct graphs for each hour of the day, Greenwich Mean Time, to study the diurnal variations which occur as the sub-solar point pro-

gresses around the globe. This will be done for each of the four months of March, June, September, and December.

It is hoped that such a study program will produce results which will aid in the refinement and optimization of trajectory and orbital parameters required in later missions.

REFERENCES

1. Beynon, W. J. G. and Minnis, C. M., "Annals of the International Geophysical Year" Vol. XV, XVII, XVIII, * XIX, Pergamon Press, New York 1961.

AN EVALUATION OF A TECHNIQUE FOR PREDICTING SOME INDICATORS OF SOLAR ACTIVITY

By

Jeanette A. Scissum

and

Robert E. Smith

SUMMARY

Results of prediction models must be monitored to insure that specific failure or low success areas are detected and corrected at the earliest possible time in the developmental stage of the system. In this report, results of the USAF Air Weather Service method for predicting solar flare occurrence probabilities, amount of 2800 MC solar noise flux, and geomagnetic activity are compared with actual observations of these parameters on the surface of the earth. It is concluded that the technique is successful; however, there is a tendency toward a persistency type of prediction, a not unusual occurrence in the formulative stage of most prediction techniques.

I. INTRODUCTION

Authors of current publications on the properties of the upper atmosphere have concluded from analyses of satellite orbit perturbations and observations from rocket-borne probes that above the level of diffusive equilibrium, approximately 105 ± 5 kilometers, the density, temperature, and molecular weight are highly dependent upon the level of solar activity. While the amount of ultra-violet radiation from the sun (the energy that actually causes the changes) cannot be measured directly on the earth's surface, there are certain indicators of the level of solar activity that can and are being measured and recorded in a systematic manner. These indicators are the number of sunspots visible on the solar disc, the amount of 10.7 centimeter solar radio noise flux, and the three-hourly geomagnetic activity.

Several models for computing or predicting the temporal and spatial variability of the natural space environment parameters (density, temperature, and molecular weight) have been derived which are functions of either the known or predicted values of these indicators. Known values of these parameters are required in post-flight mission evaluation studies while predicted values are required in pre-flight mission determination, orbital lifetime prediction, and launch

condition studies. Inasmuch as the natural environment parameter models are based on numerical values of these indicators, highly accurate methods for predicting values of these indicators, as far in advance as possible, are necessary.

Further, mission success is entirely dependent upon the reliable performance of both material and personnel in the harsh environment of outer space, particularly, the radiation environment, and more specifically, the radiation environment during and after a large solar flare or solar proton event. The accurate and reliable prediction of these events will greatly enhance the probability of mission success.

Prediction models, especially those in the developmental stage, must be monitored continuously and rigorously to insure that acceptable accuracy levels are attained. This report presents an attempt to substantiate one method of predicting these solar activity indicators.

II. DISCUSSION

Headquarters, Air Weather Service, Scott Air Force Base, Illinois, has developed a method for predicting these various solar activity indicators. Each day of the work week a message containing the following information is transmitted to several using agencies:

Part I: Current observations of activity on the solar disc as reported by the High Altitude Observatory at Boulder, Colorado.

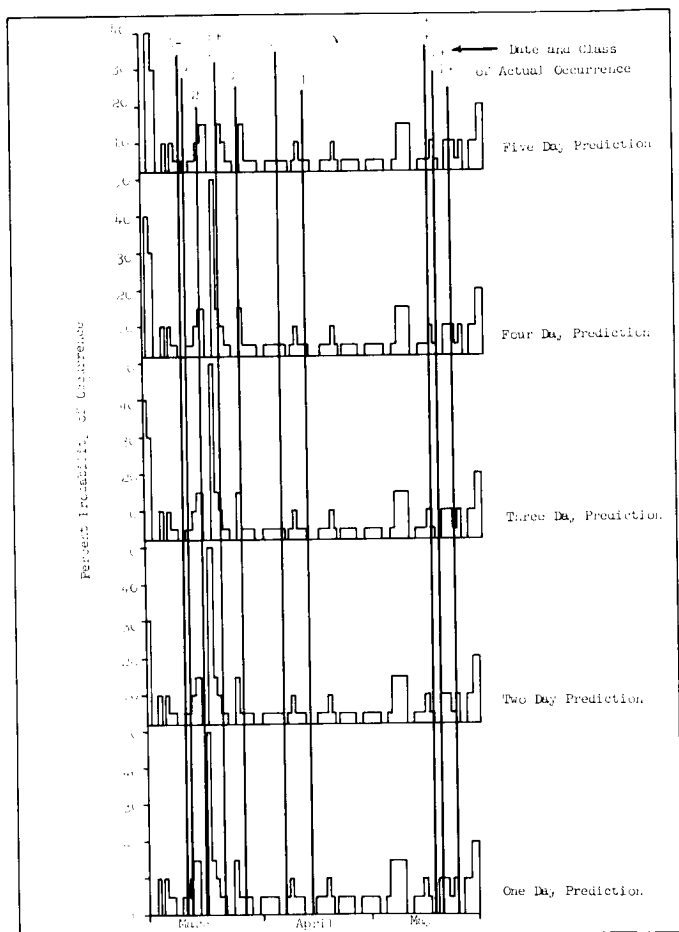
Part II: Class 2 or greater solar flare and solar proton event probabilities during the five-day period following the day of transmission of the message.

Part III: The 2800 MC solar radio noise flux for the day of transmission as recorded at Ottawa, Canada, and the predicted values for the three succeeding days.

Part IV: The geomagnetic index, A_k , for the day of transmission as recorded by Ft. Monmouth, New Jersey, and the predicted values of a_p for the three succeeding days.

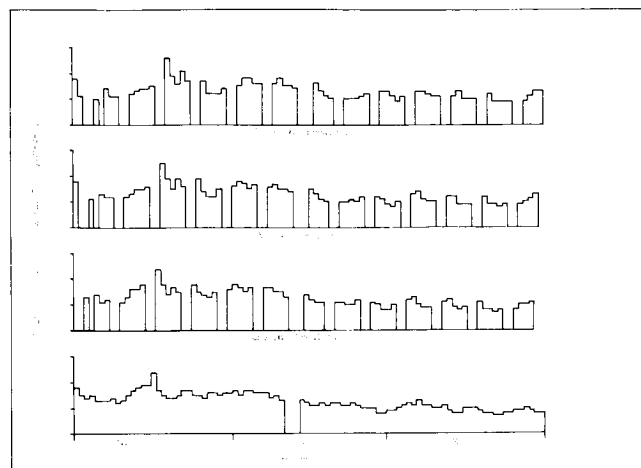
Information from these four parts of the message for the months of March, April, and May is presented graphically as follows.

Graph 1 compares one-, two-, three-, four-, and five-day predictions of the probability of occurrence with actual occurrences of solar flares. There was only one Class 2 flare during this period; it occurred on the fourth day of a period during which a fifteen percent probability of occurrence was forecast. A fifty percent probability of occurrence was forecast for one five-day period and, while no Class 2 or greater flare occurred, both a Class 1 and a Class 1+ flare occurred on the fifth day of the forecast period.



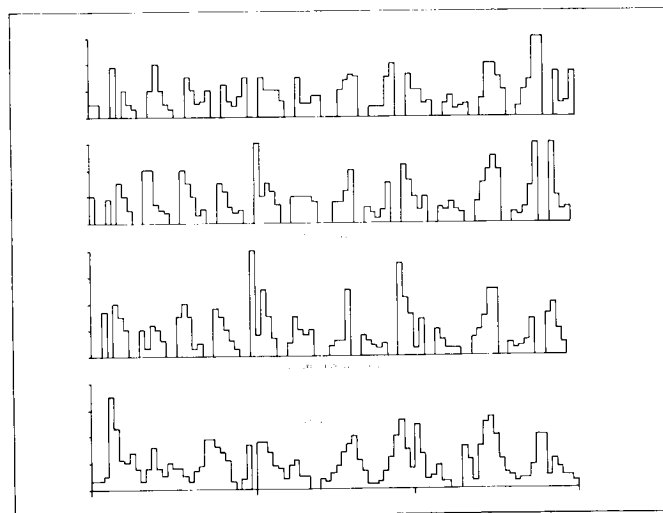
GRAPH 1. PERCENT PROBABILITY VS. ACTUAL OCCURRENCE OF SOLAR FLARES

Graph 2 compares one-, two-, and three-day predictions with observed values of the 2800 MC solar radio noise flux emanating from the sun. The predicted values are generally in phase with the observed values; however, the only major change in noise level predicted was one, two, and three days, respectively, after the actual day of occurrence, indicating a tendency towards a persistency or no change type of forecast.



GRAPH 2. PREDICTED VS. ACTUAL 2800 MC SOLAR RADIO NOISE FLUX

Graph 3 compares, one-, two-, and three-day predicted values of a_p with observed values of A_k . All



GRAPH 3. PREDICTED VALUES OF a_p VS. ACTUAL VALUES OF A_k

three prediction profiles show a close phase relationship with the observed values; however, it is impossible to determine a percentage accuracy because the A_k value reported in the message is merely an indicator of the predicted a_p , and there is no scale relationship on which a more definite comparison can be based.

Breaks in the data presented on all three graphs are due to (1) communication failures during the early stages of the program, and/or (2) the present concept of operation whereby forecasts are made only on normal work days. As the data requirements increase, the operational capability will be increased to seven days per week.

III. CONCLUSIONS

Table I shows that the one-day prediction is the most accurate with the two- and three-day accuracies usually decreasing sequentially. This result is in general agreement with most prediction methods in the developmental stages.

Preliminary conclusions from this admittedly short period are that the average overall accuracy of

TABLE I. 2800 MC PREDICTION ACCURACY

| | March 1964 | April 1964 | May 1964 | Overall |
|-----------|------------|------------|----------|---------|
| One day | 97.7% | 98.5% | 98.9% | 98.37% |
| Two day | 96.5% | 97.8% | 97.8% | 97.36% |
| Three day | 95.8% | 98.1% | 96.6% | 96.82% |
| Month | 96.7% | 98.1% | 97.8% | 97.53% |

the prediction method decreases as the time period for which the forecast is valid increases. Further, it must be remembered that this verification covers only a time period during which the solar activity is a very minimum; therefore, the conclusions as to the accuracy of the method should not be applied unreservedly to a period of high solar activity.

This verification program is being continued and periodic reports will be issued as the data sample increases and the solar activity level increases.

by

Charles C. Dalton

SUMMARY

N65-24137

Presented in this report is a model for the mean cumulative flux of meteoroids which includes the appropriate earth-shielding factor as a function of distance from the surface of the earth and which is as accurate as present information will support. A puncture model is presented for vehicles with homogeneous metallic walls. The results can be used to determine the no-puncture probability for particular vehicles and missions when the relation between bumper or sandwich-type wall structures and the equivalent thickness of a homogeneous metallic wall has been established.

DEFINITION OF SYMBOLS

| Symbol | Definition |
|-----------|-----------------------------------------------------------------------------------------------------------------|
| m | Meteoroid mass in grams. |
| F_s | Meteoroid impacts per square meter of randomly oriented surface per second of mass equal to or greater than m |
| h | Distance from the surface of the earth in kilometers. |
| β_2 | Partial derivative of $\log F_s$ with respect to $\log m$. |
| β_3 | Value of $\log F_s$ for vanishing $\log m$. |
| ρ_p | Meteoroid density in grams per cubic centimeter. |
| v_a | Meteoroid geocentric velocity in kilometers per second. |
| v_c | Meteoroid velocity relative to a moving vehicle, km per second. |
| p_o | Meteoroid crater depth in thick walls in centimeters. |
| ρ_t | Wall density in grams per cubic centimeter. |
| H_t | Wall hardness in Brinell units. |

Symbol

Definition

| | |
|--------|------------------------------------------------------------------------------------------------|
| x_2 | Angle of impact respect to the normal. |
| p | Wall thickness in centimeters punctured by meteoroids of mass m . |
| ϕ | Meteoroid puncture flux per second per square meter total area of a randomly oriented surface. |

I. INTRODUCTION

The meteoroid hazard to space vehicles, to equipment and structures in space, and to astronauts continues to be uncertain. It is expected that better information will become available from time to time, and consequent revision will be appropriate. A relation between bumper or sandwich-type wall structures and the equivalent thickness of a homogeneous metallic wall has been suggested by Nysmith and Summers [1]. Although present knowledge about the mechanics-of-materials aspects of meteoroid impact is not adequate for some design purposes, most of the uncertainty about the meteoroid hazard is due to the continued inability to interpret definitively the relevant astronomical and space data which have been published during the last ten years. This contention is supported by the error propagation in Reference 2. The sufficiently definitive interpretation may not be forthcoming until after more direct and more precise space measurements have been made.

Whipple's [3] relation between the flux of small meteoroids and distance from the surface of the earth, combined with the estimates by McCracken and Dubin [4] and by Hawkins [5] for the relation between the fluxes of larger meteoroids near the earth and on the moon, is used to extend Whipple's [6] flux model to include the distance from the surface of the earth as a parameter. The model so obtained is substituted for the flux model in Reference 2 to find the relation between material parameters and puncture flux. All logarithms have been converted to base ten. Errors on indicated values are approximately normally distributed, and probable errors are indicated. The indicated numerical estimates of uncertainty were established by the method given in Reference 2.

II. METEOROID FLUX MODEL FOR CISLUNAR SPACE

With data from rocket firings, satellites, and space probes, Whipple [3] found that the mean impact rate F_s on randomly oriented surfaces, including all particles greater than mass 10^{-9} gram and adjusted for the differing sensitivities of the equipments, varies inversely with the 1.4 power of the distance h from the surface of the earth; and that at some distance greater than $h = 10^5$ kilometers, the impact rates approximate those expected from calculations on the zodiacal cloud. Also Whipple [6], by adjusting the initial mass of the zero-visual-magnitude meteor from 25 grams to 1 gram in Hawkins and Upton's [7] flux model based on photographic meteors, and by introducing a near-earth shielding factor of $1/2$, found the following mean flux model for a randomly oriented surface near the earth:

$$\log F_s = -1.34 \log m - 14.48. \quad (1)$$

At the seventh meeting of the NASA Meteoroid Technology Advisory Working Group which was held at Goddard Space Flight Center on June 17 and 18, 1964, (Secretary: Mr. M. Charak, Code RV-1, OART, NASA Headquarters, Washington, D. C.) a motion was adopted that, for present considerations of meteoroid hazard near the earth, a non-segmented linear relation between $\log F_s$ and $\log m$ will be assumed. It seems reasonable to apply this relationship throughout cislunar space with the provision that both slope and intercept can be functions of location; i.e.,

$$\log F_s = \beta_2 \log m + \beta_3 \pm 1.3, \quad (2)$$

where both slope β_2 and intercept β_3 are independent of m .

Briggs [8] found that zodiacal-light observations are consistent with the theoretical apparent brightness due to scattered sunlight from the steady-state system of particles in the solar system under the action of the Poynting-Robertson effect when it was assumed that the concentration of particles with radii equal to or greater than 50 microns is inversely proportional to mass m at a distance of one astronomical unit from the sun. This would correspond to a negative unit value of β_2 in Eq. 2 along the earth's orbit but not necessarily near the earth. Since the 50 microns radius entailed a particle density of 0.1, Briggs' [8] result is with respect to meteoroids with $\log m$ equal to or greater than -7.3 .

Hawkins' [5] derivation from existing meteorite data shows that the flux of impacts of large stone meteoroids onto the earth with mass equal to or greater

than specified mass in kilograms is inversely proportional to the specified mass. Also Hawkins [5] indicates that the flux of large bodies onto the moon should be half as much as the flux onto the earth. It seems reasonable to assume that the flux onto the moon of meteoroids with mass equal to or greater than one gram may be only 40 percent of the corresponding value onto the earth.

McCracken and Dubin [4] in a study of "Dust Bombardment on the Lunar Surface" stated: "The geocentric distance to which the high fluxes measured near the earth apply is not known; the fluxes of small dust particles on the moon probably fall between the values indicated by the zodiacal light studies and the values indicated by the direct measurements obtained in the vicinity of the earth. The fluxes are, however, thought to be close to those indicated by the zodiacal light studies." These results can be generated by assuming that, at the moon's distance from the earth, the values of β_2 and β_3 in Eq. 2 are -1 and 40 percent of the value of β_3 in Eq. 1, respectively; i.e.,

$$\log F_s = -\log m - 14.58 \pm 1.3. \quad (3)$$

The next step toward establishing a meteoroid flux model for cislunar space is to write Eq. 2 as an appropriate function of distance h in kilometers from the surface of the earth so that Eqs. 1 and 3 are found when the values of $\log h$ are 2 and 5.59, respectively. Three approaches toward accomplishing this purpose could be pursued: (1) a theoretical approach based on considerations of particle dynamics, (2) an empirical approach based on direct measurements in space, and (3) a practical approach based on a consideration of present limitations of both the theoretical approach and the empirical approach.

The theoretical approach toward establishing a meteoroid flux model for cislunar space is not satisfactory because the distributions of dynamic parameters have not been definitively established, and the physical basis by which they might be established from theoretical considerations is problematical. Velocity information is available only from photographic and radar meteors, and it is not yet known whether the geocentric velocities of the smaller particles (those which have been detected in space) tend to be higher or lower.

The empirical approach based on direct measurements in space is so far only a little more satisfactory than the theoretical approach because the measurements (1) have been of uncertain interpretation with respect to particle mass, (2) have been limited to the small particles, (3) may have had considerable

uncertainty in the threshold of mass sensitivity from time to time and from experiment to experiment, and (4) have not been very well distributed throughout cislunar space.

The practical approach in establishing β_2 and β_3 in Eq. 2 as functions of the distance h from the surface of the earth is as follows: (1) Eq. 2 must reduce to Eqs. 1 and 3 when the values of $\log h$ are 2 and 5.59, respectively; (2) the partial derivative of $\log F_s$ with respect to $\log h$ must be -1.4 when $\log h$ and $\log m$ are 2 and -9 , respectively, in agreement with Whipple's [3] empirical model; (3) $\log F_s$ is assumed to be a continuous monotonic decreasing function of $\log h$ and the rate of decrease of $\log F_s$ with respect to $\log h$ is assumed to decrease with respect to $\log h$ throughout cislunar space. These results are given by the following expressions for β_2 and β_3 :

$$\beta_2 = -[1 + 0.34e^{0.26(\log h - 2)} - 0.24(\log h - 2)] \quad (4)$$

$$\beta_3 = -0.028(\log h - 2) - 14.48, \quad (5)$$

which are illustrated graphically over the interval $2 \leq \log h \leq 6$ in Figure 1. Corresponding values for $\log F_s$ by Eq. 2 are illustrated in Figure 2 by a family of curves for the following values of $\log m$: -10 , -7.5 , -5 , -2.5 , and 0 .

III. NUMERICAL VALUES FROM REFERENCE 2 WITH SUBSTITUTE CISELUNAR FLUX MODEL

$$\log \rho_p = -0.35 \pm 0.67 = \log 0.44 \pm 0.67 \quad (6)$$

$$\log v_a = 1.48 \pm 0.13 = \log 30 \pm 0.13 \quad (7)$$

$$v_c = v_a \quad (8)$$

$$\log p_o = (1/3) \log (\rho_p m / \rho_t H_t) + (0.500 \pm 0.075) \quad (9)$$

$$\log [(v_c/4.88) \cos x_2] + 0.778 \pm 0.054$$

$$\log p = \log p_o + 0.200 \pm 0.067 = \log 1.59 \pm 0.067 \quad (10)$$

Therefore, with random orientation, one obtains the following formulas for the hazard from meteoroids in cislunar space:

$$f(x_2) = \sin 2x_2 = \text{probability density function}$$

$$\text{for } x_2 \quad (11)$$

$$\log p_o = (1/3) \log (m/\rho_t H_t) + 0.95 \pm 0.26 \quad (12)$$

$$\log p = (1/3) \log (m/\rho_t H_t) + 1.15 \pm 0.26 \quad (13)$$

$$\log \phi = \beta_2 [\log (p^3 \rho_t H_t) - 3.45] + \beta_3 \pm 2.0, \quad (14)$$

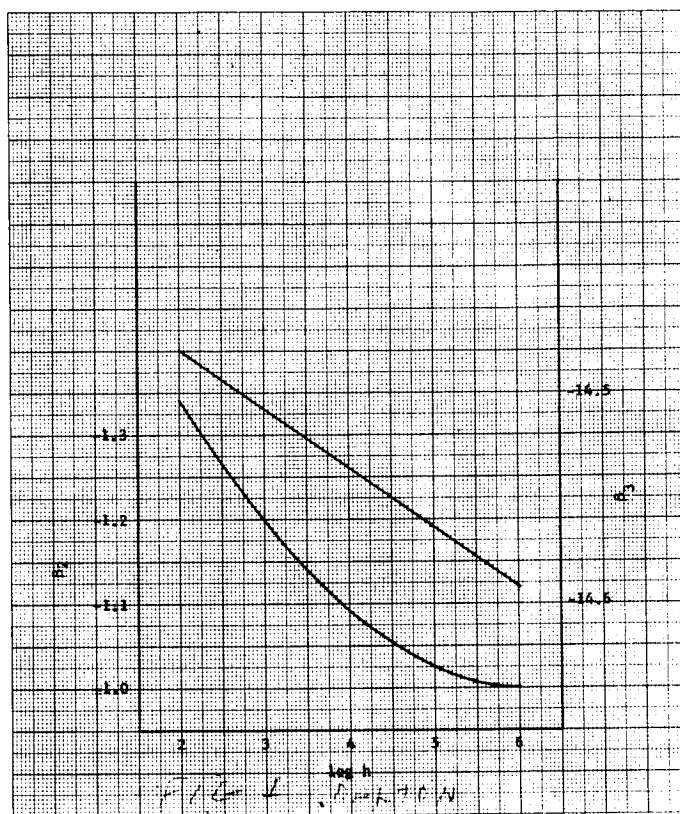


FIGURE 1. SLOPE β_2 AND INTERCEPT β_3 FOR $\log F_s$ AS A LINEAR FUNCTION OF $\log m$

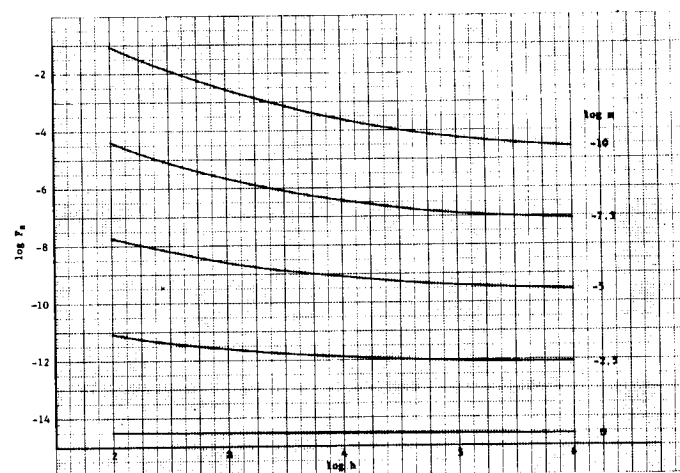


FIGURE 2. FLUX F_s OF METEORIDS PER SQUARE METER PER SECOND WITH MASS EQUAL TO OR GREATER THAN m GRAMS AT h KILOMETERS ABOVE THE SURFACE OF THE EARTH WITH RANDOM ORIENTATION

where ϕ is the puncture flux and ρ_t , H_t , and p are wall specific density, Brinell hardness, and thickness in centimeters, respectively.

IV. ILLUSTRATION

With aluminum 2219-T87, for which the density ρ_t and hardness H_t are 2.82 and 128, respectively, and with the expressions for β_2 and β_3 from Eqs. 4 and 5 substituted into Eq. 14, one obtains the results for $\log \phi$ as a function of $\log h$ which are illustrated in Figure 3 by a family of curves for the following values of wall thickness p : 0.001, 0.01, 0.1, and 1 centimeter.

V. CONCLUSIONS

The meteoroid hazard to space vehicles, to equipment and structures in space, and to astronauts in cislunar space is not well known. The puncture flux through specified thicknesses of aluminum 2219-T87, as illustrated in Figure 3, is believed to be accurate to within about two orders of magnitude probable error.

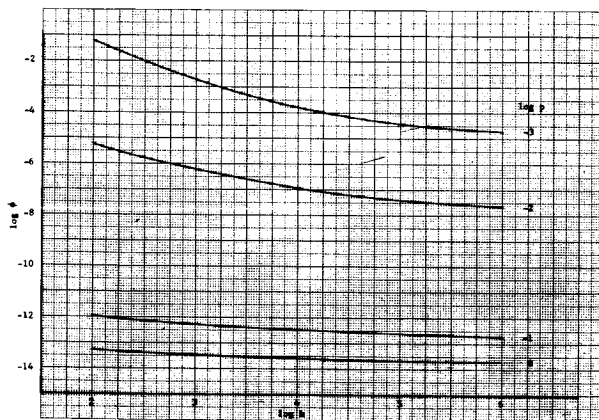


FIGURE 3. PUNCTURE FLUX ϕ OF METEORIDS PER SQUARE METER PER SECOND THROUGH A RANDOMLY ORIENTED WALL OF ALUMINUM 2219-T87 OF p CENTIMETERS THICKNESS AT h KILOMETERS ABOVE THE SURFACE OF THE EARTH

In addition to the hazard from primary meteoroids, which has been considered in this article, there may be considerable further hazard on or very near the moon due to secondary particles which are splattered up from the lunar surface.

REFERENCES

1. Nysmith, C., and Summers, J. L., "Preliminary Investigation of Impact on Multiple-Sheet Structures...", NASA TN D-1039, September 1961.
2. Dalton, C. C., "Estimation of Tolerance Limits for Meteoroid Hazard to Space Vehicles...", NASA TN D-1996, February 1964.
3. Whipple, F. L., "The Dust Cloud about the Earth," Nature Magazine, Vol. 189, No. 4759, pp. 127 - 128, January 14, 1961.
4. McCracken, C. W., and Dubin, M., "Dust Bombardment on the Lunar Surface," NASA TN D-2100, December 1963.
5. Hawkins, G. S., "Impacts on the Earth and Moon," Nature Magazine, Vol. 197, No. 4869, pp. 781, February 23, 1963.
6. Whipple, F. L., "On Meteoroids and Penetration," Journal of the Astronautical Sciences, Vol. X, No. 3, pp. 92-94, Fall 1963.
7. Hawkins, G. S., and Upton, E. K. L., "Influx Rate of Meteors in the Earth's Atmosphere," Astrophysical Journal, Vol. 128, pp. 727-735, 1958.
8. Briggs, R. E., "Steady-State Space Distribution of Meteoric Particles Under the Operation of the Poynting-Robertson Effect," Astronomical Journal, Vol. 67, No. 10, pp. 710-723, December 1962.

By

Dr. Hans A. Panofsky*

SUMMARY

N65 - 24138

Presented in this paper is a discussion on wind variations in the surface boundary layer where the vertical variation of stress is negligible. Relationships between mean wind speed profiles, gust factors, and standard deviations and spectra of horizontal wind components (lateral and longitudinal) are discussed as a function of stability and terrain conditions.

LIST OF SYMBOLS

| Symbol | Definition |
|-----------------|------------------------------------------------------------------------|
| u^* | friction velocity defined by $\sqrt{\frac{\tau}{\rho}}$ |
| τ | stress in horizontal direction due to wind |
| ρ | density of air |
| z_0 | roughness parameter |
| V | wind speed |
| z | height |
| \ln | base of natural logarithm |
| Ri | Richardson Number |
| σ_u | standard deviation of u component of wind |
| σ_w | standard deviation of w component of wind |
| x, y, z | coordinate system |
| σ_α | standard deviation of lateral wind direction (azimuth) |
| σ_θ | standard deviation of vertical wind direction (elevation) |
| u, v, w | wind components along, x, y, z axes, respectively |
| n | wave number |
| $S_u(n)$ | spectral density of u-component of wind as a function of wave number n |

| Symbol | Definition |
|------------|------------------------------------------------------------------------|
| $S_v(n)$ | spectral density of v-component of wind as a function of wave number n |
| ϵ | dissipation of turbulent energy |
| k | von Karman's constant which usually has the value 0.4 |

I. INTRODUCTION

The following will describe some of the characteristics of the "surface boundary layer," defined as the layer in which the vertical variation of stress is negligible. Thus, the stress, or better the friction velocity u^* defined by

$$u^* = \sqrt{\frac{\tau}{\rho}}$$

can be used as a parameter. It is generally derived from the wind profile or, if available, from the correlation between longitudinal and vertical wind.

Additional parameters are the roughness length, z_0 , and the Richardson number (or the ratio of height to Monin length) which describe the relative importance of mechanical turbulence and convection. During high wind conditions, convection is relatively small and the Richardson number is also small, so that the properties observed in "neutral" stratification are a good approximation. Only z_0 and u^* are then the important parameters, and once they are given, everything else is well determined.

A true constant stress layer can be assumed only over homogeneous terrain. If air has recently left rough terrain, the stress will increase with height up to an interface above which it is more or less constant. Below the interface, turbulence characteristics are those of smooth air; above the interface, they are those of the rough air. The typical slope of such interfaces is 1/10.

* Professor of Meteorology, Pennsylvania State University, University Park, Pennsylvania, and consultant to Aero-Astrophysics Office.

II. WIND PROFILES OVER ROUGH TERRAIN

A. NEUTRAL AIR

In neutral air, the wind profile is given by

$$V = 2.5 u^* \ln \frac{z}{z_0} \quad (1)$$

where V is the wind speed and \ln is base of natural log. Over uniform terrain, z_0 is a constant which may change in time only if the roughness changes with time. In principle, the roughness length can be determined from any set of two wind observations at two heights in neutral air. In practice, it is better to calibrate the site by taking many tests of such observations and then treat z_0 as known. Then, given z_0 , each wind observation allows estimation of u^* by equation (1).

B. CORRECTION FOR NONADIABATIC (DIABATIC) CONDITIONS

For diabatic conditions, equation (1) becomes

$$V = 2.5 u^* \ln \frac{z}{z_0} - \Psi(Ri), \quad (2)$$

where $\Psi(Ri)$ is a universal function of Richardson number Ri , which is positive in unstable air and negative in stable air. It is well known in unstable air only. Once z_0 is known, u^* can be computed from a wind observation, subject to a correction for Richardson number. This requires measurement of the lapse rate. It turns out that the Richardson number can be estimated from the lapse rate and a single wind. For fast winds, the Richardson number correction is usually small.

In unstable air, u^* is poorly determined by one measured wind.

III. WIND PROFILE OVER NONUNIFORM TERRAIN

Over nonuniform terrain, with fast winds, a simple logarithmic profile will not fit. The lowest portion will be representative of the local roughness, the next portion to the roughness farther upstream, the next to the roughness even farther away and so forth.

In the relatively simple case of a sharp change of roughness (with uniform roughness on either side), the profile can be approximated by two logarithmic

portions with a sharp division in between. For example, if the local roughness (at the site of measurement) is small, the lower part of the profile will have a slope corresponding to small u^* . The upper part will have a different slope reflecting the larger u^* of the ground farther upstream.

IV. STANDARD DEVIATIONS OF WIND COMPONENTS

Let u , v , and w stand for the wind components in the x , y , and z directions, the x -direction being parallel to the mean wind. (Rotation of the mean wind with height in the surface layer is negligible.)

The following give standard deviations in neutral air (to very good approximations) at many sites:

$$\sigma_u = 2.5 u^* \quad (3)$$

$$\sigma_v = 2.2 u^* \quad (4)$$

$$\sigma_w = 1.1 u^* \quad (5)$$

Using equation (1) for neutral air, we can write instead:

$$\sigma_u/V = 1.0/\ln \frac{z}{z_0} \quad (6)$$

$$\sigma_\alpha = \sigma_v/V = .88/\ln \frac{z}{z_0} \quad (7)$$

$$\sigma_\theta = \sigma_w/V = .44/\ln \frac{z}{z_0} \quad (8)$$

Here σ_α and σ_θ are the standard deviations of wind direction, lateral and vertical, respectively, in radians. Note that all the quantities in equations (6) - (8) decrease upward in neutral air, but the quantities in (3) - (5) are constants (over homogeneous terrain). Over heterogeneous terrain, all the standard deviations would increase upward if the local roughness is smooth and the roughness upstream is large. Note also that the quantities in equations (6) - (8) are independent of wind increase with z_0 .

Since frequency distributions of u , v , and w are approximately Gaussian, equations (3) - (8) can be used to derive gust factors. For example, a speed of $V + 2 \sigma_u$ would give the value exceeded 2.5 percent of the time. The gust factor would be $1 + 2.5 u^*/V = 1 + 2/\ln \frac{z}{z_0}$.

Equations (3) - (8) must be corrected for non-zero Richardson number, corrections which are small in strong winds over rough terrain. First, equations (3) - (5) must be corrected. The correction is very small for σ_w . The σ_v equation might double in unstable air; for σ_u the maximum correction is about 1.5. If we then proceed to equations (6) - (8), a further correction is needed in that equation (2) must be used for u^* in equations (3) - (5) instead of equation (1). This gives an additional increase for the quantities in equations (6) - (8) in unstable air.

V. SPECTRA OF THE HORIZONTAL WIND COMPONENTS

Of most interest here are the high frequencies (periods of 10 seconds and less). Here, the conclusions from the Kolmogorov theory of the inertial subrange are in good agreement with observations. In fact, they even apply to longer periods of V .

Further, the "universal" constants in these equations are now well known. We thus have

$$n S_u(n) = .15 \epsilon^{2/3} \left(\frac{n}{V}\right)^{-2/3} \quad (9)$$

and

$$n S_v(n) = .19 \epsilon^{2/3} \left(\frac{n}{V}\right)^{-2/3} \quad (10)$$

Here the left sides are the spectra multiplied by frequency, which come out in units of velocity squared, n is the wave number, $S(n)$ is the spectral density as a function of n , and ϵ is the dissipation, which under neutral conditions is given by

$$\epsilon = 2.5 u^{*3}/kz. \quad (11)$$

With equation (1), we finally have,

$$S_u(n) = .044 V^{8/3} (z)^{-2/3} n^{-5/3} \quad (12)$$

and

$$S_v(n) = .056 V^{8/3} (z)^{-2/3} n^{-5/3} \quad (13)$$

For longer wave lengths, it will suffice to make some general statements. The horizontal scale of lateral velocity is almost independent of height; that of longitudinal velocity increases slowly with height. The low-frequency portion of the spectra is mostly dependent on lapse rate, particularly for the lateral

components. In fact, in neutral air, lateral wind components have negligible low-frequency energy.

VI. VERTICAL STRUCTURE OF TURBULENCE

The following is based only on tower data from the Brookhaven National Laboratory, Upton, Long Island, New York, and may not be representative of other locations. Under unstable conditions, correlation coefficients between longitudinal wind components at different heights are approximately equal for equal height ratios (23 and 46 m is about the same as 46 m and 91 m). This implies that the vertical scale is approximately a linear function of height and that turbulence is homogeneous on a logarithmic height scale.

For neutral conditions, a $\sqrt[3]{z}$ scale leads to more nearly homogeneous turbulence, suggesting that the scale of turbulence varies as $z^{2/3}$.

Studies of cross spectra between different levels lead to the following conclusions:

1. Eddies slope down-wind by about 45 degrees on the average so that maximum correlation exists for upper winds preceding lower winds.

2. Separate analysis of eddies of different size shows that small eddies are nearly isotropic. Large eddies are elongated horizontally. The horizontal axis is much larger than the vertical axis in stable air, slightly larger in neutral air, and slightly shorter than the vertical axis, only in extremely unstable air.

3. If we are interested only in high-frequency variations (say, horizontal wave lengths of 10 m), the vertical wave length is about the same. Vertical correlations would drop to zero after about 1/4 wave length, and winds more than a quarter wave length apart can be taken to be independent of each other. Although there is not yet any proof, similar conclusions are likely for lateral wind components. Only extremely slow fluctuations of wind components would be in phase all along the vehicle. Because of the vertical elongation, eddies of the same horizontal wave length are more vertically coherent in unstable than in stable air. Hence, the total correlation coefficients are also greater in unstable than in stable air. But, as mentioned before, high-frequency variations at different levels tend to be fairly independent of each other under all conditions.

Many more studies of coherence between wind components at various heights are urgently needed.

VII. PRACTICAL EXAMPLE

Suppose that future measurements at Cape Kennedy had established that the roughness length there, for a certain wind direction, is 1 m. Then suppose

that the wind at 200 ft (60 meters) was 10 m/s. Then equation (1) gives a u^* of .98 m/s. Equation (6) shows that σ_u/V is .244, and the gust factor (for 2.5 percent exceedance) is 1.49. The spectrum estimate in $\text{m}^2\text{sec}^{-2}$ per unit cycle/s at a frequency of one cycle/s comes out as 1.32, equation (12).

By

A. Clifford Cohen, Jr.*

SUMMARY.

N65 24139

Techniques to resolve a mixture of two sample distributions into their respective components have applications in the statistical analysis of atmospheric data. Dealt with in this report is the problem of estimating parameters of a mixed (compound) distribution consisting of two Poisson components. Estimators based on the first three sample moments and estimators based on the first two sample moments plus the sample zero-frequency are considered. A computing routine is outlined for solving the estimating equations involved in the latter case.

I. THE PROBABILITY FUNCTION

Let μ and λ designate the parameters of two Poisson distributions that have been combined in the proportions α and $(1 - \alpha)$, respectively, to form a mixed (compound) distribution. The probability function of the resulting distribution may be written as

$$f(x) = \alpha \frac{e^{-\mu} \mu^x}{x!} + (1 - \alpha) \frac{e^{-\lambda} \lambda^x}{x!} . \quad (1)$$

For convenience, and without any loss of generality, we let $\mu > \lambda$.

II. ESTIMATORS BASED ON FIRST THREE MOMENTS

Estimators for the parameters of this distribution based on the first three sample moments were given by Rider [2]. Through the use of factorial rather than ordinary moments, the writer [1] subsequently simplified Rider's original estimating equations to the following form:

*Professor of Mathematics, University of Georgia, Athens, Georgia. The research reported in this paper was performed under NASA Contract NAS8-11175 with the Aero-Astrophysics Office, Aero-Astrodynamics Laboratory, Marshall Space Flight Center, Huntsville, Alabama. Mr. Orvel E. Smith is the NASA contract monitor.

$$\alpha = (\bar{x} - \lambda) / (\mu - \lambda) ,$$

$$\bar{x} \theta - \Gamma = \nu_{[2]} , \quad (2)$$

$$\bar{x}(\theta^2 - \Gamma) - \Gamma \theta = \nu_{[3]} ,$$

where

$$\theta = \mu + \lambda, \quad \text{and} \quad \Gamma = \mu \lambda , \quad (3)$$

and where

$$\nu_{[k]} = \sum_{x=0}^R x(x-1) \dots (x-k+1) n_x / n, \quad (4)$$

in which R is the largest observed (sample) value of x , n_x is the sample frequency of x , and n is the total sample size; i.e., $n = \sum_{x=0}^R n_x$. In the interest of a simpler notation, \bar{x} has been written in place of $\nu_{[1]}$.

On solving the last two equations of (2) simultaneously for Γ and θ , it follows that

$$\theta^* = (\nu_{[3]} - \bar{x} \nu_{[2]}) / (\nu_{[2]} - \bar{x}^2) , \quad (5)$$

$$\Gamma^* = \bar{x} \theta^* - \nu_{[2]} ,$$

where the asterisks (*) distinguish estimators from the parameters being estimated. As shown in [1], the required estimators of μ and λ follow from (3) and (5) as

$$\begin{aligned} \mu^* &= \frac{1}{2} (\theta^* + \sqrt{\theta^{*2} - 4 \Gamma^*}) , \\ \lambda^* &= \frac{1}{2} (\theta^* - \sqrt{\theta^{*2} - 4 \Gamma^*}) . \end{aligned} \quad (6)$$

These estimators are recognized as the two roots of a quadratic equation, with roots r_1 and r_2 , which may be written as

$$Y^2 - \theta^* Y + \Gamma^* = 0, \quad (7)$$

where $\mu^* = r_1$ and $\lambda^* = r_2$ ($r_1 > r_2$). The proportionality parameter α is estimated from the first equation of (2) as $\alpha^* = (x - \lambda^*)/(\mu^* - \lambda^*)$.

III. ESTIMATORS BASED ON FIRST TWO MOMENTS AND THE ZERO FREQUENCY

It is well known that the higher sample moments are subject to appreciable sampling errors. In an effort to improve on the efficiency of the three-moment estimators of the preceding section, the writer [1] obtained the following estimating equation which is based on the first two sample moments and the sample zero-frequency

$$\frac{\bar{x} - \lambda}{G(\lambda) - \lambda} = \frac{n_0/n - e^{-\lambda}}{e^{-G(\lambda)} - e^{-\lambda}} \quad (8)$$

in which

$$G(\lambda) = \frac{\nu_{[2]} - \bar{x}\lambda}{\bar{x} - \lambda} \quad (9)$$

where n_0 is the sample zero-frequency. Equation (8) can be solved for λ^{**} using standard iterative procedures, and with λ^{**} thus determined, estimators of μ and α follow as

$$\mu^{**} = [\nu_{[2]} - \bar{x}\lambda^{**}]/(\bar{x} - \lambda^{**}), \quad (10)$$

$$\alpha^{**} = (\bar{x} - \lambda^{**})/(\mu^{**} - \lambda^{**}).$$

The double asterisks (**) distinguish estimators of this section from the three-moment estimators of Section II and from the parameters being estimated. Unfortunately, no simple procedure for solving equation (8) has been devised. However, a computer routine has been developed based on iterative procedures described by Whittaker and Robinson [3] to solve equation (8) using as a first approximation the three-moment estimate of λ given by equation (6).

IV. COMPUTATIONAL PROCEDURES

The solution of the transcendental estimating equation (8) from Section III provides an interesting illustration of iterative numerical computation techniques described by Whittaker and Robinson [3]. To facilitate its solution, the denominator of the left side of (8) is interchanged with the numerator of the right side, and the resulting equation becomes

$$\frac{\bar{x} - \lambda}{n_0/n - e^{-\lambda}} = \frac{G(\lambda) - \lambda}{e^{-G(\lambda)} - e^{-\lambda}} \quad (11)$$

where $G(\lambda)$ remains as given by equation (9).

Equation (11) might be condensed to the form $L(\lambda) = R(\lambda)$ where

$$L(\lambda) = \frac{\bar{x} - \lambda}{n_0/n - e^{-\lambda}}, \text{ and } R(\lambda) = \frac{G(\lambda) - \lambda}{e^{-G(\lambda)} - e^{-\lambda}}. \quad (12)$$

Graphs of the two functions $L(\lambda)$ and $R(\lambda)$ are essentially as given in Figure 1.

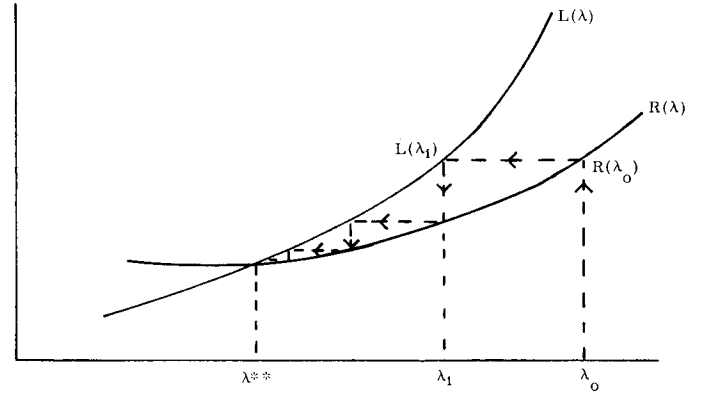


FIGURE 1. $L(\lambda)$ AND $R(\lambda)$ FUNCTIONS

We begin with an initial approximation λ_0 and iterate toward the value λ^{**} as described by Whittaker and Robinson [3, pp. 81-83]. The three-moment estimate of λ given by equation (6) of Section II provides a satisfactory value for λ_0 . This initial approximation is substituted into the second equation of (12) to obtain R_0 , which is merely an abbreviated notation for $R(\lambda_0)$. We then solve the equation

$$L(\lambda_1) = R_0 \quad (13)$$

to obtain λ_1 , the next approximation. This cycle is repeated as many times as necessary to attain the desired degree of accuracy. Equation (13) is itself a transcendental equation, though somewhat simpler in form than the original equation (11). It is amenable to solution by the Newton-Raphson method [3, page 84-86]. For the i th cycle of iteration, the equation corresponding to (13) becomes

$$L(\lambda_i) = \frac{\bar{x} - \lambda_i}{n_0/n - e^{-\lambda_i}} = R_{i-1}, \quad (14)$$

which may be written as

$$f(\lambda_i) = 0,$$

where

$$f(\lambda_i) = \lambda_i - R_{i-1} e^{-\lambda_i} - C_{i-1} \quad (15)$$

and where

$$C_{i-1} = (\bar{x} - R_{i-1} n_0/n).$$

Equation (14) may be readily solved using the Newton-Raphson method, where $\lambda_{i:r+1}$, the $(r+1)$ st iterant to λ_i , is given by

$$\lambda_{i:r+1} = \lambda_{i:r} - f(\lambda_{i:r})/f'(\lambda_{i:r}).$$

The first derivative of $f(\lambda_i)$ follows from (15) as

$$f'(\lambda_i) = 1 + R_{i-1} e^{-\lambda_i}.$$

Accordingly,

$$\lambda_{i:r+1} = \lambda_{i:r} - \frac{\lambda_{i:r} - R_{i-1} e^{-\lambda_{i:r}} - C_{i-1}}{1 + R_{i-1} e^{-\lambda_{i:r}}}. \quad (16)$$

As an initial approximation $\lambda_{i:0}$ to λ_i , it will usually be satisfactory to let $\lambda_{i:0} = \lambda_{i-1}$. The Newton-Raphson iterative technique is continued through as many cycles as may be necessary to attain the desired accuracy in λ_i . More specifically, this subroutine is terminated at the end of the r th cycle, where this is the first cycle for which

$$|L_{i:r} - R_{i-1}| < \delta_1,$$

in which δ_1 specifies the maximum permissible absolute value deviation. With λ_i thus determined, we calculate R_i , set up the new equation $L(\lambda_{i+1}) = R_i$ and the primary routine is continued through k cycles, where the k th cycle is the first for which

$$|L_k - R_k| < \delta_2,$$

where δ_2 specifies the maximum allowable absolute value deviation. The required estimate of λ is then

$$\lambda^{**} = \lambda_k.$$

V. AN ILLUSTRATIVE PROBLEM

To illustrate the application of his three-moment estimators, Rider [2] chose an example constructed by mixing equal proportions of two Poisson distributions with $\mu = 1.5$ and $\lambda = 0.5$, respectively. These data are as follows:

| x | 0 | 1 | 2 | 3 | 4 | 5 | 6 | 7 |
|-------|-----|-----|-----|-----|----|----|---|---|
| n_x | 830 | 638 | 327 | 137 | 49 | 15 | 3 | 1 |

In summary, $n = 2000$, $n_0 = 830$, $x = 0.9995$, $\nu_{[2]} = 1.243$ and $\nu_{[3]} = 1.734$. Direct substitution of these values into equations (5), (6) and (7) yields the three-moment estimates

$$\mu^* = 1.4766563,$$

$$\lambda^* = 0.47765894,$$

$$\alpha^* = 0.52236479.$$

These results differ slightly from those given by Rider due apparently to small round-off errors in his calculations.

Estimates based on the first two moments and the zero frequency calculated with the aid of an electronic computer, programmed in accordance with the computing routine of Section IV, are

$$\mu^{**} = 1.4936,$$

$$\lambda^{**} = 0.4956,$$

$$\alpha^{**} = 0.5049.$$

These estimates are in much closer agreement with the actual population parameters $\mu = 1.5$, $\lambda = 0.5$, and $\alpha = 0.5$ than the three-moment estimates. Investigations are continuing with regard to the relative efficiency of the three-moment and the two-moment plus zero-frequency estimates, but at least, in the present instance where a large proportion of the population is in the zero class, the two-moment plus zero-frequency estimates are to be preferred.

ACKNOWLEDGEMENT

The author wishes to acknowledge the assistance of Mr. Frank Clark for his work in establishing the computer program described in Section IV.

REFERENCES

1. Cohen, A. Clifford, (1963), Estimation of Mixtures of Discrete Distributions, University of Georgia, Institute of Statistics, T. R. No. 16.
2. Rider, Paul R., (1961), Estimating the Parameters of Mixed Poisson, Binomial, and Weibull Distributions by the Method of Moments, Bulletin de l'Institut International de Statistique, 38, Part 2.
3. Whittaker, E. T. and Robinson, G., (1929), The Calculus of Observations (second edition), Blackie and Son Limited, London.

VI. ORBIT THEORY AND PREDICTION

by

Wilton E. Causey

N65 24140

SUMMARY - - - - "

Presented in this report are earth-moon orbits which, when referred to a rotating coordinate system, return periodically to their original set of state variables. Such orbits offer repeated approaches to both earth and moon and could be used for instrumented exploration of earth-moon space for meteoroid concentration, radiation belts and other useful information.

I. INTRODUCTION

Characteristic features such as the period of the orbit, time spent in the region between earth and moon, close approach distance to the moon, and closest approach distance to the earth vary for each family of periodic orbits. The orbits presented in this paper have periods of 1 to 3 months and they have at least one perpendicular crossing of the earth-moon line on the back side of the moon. The orbits contained herein represent only a small portion of the families of periodic orbits that are possible in the restricted three body problem, and it should not be inferred that these are the only orbits of interest.

ACKNOWLEDGEMENTS

The author wishes to thank Dr. Richard Arenstorf and Mr. Mirt Davidson of the MSFC Computation Laboratory who by their advice and stimulation were instrumental in achieving these results. The author would also like to express his gratitude and appreciation to Mr. Thomas French for his help in generating and presenting the data contained in this report.

II. DISCUSSION

A. EXISTENCE

The existence of certain periodic orbits in the restricted three-body problem has been known for a long time. Poincaré referred to orbits which reduce to circles when the disturbance from the more distant body becomes zero as "solutions de la première

sorte" [1]. These orbits can be near either of the finite masses, but not both. Arenstorf [2] proved the existence of periodic solutions of the so-called second kind which are near rotating Keplerian ellipses. It is possible for these orbits to pass close to both finite masses, and therefore, for lunar exploration, they are more attractive than orbits of the first kind. Orbits of the first and second kind exist even if one of the bodies becomes massless. Contrary to this, there are periodic orbits that exist only in the restricted three-body problem proper. In the earth-moon system such orbits would owe their existence to the disturbance produced by the moon. This report presents periodic orbits of the second kind and orbits that are inherent in the restricted three-body problem proper.

B. BASIC ASSUMPTIONS

A restricted three-body model is assumed for the earth, moon, and probe system. In this system, the earth and moon revolve in circles in a plane around their common center of mass (barycenter). For this investigation, the probe's motion is restricted to the plane defined by the earth-moon motion. The equations of motion are normalized such that the sum of the masses of the earth and moon is unity; the constant distance between the earth and moon is unity, and the period of the earth and moon about their common center of mass is 2π . The ratio of the mass of the earth to the mass of the moon was assumed to be 80.45, and for the purpose of converting from the unitized system to a physical system of units, the distance from the center of the earth to the center of the moon was taken to be 385,000 km.

Orbits are geometrically represented in a rotating coordinate system (origin at the barycenter) in which the earth and moon lie on the x-axis. In this rotating coordinate system, periodic orbits are symmetric with respect to the x-axis. This symmetric property is attributed to image properties which occur in this system. Miele's [3] "Theorem of Image Trajectories" states that if a trajectory is possible from earth to moon, the image reflected about the x-axis is also possible. The image trajectory will be traversed in the opposite sense, that is, from moon to earth. Thus, a trajectory starting perpendicular to the earth-moon line and crossing the earth-moon line perpendicular at some later time will return to the original starting position. This image property leads one to conclude that two perpendicular crossings

of the earth-moon line (x-axis) are sufficient for periodicity in the restricted three-body problem. With this in mind, orbits were started on the back side of the moon perpendicular to the earth-moon line. This was an arbitrary choice of starting conditions, but they proved quite convenient. With one perpendicular crossing assured, the problem is to isolate transits which have a second perpendicular crossing of the earth-moon line. In this study, the velocity magnitude at the starting position (first perpendicular crossing) was varied in order to perform the isolation. Complete families were generated by changing the starting position and repeating the isolation. The period of the orbit and close approach distance to the earth vary with the close approach distance at the moon. These features are observed and presented for several families. As shown in Section III, some families contain orbits which collide with the earth. A further increase or decrease, as the case may be, in the starting position behind the moon produces orbits that are retrograde as they approach the earth. These retrograde orbits are neglected for the present; however, future investigations are planned in this area and should add insight to the general behavior of periodic orbits.

C. CLASSIFICATION

The classification of orbit families used in this report is the same as the system used by Arenstorf [4] and Davidson*. Categories such as ratio, order, and class are used in distinguishing various families of orbits. Since these terms will be used extensively, a brief explanation of each is in order.

Figures 1 and 2 depict a periodic orbit in a rotating and a space-fixed frame of reference, respectively. In the space-fixed system, the probe makes

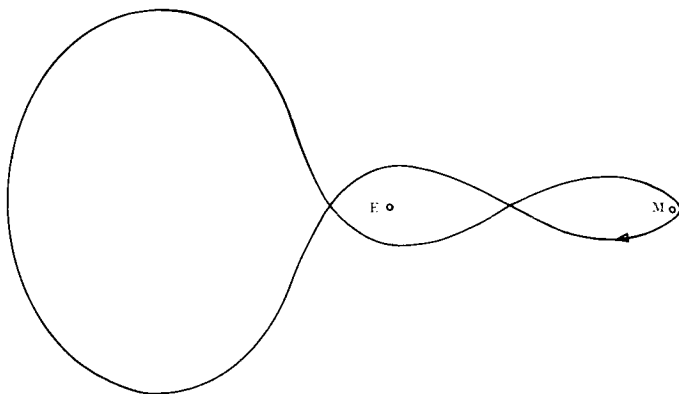


FIGURE 1. PERIODIC ORBIT RATIO $1/2$, ORDER 1, ROTATING FRAME OF REFERENCE

* Private communication with M. C. Davidson of the Computation Laboratory of MSFC.

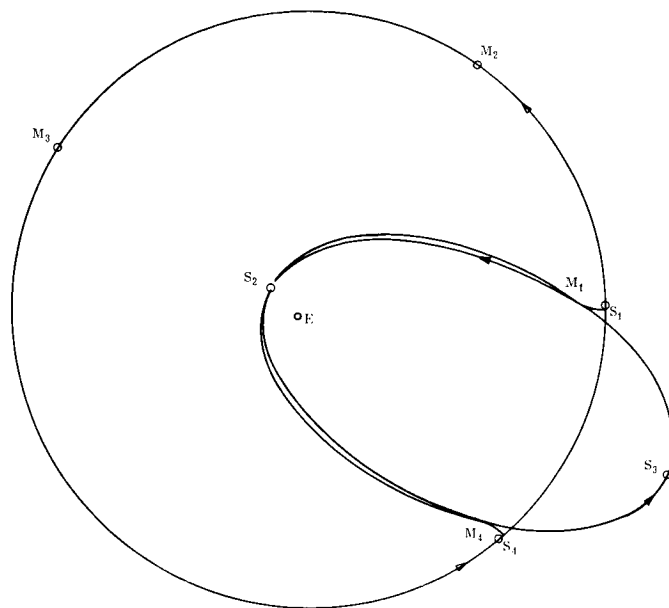


FIGURE 2. PERIODIC ORBIT RATIO $1/2$, ORDER 1, SPACE-FIXED FRAME OF REFERENCE

two revolutions in its orbit in the same time the moon makes approximately one revolution in its orbit. The major axis of the probe's orbit has been rotated slightly due to the disturbance by the moon; therefore, the period of the orbit is less than the period of the moon, and the orbit is not closed in the space-fixed frame of reference. However, the forces acting on the probe at S_4 are equal to the forces acting at S_1 . Thus, closure in the space-fixed frame of reference is not necessary for periodicity in the restricted three-body problem. If one lets m equal the number of revolutions the moon makes while the probe has to make k revolutions in its orbit before periodicity occurs, then the ratio $m/k = \frac{1}{2}$ is used to classify this orbit and the period, $t \approx 2\pi m$.

Kepler's third law provides an estimate for minimum value of m/k for orbits that encompass both the earth and moon. In the unitized coordinate system, the period of the moon is given as $P_m = 2\pi$, and the period of the probe about the earth is $P_p = 2\pi\sqrt{a^3}$ where a is the semimajor axis of the probe's orbit. If the probe's orbit is to contain both masses, then $a \geq \frac{1}{2}$. Under this assumption, the minimum value of m/k is $(\frac{1}{2})^{\frac{3}{2}} \approx .354$.

Figure 1 is an orbit of ratio $\frac{1}{2}$ order 1. Orbits with ratio $\frac{2}{4}, \frac{3}{6}, \frac{4}{8}, \dots$ will be referred to as higher order orbits (second, third, fourth ...) of ratio $\frac{1}{2}$. In general, an orbit with a ratio $\frac{nm}{nk}$ is classified as ratio m/k order n . Figures 3 and 4 show orbits of

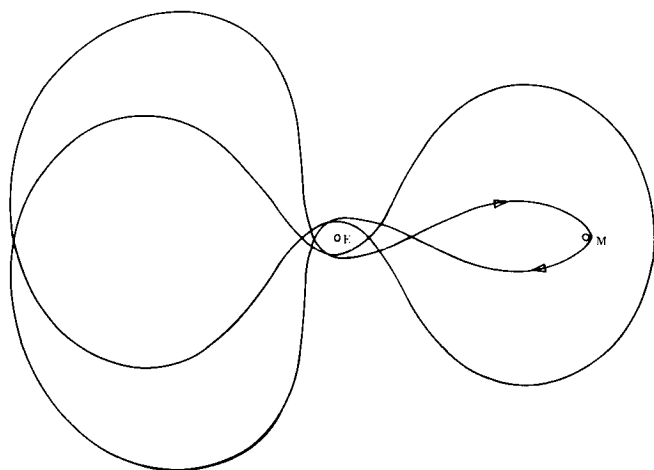


FIGURE 3. RATIO $1/2$, ORDER 2, CLASS A

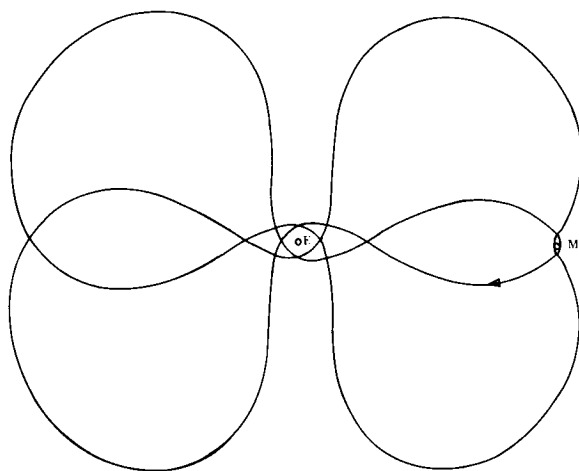


FIGURE 4. RATIO $1/2$, ORDER 2, CLASS B

ratio $\frac{1}{2}$ order 2. In Figure 3 the second perpendicular crossing of the earth-moon line occurs on the back side of the moon. Orbits with this characteristic are designated class A. The orbit shown in Figure 4 has the second perpendicular crossing on the front side of the moon. This perpendicular crossing occurs after apogee, or alternatively stated, on the descending leg of the space-fixed orbit. Orbits of this nature will be referenced to as class B. First order orbits are periodic orbits of the second kind, but the higher order orbits are orbits of the restricted three-body problem proper.

All orbits presented herein have at least one perpendicular crossing on the back side of the moon. There are orbits which do not possess this characteristic, but complete data on these orbits are not available at this time.

D. APPLICATIONS

A knowledge of the conditions that exist in earth-moon space is desirable prior to manned lunar missions. Mapping of meteoroid concentration and radiation belts in the region of earth-moon space could be provided by an instrumented probe in a long-life periodic orbit (1 year or more). Periodic orbits offer repeated close approaches to both the earth and moon and information gathered near the moon could be easily transmitted back to earth. Certain periodic orbits permit adequate coverage of the space traversed by an Apollo type trajectory; therefore, in choosing an orbit, one should consider the amount of time spent (coverage) in the desired region.

In the restricted three-body problem, the moon's orbit is assumed to be circular, but in the true physical system, the ellipticity of the moon's orbit adds a perturbative force which will require a velocity budget for orbit keeping. However, one can, in limited cases, overcome this perturbation by employing periodic orbits with periods that are exact multiples of the moon's period. If the orbit shown in Figure 2 had a period that was a multiple of the moon's period and M_1 represented the position of the moon at apogee or perigee, then S_4 would coincide with S_1 , and the orbit would be periodic even if the moon's eccentricity was non-zero.

Periodic orbits can also be used for exploration of outer space. If one replaces the earth-moon system by the sun-earth system, then an orbit of ratio $\frac{2}{3}$ order 1 (Fig. 13) offers the advantage of a return near earth at which time information could be relayed to earth via low power transmission. The orbit shape will vary slightly due to the different mass ratio of the sun-earth system, but in general the orbit will have the same basic features. The period of the orbit shown in Figure 13, instead of being twice the moon's period, would be twice the earth's period about the sun.

III. RESULTS

Families were studied by varying the starting position behind the moon, and the results are presented with this as the independent parameter. Closest

approach distance to the center of the earth, the period of the orbit, and percent time on the inner leg of the orbit are presented for various families. The inner leg of an orbit is defined as the part of the orbit that lies closest to the earth-moon line and extends from perigee at the earth to perisel at the moon and back to perigee at the earth. The second approach distance to the moon is presented for the higher order orbits. Data for orbits of ratio $\frac{1}{2}$ order 1 are presented in Figure 5. Orbits of this family exist for

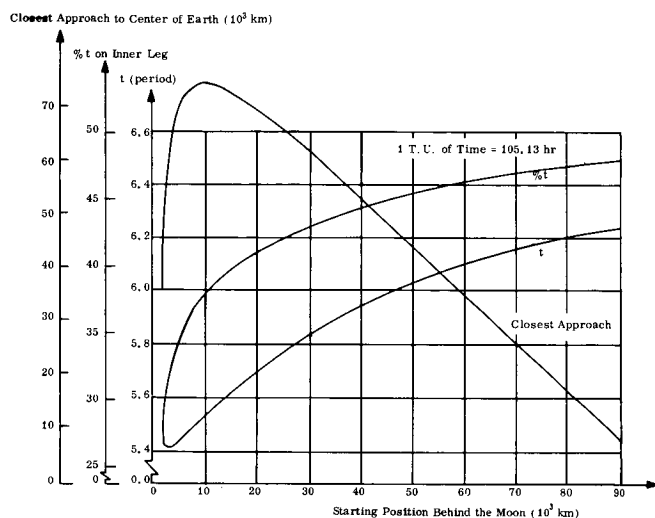


FIGURE 5. RATIO $\frac{1}{2}$, ORDER 1

starting positions (perpendicular crossing on the back side of the moon) ranging from the moon's surface out to a radius of 89,400 km. At radii slightly greater than 89,400 km, the orbits impact the surface of the earth, and a further increase in the starting radius produces retrograde orbits.

Figures 6 and 7 show data for ratio $\frac{1}{2}$ order 2 class B. These orbits exist for starting radii between 3075 km and 57,000 km. Collision with the surface of the earth occurs for starting radii less than 3075 km and greater than 57,000 km. It is evident from Figure 7 that this family contains an orbit that will be periodic even when the moon's orbit is assumed to be elliptic.

Depicted in Figures 8 and 9 are data for ratio $\frac{1}{2}$ order 2 class A. Collision with the surface of the earth occurs with a starting radius of 1928 km. For this starting radius, the second perpendicular crossing of the earth-moon line occurs on the back side of the moon at a distance of 132,000 km. As the starting radius is continuously increased, the second perpendicular crossing moves in toward the moon until the two crossings coincide. This occurs at about 15,000 km. Transits that are started beyond this radius will have their second perpendicular crossing

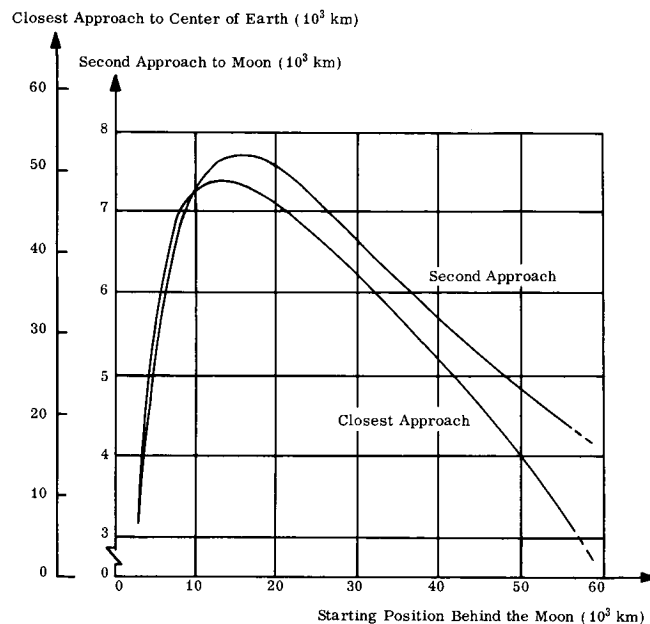


FIGURE 6. RATIO $\frac{1}{2}$, ORDER 2, CLASS B

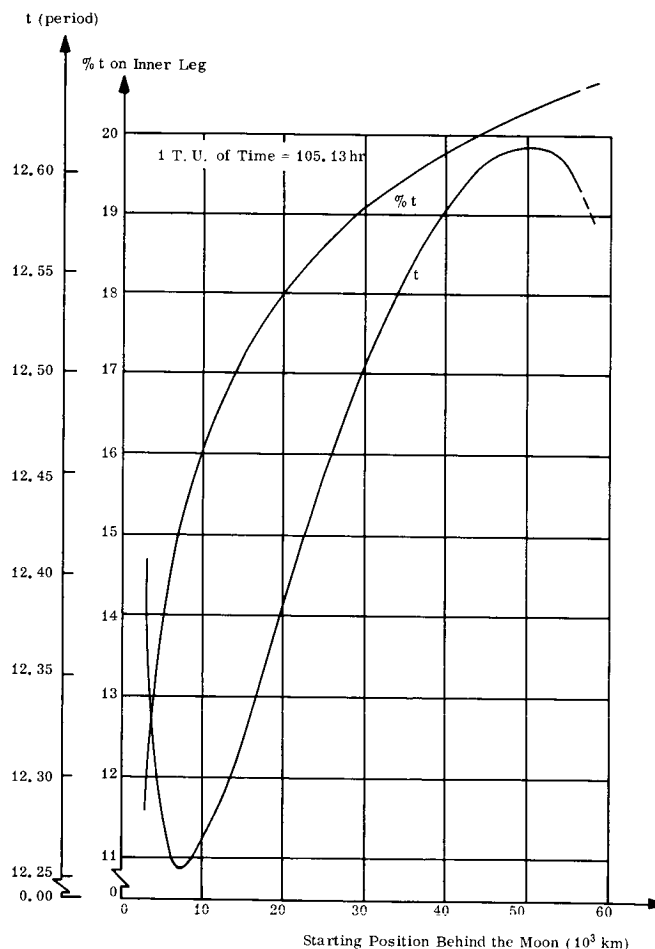


FIGURE 7. RATIO $\frac{1}{2}$, ORDER 2, CLASS B

between the moon and the starting position, and they will be duplicates of transits that were started from a position inside the 15,000 km limit.

Data for orbits of ratio $\frac{1}{2}$ order $\frac{3}{2}$ (an example is shown in Figure 10) are presented in Figures 11 and 12.

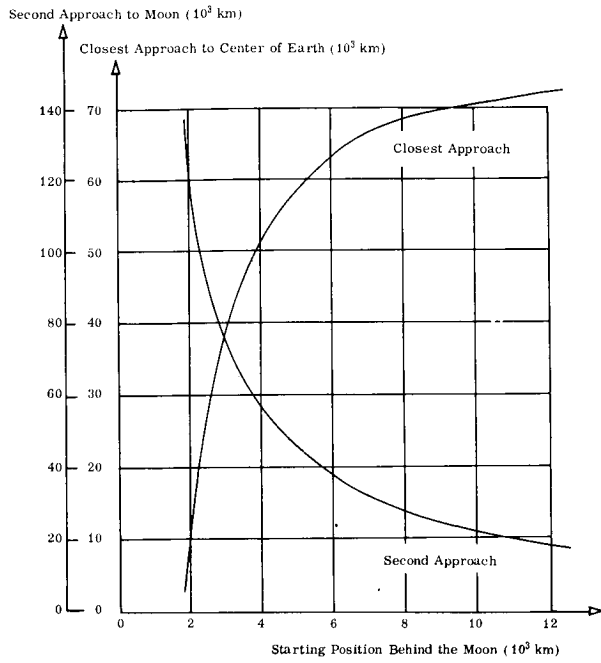


FIGURE 8. RATIO $1/2$, ORDER 2, CLASS A

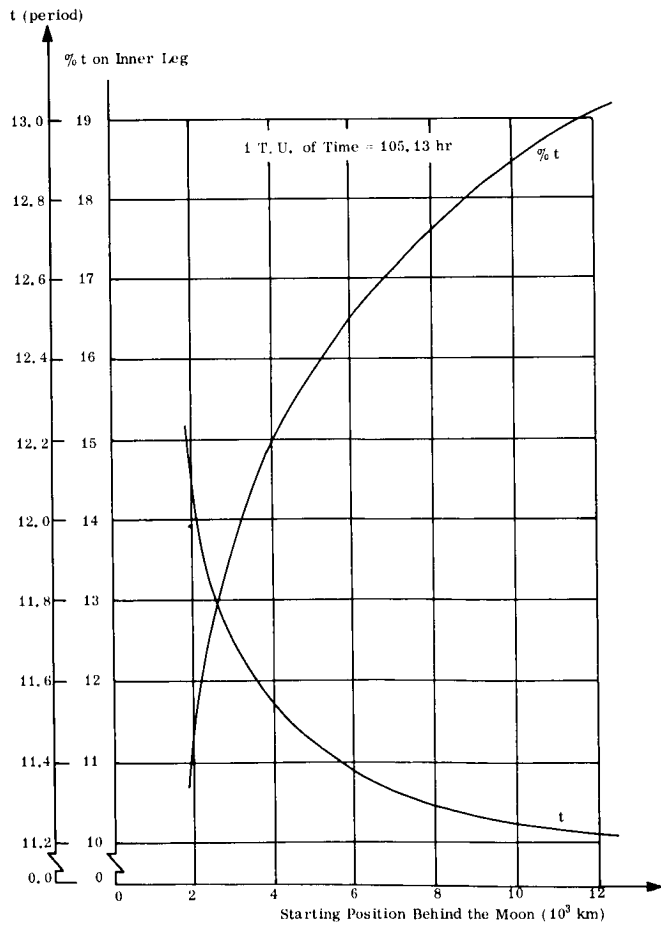


FIGURE 9. RATIO $1/2$, ORDER 2, CLASS A

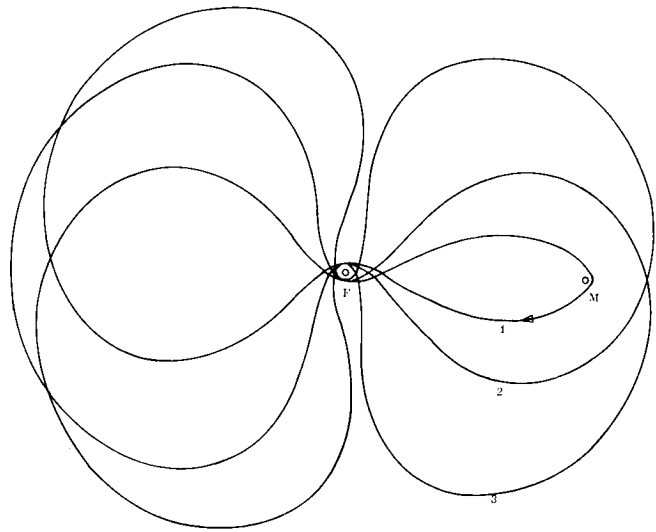


FIGURE 10. RATIO $1/2$, ORDER 3

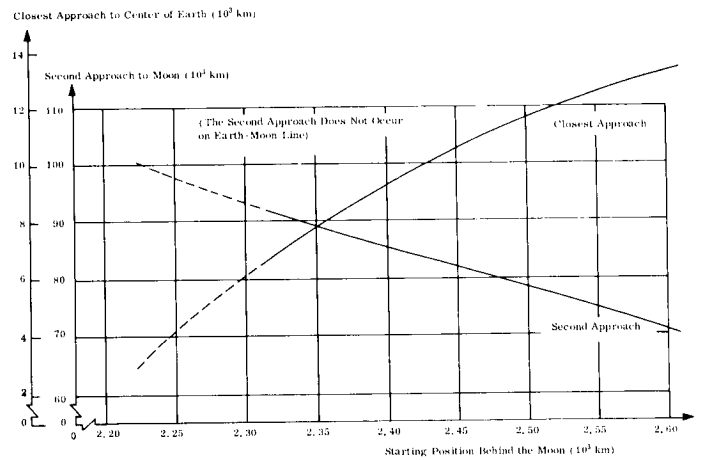


FIGURE 11. RATIO $1/2$, ORDER 3

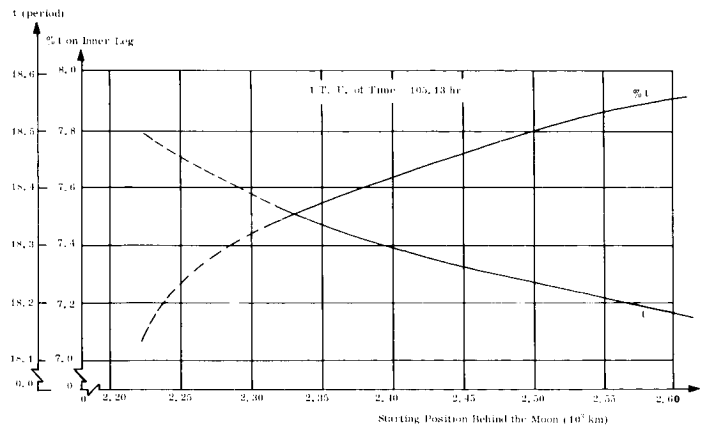


FIGURE 12. RATIO $1/2$, ORDER 3

Collision with the earth occurs for starting radii less than 2310 km. As seen in Figure 10, the second perpendicular crossing for the family occurs behind the earth.

Data for orbits of ratio $\frac{2}{3}$ order 1 are given in Figures 13 and 14. These orbits can be found with starting radii beginning at the moon's surface and extending out to 183,000 km.

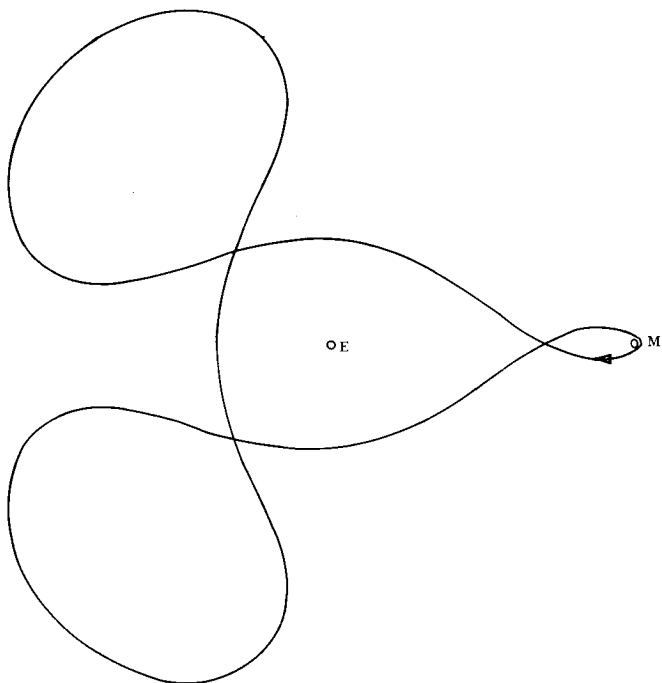


FIGURE 13. RATIO 2/3, ORDER 1

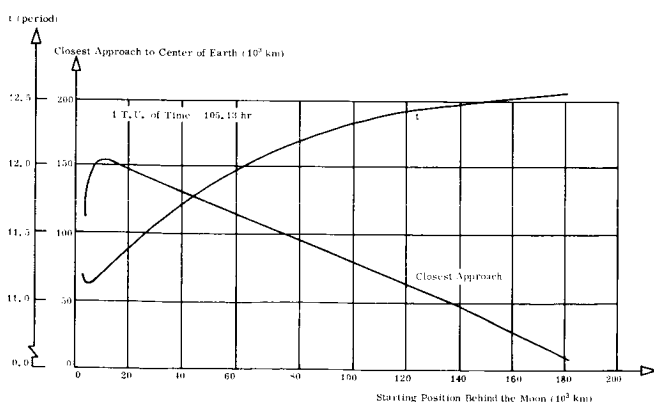


FIGURE 14. RATIO 2/3, ORDER 1

Figures 15, 16, 17, and 18 show data for orbits of ratio $\frac{2}{3}$ order 2 class B. At a starting radius of 51,000 km, there exists an orbit with a period of 8π (4 months). This family contains two solutions for the same starting radius for starting radii near 1994

km and 110,000 km; however, further investigation is necessary to determine the exact areas in which these solutions exist.

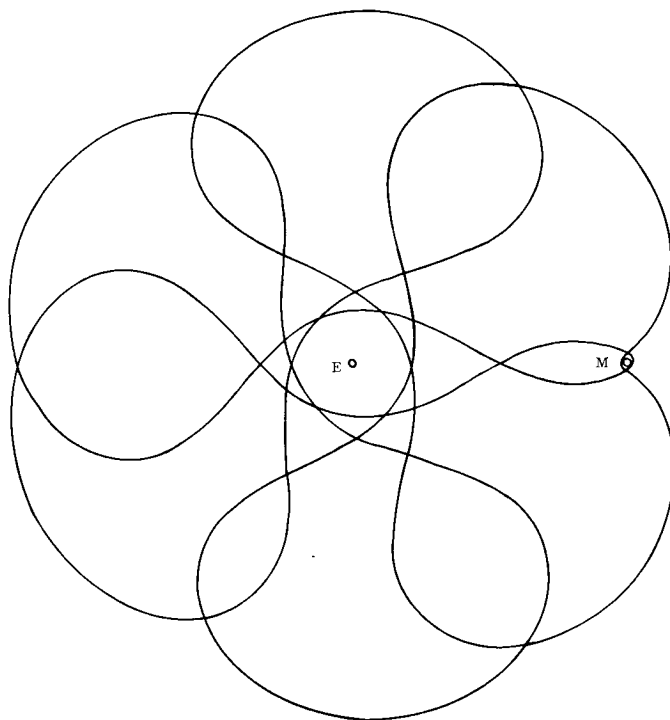


FIGURE 15. RATIO 2/3, ORDER 2, CLASS B

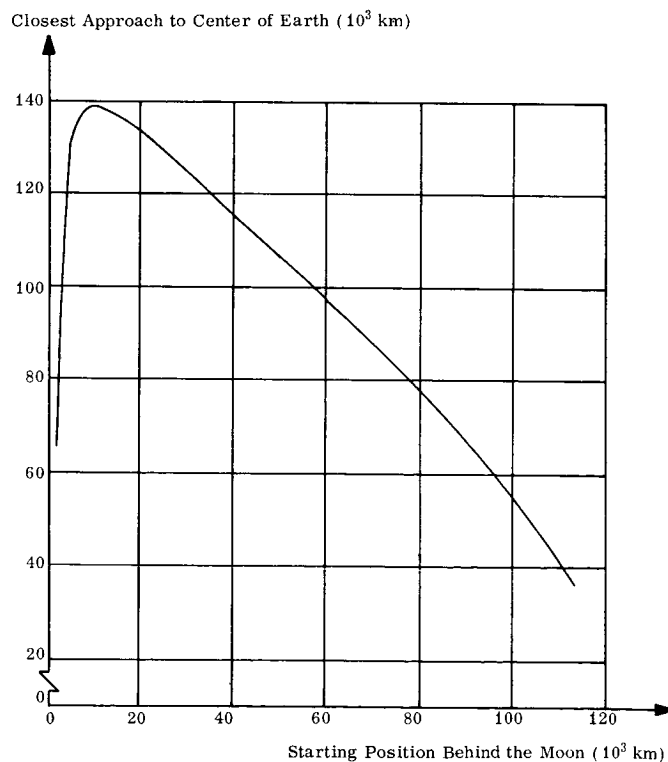


FIGURE 16. RATIO 2/3, ORDER 2, CLASS B

Data for orbits of ratio $\frac{2}{5}$ order 1 are shown in Figures 19, 20, and 21. This family of orbits exists for starting radii between 7800 km and 19,800 km. Beyond these limits the orbits collide with the surface of the earth.

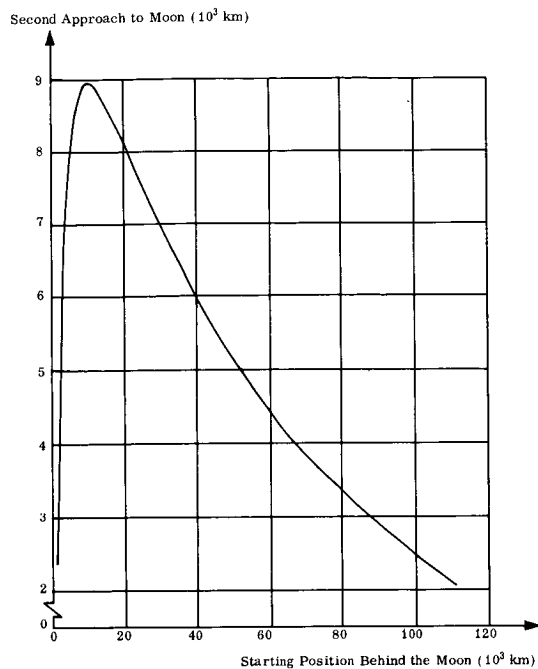


FIGURE 17. RATIO 2/3, ORDER 2, CLASS B

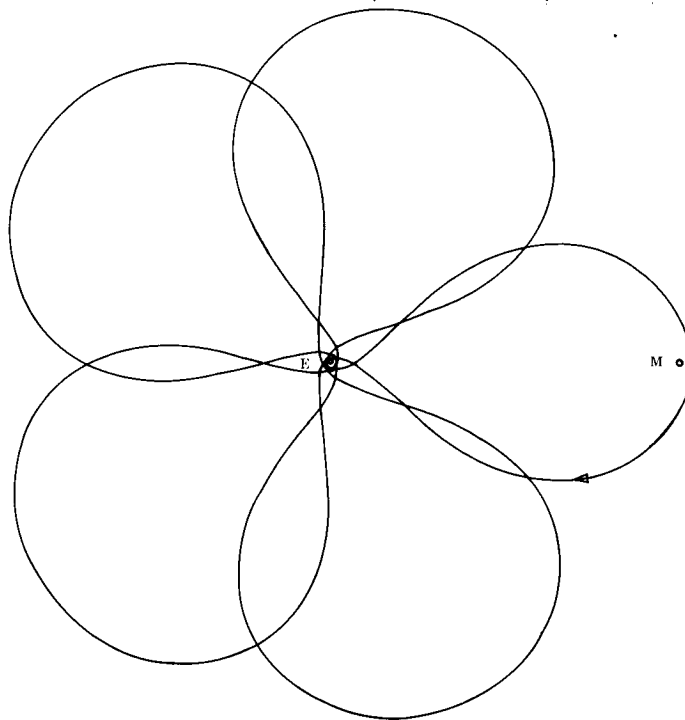


FIGURE 19. RATIO 2/5, ORDER 1

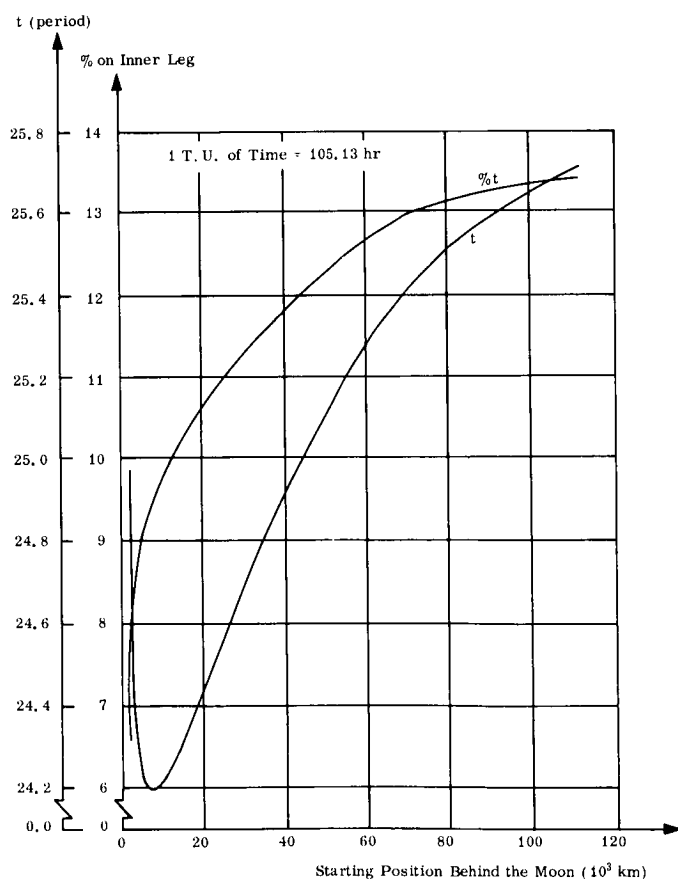


FIGURE 18. RATIO 2/3, ORDER 2, CLASS B

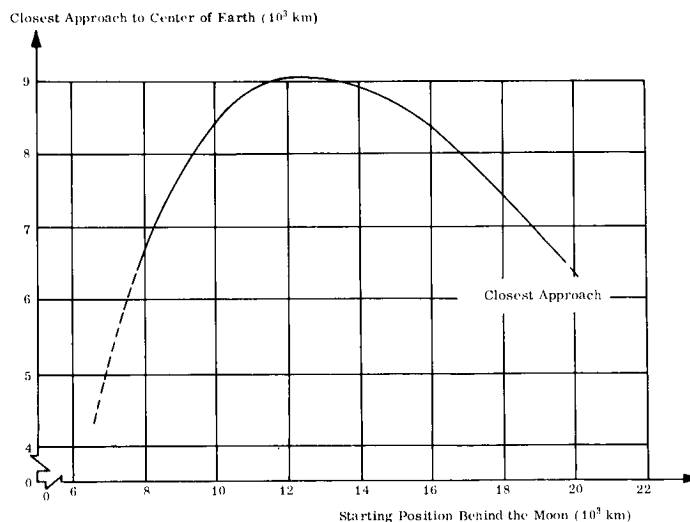


FIGURE 20. RATIO 2/5, ORDER 1

Information for orbits of ratio $\frac{3}{5}$ order 1 is given in Figures 22, 23, and 24. Members of this family were found for starting radii from 3187 km to 74,026 km. Two solutions were found for each starting position, and the alternate solution (the solution with the highest velocity) is denoted by an asterisk.

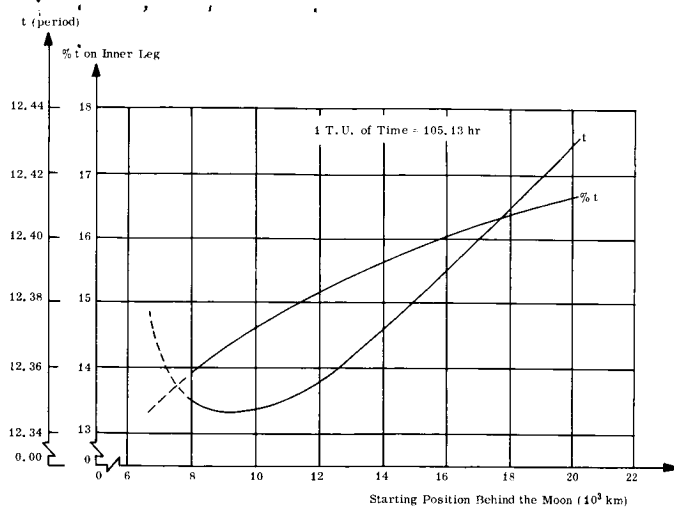


FIGURE 21. RATIO 2/5, ORDER 1

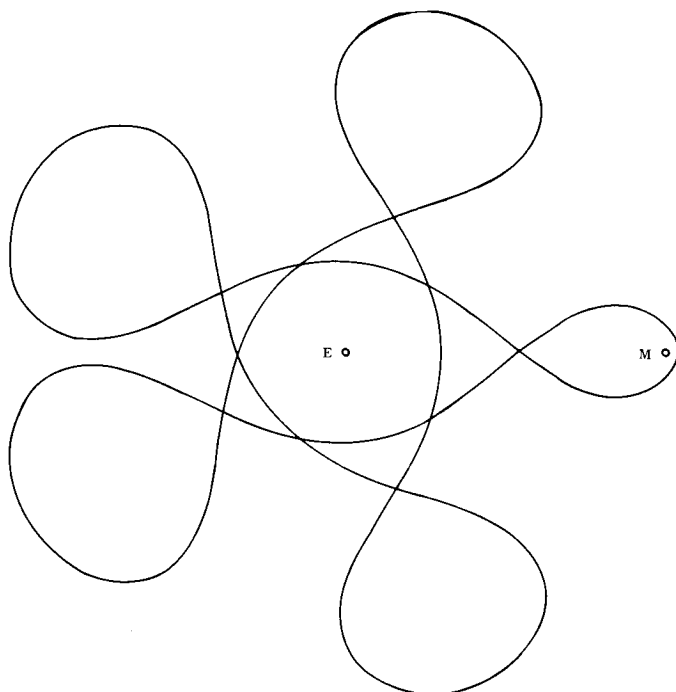


FIGURE 22. RATIO 3/5, ORDER 1

Data are given in Figures 25, 26 and 27. The velocity difference between two orbits starting from the same radius at the moon varied from 6.4 m/s to 38.4 m/s.

IV. CONCLUDING REMARKS

Periodic orbits of ratio $\frac{1}{2}$, $\frac{2}{3}$, $\frac{2}{5}$, and $\frac{3}{5}$ have been investigated. Higher order orbits of these ratios are being studied as well as different ratios; these will be described in a later paper. To aid in mission planning, Figure 28 shows a summary of some of the orbits which offer injection altitudes of the earth of approximately 100 nautical miles.

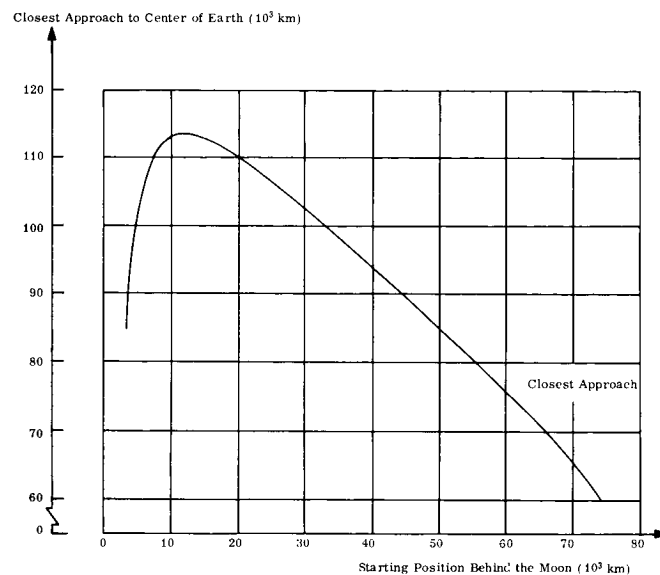


FIGURE 23. RATIO 3/5, ORDER 1

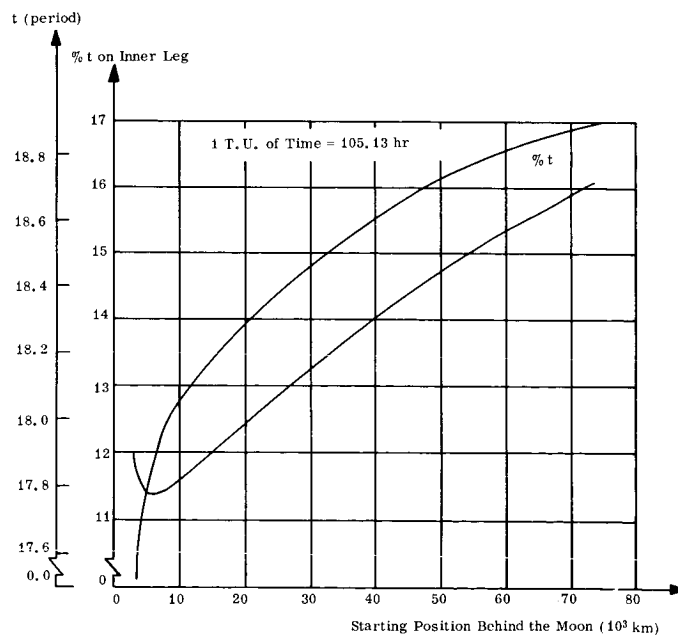


FIGURE 24. RATIO 3/5, ORDER 1

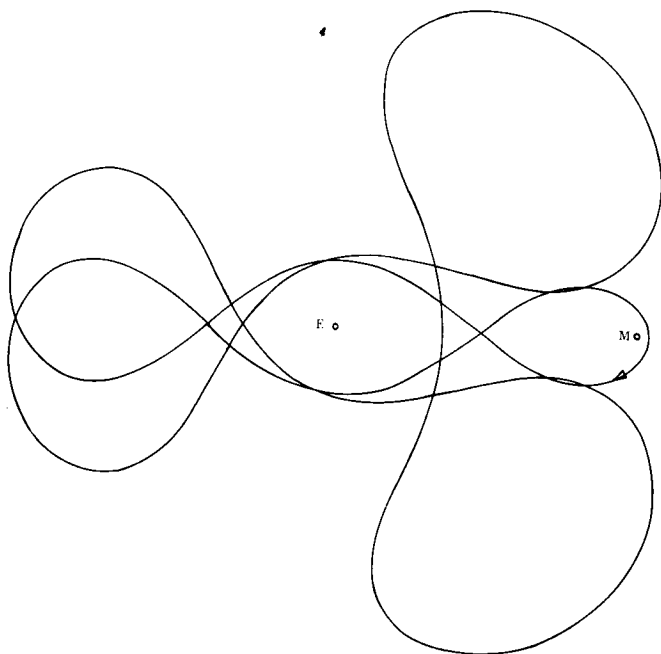


FIGURE 25. RATIO 3/5, ORDER 1*

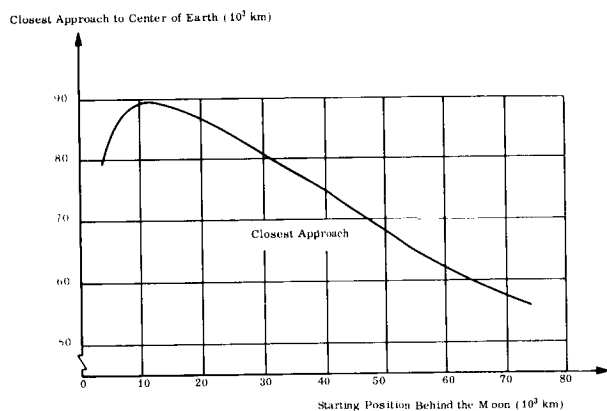


FIGURE 26. RATIO 3/5, ORDER 1*

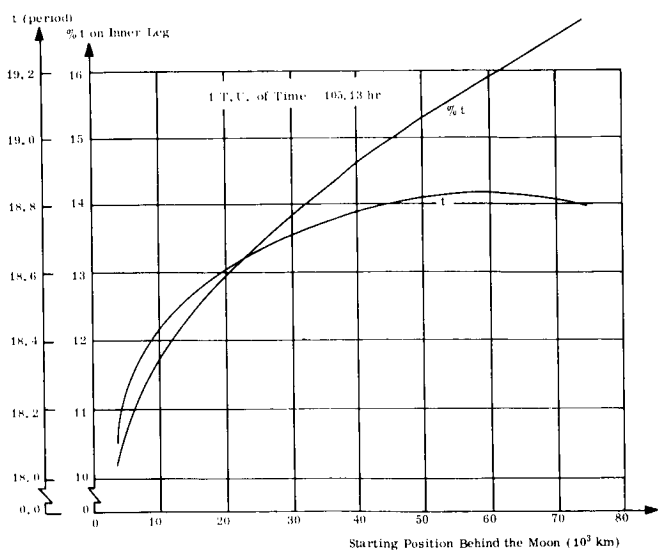


FIGURE 27. RATIO 3/5, ORDER 1*

FIGURE 28. ORBITS WITH INJECTION ALTITUDES ≈ 100 NAUTICAL MILES

| RATIO | ORDER | CLASS | FIRST APPROACH TO MOON (km) | SECOND APPROACH TO MOON (km) | CLOSEST APPROACH TO EARTH (km) | TIME FROM EARTH TO MOON (hrs) | TIME ON INNER LEG (°) | VELOCITY (SPACE-FIXED) (m/sec) | PERIOD (days) |
|-------|-------|-------|-----------------------------|------------------------------|--------------------------------|-------------------------------|-----------------------|--------------------------------|---------------|
| 1/2 | 1 | | 80,080 | - | 6,362 | 135 | 47.5 | 10,889.0 | 27.2 |
| 1/2 | 2 | A | 1,931 | 130,395 | 6,586 | 70 | 16.9 | 10,867.0 | 54.0 |
| 1/2 | 2 | B | 3,081 | 3,341 | 6,569 | 76 | 11.8 | 10,879.0 | 54.3 |
| 1/2 | 2 | B | 56,713 | 4,352 | 6,539 | 136 | 20.5 | 10,893.0 | 53.2 |
| 2/3 | 1 | | 182,561 | - | 6,374 | 208 | 31.5 | 10,882.0 | 55.0 |
| 2/3 | 1 | | 19,484 | - | 6,509 | 197 | 16.4 | 10,836.0 | 54.3 |
| 1/5 | 3 | A | 2,317 | 91,097 | 6,377 | 72 | 7.5 | 10,869.0 | 80.1 |

REFERENCES

1. Poincaré, H., *Les Methodes Nouvelles de la Mecanique Celeste*, Vol. I, p. 97.
2. Arenstorf, R. F., "Periodic Solutions of the Restricted Three-Body Problem Representing Analytic Continuation of Keplerian Elliptic Motion," NASA TN D-1859, May 1963.
3. Miele, A., "Theorem of Image Trajectories in the Earth-Moon Space," Boeing Scientific Research Laboratories, Flight Sciences Laboratory Report No. 21, January 1960.
4. Arenstorf, R. F., "Periodic Trajectories Passing Near Both Masses of the Restricted Problem of Three Bodies," Presented at the XIVth International Astronautical Congress, Paris, France, September 26 - October 1, 1963.

by

H. F. Kurtz, Jr.

and

A. R. McNair

N65-24141

SUMMARY

A brief review of the orbital lifetime prediction model currently in use at MSFC is made followed by discussion of two recent developments in lifetime studies. The first is an extension of graphical prediction charts to account for the effects of orbital inclination, argument of perigee, and date of launch. The second is a method of joint optimization of orbital lifetime and payload mass placed in orbit by a given vehicle. It is found by the latter method that significant increases in lifetime or payload mass may be obtained through the selection of an optimum elliptical orbit.

author

I. INTRODUCTION

For large vehicles of the Saturn class in low earth orbits, it becomes quite important to analyze the effects of atmospheric drag upon the orbit both for lifetime and decay prediction in mission planning and for post-flight orbit determination. This paper, after a brief review of the basic prediction model currently in use, presents a recent extension of a graphical prediction method and discusses recent findings in joint lifetime-payload mass optimization. The work described was performed partially in-house and partially by Lockheed Missiles and Space Company (LMSC) under contract NAS8-11121, and represents a continuation of studies begun in 1958 (Ref. 1) and last summarized in Reference 2. No attempt is made in this paper to present a comprehensive or detailed analysis, but rather to summarize recent progress.

II. REVIEW OF ORBITAL LIFETIME PREDICTION MODEL

The lifetime prediction model adopted is basically a common one, in which the decay rates of the orbital elements describing the altitude and shape of the orbit are represented by analytic derivatives:

$$\begin{aligned}\dot{a} &= \frac{da}{dt} = f_a(a, p, i, \Omega, \omega, \nu, \frac{C_D A}{M}, \rho) \\ \dot{p} &= \frac{dp}{dt} = f_p(a, p, i, \Omega, \omega, \nu, \frac{C_D A}{M}, \rho)\end{aligned}\quad (1)$$

where

a = apogee

p = perigee

i = inclination

Ω = right ascension of node

ω = argument of perigee

ν = true anomaly

C_D = drag coefficient

A = mass of vehicle

ρ = atmospheric density

Orbital
Elements

Parameters
of Drag

Mean decay rates \dot{a}_M and \dot{p}_M are obtained by integrating the equations (1) over an orbit, assuming that the orbital elements do not change over that time interval. Apogee and perigee are then obtained as a function of time by integration of the equations:

$$\frac{dp}{da} = \frac{\dot{p}_M}{\dot{a}_M} \quad \text{and} \quad (2)$$

$$\frac{dt}{da} = \frac{1}{\dot{a}_M}$$

The exact formulation of equations (1) and (2) is largely a matter of choice, and various formulations

are successful. The technique may vary from a relatively simple one, which has been largely used in MSFC studies (Ref. 2), to one of more sophistication such as that developed by LMSC for the Discoverer program (Ref. 3). The first technique neglects variation of the parameters i , Ω , and ω , and assumes a spherical earth model. The second technique integrates simple variational equations of the parameters i , Ω , and ω , and uses an oblate earth. The choice of parameters used in the formulation may also vary; for example, semi-major axis and eccentricity may be used instead of apogee and perigee. For many purposes a simple model carefully applied yields comparable results to the sophisticated model.

The primary factor of uncertainty in all current lifetime models is the atmospheric density ρ . Although the drag coefficient C_D and effective drag area A (for unstabilized bodies) also contribute noticeably to the uncertainty, their uncertainty is generally of lesser magnitude and may be removed to some extent by flight experience with similar vehicle configurations ("calibration" by orbit determination). Various models are used to represent ρ , which is itself a complex function of many parameters. The primary variables which are of significance in the lifetime model are (a) altitude dependence, (b) variation with solar activity, and (c) "diurnal bulge" variation.

The approach taken in MSFC studies has been to represent the altitude dependence by a standard model atmosphere (e.g., 1959 ARDC) and the diurnal bulge by an analytic multiplicative factor (Ref. 4). The variation with solar activity has been represented by a second multiplicative factor based upon an extrapolation of the solar activity level and an estimate of its effect upon the atmosphere.

This "solar activity" factor attempts to account for the mean variation due to the eleven-year solar activity cycle only. Short-period density effects such as the 27-day solar activity cycle are of much less importance. A typical form for this factor is discussed and shown graphically in Section III. A modified shift function based upon experience with the first two Saturn I orbital flights is being prepared.

For long term predictions (more than a few months in the future) substantial uncertainty exists in the solar activity shift factor, amounting to an uncertainty ($\sim 2\sigma$) of +150 percent and -60 percent in predicted lifetimes. This uncertainty magnitude is borne out by applying the prediction method to some 50 decayed satellites and comparing with actual lifetimes. The error distribution of these predictions is shown in Figure 1.

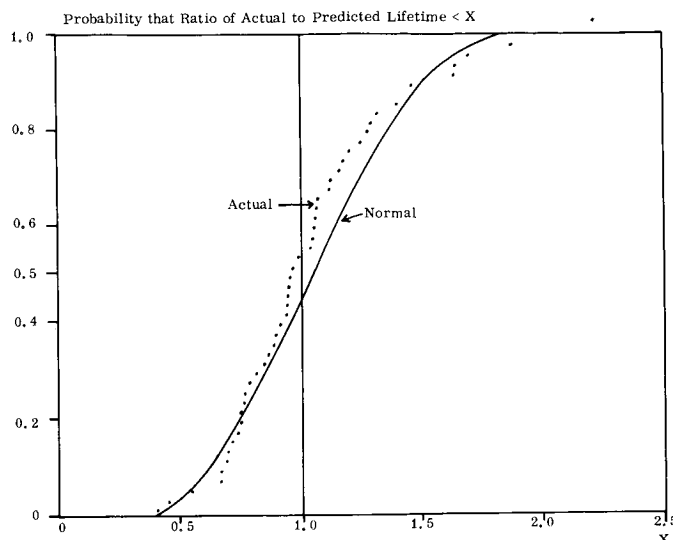


FIGURE 1. ERROR DISTRIBUTION OF LIFETIME PREDICTIONS

This uncertainty can, of course, be substantially reduced for post-launch predictions by using the observed initial orbit decay to "calibrate" the atmosphere (actually the atmosphere - ballistic factor product). The uncertainty can also be significantly reduced before launch by "calibrating" through the use of observed decay information from past flights or satellites still in orbit, providing a satellite at a similar altitude is available with sufficient tracking information.

III. IMPROVEMENTS IN GRAPHICAL MODEL

For many purposes in preliminary mission studies, the use of graphical methods to predict orbital lifetimes provides convenience, permits quick response, and affords sufficient accuracy to make it an efficient method. Graphs providing normalized lifetime as a function of apogee and perigee altitudes, as shown in Figure 2, can be found many times in the literature. Figure 2 was generated by LMSC (Ref. 5). To make an approximate lifetime prediction, the normalized lifetime L' for a given orbit is read from the graph; multiplying by the inverse ballistic factor ($M/C_D A$) yields the absolute lifetime estimate, L .

$$L = L' (M/C_D A)$$

The graphical method has been extended to permit correction for major factors affecting the lifetime other than apogee and perigee. The corrected lifetime prediction takes the form

$$L = [M/C_D A] [L'] [f(t)] [f(i, \omega)].$$

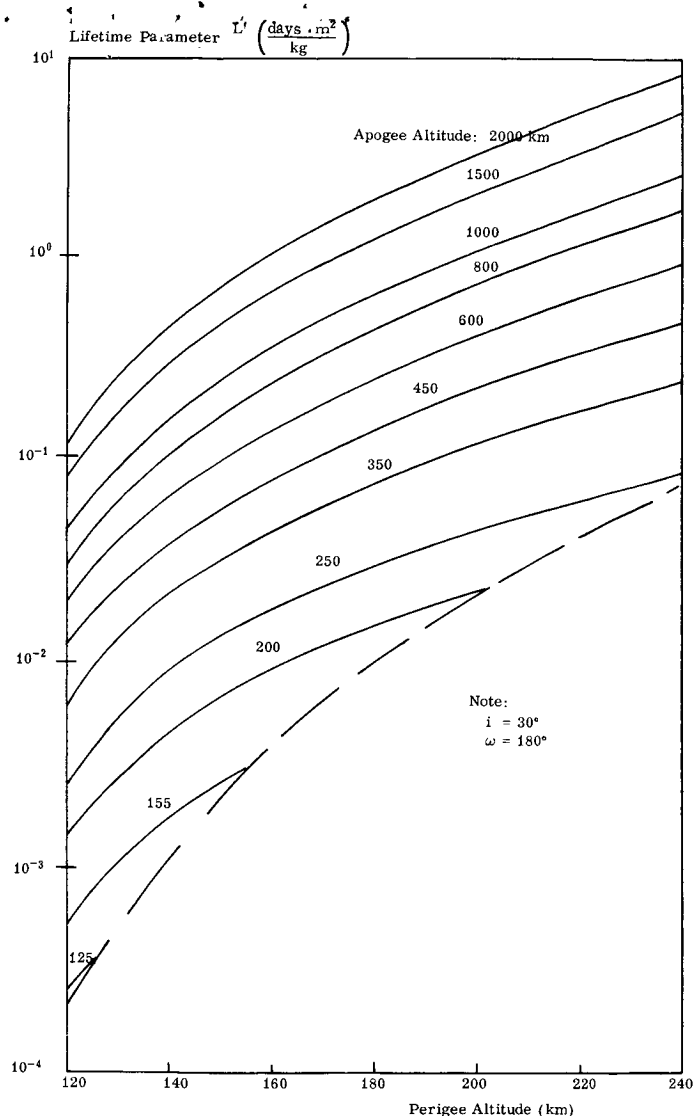


FIGURE 2. LIFETIME PARAMETER AS A FUNCTION OF ORBITAL ALTITUDE

The correction factor $f(i, \omega)$, shown in Figure 3, is a function of i , the orbital inclination, and ω , the initial argument of perigee. This factor adjusts the predicted lifetime to account for the oblate geometrical earth, which causes an effective variation in the satellite altitude and is dependent upon the orientation of the orbit relative to the earth equator. The $f(i, \omega)$ function was derived numerically from many cases computed with the LMSC sophisticated lifetime model, which includes the change of argument of perigee due to the oblate earth gravitation model. The curves shown represent average values for various orbital altitudes, eccentricities, and ballistic factors. For most purposes the variation of $f(i, \omega)$ can be neglected.

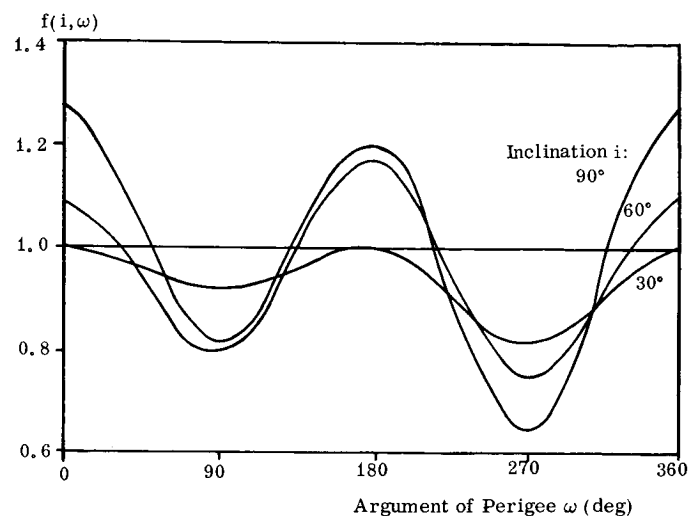


FIGURE 3. LIFETIME CORRECTION FACTOR AS A FUNCTION OF INCLINATION AND ARGUMENT OF PERIGEE

The correction factor $f(t)$ is shown in Figure 4.

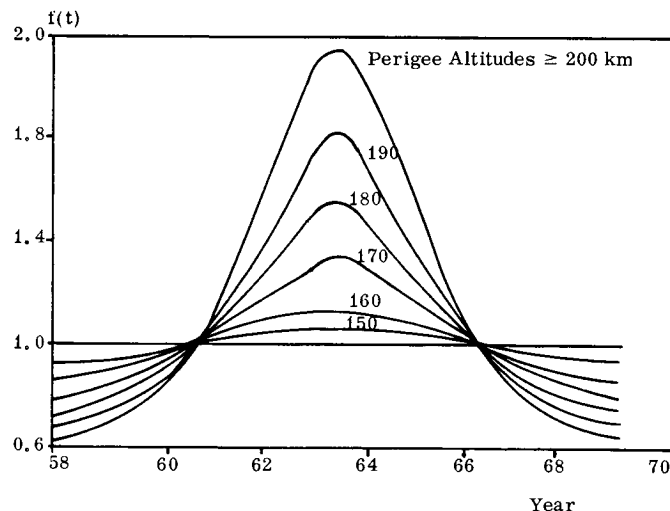


FIGURE 4. LIFETIME CORRECTION FACTOR AS A FUNCTION OF DATE

This factor corrects the lifetime prediction for the variation of atmospheric density with the eleven-year solar activity cycle, and is based upon a semi-empirical atmosphere model previously developed by LMSC in the Discoverer program (Ref. 6). For maximum accuracy in predicting lifetimes of longer than two months, the mean value of $f(t)$ over the approximate lifetime should be used. For lifetimes of less than two months, the value of $f(t)$ at the initial time may be used.

Use of the correction factors with the normalized lifetime curves yields accuracies of lifetime prediction comparable with that obtained by the more exact computational model from which they were derived. The correction factors given in Figures 3 and 4 are referenced specifically to Figure 2 and, in general, cannot be directly applied to similar graphs of lifetime versus apogee and perigee.

IV. ORBIT OPTIMIZATION

In planning the orbital altitude and eccentricity for future satellites, it is often desired to guarantee a specified orbital lifetime, and also maximize the payload mass in orbit or, conversely, to maximize the lifetime for a given payload. Payload mass - lifting capabilities of the Saturn launch vehicles are derived using calculus of variations techniques to optimize trajectory parameters for maximum payload. This optimization defines the apogee-perigee altitudes achievable by the launch vehicle for different orbital payload masses (Fig. 5).

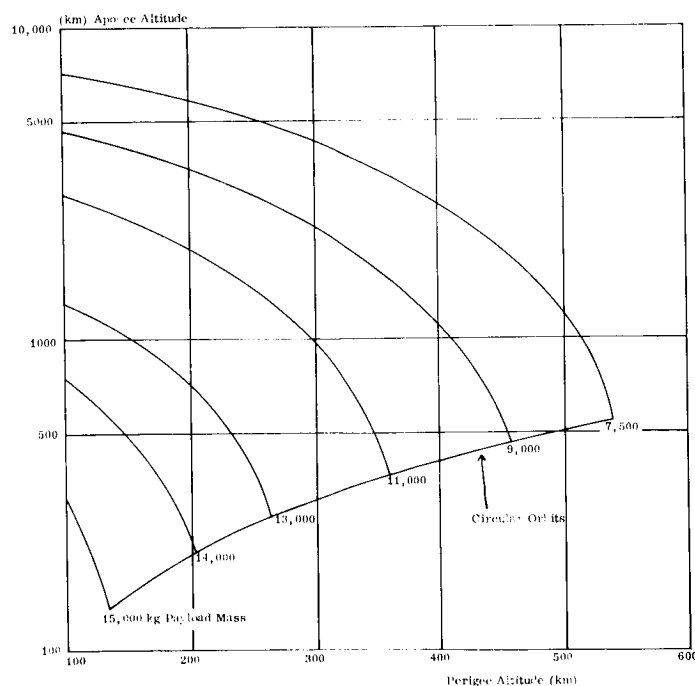


FIGURE 5. LAUNCH VEHICLE ORBITAL CAPABILITY

Orbital lifetime analysis of numerous sets of such performance data derived for Saturn launch vehicles has yielded a common result. Selecting a given payload mass, and plotting the lifetimes predicted for the possible maximum achievable orbits, we found that there is a specific elliptical orbit for which the orbital

lifetime is clearly optimized (Fig. 6). The apogee/perigee ratio which yields this best orbit appears to

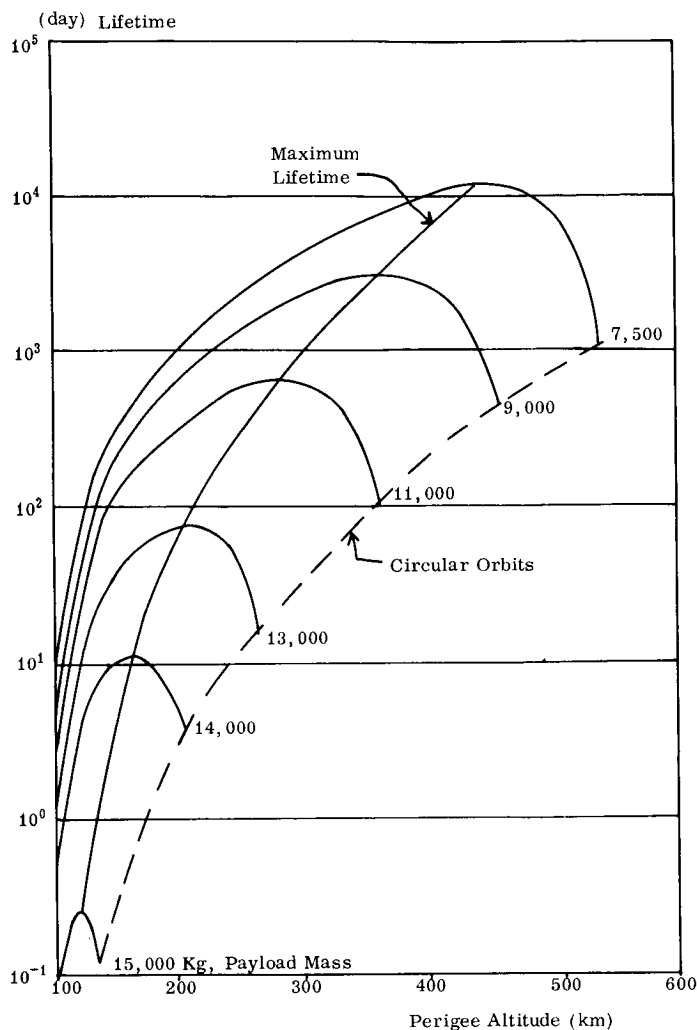


FIGURE 6. ORBITAL LIFETIME OPTIMIZATION

be dependent upon the particular set of vehicle performance data. The optimum apogee-perigee combination is independent of the ballistic coefficient of the satellite, as long as a constant configuration is considered. In analyses thus far the apogee/perigee ratio has varied between two and four, increasing with perigee altitude.

Some interesting results obtained for one case which has been studied are presented. These results illustrate an application which has been made of this principle of an optimum orbit to yield maximum lifetime for specified vehicle performance. Other applications have also been made. The fifth Saturn I test flight orbit was optimized for maximum lifetime. Extensive investigations have been made in defining the orbit of the ninth Saturn I flight carrying a meteoroid experiment.

In this illustrative case, the primary concern was maximizing payload mass for a given configuration and a specified orbital lifetime. The orbital capability of the launch vehicle was expressed in Figure 5 as maximum apogee altitude which can be achieved as a function of perigee altitude for different payload masses. The lower envelope designates the limiting case of circular orbits. The orbital lifetime obtained for the different masses is shown in Figure 6 as a function of perigee altitude, assuming the maximum possible apogee associated with the perigee and payload mass. The locus of the maximum lifetime curve is shown in Figure 7 superimposed on the performance

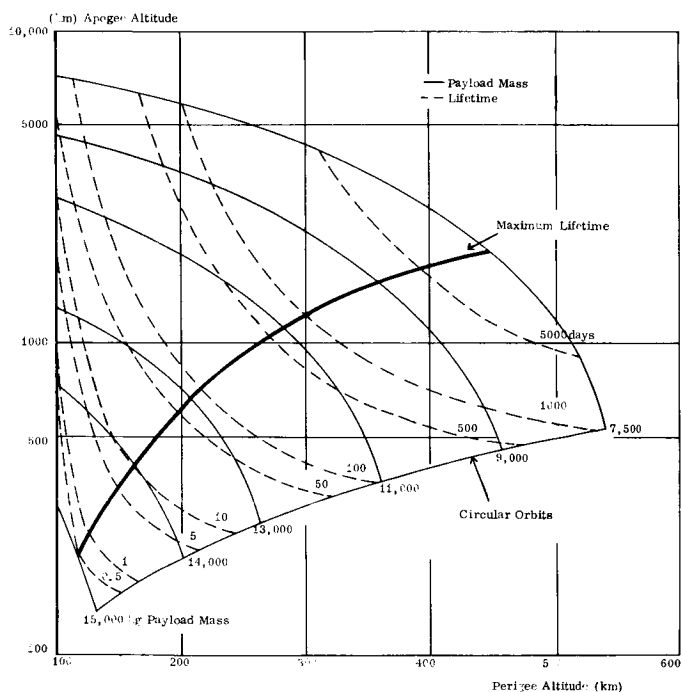


FIGURE 7. LOCUS OF MAXIMUM LIFETIME AND CONTOURS OF CONSTANT LIFETIME

data of Figure 5, with contours of constant lifetime also indicated. The orbital lifetime varies as the payload mass varies, and identical lifetimes may be obtained for different payload masses with a proper selection of the apogee-perigee combination.

Using these data, an optimization can be performed to maximize the payload mass for any desired lifetime. This is noted by observation of the lifetime contour curves of Figure 7 where maximum payload values for a given lifetime occur along the locus curve of maximum lifetime. The amount of the gain in payload mass resulting from the optimization is more clearly seen in Figure 8. The potential percentage gain or loss in payload mass which can be achieved by using an elliptical rather than a circular orbit to yield a specified lifetime is shown in Figure 8 as a

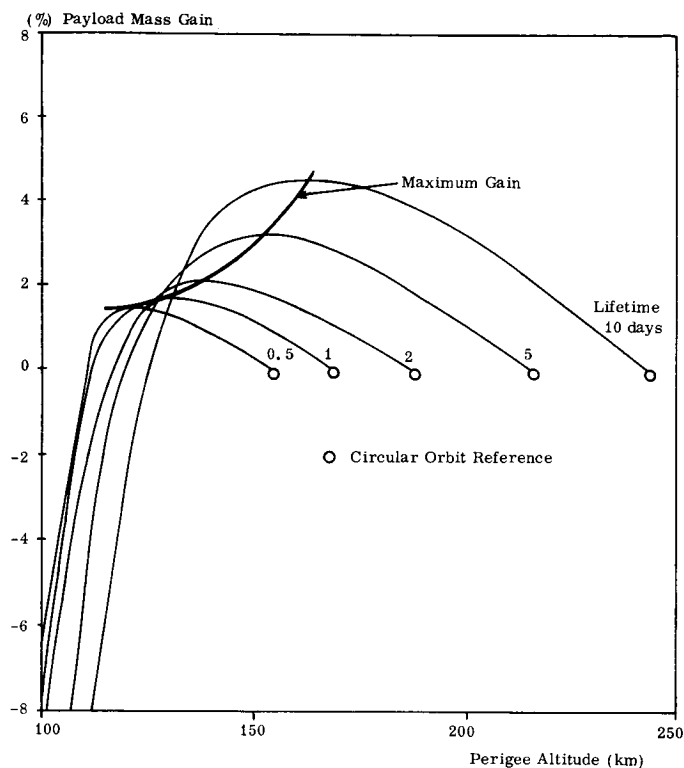


FIGURE 8. PAYLOAD MASS OPTIMIZATION

function of perigee altitude. A clear maximum is seen in each of the constant lifetime curves. The gain realized by this optimization increases in importance as the absolute lifetime required increases.

REFERENCES

1. Kurtz, F., and McNair, A., Satellite Lifetime, ABMA Report No. DA-TN-9-59, January 29, 1959.
2. Ladner, James E., and Ragsdale, George C., Earth Orbital Satellite Lifetime, MSFC Report No. MTP-AERO-62-77, October 24, 1962.
3. Small, M. W., and Johnston, R. C., A High Speed Computer Program for Predicting the Decay of Earth Satellites, LMSC Report No. TM 53-73-11, May 13, 1963.
4. Jacchia, L. G., A Variable Atmospheric - Density Model from Satellite Accelerations, Smithsonian Special Report No. 39, March 30, 1960.
5. Cassara, P. P., Seventh Monthly Status Report: Orbital Lifetime Study Contract NAS8-11121, Report No. LMSC/HREC A036147, May 12, 1964.
6. Poe, R. F., A Review of the Geophysical Model, LMSC Report No. IDC 57-13-196, September 25, 1961.

VII. PUBLICATIONS AND PRESENTATIONS

A. PUBLICATIONS

MTP-AERO-64-1

January 15, 1964

LONGITUDINAL PROPELLANT VIBRATIONS

By

Larry Kiefling

ABSTRACT

A direct iteration procedure is given for calculating the natural frequency of longitudinal vibration of propellant in a cylindrical tank with elastic walls. Tank walls are assumed to deform under pure hoop stress. Propellant is considered incompressible. The mass of the tank walls and elasticity of a hemispherical end are included. Frequency data for a simple case and the outer tanks of Saturn I, Block II vehicles are given. These vibrations are in the same frequency range as some lower bending modes for the earlier flight times.

MTP-AERO-64-2

January 15, 1964

HEAT AND MASS TRANSFER IN BINARY INERT GAS FLOW FOR DISTRIBUTIONS OF TEMPERATURE AND CONCENTRATION RENDERING THE PROPERTIES NEARLY CONSTANT

By

Ernst W. Adams, John D. Warmbrod, C. Lee Fox,
and Robert M. Huffaker

ABSTRACT

Injection of a foreign gas into the laminar air boundary layer is considered. The mixture properties are arbitrary functions of temperature T and foreign gas concentration w . Unless the properties are constant, similarity transformations are valid only at the stagnation point or for a wall at constant pressure. Solutions of the three similarity equations are quite cumbersome because triple iterations are involved at the wall to satisfy three conditions at the outer edge

of the boundary layer. A correlation formula of rigorous numerical solutions for q_w/q_{w0} has been derived in Reference 14 for the constant pressure case. Here, q_w is the heat transfer in the presence of mass transfer, whose absence is denoted by subscript o . This correlation formula is linear in the mass transfer rate $\rho_w v_w$, and, therefore, fails for large values of $\rho_w v_w$.

A simple engineering solution method of the similarity equations is proposed here, which gives those points of the q_w/q_{w0} versus $\rho_w v_w$ relationship for which five property parameters are nearly constant across the boundary layer. If these five conditions are satisfied, the differential equations in similarity variables can be uncoupled. By use of an auxiliary graph, the momentum equation can be integrated directly as an initial value problem. This solution is used to determine q_w by quadratures. Correlation formulas for q_w are presented for both the constant pressure and the stagnation point cases.

The five conditions on the mixture properties can be satisfied in an approximate way for the injection of H_2O , He , or H_2 into air, provided dissipation effects are sufficiently small. Comparison to the correlation formula of Reference 14 shows very good agreement if the Mach number $M_\infty = 0$, and some difference for $M_\infty = 3$. The results for H_2O -air mixtures cover the range of q_w/q_{w0} values from unity to values as low as 0.5. Only very small injection rates are compatible with the five conditions if He or H_2 is injected into air. The theory is worked out in this paper for the case of constant pressure and air as the primary flowing medium.

TECHNICAL MEMORANDUM X-53008

February 18, 1964

THEORETICAL AND EXPERIMENTAL INVESTIGATION OF BOUNDARY LAYER CONTROL IN LOW-DENSITY NOZZLES BY WALL SUCTION AND COOLING

By

M. R. Bottorff and K. W. Rogers*

ABSTRACT

*Engineering Center, University of Southern Calif.

Presented in this report are the results of a theoretical and experimental investigation of the reduction of boundary layer thickness in low-density nozzles by wall cooling, wall suction, and a combination of these two. Potentially there is a twofold benefit in reducing the thickness of the nozzle boundary layer: (1) a possible increase in diffuser effectiveness, and (2) a possible reduction in the amount of boundary layer flow for a specified usable test section size, or an increase in the size of the usable test section for a given nozzle mass flow. The theoretical development starts with the proper integral relationship for a compressible laminar boundary layer. The normal velocity at the wall is allowed to be finite to include the effects of wall suction. Definitions of momentum and displacement thicknesses which account for transverse curvature are used. The results of Iglisch, who developed an exact solution for incompressible flat plate flow with suction, are used to estimate skin friction coefficients. The Prandtl number is assumed to be unity, and two-dimensional values of δ^*/θ are used. An exponential velocity profile which takes wall suction into account was used to estimate boundary layer height.

The theoretical results were checked by an experiment in which a Mach number 9 - to - 11 porous nozzle was operated at unit Reynolds numbers in the range of 100/inch to 600/inch. Pitot pressure surveys were used to determine the exit Mach number and boundary layer thickness. Theoretical Mach number predictions are shown to agree with the experimental results to within 5 percent, and boundary layer height predictions to within 10 percent.

Theoretical results are presented which show the effects of suction and wall cooling at several Reynolds numbers on nozzle diameter and uniform core size for a given throat area and Mach number distribution. It is concluded that the use of suction and cooling may result in a larger test section size, but that the merits of a cooled porous wall in any specific case must be decided from an analysis of the complete wind tunnel system.

TECHNICAL MEMORANDUM X-53009

February 21, 1964

DIRECTIONAL WIND COMPONENT FREQUENCY ENVELOPES, CAPE KENNEDY, FLORIDA, ATLANTIC MISSILE RANGE

By

Orvel E. Smith and Glenn E. Daniels

ABSTRACT

Directional Wind Component Frequency Envelopes for Cape Kennedy, Florida, based on the "windiest monthly period" concept, are presented in this report for use in structural and control studies in the design of aerospace vehicles.

TECHNICAL MEMORANDUM X-53013

February 18, 1964

TEMPERATURE MEASUREMENT INSIDE A RAWINSONDE BALLOON

By

George T. Norwood, Jr.

ABSTRACT

Provided in this report is information concerning a comparison of temperature inside a Rawinsonde balloon and the ambient temperature. This study may be of use to persons working with radiosonde and associated equipment.

TECHNICAL MEMORANDUM X-53017

March 3, 1964

STABILITY ANALYSIS OF SATURN SA-5 WITH LIVE S-IV STAGE

By

Philip J. Hays and Phil Sumrall

ABSTRACT

A control feedback stability analysis of Saturn SA-5 during powered flight was performed for the S-I and S-IV stages. Sloshing stability was investigated by considering two propellant damping (ξ_s) values for booster flight: (1) $\xi_s = 1/2$ percent of critical damping (corresponding to wall friction), and (2) the predicted flight damping (due to the z-rings and the accordion baffles). The predicted flight damping values were used for the S-IV flight. The sloshing instability in the 70-inch LOX tank is caused by roll coupling, but proper tank baffling eliminates the problem;

therefore, no instability will occur during booster flight until 133 seconds when the fluid leaves the last baffle. No instability is experienced in pitch because of the large mass in the S-IV LOX tank, which counteracts the slosh masses in the S-I stage. A slight instability in the LH₂ tank exists at ignition for the S-IV flight.

Bending mode stability was achieved by two methods for booster flight: phase stabilization and attenuation stabilization. Gain stabilization was employed for all elastic modes in the roll and α -channels. The φ -channel phase stabilized the first lateral bending mode and gain stabilized the higher modes. The elastic modes in the φ -channel were attenuated for the S-IV flight. Stability was achieved for booster and S-IV flights.

TECHNICAL MEMORANDUM X-53018

March 5, 1964

SPACE RADIATIONS: A COMPILATION AND DISCUSSION

By

W. T. Roberts

ABSTRACT

The natural radiations encountered during a space mission will fall into one of five categories. There will be Van Allen belts, galactic cosmic radiations, solar winds, solar flares, and photon radiations. Each type of radiation is examined from the point of view of the Apollo program and the associated lunar logistics vehicle, but with some comments pointing to extended missions in space, to determine the importance which should be assigned to each class.

TECHNICAL MEMORANDUM X-53020

March 6, 1964

SATURN V UPRATING STUDY

By

Ronald Scott, Terrell Deaton,
Ronald Toelle, and Neva Huffaker

ABSTRACT

Presented in this report is the performance capability of several uprated Saturn V vehicle configurations.

The configurations selected for this study represent a wide spectrum of payloads and are reflected in moderate vehicle uprating to rather advanced vehicle concepts.

The presentation of the relative performance between the configurations should be a valuable aid in determining the proper steps to be taken to uprate the performance capability of the basic Saturn V vehicle.

Report classified (C).

TECHNICAL MEMORANDUM X-53021

March 9, 1964

DIRECTIONAL WIND COMPONENT FREQUENCY ENVELOPES, SANTA MONICA, CALIFORNIA, PACIFIC MISSILE RANGE

By

Orvel E. Smith and Glenn E. Daniels

ABSTRACT

Directional Wind Component Frequency Envelopes for Santa Monica, California, based on the "windiest monthly period" concept, are presented in this report for use in structural and control studies in the design of aerospace vehicles.

TECHNICAL MEMORANDUM X-53023

March 13, 1964

TERRESTRIAL ENVIRONMENT (CLIMATIC) CRITERIA GUIDELINES FOR USE IN SPACE VEHICLE DEVELOPMENT, 1964 REVISION

By

Glenn E. Daniels

ABSTRACT

Provided in this document are guidelines on probable climatic extremes and probabilities of occurrence

of terrestrial environmental data specifically for space vehicle and associated equipment development. The geographic areas encompassed are the Atlantic Missile Range (Cape Kennedy, Florida); Huntsville, Alabama; New Orleans, Louisiana; the Pacific Missile Range (Point Mugu, California); Sacramento, California; Wallops Test Range (Wallops Island, Virginia); White Sands Missile Range, New Mexico; and intermediate transportation areas. Therefore, this document omits climatic extremes for world-wide operations. This is consistent with the existing philosophy regarding the employment of large space vehicles, since launching and test areas are relatively restricted due to the availability of facilities and real estate.

This document presents the latest available information on probable climatic extremes, and supersedes previous information presented in MTP-AERO-63-8 (Ref. 1). Where differences exist between this document and MTP-AERO-63-8, the data presented herein shall be employed. The information in this document is recommended for employment in the development of space vehicles and associated equipment, unless otherwise stated in contract work specifications.

TECHNICAL MEMORANDUM X-53024

March 17, 1964

PROGRESS REPORT NO. 5

SPACE FLIGHT AND GUIDANCE THEORY

By

William E. Miner

ABSTRACT

This paper contains progress reports of NASA-sponsored studies in the areas of space flight and guidance theory. The studies are carried on by several universities and industrial companies. This progress report covers the period from July 18, 1963, to December 18, 1963. The technical supervisor of the contracts is W. E. Miner, Deputy Chief of the Astrodynamics and Guidance Theory Division, Aero-Astrodynamics Laboratory, George C. Marshall Space Flight Center.

TECHNICAL MEMORANDUM X-53026

March 18, 1964

BOOSTER PARAMETRIC DESIGN METHOD FOR PERFORMANCE AND TRAJECTORY ANALYSIS PART I: CONFIGURATION

By

V. Verderaine

ABSTRACT

A method is presented for mathematically describing the geometric configuration of a conventional liquid chemical booster stage for a vertically launched space vehicle. Geometric properties of all significant components were derived in parametric form. Results were summarized in schematic dimensional diagrams for two arrangements of tanked bipropellant fluids. These results will serve as a basis for formulating mass parametric equations as required for performance and trajectory analysis.

TECHNICAL MEMORANDUM X-53027

April 10, 1964

CAPE KENNEDY LOW LEVEL WIND STUDY FOR SEPTEMBER 23 - 25, 1963

By

Carroll Hasseltine

ABSTRACT

Compared in this report are the high winds recorded at Cape Kennedy, September 23 - 25, 1963, with the previously computed 95, 99, and 99.9 percentile wind speeds used for design criteria at Cape Kennedy and vicinity. Methods used in computing the wind speeds at Cape Kennedy are explained. Data are presented for the length of time that these percentile wind values were exceeded. A comparison of the constants describing the wind speed profiles for different wind speeds and a comparison of gust factors are also presented. Some of the computed constants which best describe the characteristics of high surface winds are shown to differ from the constants which best describe the entire spectrum of wind speeds.

TECHNICAL MEMORANDUM X-53029

April 6, 1964

By

April 22, 1964

Gale R. Ernsberger

ON SOUND INTENSITY AND SOUND PRESSURE
LEVELS

ABSTRACT

By

Willi H. Heybey

ABSTRACT

The purpose of these vibration tests is to determine the body bending and torsional dynamic behavior of a full scale prototype of the Saturn SA-6 flight vehicle. A full scale prototype was vertically suspended in the test tower and excited by shakers mounted at the engine gimbal planes. The vehicle's dynamic response at various applied forcing frequencies was recorded by vibration pickups. Since the Saturn is stabilized and controlled by a servo loop, response measurements are needed to properly design the control system filter circuits, thus preventing vehicle dynamic instability. The SAD-6 vehicle was tested for both the boost flight with the S-I booster stage and for the S-IV powered flight with the S-I stage removed.

Sound propagation through the open atmosphere is studied at MSFC mainly for an estimate of the acoustical energy that sound rays sent up by static firings and refracted back to ground level may transmit to inhabited areas. A theoretical expression derived in an earlier report (Ref. 1) for the volume density of returned energy is converted into an expression for the corresponding intensity level to accommodate it to engineering practice. A first approximation of the latter's relationship to the sound pressure level (as an observable quantity) is established. The results of the theory can thus be compared to those of field measurements by microphones, and a basis for theoretical prediction is prepared.

TECHNICAL MEMORANDUM X-53031

April 6, 1964

SA-6 PREDICTED STANDARD TRAJECTORY AND
DISPERSION ANALYSIS

By

J. L. Crafts

ABSTRACT

Presented in this report is the standard trajectory for Saturn I vehicle SA-6 to be flown over the Atlantic Missile Range. Dispersion results from $2\text{-}\sigma$ perturbations and impact dispersion of the recoverable camera capsules and launch escape system are also presented. The trajectory shaping and a brief vehicle configuration description are provided. A nominal trajectory will insert the S-IV stage and payload into a near-circular orbit with a perigee and apogee of 183.1 km and 229.4 km, respectively. This orbit has a nominal lifetime of 4.8 days. This trajectory is based on mass and propulsion data provided by P&VE Laboratory. SA-6 will be the first Block II vehicle to be flown with closed loop guidance during the burn of the S-IV stage. This trajectory assumes the Fischer Ellipsoid of 1960 as the reference ellipsoid.

Report classified (C).

TECHNICAL MEMORANDUM X-53036

April 22, 1964

CONTROL THEORY HANDBOOK

By

Doyle Garner

ABSTRACT

This report is written to present under one cover, employing a unified coordinate system and notation, the equations of motion and the basic control theory applicable to stability analyses for a flexible launch vehicle.

Five of the basic control problems are discussed to provide some background and insight in the control of large flexible boosters moving through the earth's atmosphere.

The control system coordinate and notations are shown and the rigid body equations are derived for both the pitch and yaw planes. A conventional control

system is introduced containing a position gyro, rate gyro, accelerometer and angle of attack meter. The gains of the control mechanism and the vehicle parameters are related to the frequency and damping of the rigid body. Both the "Drift Minimum" and "Load Minimum" control principles are developed.

The bending and slosh equations are derived by writing the energy expressions and subsequently applying Lagrange's equation. The method of computing bending modes and frequencies for a flexible body is shown for both a simplified continuous mass model and a lumped mass model.

The construction of a synthetic wind profile for control system studies using the 95 percent or 99 percent probability of occurrence wind speed profile and the 99 percent probability of occurrence wind shear envelope is discussed and illustrated. The method for superimposing a gust on the synthetic wind profile is also shown.

Block diagrams and the Laplace transform are introduced to relate the system equations in a form which can be studied in terms of general feedback theory.

Several stability analysis techniques are discussed, including Routh's stability criterion, Hurwitz's stability criterion, root locus, frequency response methods, and Nyquist's criterion. These techniques are applied to a vehicle containing one bending mode, a control filter and an actuator. The corresponding root locus plot, Bode plot, Nyquist plot and Nichols plot are drawn.

The basic elements of an example adaptive control system are discussed and its corresponding block diagram is shown.

The appendices contain the block diagram and transfer functions for several sensors and engine actuator. A summary of the flexible body equations includes the effects of engine inertia, bending motion and slosh motion and a derivation of the bending moment at any station along the vehicle longitudinal axis.

TECHNICAL MEMORANDUM X-53037

April 22, 1964

INTERPARAMETER STATISTICAL ANALYSIS OF
SURFACE WIND SPEED, TOTAL OPAQUE CLOUD
COVER, AND MAXIMUM WIND SPEED ALOFT AT
CAPE KENNEDY, FLORIDA

By

Orvel E. Smith, George C. Marshall Space Flight
Center; Lawrence E. Truppi and Harold L. Crutcher,
U. S. Weather Bureau, National Weather Records
Center, Asheville, North Carolina

ABSTRACT

Provided in this report is a monthly analysis of the statistical relationships of surface wind, winds aloft and total opaque cloud cover at Cape Kennedy. These data are based on five years of record, January 1957 through December 1961, and represent surface observations of wind speed and total opaque cloud cover coincident with RAWIN observations of maximum wind speeds in the 10 to 15 km-layer. Data are presented as percentage occurrence of "go" to "no go" conditions where a favorable combination of all three parameters as to vehicle launch criteria represents a "go" condition, and a combination with one or more parameters unfavorable to vehicle launch is classified as a "no go" condition. The vehicle launch criteria have been arbitrarily chosen for the purpose of this report.

TECHNICAL MEMORANDUM X-53038

April 27, 1964

HYPERSONIC STATIC LONGITUDINAL STABILITY
AND AXIAL FORCE CHARACTERISTICS OF THREE
SATURN IB UPPER-STAGE MODELS

By

David R. Carlson

ABSTRACT

Results of hypersonic wind tunnel tests are reported and analyzed for three Saturn IB second-stage configurations which differ in length and frustum half-angle. The tests were performed in the Arnold Engineering Development Center von Karman Facility (VKF) Tunnel E-2, and spanned a nominal Mach number range of 5 to 8.

Three purposes directed the test program: (1) the establishment of static aerodynamic characteristics of the second stage; (2) the separation of effects of

strakes, Launch Escape System, change in frustum angle, and mission abort; (3) the qualitative determination of the flow fields about these multiple-cone-frustum-cylinder shapes for application to future vehicles. The tests extend earlier supersonic results for the same models to the hypersonic, low-density flow regime.

The amount of flow separation and its location control the aerodynamic characteristics. Large changes in axial force and stability coefficients occur near Mach 5, at which point separated flow from the Launch Escape System completely engulfs the Command Module. High Reynolds number, concomitant with the use of spherical trips, reduces the volume of separated flow and produces large differences in stability and axial force coefficients compared with the low Reynolds number (near full-scale trajectory) results.

Strakes on the Command Module have no significant effect. Jettison of the Launch Escape System, or abort of the Command or Service Module, introduces strong, rather sudden changes in the coefficients. Newtonian impact theory correlates well with the data for tower-off models, where attached-flow concepts are applicable. The degree of simulation of flow fields and vehicle characteristics is argued. It is concluded that the data apply very well at low angles of attack and approximately at intermediate and high angles of attack.

TECHNICAL MEMORANDUM X-53040

April 30, 1964

ATMOSPHERIC ENVIRONMENT FOR SATURN (SA-5) FLIGHT TEST

By

J. W. Smith

ABSTRACT

An evaluation of atmospheric conditions during the flight test of Saturn (SA-5) on January 29, 1964, is presented. The general synoptic situation for the flight area is discussed, surface observations are presented, and upper air data, measured near launch time by rawinsonde and rocketsonde observation, are given. Wind and thermodynamic data are presented graphically and compared to the Patrick Air Force Base reference atmosphere. Atmospheric effects on the performance of Saturn (SA-5) are listed.

TECHNICAL MEMORANDUM X-53041

May 1, 1964

RIGID BODY STUDY OF CONTROL, SEPARATION, AND LIFT-OFF FOR SA-6 VEHICLE

By

E. L. Sullivan, D. O. McNiel, and W. H. Harmon

ABSTRACT

Presented in this report is a rigid body analysis of the dynamics of the control, separation, and lift-off motion of the SA-6 vehicle for the predicted standard trajectory.

A headwind restriction of 27 meters per second is imposed on the vehicle flight in order not to exceed the 5.5 degree angle-of-attack limitation due to structural considerations. The wind restriction is a headwind due to the programmed 4 degree angle-of-attack in the maximum dynamic pressure region. With this wind restriction, the launch probability is still approximately in the 3 σ confidence level for the four months May through August.

Under the disturbances considered in this study, there is no collision or control problem during separation of the S-I/S-IV stages for the predicted SA-6 flight.

The "close" launch support equipment is not an obstacle to the lift-off of the SA-6 vehicle under the disturbances considered. A collision problem with the umbilical tower does exist if control engine no. 1 should fail very early in flight; however, this occurrence must be considered highly improbable.

Report classified (C).

TECHNICAL MEMORANDUM X-53042

May 1, 1964

A TECHNIQUE FOR INCLUDING THE EFFECTS OF VEHICLE PARAMETER VARIATIONS IN WIND RESPONSE STUDIES

By

J. A. Lovingood

ABSTRACT

A method is presented for performing vehicle wind response studies including the effects of variations in vehicle data such as aerodynamic and mass characteristics. These variations are combined in such a manner as to yield a 99.87 percent probability value for the maximum bending moment experienced by the vehicle when flying through a deterministic wind profile. A step-by-step procedure is presented for calculating the moment and other flight dynamics parameters.

TECHNICAL MEMORANDUM X-53048

May 20, 1964

MATHEMATICAL WIND PROFILES¹
PART I

By

Arnold Court, Robert R. Read,² and
Gerald E. Abrahms

Office of the Chief Scientist
Lockheed-California Co.
Burbank, California

ABSTRACT

Augmented Fourier polynomials, in which constant and linear terms have been added to a complex Fourier series, appear to offer a means for representing the vertical profile of the horizontal wind velocity. Reasons for selecting this function, and methods of its computation and application, are given. Polynomial coefficients are presented for mean monthly winds over Cape Kennedy, Florida, and for four consecutive soundings over Montgomery, Alabama.

TECHNICAL MEMORANDUM X-53051

May 27, 1964

¹Prepared under Contract NAS-8-5380 with Aero-Astrodynamics Laboratory, George C. Marshall Space Flight Center, NASA, with O. E. Smith as Technical Supervisor.

²Associate Professor of Mathematics, U. S. Navy Postgraduate School, Monterey, and Consultant to the Lockheed-California Company.

SATURN SA-5 POST-FLIGHT TRAJECTORY

By

Gerald R. Riddle and Michael Naumcheff

ABSTRACT

Presented in this report is the post-flight trajectory for the Saturn SA-5 test flight. Trajectory dependent parameters are given in earth-fixed, space-fixed, and geographic coordinate systems. A complete time history of the powered flight trajectory is presented at 1.0 sec intervals from first motion through insertion. Tables of insertion conditions and various orbital parameters are included in a discussion of the orbital portion of flight. A comparison between nominal and actual trajectory dependent parameters is also presented.

Report classified (C).

TECHNICAL MEMORANDUM X-53053

June 2, 1964

BOOSTER PARAMETRIC DESIGN METHOD FOR
PERFORMANCE AND TRAJECTORY ANALYSIS
PART II. PROPULSION

By

V. Verderaine

ABSTRACT

Approximate equations for large, liquid chemical, rocket engine mass and space envelope are presented in parametric form. Well known propulsion performance equations are given with modifications to admit programming of mixture ratio shifts and throttling of propellant mass flow rate. Parameters used in mass and space envelope equations were nominal input design parameters in common with the propulsion performance equations such that their interdependence could be manifested in a vehicle trajectory and performance optimization study. Though results are based on current type engines, it is expected that coefficients and exponents used may be readily modified to define mass and size of moderately advanced rocket engines.

June 2, 1964

STABILITY ANALYSIS OF SATURN SA-6 WITH
RATE GYRO FOR S-IV CONTROL DAMPING

By

Philip J. Hays

ABSTRACT

A control feedback stability analysis was performed on Saturn SA-6 during S-I and S-IV stage powered flight. Predicted flight damping values were used in the sloshing stability analysis for both stages of flight. Stability was achieved for both stages of flight although marginal stability was observed in the S-IV LOX tank during booster flight. The marginal stability is due to the interaction between the sloshing and the vehicle structure.

Theoretical and experimental bending frequencies were compared during booster flight using the experimentally obtained structural damping. Theoretical bending data were used for the S-IV flight with one percent structural damping assumed.

Bending mode stability was achieved by two methods: phase stabilization and gain stabilization. Gain stabilization was employed for all elastic modes in the roll and α -channels. The φ -channel phase stabilized the first lateral bending mode and gain stabilized the higher modes. The elastic modes in the φ -channel were gain stabilized for the S-IV flight.

TECHNICAL MEMORANDUM X-53055

June 3, 1964

STUDY OF MANNED INTERPLANETARY FLY-BY
MISSIONS TO MARS AND VENUS

By

Rodney Wood, Bobby Noblitt, Archie C. Young,
and Horst F. Thoma

ABSTRACT

This report contains the results of an "in depth" mission analysis study of manned interplanetary

fly-by missions to Mars and Venus during the 1970's using Apollo technology and hardware wherever possible. The usual conic and impulsive velocity techniques were used in this study; however, a precision integrated fly-by trajectory to Mars during the 1975 opposition is included.

TECHNICAL MEMORANDUM X-53056

June 4, 1964

THE AERODYNAMIC CHARACTERISTICS OF
SATURN I/APOLLO VEHICLES (SA-6 AND SA-7)

By

Billy W. Nunley

ABSTRACT

Presented in this report are the final aerodynamic characteristics of the Saturn/Apollo vehicles. These data are based on wind tunnel tests of scale models. Normal force coefficient gradient, normal force coefficient, center of pressure, total power-on and power-off drag coefficient, power-on and power-off base drag coefficient, and forebody drag coefficient are presented for the Mach number range from 0 to 10. Local normal force coefficient distributions are presented for various Mach numbers ranging from 0.20 to 4.96. These data are for zero angle of attack with the exception of the gradients, which are slopes at zero angle of attack, and the normal force coefficients, which are a function of angle of attack.

TECHNICAL MEMORANDUM X-53059

June 8, 1964

SPACE VEHICLE GUIDANCE - A BOUNDARY VALUE
FORMULATION

By

Robert W. Hunt and Robert Silber

ABSTRACT

A mathematical formulation of the problem of guiding one stage of a space vehicle is given as a boundary value problem in differential equations. One approach to the solution of this problem is to generate

the Taylor's series expansion (in several variables) about a known solution. The theoretical nature of such solutions is discussed, and a method for numerically computing them is presented. This method entails the numerical integration of an associated system of differential equations, and can be used to obtain the solution to any desired degree of accuracy for points in a region to be defined. An extension of the method to the problem of guiding several stages of a space vehicle is also given, employing fundamental composite function theory.

TECHNICAL MEMORANDUM X-53062

June 10, 1964

AN AUTOMATED MODEL FOR PREDICTING AEROSPACE DENSITY BETWEEN 200 AND 60,000 KILOMETERS ABOVE THE SURFACE OF THE EARTH

By

Robert E. Smith

ABSTRACT

Described in this report is the derivation of a computer routine for predicting the vertical distribution of aerospace density in the terrestrial space environment above the surface of the earth. Solar activity, geomagnetic storm, diurnal heating, latitude, and the earth's orbital eccentricity effects are included in this model. Densities can be predicted for any time through December 1992.

TECHNICAL MEMORANDUM X-53064

June 16, 1964

LATEST WIND ESTIMATES FROM 80 KM TO 200 KM ALTITUDE REGION AT MID-LATITUDE

By

W. T. Roberts

ABSTRACT

The data from a total of forty rocket launches fired specifically to determine wind characteristics by the release of chemiluminescent trails have been

compiled and studied in an attempt to clarify seasonal and diurnal trends in upper atmospheric winds above 80 kilometers. From a series of graphs taken at 10-kilometer intervals, a general picture of the change in wind vectors with height is determined.

Below 120 kilometers there appears to be extreme variation in speed and direction with very little correlation with season or time of day discernible. Above 120 kilometers, however, the winds appear to orient more with season, and above 150 kilometers, some diurnal variations become apparent.

More experiments of this type, particularly in the summer and winter months, are needed to establish confidence in the seasonal and diurnal trends.

TECHNICAL MEMORANDUM X-53071

June 24, 1964

SA-7 PRELIMINARY PREDICTED STANDARD TRAJECTORY

By

Jerry D. Weiler

ABSTRACT

Presented in this report is the preliminary predicted standard trajectory for Saturn I vehicle SA-7 to be flown over the Atlantic Missile Range. The nominal impact area of the S-I booster, the recoverable camera capsules, and launch escape system are also presented.

A brief discussion of the trajectory shaping and a description of the vehicle configuration are presented.

The nominal trajectory will insert the S-IV stage and payload into a near-circular orbit with a perigee and apogee of 185 km and 217 km altitude, respectively. The nominal lifetime of the orbit is 3.0 days.

The final predicted standard trajectory and dispersion analysis will be published approximately 30 days prior to launch date.

Report classified (C).

TECHNICAL MEMORANDUM X-53072

MULTIPLE BEAM VIBRATION ANALYSIS OF SATURN I AND IB VEHICLES

J. W. Smith

By

ABSTRACT

Larry Kiefling

ABSTRACT

The Saturn is idealized as a system of connected beams and the equations of motion are derived by the use of Lagrange's equation. A method of calculating three-dimensional deflections from the two-dimensional solution is presented. A comparison is made between theoretical results and ten modes from the dynamic test at SA-D6 vehicle at 68 seconds flight condition.

The multiple beam bending vibration program has been developed for analysis of Saturn I and Saturn IB vehicles. The vehicle is represented by a system of nine connected beams, one beam consisting of the vehicle upper stages and the center tank of the booster and each of the other beams consisting of an outer tank of the booster. A vibration analysis is made on each of these beams using a modified Stodola method. The differential equations of motion for the system are then derived by using Lagrange's equation.

Changes have been made to decrease the matrix size while increasing the accuracy of the results. This has been done by the following four measures:

1. Attachment of outer tanks to center tank by rigid links. This permits the use of center tank coordinates in describing outer tank motion, and eliminates eight equations.
2. Addition of a fourth bending mode for the center tank.
3. Addition of a second bending mode for each of the outer tanks.
4. Addition of two degrees of freedom for longitudinal propellant vibration in outer tanks.

TECHNICAL MEMORANDUM X-53118

August 28, 1964

DISTRIBUTION OF SURFACE METEOROLOGICAL
DATA FOR CAPE KENNEDY, FLORIDA

Thermodynamic surface data for Cape Kennedy, Florida, have been analyzed, and are presented graphically in this study. The medians and extremes, plus the cumulative percentage frequency levels of 0.135, 2.28, 15.9, 84.1, 97.72, and 99.865 percent, are shown for temperature, pressure, density, vapor pressure, mixing ratio, enthalpy, refractivity, and relative humidity. These data are presented for hourly, monthly and annual periods, and are discussed briefly.

B. PRESENTATIONS

ON LINEARIZED SUB- AND SUPERSONIC FLOW AROUND PULSATING AND OSCILLATING BODIES

By

Maximilian F. Platzer

The problem of steady linearized sub- and supersonic flow around low aspect ratio bodies at zero and small angles of attack has been treated by M. Munk, H. S. Tsien, R. T. Jones, G. N. Ward, M. C. Adams, W. R. Sears, F. Keune, K. Oswatitsch, M. A. Heaslet, and H. Lomax. It is shown that in a first approximation the flow over bodies at small angles of attack can be replaced by the two dimensional cross-flow only (Munk-Jones slender body theory); whereas, for the flow around bodies at zero angle of attack, a spatial influence has to be added. K. Oswatitsch was able to show that the spatial influences of low aspect ratio wings and bodies of revolution are the same for bodies with equal cross-sectional area (Oswatitsch's equivalence rule).

The extension of these results to not so slender bodies has been obtained by M. C. Adams-W. R. Sears, and F. Keune using two basically different methods. M. C. Adams-W. R. Sears apply Laplace or Fourier transforms to the linearized potential equation with respect to x . Expansion and inversion of the appropriate solution give the higher order flow terms. This procedure is purely mathematical. F. Keune, on the other hand, develops an elementary and physically more appealing approach to the problem by using the local source-strength, the sum of the sources over the cross section, and the higher order moments of these quantities.

The present investigation is based upon the unsteady linearized potential equation. The time dependence is assumed to be purely harmonic. The objective of this paper is the extension of Oswatitsch's and Keune's results to the flow around pulsating and oscillating bodies. It is shown that the sub- and supersonic flow around low aspect ratio wings, whose skin executes symmetric pulsations, is in a first approximation given again by two terms; namely, a cross-flow and a spatial influence. This spatial influence reduces the flow around pulsating wings to the flow around the equivalent pulsating body of revolution.

Thus, a surprisingly simple approximation theory for pulsating low aspect ratio bodies has been found which may have some importance for panel flutter problems. The range of validity of this theory can be extended by considering also the higher order terms. These terms can again be obtained by generalizing either the Adams-Sears method, or the Keune method to pulsating flow. Both methods give the same results. The interpretation after Keune is advantageous, however, showing that the higher order terms also consist of a generalized cross-flow and a generalized spatial influence.

The insight gained for the pulsating body can be extended in an elementary way to the case of the oscillating body. Here, the first order approximation is given by the cross flow only (Garlick-Miles solution); but in the second order approximation, a spatial influence has to be added and an equivalence rule can be postulated also for this case.

Finally, these approximation theories are applied to cases where exact solutions of the linearized potential equation can be found. This is possible for the infinitely long tube and ribbon exhibiting a harmonic standing pulsation or oscillation. These solutions give insight not only into the range of validity of the approximate theories developed in this paper, but show also the transition to piston theory.

Presented at the German Institute of Aeronautics and Astronautics, Aachen, Germany, on June 30, 1964.

ON LINEARIZED SUB- AND SUPERSONIC FLOW AROUND PULSATING AND OSCILLATING BODIES

By

Maximilian F. Platzer

Presented in partial fulfillment for Ph.D. at Vienna Institute of Technology, Vienna, Austria, in February 1964.

AMPLITUDE DEPENDENT STATIC HYSTERESIS DAMPING AS A MODEL FOR EARTH MATERIALS

By

Richard D. Rechten

A general theory is presented for the description of the propagational characteristics of seismic wavelets in earth materials. From the general development of the theory, it is shown that no linear theory can ever predict the observed wavelet characteristics. However, the inclusion of a near-arbitrary, high frequency dissipation function in the wave equation permits a linear theory to be applicable at arbitrarily low frequencies.

The dissipation mechanism assumed operative in the seismic range is taken to be linearly dependent on the induced strain amplitude. This model essentially describes the irrecoverable plastic deformation due to local, high intensity stress at crystal boundaries. A comparison of theoretical and experimental wavelet behaviors is given, and the effects of nonlinearities are discussed.

Presented in partial fulfillment for Ph.D. at Washington University, St. Louis, Missouri, on June 12, 1964.

A SEMIEMPIRICAL DETERMINATION OF ALPHA PARTICLE ENERGIES AND HALF-LIVES IN THE HEAVY ELEMENT REGION

By

Barton Scott Perrine II

The parameters for a mass formula were determined by empirical methods for the region of nuclides with $N > 126$ and $Z > 82$. By using this newly determined mass formula, alpha particle energies were predicted for this region. With these alpha particle energies the half-lives were found using a modification of a relation developed by Bethe between half-life and alpha decay energy.

The parameters associated with the liquid drop model were not changed significantly from previous values. However, the parameters for the correction terms were changed enough to yield somewhat better predictions for alpha particle energies than the older parameters. The root-mean-square error for the alpha particle energies was less than .2 Mev. The errors in the predictions for the half-lives were quite

large but these results should still be useful in determining the methods to use in looking for alpha decay in this region.

Presented in partial fulfillment for M. S. at Oklahoma State University, Stillwater, Oklahoma, on May 24, 1964.

WALL PRESSURE FLUCTUATIONS AND SKIN VIBRATIONS WITH EMPHASIS ON FREE SHEAR LAYERS AND OSCILLATING SHOCKS

By

Fritz R. Krause

Ever since the failure of the first Centaur flights, high frequency skin vibrations have been of much concern. Large wall pressure fluctuations below separated flows and oscillating shocks lead to a dangerous resonance excitation over the entire transonic and supersonic portion of the flight. A new relation between pressure and force correlations has been established for inhomogeneous turbulence in order to account correctly for the largest pressure fluctuations below oscillating separation and reattachment lines. It shows that the power spectra of the generalized forces can be found from rigid model tests by a curve fit of a special pressure cross correlation function. However, a curve fit of experimental pressure correlations is useful only as long as the statistical error of a cross correlation estimate is smaller than the numerical error of the curve fitting procedure. Non-linear transfer functions and dynamic shifts in presently available pressure transducers and tape recorders are so large that the more refined force estimates, which consider the spatial structure of the pressure field, might lead to ambiguous results.

Presented at the Sixty-Seventh Meeting of the Acoustical Society of America, New York, New York, May 6-9, 1964.

PERFORMANCE OF THE MISTRAM TRACKING SYSTEM AT ELEVATION ANGLES LESS THAN FOURTEEN DEGREES

By

Max A. Horst

Presented in this paper is the cyclic and random error buildup at low elevation angles for the MISTRAM

tracking system. The error buildups are based on actual SA-5 final tracking data. The results of a Fourier analysis on MISTRAM velocity data are also presented.

Presented at the MISTRAM Technical Working Group Meeting, Cocoa Beach, Florida, on April 30, 1964.

A SURVEY OF METHODS FOR GENERATING LIAPUNOV FUNCTIONS

By

C. C. Dearman and A. R. Lemay

The principal difficulty encountered in applying Liapunov's second method to determine the stability properties of nonlinear dynamical systems lies in generating suitable Liapunov's functions. An extensive study of the several methods of generating these functions has been made and from these methods the most promising for use in investigating the stability properties of the differential equations of motion of a guided space vehicle have been selected. The derivation of the methods in this sub-class and the differential equations to which they are applicable is the subject of this survey.

Presented at the Conference on Mathematical Methods of Celestial Mechanics and Astronautics and Related Questions of Numerical Mathematics, Oberwolfach-Walke, Germany, March 15-21, 1964.

VARIABLE POROSITY WALLS FOR TRANSONIC WIND TUNNELS

By

A. Richard Felix and J. W. Davis

Recently, variable porosity walls were installed in the transonic test section of the 14 x 14 Inch Transonic Tunnel at Marshall Space Flight Center. Evaluation tests indicated that use of these walls greatly improve the ability of this facility to produce reasonably accurate model pressure distribution data throughout the critical and difficult Mach number range from 1.0 to 1.25. The evaluation was accomplished by comparing pressure distributions for a 20 degree cone-cylinder model with interference free data for the same model. The range of porosities utilized is between 0.5 percent and 5.4 percent with the holes being 60 degrees slanted.

Presented at the Twenty-First Semi-Annual Meeting of the Supersonic Tunnel Association, Princeton, New Jersey, in April 1964.

APOLLO LOGISTIC SUPPORT SYSTEM

By

Herbert Schaefer and Leonard S. Yarbrough

One possible conceptual definition of an early Apollo Logistics Support System (ALSS) is presented and various payloads for the System are briefly discussed. A more detailed discussion of one payload, a Lunar Mobile Laboratory (MOLAB), is given, including a summary discussion of the major sub-systems and critical features. Some of the considerations for planning a lunar scientific mission are discussed. A hypothetical traverse and general operations plan for the MOLAB are defined in a manner suitable for mission optimization, once valid design data becomes available. Some aspects of the MOLAB testing program are presented. It is concluded that this system appears feasible and the problems which presently confront its design and development do not seem insurmountable.

The ideas expressed herein are those of the authors and should not be construed as being official NASA policy.

Presented at the Tenth Annual Meeting of the American Astronautical Society on May 7, 1964.

SATURN I FLIGHT TEST EVALUATION

By

Dr. F. A. Speer

Presented in this paper is, in very condensed form, a representative cross section of the major Saturn I flight test achievements. The Saturn I flight test program discussed includes the first five flights, launched between October 1961, and January 1964. The overall Saturn I test program is discussed briefly along with the resources available for flight testing.

The report also contains many illustrations which are indicative of the type of information which is being compiled and utilized, from the rough estimate of 550 million bits of information received from these flights, in designing and building the two major NASA launch vehicles of the future: the Saturn IB and the Saturn V.

Presented at the First Annual Meeting and Technical Display (AIAA), Washington, D. C., June 28-July 2, 1964.

SIMULATION OF THE SATURN V VEHICLE ON THE ELECTRONIC ANALOG COMPUTER

By

Dieter Teuber

The development of large space vehicles of the Saturn V type presents numerous problems not encountered in the development of smaller missiles. The increase of dynamic analysis efforts is apparent if the effect of atmospheric disturbances on a nonlinear controlled space vehicle is studied. Because of the uncertainty in predicting the nature of atmospheric disturbances, statistical methods are used. The GPS high speed repetitive analog computer is suited for the task to evaluate thousands of solutions for the overall system performance of the Saturn V.

The systems of differential equations describing the behavior of the Saturn V are represented. With the addition of bending and sloshing modes, the problem is represented on the analog computer by a 12-degrees-of-freedom simulation. Driving function of this set of equations is wind magnitude as function of the flight time. A reel-to-reel tape recorder is used for measured wind profiles. In a different approach, the statistical driving function is generated from a noise generator and shaping filters based on the spectral characteristics and amplitude distribution of wind. Exceedances of maximum values for the bending moment, engine deflection or angle of attack are registered by the analog computer. Thus, an optimization by changing control parameters becomes feasible. Methods of programming the analog computer and typical transients during powered flight of the Saturn V are represented.

Presented at the Hermann Oberth Society, Darmstadt, Germany, on June 24, 1964.

FAR-FIELD SOUND PROPAGATION AS RELATED TO SPACE VEHICLE STATIC FIRINGS

By

Orvel E. Smith

As space vehicle boosters become larger in thrust, the emitted sound energy that is propagated

through the atmosphere becomes of greater concern to the organizations performing the static firings due to disturbance or nuisance to the near-by communities. Far-field sound intensity levels are calculated using the inverse square law and theoretical model based on the acoustical equivalence to Snell's refraction law. The theoretical model requires a knowledge of the sound source intensity and the velocity of sound profile. This model requires accurate measurements of the vertical structure of virtual temperature, wind speed and direction from which the velocity of sound profile is derived. The necessary simplifying assumptions used in deriving the theoretical model will be discussed. The sound intensity level as derived from the theoretical model and empirical measurements from an acoustical horn and the static firings of the Saturn booster are compared. Practical operational techniques used in performing atmospheric measurements, atmospheric predictions, and sound intensity level calculations for the static firing of large boosters are discussed.

Presented at the Fifth AMS Conference on Applied Meteorology - Atmospheric Problems of Aerospace Vehicles, Atlantic City, New Jersey, March 2-6, 1964.

AN EVALUATION OF VARIOUS GEOMAGNETIC FIELD EQUATIONS

By

Harold C. Euler

The dipole and multipole approximations of the earth's main magnetic field are evaluated using Jensen and Whitaker's 568 Gaussian coefficients for Epoch 1955.0. The total geomagnetic field, which was computed to 16 earth radii for various geographic locations, is compared to values computed with the inverse cube law and to some of the Vanguard III geomagnetic field observations.

Presented at the National Annual Meeting of the American Geophysical Union, Washington, D. C., April 22-25, 1964.

PROPOSED SOLUTION TO THE GEOMAGNETIC ANOMALIES IN THE IONOSPHERE

By

William T. Roberts

In order to determine the driving and controlling mechanisms which predominate in the ionosphere, a series of contour maps was drawn from IGY data taken at stations lying approximately along the seventy-fifth meridian. An attempt was then made to interpret the anomalous behavior of the F_2 peak of the ionosphere in the vicinity of the geomagnetic equator. If one assumes the existence of an equatorial electrojet and further assumes that the magnetic field which is associated with this electrojet is sufficient to perturb the earth's main magnetic field, electrons may be deflected away from the geomagnetic equator. Furthermore, if the atmosphere tends to expand and contract diurnally, ions and electrons may be deflected into regions at times which could account for the nocturnal increase in electron density north and south of the geomagnetic equator. Special emphasis is placed upon this nocturnal increase in electron density, and when its seasonal variation is investigated one finds that the phenomenon is greatest during and around the months of equinox and least so during and around the months of solstice.

Presented at the National Annual Meeting of the American Geophysical Union, Washington, D. C., April 22-25, 1964.

SPHERICAL BALLOON WIND SENSOR BEHAVIOR

By

James R. Scoggins

An analysis is presented which shows the response characteristics of freely rising superpressure spheres of different configurations. Wind profile data measured by the superpressure balloon method, the smoke trail method, the AN/GMD-1 rawinsonde system, and from low level open air tests were used in the analysis. Results are reported on data measured at Huntsville, Alabama, at night during stable conditions to an altitude of 120 m and at Cape Kennedy to an altitude of 12 km. The results show that (1) the average drag curve for a freely rising 2-m diameter, smooth superpressure sphere differs considerably from the drag curve obtained in wind tunnels using smaller spheres; the average value of the drag coefficient is larger over all Reynolds numbers except near the transition region; (2) the drag coefficient for roughened spheres is nearly independent of the Reynolds number but decreases slightly as the Reynolds number decreases; (3) by the addition of surface roughness elements the aerodynamically induced horizontal

motions of the smooth sphere are reduced; and (4) the average aerodynamic lift force, which acts primarily in the horizontal direction and is responsible for the aerodynamically induced horizontal motions, is negligible indicating that it does not act in any preferred

direction.

Presented at the Fifth AMS Conference on Applied Meteorology - Atmospheric Problems of Aerospace Vehicles, Atlantic City, New Jersey, March 2-6, 1964.